

Tuning the amphiphilicity of graphene oxide and reduced graphene oxide for controllable assembly and architectural design

Yiwen Chen, M. Eng.



McGill

Department of Mining and Materials Engineering McGill University,
Montreal, Canada

March 2023

A thesis submitted to the Faculty of Graduate and Postdoctoral Studies of McGill
University in partial fulfillment of the degree of Doctor of Philosophy

© Yiwen Chen, 2023

Abstract

Graphene-based materials have gained great interest for broad applications. Both two-dimensional (2D) and three-dimensional (3D) graphene-based materials can be fabricated using inexpensive and sustainable approaches, starting from graphene oxide (GO) and reduced graphene oxide (rGO) sheets as building blocks. The architecture and composition of final products can be tailored to the desired application by controlling sheet assembly.

The amphiphilicity of GO and rGO directly affects their surface activity. By tuning the amphiphilicity, one can control the assembly of sheets at interfaces or in response to environmental stimuli. In this thesis, we conducted two studies to control the assembly of GO at interfaces of Pickering emulsions to develop GO and rGO materials designed for bone tissue engineering (BTE) and seawater electro-oxidation applications. In a third study, we demonstrated temperature responsive rGO self-assembly by a combination of surface modification and supramolecular design. Through these studies, we controlled GO and rGO assembly by tuning amphiphilicity and developed facile strategies to build graphene-based materials with architectures tailored for specific applications.

Our first study introduced a dual-templating approach to creating GO, rGO, and composite scaffolds with interconnected pores, hierarchical porosity and tunable compositions for BTE. To promote bone regeneration, BTE scaffolds should have interconnected, large pores for cell infiltration, and small pores for molecular diffusion. However, this ideal structure of graphene scaffolds had not been achieved in prior works. To fill this gap, we developed high internal phase emulsions (HIPEs) in which GO sheets serve as both emulsion stabilizers and building blocks for scaffolds. Upon freezing and drying the emulsions, large pores are templated by the oil droplets, and small pores form by ice crystal templating in water, whose size can be controlled by the

freezing temperature. We showed that GO scaffolds with architectures tailored for BTE are excellent substrates for mesenchymal stem cell (MSC) penetration and growth.

In our second study, motivated by the desire to suppress interfering reactions in seawater electrolysis, we aimed to prevent the diffusion of Cl^- by developing an electrode architecture with cobalt oxide catalytic particles selectively deposited on the internal walls of closed rGO pores. By adjusting the GO assembly on emulsions, we generated closed pores templated by oil droplets, enclosing Co_3O_4 particles that were dispersed in oil. After reduction, the rGO pore walls are permeable to water and gases while limiting the diffusion of Cl^- to the catalyst. This prevents competition from Cl^- in water electro-oxidation, allowing direct application of these anodes for seawater oxidation.

In the last study, we studied the temperature responsive rGO self-assembly. Temperature response of rGO was achieved without introducing a responsive polymer or multistep synthesis. Through the reduction of GO by dopamine, we obtained rGO sheets modified with polydopamine (PDA), which formed stable aqueous suspensions. The rGO/PDA sheets include hydrophobic rGO domains and hydrophilic PDA clusters, mimicking the amphiphilic structure of temperature responsive poly (N-isopropylacrylamide) (PNIPAM). Upon heating to 30 °C, the hydrogen bonds between PDA and water break, and rGO sheets start assembling due to hydrophobic and π - π interactions. The self-assembly in response to heat enhances rGO sheet alignment, resulting in higher electrical conductivity of 2D nacre-like rGO films and smaller pore size in 3D porous rGO monoliths upon drying rGO/PDA suspensions. This work is the first to show temperature response in graphene achieved through a supramolecular strategy. Through a one-step surface modification, the strategy integrates two non-responsive components and exploits the interactions between surface-modified rGO sheets to achieve responsive self-assembly.

Résumé

Les matériaux à base de graphène ont suscité un grand intérêt pour beaucoup des applications. Les matériaux en graphène 2D et 3D peuvent être fabriqués de manière peu coûteuse et durable, avec des feuilles d'oxyde de graphène (GO) et réduites (rGO) comme blocs de construction. L'architecture et la composition des produits finis peuvent être adaptés à l'application souhaitée en contrôlant l'assemblage. L'amphiphilie de GO et rGO affecte directement leur activité de surface. En réglant l'amphiphilie, on peut contrôler l'assemblage aux interfaces ou en réponse aux stimuli environnementaux. Dans cette thèse, nous avons mené deux études pour contrôler l'assemblage de GO dans les émulsions de Pickering pour développer des matériaux de graphène pour le génie des tissus osseux (BTE) et des applications d'électro-oxydation de l'eau de mer. Dans la troisième étude, nous avons démontré l'auto-assemblage rGO réactif à la température via la modification de la surface et la conception supramoléculaire. Grâce à ces études, nous avons contrôlé l'assemblage de GO et de rGO en ajustant l'amphiphilie et développé des stratégies faciles pour construire des matériaux en graphène avec des architectures adaptées.

La première étude a introduit une approche à double modèle pour la création de stands GO, rGO et composite avec des pores hiérarchiques interconnectés et des compositions réglables pour BTE. Pour la régénération osseuse, les fauteuils doivent avoir des pores interconnectés, de grands pores pour l'infiltration cellulaire, et de petits pores de diffusion de la matière. Cependant, la structure idéale des fauteuils en graphène n'a pas été atteinte. Pour combler cette lacune, nous avons développé des émulsions à phase interne élevée où GO agit à la fois comme stabilisateurs et comme blocs de construction. Lors du gel et du séchage, de grands pores sont moulés par des gouttes d'huile, et de petits pores se forment par moulage de glace, dont la taille peut être contrôlée par la

température. Nous avons montré que les fauteuils GO avec des architectures adaptées à BTE sont d'excellents substrats pour la pénétration et la croissance des cellules souches.

Dans la deuxième étude, afin de supprimer les réactions d'interférence dans l'électrolyse de l'eau de mer, nous avons visé à prévenir la diffusion de Cl^- en développant une architecture avec des particules catalytiques déposées sur les parois internes des pores rGO fermés. Avec les émulsions GO, nous avons généré des pores fermés moulés par des gouttes d'huile, piégeant les particules de Co_3O_4 dans l'huile. Après réduction, les parois des pores rGO sont perméables à l'eau et aux gaz tout en limitant la diffusion de Cl^- au catalyseur. Cela empêche la concurrence de Cl^- dans l'électro-oxydation, ce qui permet une application directe pour l'oxygénation de l'eau de mer.

Dans la dernière étude, nous avons étudié l'auto-assemblage rGO réactif à la température. La réponse de température de rGO a été obtenue sans polymère réactif ou synthèse multistep. Grâce à la réduction de GO par la dopamine, nous avons obtenu rGO/PDA dans des suspensions aqueuses stables. Les feuilles ont des domaines rGO hydrophobes et des clusters PDA hydrophiles, imitant la structure amphiphile du réactif à la température poly(N-isopropylacrylamide). À 30 °C, les liaisons d'hydrogène entre le PDA et l'eau se brisent et les feuilles s'assemblent en raison des interactions hydrophobes et π - π . L'assemblage réactif améliore l'alignement de la feuille rGO, ce qui entraîne une conductivité électrique plus élevée des films 2D et une taille des pores plus petite dans la rGO poreuse 3D. Ce travail est le premier à montrer la réponse de température du graphène obtenue dans une stratégie supramoléculaire. Grâce à une modification en un pas de la surface, la stratégie intègre deux composants non réactifs et exploite les interactions entre les feuilles rGO modifiées par la surface pour obtenir un auto-assemblage réactif.

Acknowledgement

Foremost, I would like to express my deepest gratitude to my supervisors, Prof. Marta Cerruti and Prof. Thomas Szkopek, for giving me the opportunity to explore the exciting field of graphene and materials science and to work in such an innovative, collaborative, and inclusive environment. Your unlimited guidance, patience, commitment to students, and enthusiasm for science have all taught me a lot and always motivated me to do my best. Thank you for consistently encouraging me to go beyond and dare to dream, to believe in myself, and to pursue excellence throughout the last five and a half years. It's my true privilege to work and learn under your supervision.

My thanks also go to our collaborator, Prof. Simon D. Tran, for the guidance on the cell-culture experiments in his lab. I appreciate the supportive atmosphere in your lab and the help your lab members gave me. A special thanks to Dr. Xinyun Su for the great time learning and working with you. I would like to also thank Dr. Gabriele Capilli, for all the enlightening discussions, the positive attitude, the sharing of your insights and knowledge and the great teamwork!

I'm also grateful to my advisory committee: Prof. Showan Nazhat, Prof. Kirk H. Bevan, Prof. Nate Quitoriano, Prof. Kristian Edmund Waters, and Prof. Jun Song. Your profound knowledge, professionalism, and inspiring advice greatly helped me move forward during this journey.

I would like to thank Prof. Dmitrii Perepichka, Prof. Nathalie Tufenkji, Prof. Matthew J. Harrington, and Prof. Noémie-Manuelle Dorval Courchesne for providing me access to the equipment in your labs. I appreciate the help and coordination from your lab members, especially Ehsan Hamzehpoor, Dr. Rafael Kurusu, Mostafa Rammal and Masoud Aminzare.

My thanks extend to Department of Mining and Materials Engineering at McGill University, and various facilities where I conducted my research inside and outside McGill. I sincerely thank the amazing people who helped and assisted me: Dr. Lihong Shang, Dr. Hatem M. Titi, Mr. Petr

Fiurasek, Ms. Mohini Ramkaran, Dr. Ning Zhu, Mr. Omar Marinos, Dr. Adam Webb, Dr. Sergey Gasilov, Ms. Barbara Hanley, and many others.

I would like to acknowledge funding sources that supported this project: Natural Sciences and Engineering Research Council of Canada (NSERC), the Canada Research Chair Foundation, the Fonds de Recherche du Québec–Nature et Technologies (FRQNT Doctoral research scholarship), McGill Engineering Doctoral Award (MEDA), McGill Graduate Excellence Award, and Canadian Biomaterials Society Merit and Travel Award.

My thanks also go to all the current and former members of Biointerface Lab and Nanoelectronics devices and Materials Lab, especially Dr. Kaiwen Hu, Minh Tran, and Dr. Siyu Liu for sharing your time, knowledge, and skills with me. A very special thank you go to my dear friends at McGill University: Sophia, Emily, Ophélie, Danae, Marianna, Mojdeh, Zewei, Bo, Lei, Yang, Richard, Hao, Tao, Yiqing, Rapheala. Thank you for the treasurable memories and your moral support. You made my Ph.D. a beautiful journey.

I would like to thank my supervisors of master's degree, Prof. Ning Ma and Prof. Yapei Wang, you introduced me to the research world, showed me how fascinating science is, encouraged me to pursue my dreams, and led me to where I am. Thank you!

Last but certainly not the least, I would like to thank my husband and dearest friend, Zhida, for the laughs and travels we had, every little thing you do for me every day, and for always being by my side. I acknowledge my parents, my parents-in-law, my family and friends. A special thank you to my mom, for your caring, open heart, and unconditional love. To my grandparents, who instilled in me at a young age a powerful philosophy, “there are always solutions.”

Table of contents

Abstract	i
Résumé	iii
Acknowledgement	v
Table of contents	vii
List of Figures	xii
List of Tables	xxvii
Contributions of authors	xxviii
1 General introduction	1
1.1 Background and motivation	1
1.2 Research objectives.....	6
1.3 Thesis outline	8
2 Literature review	9
2.1 Chemistry of graphene oxide	10
2.1.1 Synthesis of GO	10
2.1.2 Structure and chemistry of GO	15
2.1.3 GO colloidal stability	19
2.1.4 Amphiphilicity of GO	23
2.2 Pickering emulsions stabilized by GO	26
2.2.1 First-principle study of emulsions stabilized by Pickering particles	26

2.2.2	Factors affecting GO Pickering emulsions	31
2.3	Towards porous architectures: GO assembly templated by Pickering emulsions	36
2.3.1	Preparation of GO Pickering emulsion templates for porous materials	37
2.3.2	Post-emulsification treatments: reduction and drying methods.....	45
2.4	Stimuli-responsive GO systems.....	52
2.4.1	pH or light responsive GO and rGO systems.....	53
2.4.2	Temperature responsive polymer: PNIPAM	57
2.4.3	Functionalization of GO and rGO for temperature responsive systems.....	59
2.5	Polydopamine functionalization of GO and rGO	66
2.5.1	Dopamine polymerization and chemistry of PDA.....	66
2.5.2	PDA and surface modification of GO.....	69
2.5.3	PDA composites with GO or rGO	71
2.6	Summary.....	75
3	Dual-templating strategy for the fabrication of graphene oxide, reduced graphene oxide and composite scaffolds with hierarchical architectures	77
3.1	Abstract.....	78
3.2	Introduction.....	78
3.3	Material and methods.....	80
3.3.1	Materials	80
3.3.2	Preparation of GO/CTAB suspensions	81
3.3.3	Preparation of GO HIPEs.....	81
3.3.4	Preparation of GO scaffolds, 2D GO membranes and rGO scaffolds	81

3.3.5	Preparation of GO composite scaffolds	82
3.3.6	Cell proliferation, morphology and infiltration	84
3.3.7	Characterization	85
3.4	Results and discussion	88
3.4.1	Strategy and formation of GO/CTAB HIPEs	88
3.4.2	GO based scaffolds	92
3.4.3	Stabilization of GO scaffolds in aqueous medium and cell culture.....	96
3.4.4	Versatility of the dual-templating strategy	100
3.5	Conclusions.....	107
3.6	Acknowledgement	108
3.7	Supporting information.....	109
4	Selective catalytic electro-oxidation of water with cobalt oxide in ion impermeable reduced graphene oxide porous electrodes.....	126
4.1	Abstract.....	126
4.2	Introduction.....	127
4.3	Results and discussion	129
4.3.1	General procedure of rGO/cobalt oxide electrode fabrication.....	129
4.3.2	Modification and characterization of Co_3O_4 and GO emulsions	131
4.3.3	Structural and physicochemical characterization of rGO/CoOx aerogels	134
4.3.4	Selective electrocatalytic water oxidation on rGO/CoOx electrodes	140
4.4	Conclusions.....	148

4.5	Methods.....	150
4.5.1	Chemicals and materials	150
4.5.2	Cobalt oxide-in-hexane dispersion	150
4.5.3	Graphene oxide dispersion and GO/Co ₃ O ₄ emulsions.....	150
4.5.4	rGO and rGO/CoOx macroporous aerogels.....	151
4.5.5	rGO and rGO/CoOx electrodes.....	151
4.5.6	Physicochemical and structural characterization	152
4.5.7	Electrochemical characterization	154
4.5.8	Selective electrocatalytic water oxidation by rGO and rGO/CoOx electrodes.....	155
4.6	Acknowledgement	157
4.7	Supporting information.....	158
5	Temperature responsive self-assembly of polydopamine reduced graphene oxide	173
5.1	Abstract.....	174
5.2	Introduction.....	175
5.3	Results and discussion	178
5.3.1	Fabrication and characterization of rGO modified with PDA	178
5.3.2	Temperature induced self-assembly	180
5.3.3	Controlled structure of 2D and 3D materials via temperature induced self-assembly	186
5.4	Conclusions.....	189
5.5	Methods.....	189
5.5.1	Materials	189
5.5.2	Preparation of polydopamine modified GO and rGO suspensions.....	190

5.5.3	Fabrication of RP50 porous monoliths and films	190
5.5.4	Characterization	191
5.6	Acknowledgement	193
5.7	Supporting Information.....	194
6	Contributions to original knowledge.....	201
7	General discussion and conclusions	204
7.1	General discussion	204
7.2	Conclusions.....	214
8	Copyright permissions.....	216
9	References	217

List of Figures

- Figure 2.1.** (a) GO chemistry control through modified Hummer's methods. Adapted from Reference (Ref.) [61] with permission from the Royal Society of Chemistry. (b) Proposed mechanism for water-enhanced oxidation of graphite as shown in Figure 2.1a, 1. GrO: graphite oxide [61]. (c) Scanning electron microscope (SEM) image of GO pieces as results of over-oxidation at high temperature. Reprinted with permission from [62]. Copyright 2010 American Chemical Society. 12
- Figure 2.2.** (a) Schematic of bulk graphite's conversion into GO with corresponding micrographic images or sample appearances at each phase during synthesis using modified Hummers' method. The steps signify formation of the two intermediate products (stage-1 GIC and PGO) and the final GO product. The solid black lines represent graphene layers; dotted black lines represent single layers of GO; wide blue lines represent $\text{H}_2\text{SO}_4/\text{HSO}_4^-$ intercalant; wide purple lines represent a layer of the mixture of $\text{H}_2\text{SO}_4/\text{HSO}_4^-$ intercalant with the reduced form of the oxidizing agent. Reprinted with permission from Ref. [65]. Copyright 2014 American Chemical Society. (b-c) SEM images of graphite particles during oxidization. Reprinted with permission from Ref. [66]. Copyright 2011 American Chemical Society. (d) Schematic of crack propagation and penetration of oxidizing solution during the oxidation of a graphite [66]. 14
- Figure 2.3.** Lerf-Klinowski model of GO. Reproduced from Ref. [5] with permission from the Royal Society of Chemistry. 16
- Figure 2.4.** (a) A GO flake suspended on a carbon grid under TEM. Reprinted with permission from Ref. [84]. Copyright 2016 American Chemical Society. (b-c) SAED patterns showing polycrystallinity in a region of about 200 nm (b), in a larger region (c) indicated by the yellow circle in panel (a) [84]. (d) SAED patterns showing sharp spots of monocrystalline for monolayer graphene [84]. (e-f) High resolution TEM (HR-TEM) images of single suspended GO sheet (e) and single suspended graphene sheet (f). The sp^2 graphene, the oxidized sp^3 regions and holes are indicated in green, pink and blue respectively. Reproduced with permission from [85]. Copyright 2010 WILEY - VCH Verlag GmbH & Co. KGaA, Weinheim. (g) HR-TEM images of single suspended GO sheet in the middle. (A.): oxidized region image (left), proposed possible atomic structure (middle) (carbon in gray, oxygen in red), and the average of a simulated TEM image that agrees with the TEM image (right); (B.): partially oxidized regions image (top), proposed possible atomic structure (middle) and the average of a simulated TEM image (down); (C.): sp^2 graphene region image (left) and atomic structure (right). Scale bar in panels e-g = 2 nm [85]. 17
- Figure 2.5.** (a) AFM image of GO sheets and height profile. Scale bar = 2 μm [89]. (b) HR-TEM image color-coded to represent monolayer regions (blue, and pink) and multilayer regions (purple, yellow, orange and green). Scale bar = 2 nm. Adapted with permission from Ref. [84]. Copyright 2016 American Chemical Society. (c) Concentration of ionized groups measured by sodium binding isotherm as a function of pH for GO. The inset shows the pK distribution of the oxygen-containing groups. The fitted curve is shown in red, and the individual Gaussians are shown as dashed lines. Adapted with permission from Ref. [90]. Copyright 2012 American Chemical Society. (d) Cartoon representation (carbon, gray; oxygen, red; hydrogen, blue) of the sequence of ionization of carboxyl and hydroxyl groups at the indicated pH values. The ionized groups are highlighted [90]. 18
- Figure 2.6.** (a) GO deprotonation of the carboxylic acid groups at the edges and hydroxyl groups on plane as pH increases. Adapted with permission from Ref. [96]. Copyright 2013 American

Chemical Society. (b) Photograph illustrating the influence of pH on the aggregation behaviors of GO suspension after 24 h. GO concentration = 0.01 g/L [96]. (c) Zeta potential of GO and rGO aqueous dispersion as a function of pH. The rGO was reduced by hydrazine (N₂H₄) from GO suspension. Adapted with permission from Ref. [90]. Copyright 2012 American Chemical Society. (d) Aggregation modes of GO [96]. (e) Photograph illustrating the influence of monovalence (Na⁺) and divalence (Mg²⁺ and Ca²⁺) on aggregation behaviors of GO after 2 h [96]. (f) Zeta potential of GO in different electrolytes (Na₂SO₄, MgSO₄) as a function of salt concentration. GO concentration = 0.05 g/L. Adapted with permission from Ref. [97]. Copyright 2018 Elsevier B.V.. (g) Concentration of ionized groups measured by sodium binding isotherm as a function of pH for rGO. The inset graph shows the pK distribution of the oxygen-containing groups. The fitted curve is shown in red, and the individual Gaussian is shown in black. The rGO, namely N₂H₄-rGO, was reduced by hydrazine from GO suspension. Adapted with permission from Ref. [90]. Copyright 2012 American Chemical Society. Inset photograph shows hydrazine reduced rGO in water. Adapted with permission from Ref. [100]. Copyright 2011 Elsevier Ltd.. (h) Cartoon representation (carbon, gray; oxygen, red; hydrogen, blue) of the ionization of carboxyl groups of rGO obtained by hydrazine reduction, at the indicated pH values. The ionized groups are highlighted [90]. (i) EPM as a function of pH. GO or rGO concentration = 0.01 g /L. The rGO named as VC-rGO, NaBH₄-rGO, and N₂H₄-rGO correspond to reduction of GO in water by ascorbic acid (VC), NaBH₄, and N₂H₄, respectively. Reproduced from Ref. [101] with permission from the Royal Society of Chemistry. (j) EPM as a function of NaCl concentration. pH was 5.6 ± 0.2 for GO, 5.5 ± 0.2 for VC-rGO, 6.0 ± 0.2 for NaBH₄-rGO, and 6.0 ± 0.2 for N₂H₄-rGO. Error bars indicate standard deviation of at least three measurements [101]. Inset: photograph of VC-rGO suspension in water. Reproduced from Ref. [102] with permission from the Royal Society of Chemistry..... 21

Figure 2.7. (a) Photographs of GO in water and organic solvents after ultrasonication for 1 h. Top: immediately after sonication. Bottom: 3 weeks after sonication. Adapted with permission from [106]. Copyright 2008 American Chemical Society. (b) Photographs of rGO in organic solvents after ultrasonication for 1 h. Top: immediately after sonication. Bottom: 24 h after sonication. Adapted with permission from Ref. [109]. Copyright 2014 Elsevier Inc..... 23

Figure 2.8. (a) Illustration showing the flotation of GO in carbonated water. GO was first captured by the rising CO₂ bubbles and then transported to the water surface. (b) Brewster angle microscopy (BAM) images without (left) and with (right) GO on the surface. As GO flakes floated up to the air-water interface, the surface refractive index changed, allowing the observation of GO through BAM. (c) The carboxyl groups can be reversibly protonated and charged, rendering pH-dependent amphiphilicity of GO. Photographs below show the toluene-GO suspension biphasic mixtures at different pH. At pH of 10, GO remained in aqueous phase as flakes were deprotonated and more hydrophilic. At pH of 5, GO preferred the oil-water interface to stabilize emulsion droplets as the flakes were protonated and more hydrophobic. At pH of 2, GO can be completely extracted from water to the oil-water interfaces and stabilize more emulsions. When the pH was back to 10, the emulsions were destabilized, and GO flakes were re-dispersed in the aqueous phase. (d) Interfacial tension between toluene and water, and between toluene and GO water dispersions at different pH. The interfacial tension was measured as the droplet was shrunk and the overall interfacial area decreased from an initial value of A₀ to a lower value of A. (a-d) Adapted with permission from [8]. Copyright 2010 American Chemical Society..... 25

Figure 2.9. (a) Illustration of a spherical particle of radius (*r*) at a planar oil and water interface with a contact angle $\theta < 90^\circ$ measured through water phase. (b) Illustration of particle at oil-water

interface with interfacial tensions: γ_{so} , γ_{sw} , and γ_{ow} , and the contact angle. (c) Illustration of a hydrophilic particle's adsorption process from water phase to the oil-water interface. (d) Positions of a hydrophilic (top) and a hydrophobic (down) spherical particle at a planar oil-water interface, and corresponding positioning of particle when stabilizing emulsion droplet interface. 27

Figure 2.10. Schematic overview of the stabilizing features of GO compared with particles. Adapted with permission from Ref. [133]. Copyright 2014 American Chemical Society..... 30

Figure 2.11. Optical microscope images and photos of benzyl chloride in water GO emulsions prepared with different oil volume fractions (ϕ_o). (a) 0.1, (b) 0.2, (c) 0.4, (d) 0.5, (e) 0.6, and (f) 0.8. Concentration of GO: 1 g/L. Scale bar=20 μm . (g) The stable emulsions volume fractions were monitored after preparation. Adapted with permission from Ref. [115]. Copyright 2013 American Chemical Society 32

Figure 2.12. Optical microscope images and photos of benzyl chloride in water emulsions stabilized by GO, taken 72 hours after emulsification. The aqueous phase is the top and its color (transparent, light or dark brown) indicate that few or many GO flakes are present in it. Emulsions containing benzyl chloride droplets are shown in the bottom phase. Volume ratio of benzyl chloride: water = 1:1. Scale bar=20 μm . (a) GO emulsions with increasing concentrations, from left to right: 0.1, 0.5, 1, and 3 g/L. More stable emulsions formed, and smaller droplets were observed as GO concentration increased. (b) Emulsions stabilized by GO at various pH, from left to right: pH=1, 3, 6, and 11, GO concentration = 1 g/L. The upper aqueous phase became darker as pH increases, showing that more GO flakes stayed in the water phase rather than stabilizing o/w emulsions. (c) Emulsions stabilized by GO reduced by glucosamine at 80 °C, concentration = 1 g/L. From left to right, the reduction degree increased, as indicated by the increasing maximum absorption peaks of rGO (234.8, 241.8, 252.6, and 257.8 nm) through UV-vis absorption spectroscopy measurements. (d) Emulsions stabilized by GO with different NaCl concentrations, from left to right: 0.1, 10, 100, and 1000 mM, GO concentration = 1 g/L. As shown in the last two images in the panels b and c, flocculation of flakes and destabilization of emulsion droplets can be observed. Panels a-d are adapted with permission from Ref. [115]. Copyright 2013 American Chemical Society. 34

Figure 2.13. Surface modification of GO with CTAB for emulsion stabilization. (a) Zeta potential of GO modified with different amounts of CTAB. (b) Static contact angle against water of GO modified with different amount of CTAB. (c) Optical microscopy images of HIPEs stabilized by CTAB modified GO flakes. CTAB to GO mass fractions are 0, 2, 4, 6, 8 and 10 wt%. GO concentration = 0.8 g/L. Volume ratio of cyclohexane: water= 3:1. Adapted with permission from [122]. Copyright 2016 American Chemical Society..... 36

Figure 2.14. Controlling pore size and interconnectivity of monoliths by changing GO concentration. Note that the interconnectivity in the studies on GO emulsion templated porous monoliths was qualitative rather than quantitative. (a-c) Confocal laser scanning microscopy images of GO emulsions with GO concentrations of (a) 0.75 g/L, (b) 1.25 g/L, and (c) 2 g/L. Droplet size distributions of the emulsions are shown in the insets. (d-i) SEM and TEM images of porous rGO prepared by GO emulsions in panels a-c. The insets in g-i are the electron diffraction of the pore walls. The thickness of the wall increased with the increasing GO concentration. Cyclohexane-to-water volume ratio = 1:1. Scale bars, 100 μm in (a-f) and 1 μm in (g-i) [151]. (j-m) SEM images of GO/PAA porous monoliths prepared using GO stabilized o/w HIPE templates with different GO concentrations: (j) 0.8 g/L, (k) 1 g/L, (l) 1.2 g/L, (m) 1.4 g/L. Cyclohexane-to-water volume ratio = 3:1. Previous to emulsification, the GO flakes are modified with CTAB, with

CTAB to GO mass fraction of 6 wt%. The scale bars for j-m are 100 μm . Adapted with permission from Ref. [122]. Copyright 2016 American Chemical Society. 41

Figure 2.15. Influence of oil to water ratio on the GO emulsion droplet size and morphology of porous monoliths. (a-c) Polarized optical microscopy (POM) images of emulsions, and (d-f) SEM images of the corresponding rGO monoliths. Water to oil volume ratio: (a, d) 4:1, (b, e) 4:4, and (c, f) 4:6. Size distribution, average diameter of the emulsion droplets and diameter of the pores are inserted in each image. Cotton seed oil-to-water ratio = 1:2. GO concentration = 3 g/L. Reproduced with permission from Ref. [163]. Copyright 2014 Elsevier Ltd.. 42

Figure 2.16. SEM images of porous monoliths templated by o/w GO HIPES. GO was modified by CTAB. As CTAB to GO mass fraction increased from 0, 2, 4, to 6 wt%, more open pores were created. When CTAB to GO mass fraction further increased to 8 and 10 wt%, more closed pores appeared. GO concentration: 0.8 g/L. Volume ratio of cyclohexane: water = 3:1. Adapted with permission from [122]. Copyright 2016 American Chemical Society. 43

Figure 2.17. Morphology of porous monoliths templated by co-emulsifiers stabilized emulsions. (a-c) Optical microscopy images of o/w emulsions at different GO/nano-cellulose mass ratios. The total concentrations of GO and cellulose was 6 g/L in all cases. Cyclohexane-to-water volume ratio = 1:1. (d-i) SEM images of corresponding rGO/nano-cellulose porous monoliths. Droplet size (j) and pore size (k) distribution of the emulsions and porous monoliths. Adapted with permission from [176]. Copyright 2020 American Chemical Society. (l-m) Emulsion ink for 3D printing stabilized by GO/SiO₂ particles. GO was modified by PLLA-COOH so that the flakes can be dispersed in dichloromethane (CH₂Cl₂). CH₂Cl₂-to-water volume ratio = 2:3. Concentration are 40 g/L (GO), 100 g/L (PMLC), and 15 (SiO₂). (l) Photograph of emulsions (left), illustration of 3D printed emulsion scaffold (middle), and photograph of porous monolith (right) (scale bar = 1 cm). (m) SEM images showing the microstructure of the 3D printed scaffold with both large pores from 3D printing and small pores templated from emulsion droplets. Adapted with permission from Ref. [157]. Copyright 2021 Wiley Periodicals LLC..... 45

Figure 2.18. Reduction methods to prepare porous rGO monoliths. (a-d) Hydrothermal reduction: SEM images of porous rGO prepared with GO emulsion templating (a) and with GO suspension without emulsions (b). (c) Photographs of rGO monoliths prepared with (left) and without (right) emulsion templating. (d) Compressive stress-strain curves of the first 10 cycles of compression of rGO monoliths prepared by emulsion templating. The inset is an SEM image of a pore after the first compression to 50%, scale bar = 50 μm . Adapted with permission from Ref. [152]. Copyright 2014 WILEY - VCH Verlag GmbH & Co. KGaA, Weinheim. (e-h) rGO porous monoliths templated by GO emulsions reduced by NaHSO₃. (e-g) SEM images of a rGO porous monolith at lower (e) and higher magnification showing closely packed pores with polyhedral morphology (f), and a hexagonal pore sharing its boundaries with other six adjacent pores (g). Scale bar = 150 μm (e), 50 μm (f), 8 μm (g). (h) Stress-strain curves of 10 compression cycles on the rGO monolith shown in panel e, exhibiting elastic deformation. Inset, photographs of the monolith under compression and release [151]. 47

Figure 2.19. (a) Illustration of the directional freezing and pores oriented in parallel after drying. Reprinted with permission from Ref. [188]. Copyright 2016 Elsevier Ltd.. (b) Illustration of ice crystallization and growth under different freezing temperatures, and porous monoliths with different pore size obtained after drying. Reproduced from Ref. [187]. with permission from the Royal Society of Chemistry. 49

Figure 2.20. (a) Assembly process, including emulsification, unidirectional freezing, and freeze drying to obtain rGO monoliths. Following the arrows: emulsification with 75 vol% of the internal

toluene phase, emulsions moulded and subsequently directionally frozen. While growing, ice crystals template the patterns and wrinkles on the GO pore walls. After eliminating the solvents by freeze-drying and reduction, porous rGO monoliths were obtained. (b-e) SEM images showing the architecture of porous rGO. Scale bars, 10 μm (b), 2 μm (c), 1 μm (d) and 2 μm (e) [141]. .. 50

Figure 2.21. pH response of GO sheets. (a) Illustration of solution-gelation transition of GO sheets upon switching pH. Reproduced from Ref. [10] with permission from Nature. (b) Solution-gelation transition of GO (5 g/L) or GO (5 g/L) mixed with PEO (1 g/L). On the left: GO at pH of 0.6 or at pH of 4.6. On the right: GO/PEO at pH of 4 or at pH of 9. Reproduced with permission from Ref. [31]. Copyright 2011 American Chemical Society. (c) Illustration of pH controlled drug delivery of GO to tumour cell through cellular uptake [10]. 54

Figure 2.22. Light responsive systems based on GO or rGO. (a) Illustration of the use of NIR light in conjunction with GO and rGO flakes for light controlled drug release and photothermal therapy. Reproduced from Ref. [10] with permission from Nature. (b) Illustration of PMMA/rGO/Au nanorods layer-designed actuators and the light induced deformations. Reproduced with permission from Ref. [205]. Copyright 2018 WILEY - VCH Verlag GmbH & Co. KGaA, Weinheim. (c) Light-driven walking spider robot made with PMMA/rGO/Au nanorods actuators [205]. (d) Illustration of water adsorption/desorption between GO/rGO bilayers induced asymmetric volume changes. Reproduced with permission from Ref. [216]. Copyright 2018 WILEY-VCH Verlag GmbH & Co. KGaA, Weinheim. (e) Schemes for the graphene “insect” responding to surroundings humidity, temperature, and light changes. The “chela” for grasping was made with rGO at higher reduction degree than the “legs” [216]. 56

Figure 2.23. Illustrations of transmittance curves obtained with UV-vis spectrophotometry as a function of temperature for (a) UCST and (b) LCST polymers in solvent. The transmittance change of sample upon heating reflects the coil-globule transition. Reproduced with permission from Ref. [232]. Copyright 2011 Wiley Periodicals Inc.. (c) Schematic showing the coil-to-globule transition of PNIPAM: the polymer chains are extended coils below LCST and become coalesced globules due to hydrophobic interactions above LCST. Reproduced with permission from Ref. [233]. Copyright 2019 Wiley-VCH Verlag GmbH & Co. KGaA, Weinheim. 58

Figure 2.24. Surface functionalization of GO and rGO flakes with temperature responsive PNIPAM by covalently grafting: (a) rGO with PNIPAM brushes through click chemistry and RAFT polymerization. Reproduced from [254] with permission from Wiley Periodicals, Inc.. (b) GO surface modified with PNIPAM by turning GO into an initiator and *in situ* polymerization. Reproduced from Ref. [255] with permission from Wiley-VCH Verlag GmbH & Co. KGaA, Weinheim. (c) Reversible temperature responsive aggregation and dispersion of rGO/PNIPAM sheets in water. LCST = 24 $^{\circ}\text{C}$. Reproduced from Ref. [261] with permission from Wiley Periodicals, Inc.. (d) Illustration and photos of reversible temperature responsive aggregation at 40 $^{\circ}\text{C}$ and dispersion at 20 $^{\circ}\text{C}$ of GO/PNIPAM flakes in aqueous solution [255]. (e) Static contact angles of water droplets on GO/PNIPAM films at temperatures lower and higher than LCST. Reproduced from Ref. [262] with permission from the Royal Society of Chemistry. (f) Temperature responsive “on” and “off” switchable electrocatalytic detection of 1,4-dihydro- β -nicotinamide adenine dinucleotide (NADH) using a glassy carbon electrode modified by GO/PNIPAM [255]. (g) Loading of ibuprofen drug on GO/PNIPAM through hydrogen bonding between ibuprofen and PNIPAM, and temperature responsive drug release due to the breakage of hydrogen bonding. Reproduced from Ref. [243] with permission from Springer Science Business Media B.V. 61

Figure 2.25 (a) Temperature-responsive swelling-to-shrinking transition of GO/PNIPAM networks. Reproduced from Ref. [264] with permission from Royal Society of Chemistry. (b) Typical stress–strain curves of GO/PNIPAM hydrogels with different contents of GO. The hydrogels named as “GOX-Y” have X wt% of GO and Y wt% of BIS, relative to NIPAM. Reproduced from Ref. [204] with permission from the Royal Society of Chemistry. (c) Temperature dependence of the equilibrium swelling ratios of GO/PNIPAM hydrogels with GO content from 0 to 4 wt% and BIS content between 0.01 wt% and 1 wt% [204]. Swelling ratio = V_T/V_{45} . V_T and V_{45} represent the equilibrium volumes of hydrogels at the temperature shown on the x axis for each point and 45 °C, respectively [204]. (d) Illustration for the reduction of GO dispersed in the PNIPAM hydrogel. The GO/PNIPAM composites were immersed in aqueous hydrazine monohydrate to obtain rGO/PNIPAM. Inset: photographs of rGO/PNIPAM hydrogels [266]. (e) Example of preparation of rGO/PNIPAM hydrogels. An rGO porous monolith was prepared by freezing a GO suspension and reduction. The NIPAM solution mixed with crosslinkers, and initiators was infiltrated in the rGO porous monolith. Then, polymerization was carried out for 12h. Reproduced with permission from Ref. [267]. Copy right 2014 WILEY-VCH Verlag GmbH & Co. KGaA, Weinheim. 63

Figure 2.26 (a) Loading of doxorubicin hydrochloride (DOX) on GO/chitosan/PNIPAM composite nanospheres (< LCST) and NIR-induced temperature responsive release of DOX (> LCST) upon contraction of the nanospheres. Reproduced from Ref. [276] with permission form Elsevier Inc.. (b) GO/PNIPAM/PAAm hydrogel shrinking under NIR light and swelling when the NIR light was off. Temperature changed as a function of NIR laser on–off cycles. The insets show the corresponding photograph of the hydrogels; the sizes of squares are the same. Reproduced with permission from Ref. [268]. Copyright 2013 WILEY - VCH Verlag GmbH & Co. KGaA, Weinheim. (c) SEM images of freeze-dried GO/PNIPAM/PAAm hydrogels in different states: (1) the original swollen state before NIR light exposure; (2) NIR-induced contracted state; (3) the recovered swollen state after NIR laser was turned off. Scale bars are 200, 30, and 200 μm , respectively [268]. (d) Schematic of the encapsulation and NIR-induced cell release [268]. 65

Figure 2.27. (a) Photo of a mussel attach to a PTFE substrate. (b) Schematic illustrations of the interfacial location and (c) the amino acid sequence of Mefp-5. S: serine, E: glutamate, Y: tyrosine, K: lysine, G: glycine, P: proline, N: asparagine, A: alanine, H: histidine, L: leucine, R: arginine. (d) A simplified molecular representation of characteristic amine and catechol groups from Mefp-5 shown in the red square. (e) Dopamine contains both amine and catechol functional groups found in Mefp-5 and was used as a molecular building block for polymer coatings. Reproduced with permission from Ref. [38]. Copyright 2007 The American Association for the Advancement of Science. 67

Figure 2.28. Representative covalent (chemical) and physical assembly pathways for PDA formation. (a) Covalent pathway: dopamine is sequentially oxidized to heterogeneous derivatives and polymerize *via* covalent bonds, adapted from reference [298] with permission from American Association for the Advancement of Science. (b) Proposed PDA structure with DHI and indole-dione units in different degrees of (un)saturation that are covalently linked by C–C bonds between the benzene rings. Reproduced with permission from Ref. [289]. Copyright 2013, American Chemical Society. (c) (DHI)₂/PCA trimer complex through covalent bonds, adapted from reference. Reproduced with permission from Ref. [292]. Copyright 2014, American Chemical Society. (d) Tris bonded to dopamine and DHI that ends the chain growth, adapted from reference. Reproduced with permission from Ref. [295]. Copyright 2014, American Chemical

Society. (e) The oligomers physically assemble *via* hydrogen bond, π - π stacking, and cation- π interaction, adapted from reference [298]...... 69

Figure 2.29. (a) Proposed mechanism for the reduction and surface modification of GO by DA. Reproduced with permission from Ref. [42]. Copyright 2013 Elsevier B.V.. (b-c) AFM images and cross-section height analyses for rGO/PDA obtained with 0.15 g/L DA (b) and 0.8 g/L DA (c). GO concentration = 0.1 g/L. Scale bar = 2 μ m. Adapted from reference [42]...... 71

Figure 2.30. (a) Tensile strength of rGO/PDA films with different GO contents (wt%) [309]. (b) SEM cross-section morphology of the rGO/PDA nacre-like film with 95 wt% GO before break in tensile test. Reproduced with permission from Ref. [309]. Copyright 2014 American Chemical Society. (c) SEM surface morphology at different magnifications of the fractures of rGO/PDA (95 wt% GO) after tensile test [309]. (d-e) SEM images of rGO/PDA films (d) and rGO/PDA/PVA (e) films. Reproduced with permission from Ref. [313]. Copyright 2017 American Chemical Society. 73

Figure 2.31. (a) Photographs of GO dispersions mixed with dopamine before reduction (left) and after reduction by DA, leading to an rGO/PDA hydrogel (right). (b-c) SEM images of rGO/PDA (b) and rGO (c) porous monoliths after freeze-drying. Reproduced with permission from Ref. [286]. Copyright 2013 American Chemical Society. 74

Figure 2.32. Illustration *in situ* deposition of noble metals, metal oxide and semiconductor nanoparticles on surfaces of rGO/PDA. Reprinted with permission from Ref. [303]...... 75

Figure 3.1. (a-h) Dual-templating strategy to create free-standing GO scaffolds with pores in bimodal diameter distributions. **Figure 3.1d** shows HIPEs in an inverted vial made with 10 mg/mL of GO modified by 1 wt% of CTAB, with $\phi_o = 80\%$ of hexane. **Figure 3.1h** shows a GO scaffold supported on a strand of hair. (i-k): Optical microscopy images of GO HIPEs: 10–75% (i), 10–83% (j), and 6–75% (k). Scale bar in all images = 500 μ m. (l): emulsion droplet size distributions of HIPEs shown in i-k and nonlinear regression based on Gaussian model. 89

Figure 3.2. (a-f) SEM images of GO scaffolds prepared from HIPEs frozen at $-190\text{ }^\circ\text{C}$ (a, c and e) or $-20\text{ }^\circ\text{C}$ (b, d and f), corresponding to HIPE 10–75% (a, b), 10–83% (c, d) and 6–75% (e, f). In all panels the scale bars correspond to 200 μ m for the images to the left and 50 μ m for the zoomed-in images to the right. The yellow arrows point at some examples of openings between pores. (g) Primary pore diameter plotted against the corresponding HIPE droplet size ($n = 100$ from 3 independent experiments). (h) Wall thickness of the primary pores ($n = 50$ from 3 independent experiments), and (i) secondary pore diameter ($n = 100$ from 3 independent experiments). (j-k) 3D reconstruction images of GO scaffolds prepared from HIPE 10–75% frozen at $-190\text{ }^\circ\text{C}$ (j) and $-20\text{ }^\circ\text{C}$ (k) through synchrotron-based PCI. (l) Porosity obtained through weighing measurement and PCI, and connectivity obtained through PCI of GO scaffolds prepared from HIPE 10–75% frozen at $-190\text{ }^\circ\text{C}$ or $-20\text{ }^\circ\text{C}$ ($n = 3$ independent experiments). The data represent the mean \pm standard deviation. The asterisks indicate statistically significant differences calculated by the two-tailed Student's *t*-test, with $***P < 0.001$ 93

Figure 3.3. (a-b) Pictures showing an example of GO scaffolds before (a) and after (b) GA crosslinking and thermal treatment when immersed in DI water for 7 days. (c) SEM image of GO scaffold after crosslinking and thermal treatment. The scaffolds in (a-c) are prepared from hexane based HIPE 10–75% frozen at $-20\text{ }^\circ\text{C}$, scale bar = 200 μ m. (d) C:O atomic ratios from XPS survey scans and (e) percentage of C–C bonds from XPS high resolution C1s spectra (binding energy $\sim 284.8\text{ eV}$) of pristine GO, GO scaffolds, GO scaffolds with GA crosslinking (+GA), and GO scaffold after GA crosslinking and thermal treatment (+GA & +TT). $n = 3$ independent experiments. The data represent the mean \pm standard deviation. The asterisks indicate the

statistical significance calculated by the two-tailed Student's *t*-test, where $*P < 0.05$, $**P < 0.01$, $***P < 0.001$ are considered to be significant difference. (f–g) SEM images of mouse MSCs after 7 days of culture on GO membrane (f) and GO scaffold (g). The cells are colored in orange; yellow stars label some of the cellular filamentous extensions interacting with the materials. The scale bars in panels f and g correspond to 20 μm for the images to the top and 5 μm for the zoomed-in images to the bottom. (h) MSC proliferation curves on 2D GO membrane and 3D GO scaffolds up to 10 days ($n = 3$ independent experiments). (i) Confocal microscopy image of MSCs inside a GO scaffold (~ 1 mm from the top) after 7 days of culture, with actin cytoskeleton in red (phalloidin staining labeled with Alexa Flour594) and nuclei in blue (DAPI staining), scale bar = 40 μm .. 97

Figure 3.4. (a–h) SEM images of scaffolds produced with dual template strategy frozen at either -190 $^{\circ}\text{C}$ (a–d) or -20 $^{\circ}\text{C}$ (e–h) with different composition: rGO (a, e; C:O ratios from XPS survey data reported on the images), GO/PAA (b, f), GO/HA (c, g), GO/elastin (d, h). Scale bars in all panels are 200 μm . (i) FTIR absorption intensity ratio between peaks relative to $\nu_{\text{C}=\text{O}}$ at 1714 cm^{-1} and $\nu_{\text{C}=\text{C}}$ at 1630 cm^{-1} for GO and GO/PAA scaffolds frozen at -190 $^{\circ}\text{C}$ and -20 $^{\circ}\text{C}$ (left y axis); atomic percentage of calcium and phosphorus on GO/HA scaffolds, and nitrogen on GO/elastin scaffolds, according to XPS survey scans (right y axis). (j) Yield stress for GO, GO/PAA, GO/HA and GO/elastin scaffolds prepared at -190 $^{\circ}\text{C}$ and -20 $^{\circ}\text{C}$. The data represent the mean \pm standard deviation. The pound signs indicate statistically significant differences between each scaffold and the corresponding GO scaffold frozen at the same temperature. The asterisks indicate statistically significant differences between scaffolds made at different temperatures. Statistical differences are calculated by the two-tailed Student's *t*-test, with * or $\#P < 0.05$, ** or $\#\#P < 0.01$ and *** or $\#\#\#P < 0.001$, $n = 3$ independent experiments..... 102

Figure 3.5. Comparison of pore diameters achieved so far with different fabrication methods for (a) scaffolds mainly based on graphene, rGO, GO or composite scaffolds and (b) Pure GO and GO composite scaffolds with organics or inorganics as additives. As indicated in the figure, light magenta, yellow, orchid, cyan, teal, and grey shading indicate CVD, hard templating, emulsion templating, reduction, crosslinking and ice templating methods, respectively. The y axis is shown as scaled logarithmically in both graphs. The sections circled in red refer to this study..... 107

Figure 3.S1. FTIR spectra of GO, CTAB, and GO/CTAB (made from suspension with GO concentration of 4 mg mL^{-1} , and CTAB to GO ratio at 1wt%). 110

Figure 3.S2. Zeta potential and hydrodynamic diameter of pristine GO and GO/CTAB aqueous dispersions modified with different CTAB to GO weight percentage. 110

Figure 3.S3. Static water contact angle of pristine GO and GO/CTAB with different CTAB to GO weight percentage. Representative images showing water droplets spreading on the samples are shown on top of the bars. 111

Figure 3.S4. Digital pictures showing (a) phase separation using 4 mg mL^{-1} , or 10 mg mL^{-1} GO suspensions as the aqueous phase; (b) phase separation using GO/CTAB suspensions, with CTAB to GO ratio at 0.1 wt% or 0.5 wt%; (c) formation of HIPE with CTAB to GO ratio at 1 wt%; (d) emulsion aggregation and flocculation with CTAB to GO ratio at 5 wt% or 10 wt%. The concentration of GO is 4 mg mL^{-1} in figures (b-d); (e) phase separation using 0.04 mg mL^{-1} , or 0.1 mg mL^{-1} CTAB solution as the aqueous phase (corresponding to the same concentration of CTAB when CTAB to GO ratio is at 1 wt% in 4 mg mL^{-1} or 10 mg mL^{-1} GO suspensions). All the samples in (a-e) have hexane as the oil phase with $\phi_o=75$ % 112

Figure 3.S5. Digital pictures showing HIPEs using hexane with $\phi_o=75\%$, 80% or 83% , when GO concentrations are 4 , 6 , 8 , or 10 mg mL^{-1} in the GO/CTAB suspensions, with CTAB to GO ratio

at 1wt%. The stability of HIPEs with gel-like status is enhanced by increasing the GO concentration.....	113
Figure 3.S6. Optical microscopy image (a) and droplet size distribution (b) of HIPE when CTAB to GO ratio is at 1 wt% with GO concentration of 10 mg mL ⁻¹ and using toluene as the oil phase ($\phi_o = 75\%$). Scale bar=200 μm	114
Figure 3.S7. SEM image of the GO scaffold prepared from toluene based HIPE with GO concentration of 10 mg mL ⁻¹ , and $\phi_o=75\%$ of toluene, frozen at -190 °C. Scale bar = 200 μm	115
Figure 3.S8. Front view through x-axis of 3D reconstruction images (a and c) and corresponding segmented 2D cross section (b and d) of GO scaffolds prepared from HIPE 10-75% frozen at -190 °C (a, b) and -20 °C (c, d). Scale bar = 500 μm	115
Figure 3.S9. XPS survey spectra of (a) pristine GO, (b) GO scaffold, (c) GO scaffold with GA crosslinking, and (d) GO scaffold with both crosslinking and thermal treatment, high resolution spectra of N1s inserted in (b-c).....	116
Figure 3.S10. XPS high resolution C1s spectra of (a) GO, (b) GO scaffold, (c) GO scaffold with GA crosslinking, and (d) GO scaffold with both crosslinking and thermal treatment.	117
Figure 3.S11. (a) Digital picture showing thermal treated GO-C monolith without GA crosslinking immersed in DI water for 7 days. (b) Atomic percentages of C-C bonds measured from the high resolution C1s spectra (binding energy peak ~ 284.8 eV) of thermally treated scaffolds prepared with or without GA crosslinking. (c) XPS high resolution C1s spectrum of thermal treated GO scaffold without GA crosslinking. n=3 independent experiments, **indicates significant difference with $0.001 < P < 0.01$	118
Figure 3.S12. FTIR spectra of GO scaffolds, GO scaffolds +GA, and GO scaffolds +GA & +TT.	118
Figure 3.S13. (a) Digital photo of a 2D GO membrane. (b) SEM image of MSCs after 7 days of culture on a GO membrane. The cells are colored in orange.....	119
Figure 3.S14. (a) XPS survey spectra and (b) high resolution XPS C1s spectra of rGO scaffolds reduced at 180 °C and 800 °C. (c) Raman spectra of pristine GO, GO scaffold, and rGO scaffolds reduced at 180 °C or 800 °C.....	119
Figure 3.S15. Digital photos of GO based emulsions with 20 wt% PAA (a), 24 wt% HA (b), 10 wt% elastin (c-d), ratio respect to GO. The GO concentration in all composite aqueous suspensions is 6 mg mL ⁻¹ , the CTAB to GO ratio is 1 wt% in (a-b). Hexane is used in all samples, with $\phi_o=75\%$ (a, b and d) and $\phi_o=50\%$ (c).....	120
Figure 3.S16. ATR-FTIR spectra of scaffolds: GO, GO/PAA with 20 wt% PAA, and GO/HA with 24 wt% HA.	120
Figure 3.S17. XPS survey spectra of scaffolds: (a) GO/HA prepared at -20 °C, (b) GO/HA prepared at -190 °C, (c) GO/elastin prepared at -20 °C and (d) GO/elastin prepared at -190 °C. The presence of sodium is due to impurity from the HA preparation method [15]......	121
Figure 3.S18. TGA curves of GO and GO/HA scaffold under nitrogen atmosphere.	121
Figure 3.S19. SEM image (a) and EDS mappings of carbon (b), calcium (c) and phosphorus for GO/HA scaffold with 24 wt% HA relative to GO (prepared at -20 °C). Scale bar=200 μm	122
Figure 3.S20. Representative compressive stress-strain curves for GO (made from HIPE 6-75%) (orchid), GO-7.2 (made from HIPE 7.2-75%) (sky blue), GO/PAA (teal), GO/HA (magenta), and GO/elastin scaffolds (purple) prepared at (a) -20 °C and (b) -190 °C. Linear regressions of the linear elastic and plastic plateau regimes are used to determine the yield point and yield stress (e.g., GO/elastin frozen at -190 °C, inset).....	122

Figure 3.S21. Compressive stress at 80% strain (a) and density (b) of GO (made from HIPE 6-75%), GO/PAA, GO/HA and GO/elastin scaffolds frozen at -190 °C and -20 °C. The data represent the mean \pm standard deviation. The pound signs indicate statistically significant differences between the composite scaffolds and the corresponding GO scaffold frozen at the same temperature. The asterisks indicate statistically significant differences between the same type of scaffolds made at different temperatures. Statistical differences are calculated by the two-tailed Student's *t*-test, with * or #*P* < 0.05, ** or ##*P* < 0.01 and *** or ###*P* < 0.001, n = 3 independent experiments. 123

Figure 3.S22. Density (a) and yield stress (b) of GO-7.2 (made from HIPE 7.2-75%), GO/PAA, and GO/HA scaffolds frozen at -190 °C and -20 °C. The data represent the mean \pm standard deviation. The asterisks indicate statistically significant differences calculated by the two-tailed Student's *t*-test, with **P* < 0.05, ***P* < 0.01 and ****P* < 0.001, n = 3 independent experiments. 124

Figure 4.1. Overview of electrode fabrication. (a) Dispersion of Co₃O₄/SA in hexane. The scattered green light shows the strong Tyndall effect of the dispersion. (b) Photograph of GO/Co₃O₄ emulsions. (c) Photographs of rGO cobalt oxide hydrogels prepared after the HT of GO/Co₃O₄ emulsions. (d) Photographs of rGO/cobalt oxide aerogels after freeze-drying the hydrogel in (c). (e) Electrode prepared by impregnating the bottom of the aerogel with Ag paint supported on glass. (f) Preparation of electrodes with integrated Ag mesh. The final result is shown in (g). 130

Figure 4.2. Characterization on Co₃O₄ and GO modifications, as well as GO emulsions. (a–c) TEM images of Co₃O₄/SA particles at different magnifications. In (b), the diameter of representative Co₃O₄ particles is indicated. Inset in (c): magnification of the area highlighted by the yellow square from an HRTEM analysis. (d) SAED patterns obtained from Co₃O₄/SA particles reflecting the diffraction bands of the cubic Co₃O₄ lattice, whose most prominent zone axes are labeled and indicated by solid lines. (e) FTIR spectra of Co₃O₄, Co₃O₄/SA, and SA. (f) Raman spectra of Co₃O₄ and Co₃O₄/SA particles. (g) C:O atomic ratios from XPS survey scans and atomic percentage of C–C bonds (binding energy \sim 284.8 eV) from XPS high-resolution C 1s spectra of GO and GO/CTAB. The asterisks indicate statistically significant differences between GO and GO/CTAB calculated by the two-tailed Student's *t* test (***P* < 0.01). (h) Optical microscopy image of hexane-in-water GO/Co₃O₄ emulsions. (i) Emulsion droplet size distribution of GO/Co₃O₄ emulsions (*n* = 200 droplets) and nonlinear regression based on a Gaussian model. (j) Optical microscopy image of GO/Co₃O₄ emulsions at higher magnification, with aggregates of Co₃O₄/SA particles being highlighted by blue arrows. 131

Figure 4.3. Structural characterization of the rGO/CoOx scaffold through SEM, PCI, and TEM. (a–c) SEM images of rGO/CoOx aerogels at different magnifications. (d–f) 3D reconstruction maps of rGO/CoOx aerogel obtained through synchrotron-based PCI, showing (d) the overall structure, (e) the CoOx particles (blue), and (f) the distribution of CoOx particles (blue) at the boundaries of rGO pores (gray), on the basis of the color mapping. (g–i) TEM images of the rGO/CoOx aerogel showing CoOx particles of different sizes embedded in rGO flakes. CoOx particles with sizes in the nanometer range are indicated by yellow arrows. Insets: SAED patterns of the areas highlighted by yellow circles in (h) and (i). A detailed identification is shown in **Figure 4.S9**. Scale bars: 10 nm⁻¹. (j–l) EDS elemental maps of the CoOx particles shown in (i). 135

Figure 4.4. Physicochemical characterization of the electrodes. (a) Atomic percentage of C from XPS survey scans and atomic percentage of C–C bonds from XPS high-resolution C 1s spectra (binding energy \sim 284.8 eV) of rGO and rGO/CoOx. No significant differences are found between

the two samples ($P > 0.05$). (b) High-resolution XPS Co 2p spectra of the Co_3O_4 particles and rGO/CoOx. (c) Raman spectrum of rGO/CoOx showing peaks from both CoO and Co_3O_4 . (d) Raman spectra of GO, rGO, and rGO/CoOx with the corresponding I_D/I_G values. (e) Electrical conductivity of rGO and rGO/CoOx aerogels. No statistically significant difference is found between rGO/CoOx and rGO aerogels, as calculated by a two-tailed Student's t test. 138

Figure 4.5. Electrocatalytic performance of rGO/CoOx electrodes for selective water oxidation. Measurements are performed in NaCl 0.5 M + KOH 1 M aqueous electrolyte, versus Ag/AgCl. (a) Linear sweep voltammetry scans of the Ag support (conducting Ag-coated glass substrate, gray), rGO on Ag support (black), rGO/CoOx on Ag support (red), rGO/CoOx incorporating an Ag mesh (blue) at a scan rate of 10 mV s^{-1} . Inset: detail of the scans from 0.0 to +1.4 V vs Ag/AgCl. (b) Nyquist plots of rGO and rGO/CoOx electrodes at +0.85 V vs Ag/AgCl and equivalent circuit used to fit the experimental data. (c) Schematic of the cell used to perform water electrolysis and assess the selectivity of the rGO/CoOx electrodes. (d) Chronoamperometry scans recorded during bulk electrolysis of simulated seawater at rGO/CoOx electrodes (WE_1) biased at +1.2 V vs Ag/AgCl. Inset: digital photograph showing the evolution of O_2 bubbles on the surface of an Ag_m/rGO/CoOx electrode during bulk water electrolysis. (e) Chronoamperometry scans recorded on WE_2 (Pt sheet biased at $-0.25 \text{ V vs Ag/AgCl}$) during water bulk electrolysis at rGO/CoOx (WE_1), corresponding to the generation of free chlorine (*i.e.*, ClO^-) at WE_1 . (f) O_2 generated by the two types of rGO/CoOx electrodes during water bulk electrolysis shown in (d), measured through gas chromatography. Error bars indicate the SD values based on the results from three electrodes. The graph also shows the calculated Faradaic efficiencies for the two catalysts (values on the right y axis). 142

Figure 4.S1. Digital photographs showing (a) pristine Co_3O_4 particles in hexane, (b) pristine Co_3O_4 particles in hexane (top) and water (bottom) after shaking, (c) $\text{Co}_3\text{O}_4/\text{SA}$ particles in hexane, (d) $\text{Co}_3\text{O}_4/\text{SA}$ particles in hexane (top) and water (bottom) after shaking. A green laser is pointed at the vials to evaluate the Tyndall effect in the dispersions. A clear solution without suspended particles shows no light scattering. In panel b, the absence of light scattering in the hexane phase (top) suggests the absence of dispersed Co_3O_4 particles in this medium after shaking. In panel d, the strong Tyndall effect observed in the hexane phase together with the absence of the Tyndall effect in the water phase after shaking suggests that the dispersion of $\text{Co}_3\text{O}_4/\text{SA}$ particles in the hexane phase and at the hexane/water interface. 158

Figure 4.S2. (a-b) Representative TEM images of aggregates of pristine Co_3O_4 particles. (c) HRTEM analysis of Co_3O_4 particles. The magnification of the area highlighted by the yellow square, shown as an inset figure, allows to measure the d -spacing and identify the (220) diffraction planes of the Co_3O_4 cubic phase (JCPDS 00-42-1467). (d) The selected area electron diffraction (SAED) patterns obtained from Co_3O_4 particles reflect the diffraction bands of the cubic Co_3O_4 lattice, whose most prominent zone axes are labelled and indicated by solid lines. The SAED patterns in panel (d) and **Figure 4.2d** are identical within the experimental error. Scale bars: $5 \mu\text{m}$ (a), 100 nm (b), 10 nm (c), and 10 nm^{-1} (d). 159

Figure 4.S3. (a) SEM image of the GO flakes used in this study. (b) GO flake size distribution and nonlinear regression based on a Gaussian model. The flake size is shown as the effective diameter of a circle that has the same area as the GO flake, as observed in the SEM. 159

Figure 4.S4. Representative XPS survey spectra of (a) GO and (b) GO/CTAB. XPS high-resolution C1s spectra of (c) GO and (d) GO/CTAB. 160

Figure 4.S5. Pore diameter distribution of rGO/CoOx aerogels and nonlinear regression based on Gaussian model. The pore diameter is calculated based on the analysis of 200 pores observed in SEM images.....	161
Figure 4.S6. (a-c) EDS mapping of carbon and oxygen of the SEM image of rGO/CoOx aerogel shown in Figure 4.3b	161
Figure 4.S7. (a-c) SEM images of rGO aerogel synthesized without Co ₃ O ₄ particles (control sample) at different magnifications. (d, e) EDS mapping of carbon and oxygen.....	162
Figure 4.S8. Phase contrast image (PCI) analysis of rGO/CoOx scaffolds. (a) Greyscale reconstruction slice (8-bit) showing the rGO pores as grey contour and CoOx particles as bright dots. Because of the higher X-ray absorption of cobalt oxide, the CoOx particles show with higher contrast. (b) With the interactive thresholding module in Avizo software, we set a certain grey level range (200-255) as a threshold (highlighted in blue) that only includes bright particles in the greyscale image. (c) After applying the interactive thresholding, the greyscale image is transformed into a binary image showing the CoOx in light blue. (d) With the label analysis module in Avizo, we obtain the volume of visualized particles, and thus the equivalent sphere diameter of particles. The equivalent diameter is equal to the diameter of a sphere that has the same volume of the particle.....	163
Figure 4.S9. SAED patterns and the most prominent diffraction bands obtained from CoOx particles inside the rGO/CoOx aerogel shown in Figure 4.3h (a) and 3i (b) of the main text. (a) The SAED pattern of the aggregate highlighted with a yellow circle in Figure 4.3h contains the most prominent diffraction bands of both the cubic Co ₃ O ₄ (JCPDS 00-42-1467) and cubic CoO (JCPDS 00-043-1004) crystalline phases, indicated by the white and yellow labels, respectively. (b) The SAED pattern of the octahedral particles highlighted with a yellow circle in Figure 4.3i matches the interlayer spacing of a single-crystal Co ₃ O ₄ cubic phase, and its four most intense diffraction planes are indexed in white. Scale bars: 10 nm ⁻¹	164
Figure 4.S10. (a) HAADF image the CoOx particles shown in Figure 4.3i . (b) HAADF image and (c-e) the corresponding EDS elemental maps of CoOx particles shown in Figure 4.3h	165
Figure 4.S11. Representative XPS survey spectra of (a) rGO and (b) rGO/CoOx. XPS high-resolution C1s spectra of (c) rGO and (d) rGO/CoOx.....	166
Figure 4.S12. (a) FTIR spectra of pristine GO, rGO, and rGO/CoOx aerogels; (b) zoom-in into the low wavenumber region where the Co–O vibrations are visible. These spectra provide further evidence of the reduction of GO after the HT and the presence of cobalt oxide. After HT, the peaks assigned to $\nu(\text{C}=\text{O})$ and $\delta(\text{O}-\text{H})$ disappear, and the broad peak related to $\nu(\text{O}-\text{H})$ decreases. A broad band spanning from 560 to 660 cm ⁻¹ , which corresponds to $\nu(\text{Co}-\text{O})$, appears in the rGO/CoOx aerogel spectra [420]–[422].	167
Figure 4.S13. Durability test of Ag _m /rGO/CoOx electrode during selective water oxidation of simulated seawater, consisting of NaCl 0.5 M + KOH 1 M electrolyte. The chronoamperometric measurement is performed at room temperature, with the working electrode biased at +1.2 V vs Ag/AgCl.....	167
Figure 4.S14. Structural characterization of Ag _m /rGO/CoOx electrode after selective water oxidation of simulated seawater for 25 hours, and subsequent washing in DI water before analysis. (a) Photograph and (b-d) SEM images of the electrode at different magnifications. The intact electrode porous structure and the particles embedded in the rGO pore walls closely resemble those recorded before electrolysis (Figure 4.3).	168
Figure 4.S15. Characterization of the catalytic particles inside the Ag _m /rGO/CoOx structure after selective water oxidation of simulated seawater for 25 hours, and subsequent washing in DI	

water before analysis. (a) TEM image of representative aggregates of cobalt oxide nanoparticles embedded in the rGO flakes. These sub-micrometric aggregates are similar to those imaged before electrolysis (**Figure 4.3** and **Figure 4.S10**). (b) HRTEM analysis of the cobalt oxide particles shown in panel a. The magnification of the area highlighted by the yellow square, shown as the inset figure, allows to measure the *d*-spacing of the nanoparticle and identify the (111) diffraction planes of the Co₃O₄ phase (JCPDS 00-42-1467). (c) The SAED patterns obtained from the particles in panel b reflect the most prominent diffraction bands of the cubic Co₃O₄ lattice. (d) EDS spectrum of the particles shown in panel a. The Au and Cu signals arise from the TEM grids utilized. After the electrolytic process, the physicochemical composition and morphology of the cobalt oxide catalytic particles in the electrode appear substantially unchanged. 169

Figure 4.S16. High-resolution XPS Co2p spectrum of the Ag_m/rGO/CoOx electrode after selective water oxidation of simulated seawater for 25 hours. The satellite peak at 786.7 eV indicates the presence of CoO, as it has been observed prior to electrolysis (**Figure 4.4b**), suggesting that the electrolytic process does not affect the composition and phases of the catalyst particles. 170

Figure 5.1. Characterization of GO, RP and GP. (a) Digital photographs showing GO, RP and GP suspensions in water (1 g/L). Pictures were taken 3 months after suspension preparation. (b) Representative UV-vis absorption spectra of GO, RP10, RP50, RP90 and GP50. (c) Atomic percentage of N1s from XPS survey scans measured on GO, RP10, RP50, RP90 and GP50. (d) The total atomic percentage of C-N, C-O and C=O bonds (binding energy ~ 285.8, 286.6 and 288.4 eV respectively), evaluated from high resolution C1s XPS spectra. n = 3 independent experiments. The data are represented as the mean ± standard deviation. The #, * and § signs indicate statistically significant differences, #: between GO and RP10, RP50, RP90; *: between RP10 and RP50, RP50 and RP90; §: between GP50 and RP10, RP50, RP90. Differences are based on Student's *t*-test (§*P* <0.05, ** and §§*P* <0.01, ### and *** *P* <0.001). 180

Figure 5.2. Temperature responsive self-assembly of RP. (a) Digital photographs showing the suspensions or aggregations of RP50 and GP50 at 25 and 70 °C (1.5 mL, 0.05 g/L). Optical microscopy images of GP50 (b) and RP50 (c) in water at 25 °C, 30 °C, and 70 °C. Scale bar = 100 μm. The liquid samples were carefully added onto petri dishes and the images were taken without covers. (d) Representative UV-vis transmittance values measured at 750 nm for GO, RP10, RP50, RP90 and GP50 (concentration 0.05 g/L) as the temperature gradually increased from 25 °C to 70 °C at a speed of 0.5 °C/min. (e) Zeta potential of GO, RP10, RP50, RP90 and GP50 flakes at 25 °C and 70 °C. Zeta potential of RP50 was also measured at 30 °C to explain the assembly observed at a lower temperature. (f) Static water contact angle of pristine GO, RP10, RP50, RP90 and GP50 at 25 °C and 70 °C. Representative images showing water droplets spreading on the air-dried flakes on glass slides are shown on top of the bars. n = 3 independent experiments. The data are represented as mean ± standard deviation. Asterisks indicate statistically significant differences calculated by the Student's *t*-test (***) *P* <0.001). 182

Figure 5.3. TEM and AFM visualization of temperature-induced self-assembly of RP50. (a-c) TEM images of RP50 flakes at 25 °C (a), 30 °C (b), and 70 °C (c). Insets: corresponding SAED patterns. (d-f) AFM images and corresponding histogram of counts versus height of RP50 at 25 °C (d), 30 °C (e), and 70 °C (f). 184

Figure 5.4. Reversibility of temperature-induced self-assembly. (a) Digital photographs showing suspensions or aggregations of RP50 (0.05 g/L) upon heating to 70 °C, cooling to 25 °C and shaking, as well as heating again to 70 °C. (b) UV-vis transmittance values measured at 750 nm for RP50 (0.05 g/L) at 25 °C, 70 °C, cooled down to 25 °C and redispersed, and re-heated to 70 °C.

Inset: representative UV-vis transmittance values measured at 750 nm while heating (0.5 °C/min) RP50 (black), and re-dispersed RP50 (light grey). 186

Figure 5.5. (a) Digital photographs showing GO, RP10, RP50, RP90, and GP50 (10 g/L) before and after heating at 70 °C for 30 minutes. SEM images of freeze-dried RP50 suspension (10 g/L) (b) and of an RP50 hydrogel formed after heating at 70 °C (c), and of GP50 suspensions (10 g/L) before (d) and after (e) heating at 70 °C. (f-g) SEM images of cross-sections of films prepared by drop-casting RP50 suspensions (1 g/L) at 25 °C (f) or heated at 70 °C (g). (h) Electrical conductivity of films prepared from RP50 suspensions (1 g/L) at 25 °C and 70 °C, and the films prepared from suspensions at 25°C but annealed at 70 °C. n = 3 independent experiments, measured through a four-point van der Pauw method. The data are represented as the mean ± standard deviation. The asterisks indicate statistically significant differences calculated by the Student's *t*-test (**P* <0.05, ***P* <0.01). 188

Figure 5.S1. Representative XPS (a) survey and (b) high resolution C1s spectra of pristine GO. The numbers shown in the figures display the atomic percentage of C1s, N1s, O1s from survey scans, and C-C, C-O, C=O atomic percentage from high resolution C1s scans. Nitrogen is an impurity deriving from sodium nitrate used in the Hummers' method for GO preparation. (c) AFM topography of a GO flake and (d) height profile corresponding to the cross section along the white line in panel (c). 194

Figure 5.S2. Wavelength and corresponding maximum absorbance of the π - π^* transition peaks from UV-vis spectrophotometry data of GO, GP, and RP (concentration 0.05 mg/mL). ns: no significant difference between GO and GP50 (*P*>0.05). *** and *: significant difference between GO and RP10 (****P*<0.001, **P*<0.05). ## and ###: significant difference between RP10 and RP50, RP50 and RP90 (##*P*<0.01, ###*P*<0.001). 195

Figure 5.S3. Representative XPS survey (a-c) and high resolution C1s spectra (e-h) of rGO/PDA: (a, e) RP10, (b, f) RP50, (c, g) RP90, and GO/PDA: (d, h) GP50. 197

Figure 5.S4. Optical microscopy images of (a) RP10, (b) RP50, (c) RP90 and (d) GP50, at different temperatures. Scale bars = 500 μ m in all panels. 198

Figure 5.S5. Hydrodynamic diameter *D_h* of RP10, RP50, RP90 and GP50 after maintaining the indicated temperatures for 30 mins. There are n = 3 independent experiments. The data are represented as mean ± standard deviation. 199

Figure 5.S6. (a) 3D AFM topography image of RP50 with corresponding histogram distribution of counts vs height. Representative PDA clusters are circled in yellow. (b) Height profile corresponding to the line in panel (a). The peaks indicated by red asterisks show the height of PDA clusters in panel (a). The height difference (1.51 nm) between blue arrows represents the height difference between RP50 flake (shown as green in panel a) and the substrate (shown as purple in panel a). 199

Figure 5.S7. (a) 3D AFM topography image of RP90 with corresponding histogram distribution of counts vs height. (b) Height profile corresponding to the line in panel (a). 200

Figure 5.S8. XRD diffraction patterns of films prepared from RP50 at 25°C (bottom) and 70°C (top). The broad diffraction peaks at 2-theta ~ 8° indicate an expansion of the interlayer spacing due to the incorporation of PDA between layers [309],[472]. The broad peaks at 2-theta ~ 12° indicate an expansion due to the presence of oxygen-containing groups on the rGO attached between layers [474]. The peaks are assigned to the (0 0 2) graphitic diffraction order typical of rGO [100],[475]. 200

Figure 6.1. Illustrations of controlling the oil volume fraction to obtain (a) HIPE templates for porous monoliths with interconnected pores in Chapter 3, or (b) non-HIPE templates for porous monoliths with closed pores in Chapter 4.....	206
Figure 6.2. Illustrations of controlling the distribution of additives in porous monoliths. (a) Introducing water-soluble components to GO scaffolds by mixing additives with GO in the aqueous phase of emulsions (Chapter 3). (b) Introducing oil-stable components to rGO porous monoliths by dispersing additives in the hexane phase of emulsions (Chapter 4).	207
Figure 6.3. Illustrations of different post-treatments to obtain GO or rGO porous monoliths. .	208
Figure 6.4. Illustration showing the change of X-ray intensity and phase when propagating through an object in X-ray PCI. Reproduced with permission from Ref.[476]. Copyright 2019, Springer Nature Switzerland AG.....	209
Figure 6.5. Simplified illustrations of amphiphilic structures of PNIPAM and rGO/PDA.	210

List of Tables

Table 2.1. Common chemical exfoliation methods for GO synthesis [54].....	11
Table 2.2. Summary of emulsion formation conditions and corresponding structural parameters of the 3D porous monoliths templated by GO Pickering emulsions.....	38
Table 2.3. Post-emulsification treatments, properties and proposed applications of GO and rGO based porous monoliths obtained by GO/rGO emulsion templating.....	51
Table 3.S1. Preparation of GO HIPEs. The HIPEs discussed in Figure 3.1 are bolded.	114
Table 3.S2. Surface chemistry from XPS survey data of GO, GO scaffolds, GO scaffolds with GA crosslinking (+GA) and GO scaffolds with GA crosslinking and thermal treatment (+GA & +TT) (n=3 independent experiments).....	116
Table 4.S1. Surface chemistry from XPS survey data of GO and GO/CTAB (n=3 experiment points)	160
Table 4.S2. Surface chemistry from XPS survey data of rGO and rGO/CoOx (n=3 experiment points). XPS analysis was carried out on the interior structure of purposely broken rGO and rGO/CoOx aerogels, to ensure that the results are representative of the bulk electrodes. Even though the XPS probe depth is <10 nm [445], the spot analysed with XPS is 400 μm in diameter and includes not only the surface of CoOx particles but also that of several rGO pores.	165
Table 4.S3. Comparison between rGO/CoOx and the most active electrocatalysts reported for selective oxidation of alkaline simulated seawater (KOH 1 M + NaCl 0.5 M, pH = 14), at room temperature. Most of the catalytic activities in the literature are reported normalized by electrode area, but in the case of an extended 3D GO structure, it is more appropriate to compare specific activity per unit mass. All the catalysts chosen for this comparison are supported on thin sheets of nickel foam (1-1.5 mm thick) with areal density ranging from 35 to 45 g cm^{-2}	171
Table 5.S1. Surface composition derived from XPS survey data of RP and GP (n=3). C1s and O1s amounts were not compared because GO, rGO and PDA both contribute to these elements.	195
Table 5.S2. Atom% obtained from the deconvolution of high resolution XPS C1s spectra of RP and GP (n=3 experiment points). Statistical analysis for atom% of C-N, C-O and C=O is shown in Figure 5.1	196

Contributions of authors

The thesis is composed of three original manuscripts written by the candidate under the supervision of Prof. Marta Cerruti and Prof. Thomas Szkopek. Thesis papers are presented as individual chapters of the thesis (Chapters 3, 4, and 5).

The projects in the manuscripts were interdisciplinary, and several collaborators helped us perform the necessary experiments. The role of each author is described here, and all the authors have approved the final versions of the manuscripts presented in the thesis.

Chapter 3:

As the **first author of this manuscript**, I proposed research plans, developed methodologies, and synthesized materials. I designed and performed characterization experiments, including dynamic light scattering (DLS), zeta potential measurements, optical microscopy, contact angle measurements, scanning electron microscopy (SEM), energy dispersive X-ray spectroscopy (EDS), synchrotron-based phase contrast X-ray imaging (PCI), porosity measurements, Fourier transform infrared (FTIR), Raman, X-ray photoelectron spectroscopy (XPS), and thermogravimetric analysis (TGA), compressive strength measurements, cell proliferation, infiltration, and attachment tests. I collected and analyzed data, performed statistical tests, prepared the graphs, and wrote the manuscript.

Prof. Marta Cerruti supervised and directed this project, provided guidance with data interpretation, and extensively revised the manuscript.

Prof. Thomas Szkopek supervised and directed the project, revised the manuscript, and help with the data interpretation.

Dr. Xinyun Su was a Ph.D. Candidate in Prof. Simon D. Tran's lab in the Faculty of Dentistry at McGill University. She prepared the cells for *in vitro* experiments and helped to evaluate the proliferation of cells on GO scaffolds.

Dominic Esmail was an undergraduate student in the Materials Engineering Department at McGill University, and he did a co-op internship in Prof. Cerruti's lab. He helped prepare the GO composite scaffolds and did a preliminary study on the mechanical properties of GO composite scaffolds in Chapter 3.

Dr. Emily Buck was a Ph.D. Candidate in Prof. Cerruti's lab in the Materials Engineering Department at McGill University. She assisted with the method and experiments in the confocal microscope imaging study to visualize cell infiltration on GO scaffolds in Chapter 3.

Prof. Simon D. Tran is a professor in the Faculty of Dentistry at McGill University. He provided advice and feedback on the *in vitro* experiments, helped with the data interpretation, and offered access to equipment for the *in vitro* studies.

Chapter 4:

As the **co-first author of this manuscript**, I developed methodologies on the material design and preparation, including Co_3O_4 particle surface modification, stabilization in hexane, designing the GO/ Co_3O_4 emulsion system, and obtaining rGO and rGO/cobalt oxide monoliths with desired architecture. I carried out characterization using SEM, EDS, optical microscopy, XPS, synchrotron-based PCI, FTIR, and Raman. I analyzed data, performed statistical tests, and visualized results in the figures. I participated in the preparation of rGO and rGO/cobalt oxide electrodes, transmission electron microscopy (TEM) characterization, and electrical conductivity tests. I wrote the discussions on Co_3O_4 particle surface modification, emulsion stabilization and

characterization, the morphologies and 3D architectures of rGO and rGO/cobalt oxide aerogels, and the physicochemical characterization of the electrodes.

Dr. Gabriele Capilli is the co-first author of this manuscript, and he is a postdoctoral researcher in Prof. Cerruti's lab in the Materials Engineering Department at McGill University. He envisioned the application of graphene-based electrodes in seawater oxidation and proposed the research plans. He designed, established, and performed the selective electrocatalytic water oxidation experiments, analyzed the data, discussed the results, and summarized the relevant discussions and conclusions in the manuscript. He collaborated with me in the fabrication of rGO and rGO/cobalt oxide electrodes, TEM characterization and electrical conductivity tests. He also worked with me on the introduction, the overall results interpretation, and the manuscript revisions. Permission has been obtained from Dr. Capilli to include the manuscript in this thesis.

Prof. Marta Cerruti supervised and directed this project, provided guidance with data interpretation, and revised the manuscript.

Prof. Thomas Szkopek supervised and directed this project, provided guidance with data interpretation, and revised the manuscript.

Chapter 5:

As the **first author of the manuscript**, I proposed the supramolecular strategy to obtain the temperature responsive rGO/PDA colloidal system. I designed research methodology, prepared materials, and performed characterization experiments, including ultraviolet-visible (UV-vis) spectrophotometry, XPS, optical microscopy, DLS, zeta potential measurements, contact angle measurements, SEM, electrical conductivity tests, and X-ray diffraction (XRD) measurements. I collected and analyzed data, performed statistical tests, visualized the results, and wrote the manuscript.

Prof. Marta Cerruti supervised and directed this project, provided guidance with data interpretation, and revised the manuscript.

Prof. Thomas Szkopek supervised and directed this project, provided guidance with data interpretation, and revised the manuscript.

1 General introduction

1.1 Background and motivation

Due to its large surface area (2610 m²/g), high Young's modulus (>1 TPa), and high carrier mobility (200,000 cm²/V), graphene has attracted considerable interest, leading to broad applications such as biomedical engineering, energy, pollutant absorption, and sensors [1],[2].

To fully exploit the properties and maximize the performance of graphene materials, many applications require macroscopic graphene objects with different architectures. However, graphene flakes easily stack on each other, leading to compact materials that do not allow control of the structures nor exploiting the properties of individual sheets. To avoid this, studies have focused on a water-soluble, oxidized graphene derivative, graphene oxide (GO), as a precursor to fabricate graphene-based materials with various architectures [3],[4].

GO flakes are obtained through chemical exfoliation of graphite and contain defects, sp² graphene domains, and sp³-hybridized carbon with oxygen-containing groups [5],[6]. Oxygen containing groups can be removed to obtain reduced graphene oxide (rGO), another graphene-family material, with properties similar to graphene [7]. Due to the presence of hydrophilic oxygen-containing groups and hydrophobic sp² graphene domains, GO has features such as amphiphilicity, stability in water, sensitivity to stimuli (*e.g.*, pH), as well as affinity with ions and molecules [8]–[10]. Different assembly methods have been developed based on these features. GO flakes assemble into films or porous monoliths at various interfaces, *i.e.*, liquid-air, liquid-liquid, and liquid-solid. In addition, the flakes can crosslink into networks through covalent bonds or non-covalent interactions, either with the presence of crosslinkers or under stimuli [4].

The ideal architecture of graphene-based materials depends on the application. Graphene, GO, and rGO have shown promising applications in bone tissue engineering (BTE). BTE involves the use of natural or synthetic materials as scaffolds for cell transplantation or to serve as conduits to guide new bone growth [11]. Scaffolds for BTE are biocompatible three-dimensional artificial matrixes, which provide support and the necessary sites for bone cell attachment, infiltration and proliferation [12]. Graphene-based scaffolds can support mesenchymal stem cell (MSC) proliferation and osteogenic differentiation [13]–[15]. The oxygenated functionalities and sp^2 domains on GO and rGO promote the adsorption of growth factors through non-covalent interactions. In addition, GO and rGO allow for the functionalization of scaffolds when composited with additives, such as hydroxyapatite and biomolecules promoting bone regeneration [15]–[18].

BTE scaffolds should have both interconnected large pores ($> 100 \mu\text{m}$) that allow for cell infiltration, and small pores in the micron or nano size range to facilitate growth factor and nutrient diffusion [19],[20]. Failure to meet the structural requirements may lead to the formation of unmineralized osteoid tissue or fibrous tissue [21]. Graphene-based BTE scaffolds developed so far failed to meet the structural requirements. For example, rGO scaffolds made by hydrothermal reduction of GO have pores of a few microns, which inhibits the cell infiltration [15],[22]. Graphene scaffolds with sufficiently large pores can be obtained through chemical vapor deposition, but secondary small pores can't be obtained [23]. It remains a challenge to obtain 3D porous GO and rGO based scaffolds with interconnected pores in hierarchical size distributions for BTE. To fill this gap, it's essential to understand and control the assembly of GO flakes to build both large and small pores.

The application of the graphene family materials in seawater oxidation also requires specific architectural design and fabrication approaches. The direct electrolysis of seawater is greatly

inhibited by the oxidation of Cl^- to corrosive byproducts such as Cl_2 , HOCl , or ClO^- , hindering the direct use of seawater for water electrolysis [24],[25]. Benchmark electrocatalysts based on noble metals or earth-abundant oxides and (oxy)hydroxides are not selective to Cl^- oxidation. Selective transition-metal hexacyanometalates and oxidic metalates require overly high overpotentials and suffer from long-term instability [26] [25]. GO and rGO have a promising potential application in seawater desalination because the defects and channels between flakes hinder the diffusion of hydrated ions, thanks to size exclusion and electrostatic repulsion [27],[28]. Presently, the research to fully exploit the filtration feature of GO and rGO for direct seawater oxidation is still in early stage. For example, electrodes coated with GO as protective layers were recently prepared [29]. Even better than this would be to have a 3D porous rGO scaffold that can act as a selective electrode itself, due to its electrical conductivity, large surface area, and selective permeability. However, rGO-based electrodes that inhibit chlorine evolution during seawater oxidation haven't been developed. To achieve this goal, the architecture of porous rGO should be carefully designed, with closed pores that enclose the catalyst, and the pore walls acting as selective membranes permeable to water, OH^- and gas, but not to hydrated Cl^- . The present key challenges are how to control the assembly of GO flakes into closed pores and how to deposit catalyst inside the pores.

To develop porous materials designed for BTE and seawater oxidation applications, we proposed to prepare and control the architecture of GO and rGO using Pickering emulsion templating. Due to their amphiphilicity, GO flakes can assemble at the interface of oil-in-water emulsion droplets, which can be used as templates to create porous graphene-based materials. Water-soluble additives can be mixed with GO in the water phase, whereas hydrophobic components can be suspended in the oil droplets and be selectively incorporated inside the pores.

The crucial steps are to tune the amphiphilicity of GO, obtain stable emulsion systems, incorporate additives in the oil or water phases, control the pore size and interconnectivity by manipulating the emulsion templates, and preserve the porous network with desired architectures after removing templates.

In the last part of this PhD research, we further exploited the amphiphilicity of GO to add a temperature responsive feature to the flakes and control the architecture of rGO-based materials by responsive self-assembly. Previous studies showed that GO flakes can respond to stimuli such as pH and ionic strength [30],[31] due to the changes in electrostatic and van der Waals interactions between the flakes. However, the only temperature responsive systems shown so far had the GO or rGO flakes modified with temperature-responsive polymers, such as polymer poly (N-isopropylacrylamide) (PNIPAM), through complex routines of synthesis. In our third work, we showed that it is possible to create temperature responsive rGO without including any temperature responsive components. To achieve this purpose, we took inspiration from PNIPAM. Due to its amphiphilic structure, upon temperature increase, hydrogen bonds between amide groups in PNIPAM and water break; hydrophobic interactions occurring within PNIPAM chains prevail and cause its transition from expanded coil to globule [32]–[37]. To mimic the amphiphilic structure of PNIPAM, we aimed to modify hydrophobic rGO flakes with hydrophilic moieties. We used dopamine (DA) to reduce GO and to modify rGO with polydopamine (PDA) in a one-step reaction. DA is a relative of 3,4-dihydroxyphenylalanine (DOPA), an amino acid highly expressed in marine mussel foot proteins [38]. Under alkaline conditions ($\text{pH} > 7.5$), DA oxidizes and polymerizes into PDA that adheres onto a broad range of organic, inorganic and metallic substrates [39],[40], and enhances hydrophilicity of surfaces [38],[41]. By heating DA in alkaline conditions in the presence of GO, hydrophilic PDA clusters can form on the surface of flakes [42]–[45], and GO can be

reduced to hydrophobic rGO due to the release of electrons during DA polymerization. We hypothesized that the interactions between rGO/PDA flakes can be employed to induce temperature responsive self-assembly. Through this study, we aimed to demonstrate how the amphiphilicity of rGO can be used to induce responsive self-assembly and proposed a supramolecular strategy to introduce temperature responsiveness in nanomaterials.

1.2 Research objectives

The main goals of this thesis are to control the assembly of GO and rGO by tuning the amphiphilicity of flakes, investigate the assembly process at interfaces or in response to temperature, and tune the architecture of GO and rGO based materials. To achieve these goals, we established three main objectives.

I. Develop a dual-templating strategy to obtain GO-based scaffolds with interconnected pores in hierarchical pore size distributions for BTE

To obtain BTE scaffolds with controllable architectures, we investigate GO assembly at liquid-liquid and liquid-solid interfaces. We seek to modify GO to adjust the amphiphilicity of flakes and prepare high internal phase emulsions (HIPEs), which have highly packed droplets due to the presence of an oil phase volume fraction (ϕ_o) > 74 vol.%. We aim to obtain HIPEs solely stabilized by GO flakes and investigate how to adjust the droplet size. After freezing the HIPEs at different temperature and lyophilization, the GO-stabilized oil droplets become templates for interconnected, large pores, while the ice crystals formed in the water phase become templates for secondary, smaller pores. By developing stable GO emulsions with polymeric, inorganic, and biomolecular additives, we seek to investigate the versatility of this dual-templating method and obtain composite scaffolds with hierarchical pore size distributions. We show that it is possible to obtain GO scaffolds that are stable in aqueous medium by crosslinking and thermal treatment, while maintaining the morphology. We conduct *in vitro* studies to investigate MSC proliferation, attachment, and infiltration in GO scaffolds. The results from this work have been published in *Carbon* [46].

II. Develop an emulsion templating strategy to build selective rGO-based electrodes for seawater electro-oxidation.

In the second objective, we propose an approach to build seawater oxidation electrodes that are inherently selective due to their architecture. We further study GO assembly through emulsion templating. Different from the first study, though, rather than interconnected pores, we seek to obtain closed pores that can encapsulate Co_3O_4 nanoparticle catalysts for water electro-oxidation. The goal is to exploit the tightly packed GO flakes that make the pore walls as selective membranes that can hinder the transport of competitor ions such as Cl^- . Like in our first study, we tune the amphiphilicity of GO flakes and adjust the oil to water volume ratio to obtain stable emulsions, in which the droplets are dispersed without compact packing unlike in HIPES. To contain the Co_3O_4 particles inside the oil droplets, we modify their surface and stabilize them in the oil phase. We obtain electrically conductive porous rGO/cobalt oxide electrodes through hydrothermal reduction. We investigate the physicochemical and structural properties of electrodes and study their selective electrocatalytic water oxidation. The results from this work have been published in *ACS Nano* [47].

III. Achieve temperature responsive self-assembly of rGO flakes through surface chemistry design

Our last objective is to achieve temperature response in rGO without introducing any temperature responsive components. We optimize the ratio between GO and DA, control the surface chemistry of rGO/PDA flakes and obtain flakes with hydrophobic rGO domains and hydrophilic PDA clusters, mimicking the amphiphilic structure of temperature responsive PNIPAM. We study the reduction of GO, PDA formation, the

colloidal properties, temperature responsive self-assembly and the reversibility of the assembling process of rGO/PDA. Finally, we control the structure and properties of 2D films and 3D porous rGO through responsive self-assembly.

1.3 Thesis outline

This thesis adheres to the manuscript-based format guidelines required by Graduate and Postdoctoral Studies at McGill University. Chapter 1 provides an overview of background and objectives of the study. Chapter 2 provides a comprehensive literature review of GO chemistry, GO Pickering emulsions, porous materials templated by GO emulsions, stimuli-responsive GO systems, PDA and functionalization of GO. Chapters 3, 4 and 5 are the manuscripts with results and discussions for objectives I, II and III. Chapter 6 summarizes the contributions to the original knowledge from the thesis. Chapter 7 gives a general discussion of the three studies and the conclusions of this thesis.

2 Literature review

In this chapter, we aim to provide fundamental insights into the major topics covered in this thesis, including chemistry and properties of GO, GO Pickering emulsions, responsive GO systems, and PDA functionalization of GO. First, we review the studies presenting the common GO synthesis methods, the chemistry, the colloidal stability and amphiphilicity of GO, in order to establish principal understandings of GO properties and help to understand the purpose and results in this thesis. We then explain the mechanism of GO assembly at the oil/water interfaces of Pickering emulsions, and the stabilization of emulsion droplets to understand the methodology we use for templating. Following this, we summarize the factors affecting GO emulsions to learn how to control emulsion properties, such as droplet size and stability. We review the studies that obtained porous materials, including polymer-based materials, by using GO Pickering emulsions, and assess the post-emulsification treatments, such as reduction, freezing, and drying, in obtaining and affecting the porous architecture. Next, we discuss the GO and rGO systems that are able to respond to pH and light, to learn how the interactions between flakes were exploited to induce responsive behaviors. Aiming to mimic the responsiveness of PNIPAM, we introduce its mechanism of response to temperature, and review the existing temperature responsive GO and rGO systems via polymer functionalization. Finally, we report current studies on PDA formation pathways, PDA modification of GO and rGO, and related composite materials in order to understand the methodology for rGO surface chemistry control *via* mussel-inspired chemistry that is used in our study.

2.1 Chemistry of graphene oxide

The chemistry of GO plays a crucial role in the assembly process. It determines flake stability and interactions with various environments, significantly affects the assembly at interfaces and influences the final material properties. In order to lay the groundwork for assembly, we summarize the synthesis, chemistry, colloidal stability and amphiphilicity of GO in this section.

2.1.1 Synthesis of GO

GO synthesis is considered a “top-down” method where the flakes are extracted from graphite. It relies on the chemical treatment of graphite through oxidation, followed by dispersion and exfoliation in water or other solvents. The starting material, graphite, consists of layers of carbon atoms where each atom is covalently bonded to 3 other carbon atoms with a length of 1.4 Å [48]. The relatively weak van der Waals interactions connect the layers at an interlayer distance of 3.4 Å [49]. Such structure allows the intercalation of graphite and the introduction of defects and oxygen-containing groups to the graphite layers with the presence of oxidizers in acidic conditions. The obtained graphite oxide is further exfoliated under ultrasonication and dispersed into a stable colloidal suspension with single or multiple layers of graphene oxide flakes.

There are several synthesis routes of GO with different chemicals and conditions that originated from four major methods, *i.e.*, the Brodie [50], Staudenmaier [51], Hoffman [52], and Hummers methods [53]. GO was synthesized for the first time through the Brodie method in 1859 [50], in which fuming nitric acid (HNO_3 , >90 wt%) was added dropwise to graphite that was mixed with potassium chlorate (KClO_3 , with three times the weight of graphite), and a long oxidation time ranging from 72 to 96 hours was required. Staudenmaier modified Brodie's methods by increasing acidity using sulfuric acid (H_2SO_4 , 98 wt%) and less amount of fuming nitric acid. This resulted in a shorter reaction time while reducing emission of toxic gases, such as NO_2 [51]. An even safer

method was Hoffman's, which used non-fuming nitric acid (63 wt%), which resulted in less oxygen-containing groups to GO reflected through a higher carbon to oxygen (C:O) ratio (**Table 2.1**).

Table 2.1. Common chemical exfoliation methods for GO synthesis [54]

Method	Oxidizer	Condition	C:O ratio
Brodie	KClO ₃	Fuming HNO ₃ , 60 °C, 3-4 days	2.2-3.4 [50],[55]
Staudenmaier	KClO ₃	Fuming HNO ₃ (stepwise) + H ₂ SO ₄ , 60 °C, 1-2 days	2.47 [53],[56]
Hoffman	KClO ₃	Non-fuming HNO ₃ + H ₂ SO ₄ , room temperature, 3-4 days	2.5-3.5 [52]
Hummers	NaNO ₃ + KMnO ₄	H ₂ SO ₄ , below 98 °C, ~ 2 hours	2.05-2.5 [53],[55]
Tour	H ₃ PO ₄ + KMnO ₄	H ₂ SO ₄ , 50 °C, 12 hours	~ 2.2 [57]

Hummers' method, which is now the most used one for GO chemical exfoliation, can produce GO more efficiently and safely [5],[54]. Different from the other methods, it involves potassium permanganate (KMnO₄) and sodium nitrate (NaNO₃) as the oxidizers [53]. By using an excess amount of a strong oxidizing agent, KMnO₄, and a small amount of NaNO₃ which forms nitric acid *in situ*, this method dramatically shortens the reaction time as well as avoids the use of HNO₃ and the production of toxic gas ClO₂. Studies have shown that compared with the chlorate-based oxidization methods (Brodie, Staudenmanier and Hoffman methods), Hummers' method results in more oxidized GO with lower C:O ratio (**Table 2.1**) [54] [56]. This is due to the relatively harsh reaction conditions, where dimanganese heptoxide (Mn₂O₇) forms from the reaction of potassium permanganate with sulfuric acid, and a greater extent of oxidation occurs compared to the other methods [56]. However, there are disadvantages to Hummers' method. Nitrogen is likely to be present as impurity due to the adsorption of nitric acids or nitrate [58]. Also, the addition of NaNO₃ can cause the reduction in flake size, loss of carbon and produce toxic NO₂ and N₂O₄. Therefore, other methods have been proposed to produce GO with similar C:O ratio using milder reaction

conditions and without nitrates, by leveraging oxidizers such as H_3PO_4 [57], K_2FeO_4 [59], or $\text{K}_2\text{S}_2\text{O}_8$ [60] (*e.g.*, the Tour method (**Table 2.1**)).

The oxygen-containing groups on GO can be controlled during the synthesis based on Hummer's method, by varying reaction temperature and the amount of water added (**Figure 2.1a** and **b**) [61]. GO with more hydroxyl and epoxide groups can be obtained if water is added to H_2SO_4 at the beginning of the synthesis due to the formation of O_3 in the presence of Mn_2O_7 (**Figure 2.1a**, 1 and **Figure 2.1b**). On the other hand, increasing the reaction temperature results in the formation of flakes with smaller size and larger content of carboxyl groups (**Figure 2.1a**, 2&3). Other studies confirmed these findings showing that higher reaction temperature and oxidizer concentration cause more cracks on GO flakes (**Figure 2.1c**) [62]–[64].

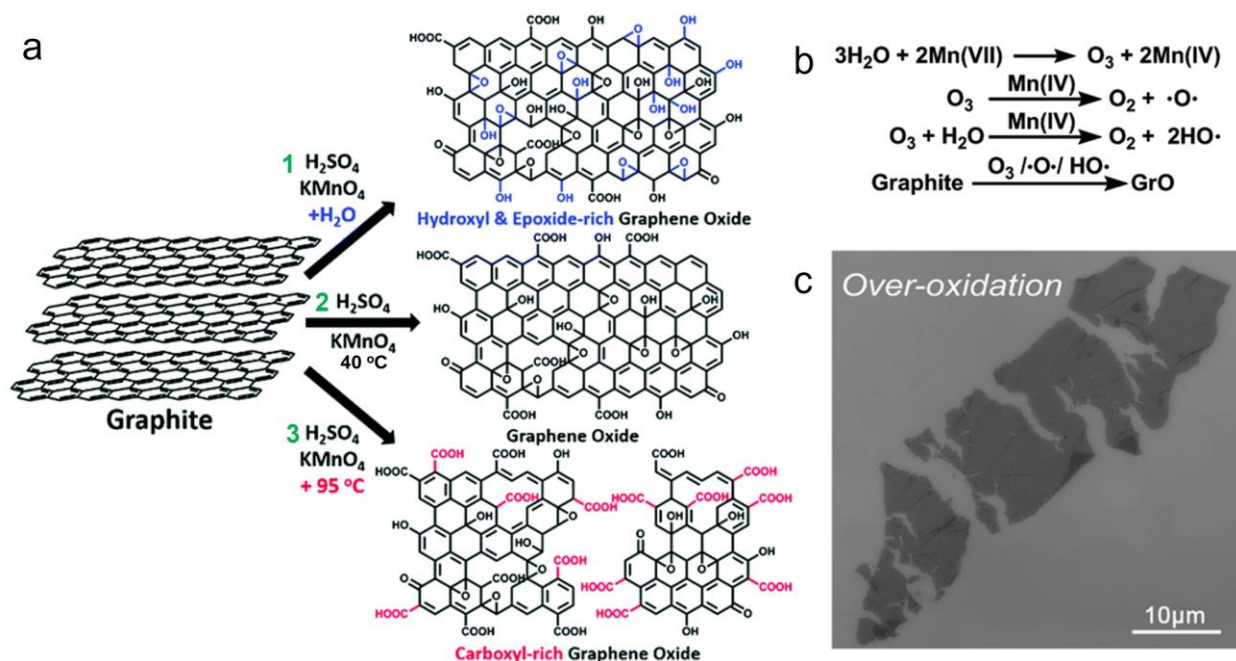


Figure 2.1. (a) GO chemistry control through modified Hummer's methods. Adapted from Reference (Ref.) [61] with permission from the Royal Society of Chemistry. (b) Proposed mechanism for water-enhanced oxidation of graphite as shown in Figure 2.1a, 1. GrO: graphite oxide [61]. (c) Scanning electron microscope (SEM) image of GO pieces as results of over-oxidation at high temperature. Reprinted with permission from [62]. Copyright 2010 American Chemical Society.

Many studies have been conducted to clarify the mechanism of the permanganate-based chemical exfoliation methods (Hummers and modified Hummers), and it's commonly accepted that there are three major steps involved [6],[65]–[67]. First, graphite is intercalated by sulfuric acid and converted into a graphite intercalation compound (GIC) (**Figure 2.2a**, 1&2) [65]. The second step is initiated by the oxidation of graphite at flake edges, and the GIC becomes an oxidized form of graphite, which is defined as pristine graphite oxide (PGO) (**Figure 2.2a**, 3&4) [65]. This step is a diffusion-controlled process because it relies on the penetration of the active oxidants, including Mn_2O_7 and MnO^{3+} , through the interlayer space of graphite [67]. A previous study suggested that diffusion happens not only from the edge but also from cross-planar cracks (**Figure 2.2b-d**) [66]. Graphite grains with a large aspect ratio (width to thickness) have several cross-planar cracks; as the cracks reach the center before the core is fully oxidized, smaller GO flakes are achieved [66]. In the last step, PGO is converted to GO by adding water (**Figure 2.2a**, 5). In acid, water can remove the reduced oxidants that remain at the interlayers, hydrolyze covalent sulfate and ester groups that bond the PGO layers, and form hydrogen bonds with GO, which consequently exfoliates PGO into GO.

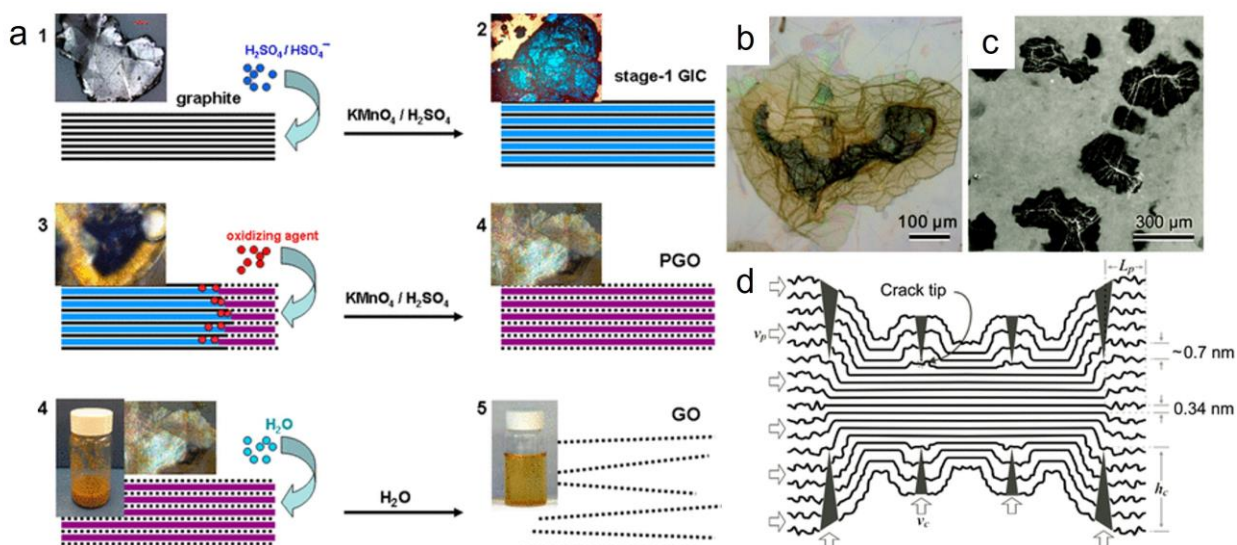


Figure 2.2. (a) Schematic of bulk graphite's conversion into GO with corresponding micrographic images or sample appearances at each phase during synthesis using modified Hummers' method. The steps signify formation of the two intermediate products (stage-1 GIC and PGO) and the final GO product. The solid black lines represent graphene layers; dotted black lines represent single layers of GO; wide blue lines represent $\text{H}_2\text{SO}_4/\text{HSO}_4^-$ intercalant; wide purple lines represent a layer of the mixture of $\text{H}_2\text{SO}_4/\text{HSO}_4^-$ intercalant with the reduced form of the oxidizing agent. Reprinted with permission from Ref. [65]. Copyright 2014 American Chemical Society. (b-c) SEM images of graphite particles during oxidation. Reprinted with permission from Ref. [66]. Copyright 2011 American Chemical Society. (d) Schematic of crack propagation and penetration of oxidizing solution during the oxidation of a graphite [66].

Following the oxidation step, there is a purification step to remove contaminants from GO, such as soluble Mn^{2+} , nitrate, sulfate, phosphate, and insoluble debris and graphite particles [57],[58],[68]. Conventionally, the soluble impurities can be washed away with hydrogen peroxide, diluted hydrogen chloride (5-10%), and water [53],[69]. Vacuum filtration or centrifugation between each wash are applied to separate GO and soluble impurities [53],[69],[70]. Another standard method, dialysis, can remove both soluble salt and debris particles, usually using cellulose membranes with a molecular cut-off of 1k to 3k [71]–[73]. Centrifugation at low speed or filtration through polyester fibers remove other insoluble impurities like graphite in a fast way [54],[57]. After intensive washing, the presence of stable brown suspensions indicates the completion of the purification. The purified GO can be dehydrated under vacuum or at mild temperatures (*e.g.*, 40 $^{\circ}\text{C}$) to obtain GO paste or powder [53].

The last step of the synthesis is the exfoliation by mechanical agitation. It's conventionally based on ultrasonication, which generates high shear force to delaminate the stacks of GO into single or few-layer graphene oxide sheets [66],[74],[75]. GO paste or powder are dispersed into deionized (DI) water by stirring at room temperature with a magnetic stirrer. Then the dispersions are immersed into a sonication water bath and sonicated at room temperature for less than 30 mins [54]. A longer period of ultrasonication can increase the oxidation level of GO, and lead to smaller flakes [76],[77]. Therefore, specifying the sonication time is crucial and further characterizations such as SEM or dynamic light scattering (DLS) are required to evaluate the size of GO flakes and their polydisperse nature [78],[79].

2.1.2 Structure and chemistry of GO

Based on the discussion above, it's clear that GO is a family of materials rather than a single composition. Therefore, identifying the structure and chemistry of GO is crucial but also remarkably challenging. Several structural models have been proposed; the Lerf-Klinowski (LK) model is the most widely accepted (**Figure 2.3**) [5],[6]. Based on experimental results, such as carbon-13 and hydrogen-1 solid state nuclear magnetic resonance (SSNMR) and Fourier-transform infrared spectroscopy (FTIR), Lerf-Klinowski *et al.* proposed a model for the structure of GO prepared through a permanganate-based chemical exfoliation method [73],[80]–[82]. They proposed that GO is composed of sp^2 domains in variable size, and sp^3 -hybridized carbon atoms with oxygen containing groups. The hydroxyl and epoxide groups decorate the basal plane where the oxidized regions separate the “graphene-like” islands randomly, and carboxylic acid and carbonyl groups are present at the edges of the GO flake. The model also shows the existence of holes on the GO planes which are caused by the CO and CO₂ released during oxidation and exfoliation [83].

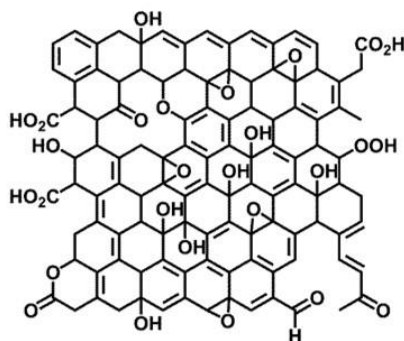


Figure 2.3. Lerf-Klinowski model of GO. Reproduced from Ref. [5] with permission from the Royal Society of Chemistry.

Selected area electron diffraction (SAED) results show the presence of polycrystalline regions (**Figure 2.4a-c**) on GO, compared to the monocrystalline region on graphene (**Figure 2.4d**) [84], and transmission electron microscopy (TEM) results indicate holes (**Figure 2.4e**, blue), islands of sp^2 domains (**Figure 2.4e**, green, with panel f showing a TEM image of graphene as comparison), and randomly distributed oxidized regions (**Figure 2.4e**, pink) [85]. The local atomic structure of highly and lightly oxidized domains, and the sp^2 domains are shown in **Figure 2.4g** [85], corresponding to the structures proposed in LK model. Further studies also reported modifications of the LK model that include groups such as esters, 5- and 6-membered-ring lactols, and organo-sulfates, but overall confirmed the main components as hydroxyl, epoxide and carboxyl groups [86]–[88].

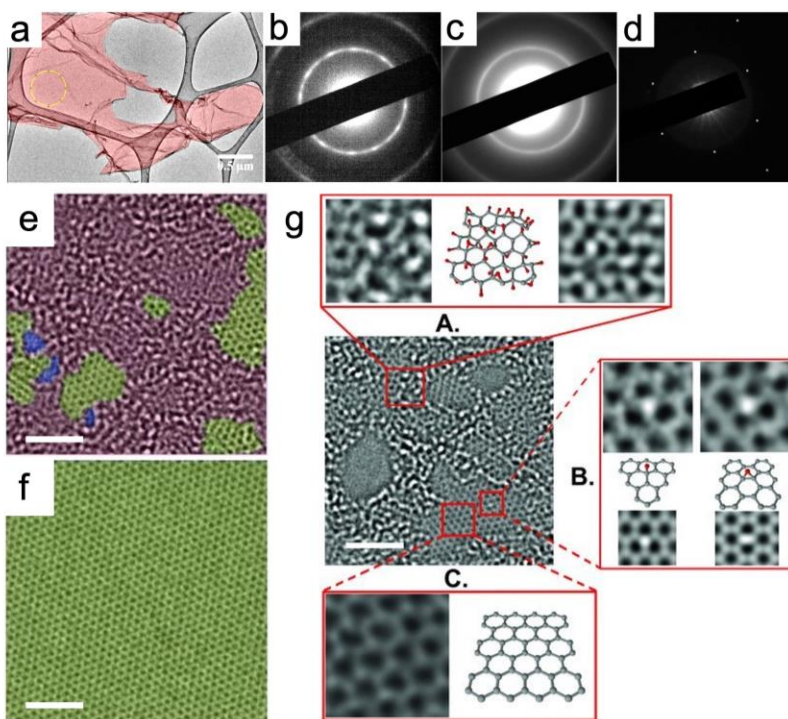


Figure 2.4. (a) A GO flake suspended on a carbon grid under TEM. Reprinted with permission from Ref. [84]. Copyright 2016 American Chemical Society. (b-c) SAED patterns showing polycrystallinity in a region of about 200 nm (b), in a larger region (c) indicated by the yellow circle in panel (a) [84]. (d) SAED patterns showing sharp spots of monocrystalline for monolayer graphene [84]. (e-f) High resolution TEM (HR-TEM) images of single suspended GO sheet (e) and single suspended graphene sheet (f). The sp^2 graphene, the oxidized sp^3 regions and holes are indicated in green, pink and blue respectively. Reproduced with permission from [85]. Copyright 2010 WILEY - VCH Verlag GmbH & Co. KGaA, Weinheim. (g) HR-TEM images of single suspended GO sheet in the middle. (A.): oxidized region image (left), proposed possible atomic structure (middle) (carbon in gray, oxygen in red), and the average of a simulated TEM image that agrees with the TEM image (right); (B.): partially oxidized regions image (top), proposed possible atomic structure (middle) and the average of a simulated TEM image (down); (C.): sp^2 graphene region image (left) and atomic structure (right). Scale bar in panels e-g = 2 nm [85].

The chemical groups on GO affect the stacking and acidity of sheets. Studies showed that the exfoliated GO flakes in water have atomic-scale thickness around 1 nm indicated by atomic force microscopy (AFM) (**Figure 2.5a**) [89]. GO sheets stack together to form regions with inhomogeneous thickness, bonded by hydrogen bonds between the oxygen-containing groups and water (**Figure 2.5b**) [84]. The acidity of GO is lower than that expected for carboxylates [5],[90]. Previous study showed that GO had three distinct pK_a at 4.3, 6.6, and 9.8 in water, corresponding to the ionization of carboxyl close to hydroxyl groups in an ortho position, the remaining carboxyl

groups, and hydroxyl groups at edge of GO flakes (**Figure 2.5c** and d) [90]. The hydroxyl groups in proximity to the carboxyl groups in GO enhance their acidity by stabilizing the carboxylate anion through intramolecular hydrogen bonding [90]. A previous study suggested that GO's structure is dynamic because neighboring hydroxyl and carbonyl groups can transform to vinylogous carboxylic acid groups, which explains the gradual degradation and acidity increase of GO flakes in water [91].

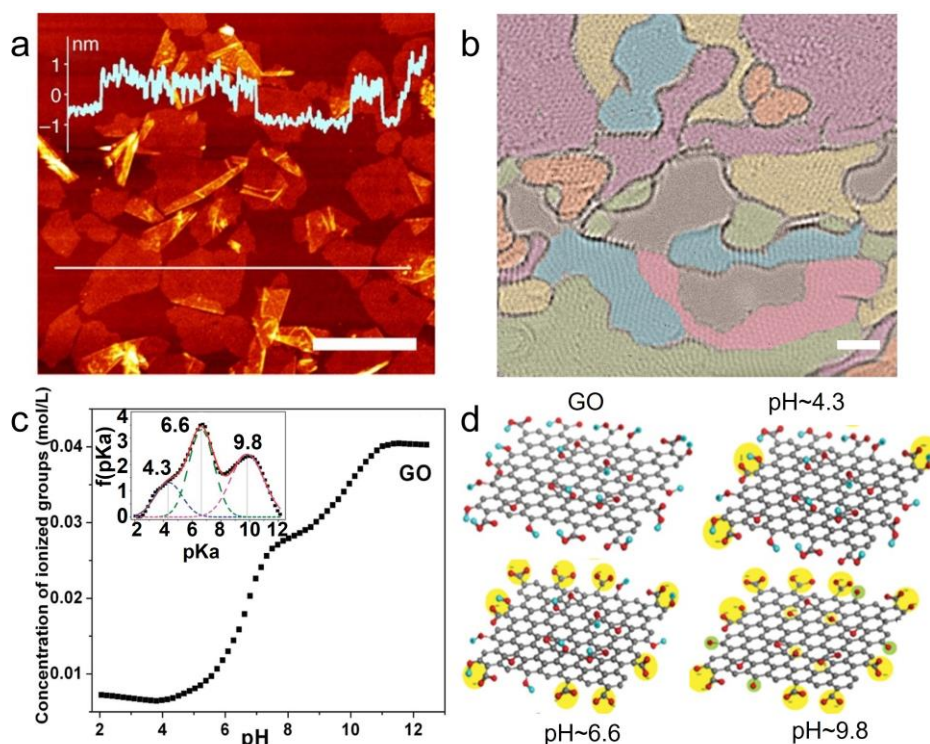


Figure 2.5. (a) AFM image of GO sheets and height profile. Scale bar = 2 μm [89]. (b) HR-TEM image color-coded to represent monolayer regions (blue, and pink) and multilayer regions (purple, yellow, orange and green). Scale bar = 2 nm. Adapted with permission from Ref. [84]. Copyright 2016 American Chemical Society. (c) Concentration of ionized groups measured by sodium binding isotherm as a function of pH for GO. The inset shows the pK distribution of the oxygen-containing groups. The fitted curve is shown in red, and the individual Gaussians are shown as dashed lines. Adapted with permission from Ref. [90]. Copyright 2012 American Chemical Society. (d) Cartoon representation (carbon, gray; oxygen, red; hydrogen, blue) of the sequence of ionization of carboxyl and hydroxyl groups at the indicated pH values. The ionized groups are highlighted [90].

2.1.3 GO colloidal stability

The colloidal stability of GO flakes is crucial to the self-assembly process and the solution-based methods for material design and production. In 1895, Brodie reported that graphite oxide “is insoluble in water containing acids or salts” during the first synthesis of graphite oxide [50]. Since then, much effort has been made to understand GO dispersion and stability behavior.

GO stability in water originates from its chemistry. GO flakes in water have a negative charge due to the deprotonation of oxygen-containing groups, corresponding to the fact that a GO dispersion in water is acidic.

Zeta potential can be used to evaluate GO surface charge and its stability in water [92]. The zeta potential is determined by measuring the electrophoretic mobility (EPM, velocity of a particle when subjected to an electric field) through laser-velocimetry techniques, and zeta potential is proportional to the EPM according to Smoluchowski model and Henry’s equation [93]–[95]. When GO flakes have zeta potential more negative than -30 mV in water (*e.g.*, pH > 4), the GO dispersion in water is considered as stable [90].

The classical Derjaguin-Landau-Verwey-Overbeek (DLVO) theory has been widely applied to understand GO dispersion and aggregation behaviors. According to the DLVO theory, the stability of GO is a result of the balance between attractive and repulsive forces of GO flakes. The van der Waals interactions between the GO flakes, including hydrophobic and π - π interactions from the sp^2 domains, are responsible for the attractive force, while the deprotonation of oxygen-containing groups contributes to the electrostatic repulsion force. Using this theory, studies have shown that factors including pH, ionic strength, flake size and reduction affect the dispersion and aggregation of GO flakes [78],[90],[95]–[97].

GO dispersions are stable in the pH range where carboxylate groups are negatively charged (*i.e.*, pH 5~12), while visible aggregates form at pH of 2 where GO flakes are less negatively charged (**Figure 2.6a-c**) [96]. The electrostatic repulsion decreases due to the protonation of oxygen-containing groups, thus, the van der Waals attraction forces dominate and cause GO aggregation in a face-to-face orientation (**Figure 2.6d**).

GO suspensions become unstable as cation concentration increases, as reflected by the aggregations and less negative zeta potential (**Figure 2.6e and f**); Mg^{2+} and Ca^{2+} are more effective to destabilize GO compared with Na^+ [95],[96]. According to the DLVO theory, the monovalent ions compress the electrical double layer of GO flakes at high concentration, screen the surface charge, and reduce the repulsive electrostatic interactions. The divalent ions not only can screen the surface charge, but also crosslink the edges of flakes by chelating the carboxylate groups, resulting in more aggregation (**Figure 2.6d**) [96].

Since the carboxylic groups are at the edges of GO [81],[98], smaller flakes show higher stability than larger counterparts due to the higher density of -COOH groups, providing more electrostatic repulsion against aggregation [78],[99]. For example, nanoscale GO flakes (~ 150 nm) were more stable over a broader pH window (pH 2.5 ~ 13), and had higher tolerance against cations compared to GO with flakes in the micron scale range (~1460 nm) [78]. Taking advantage of this difference, larger GO flakes ($> 40 \mu m^2$) can be separated by precipitation at a pH of 4 [99].

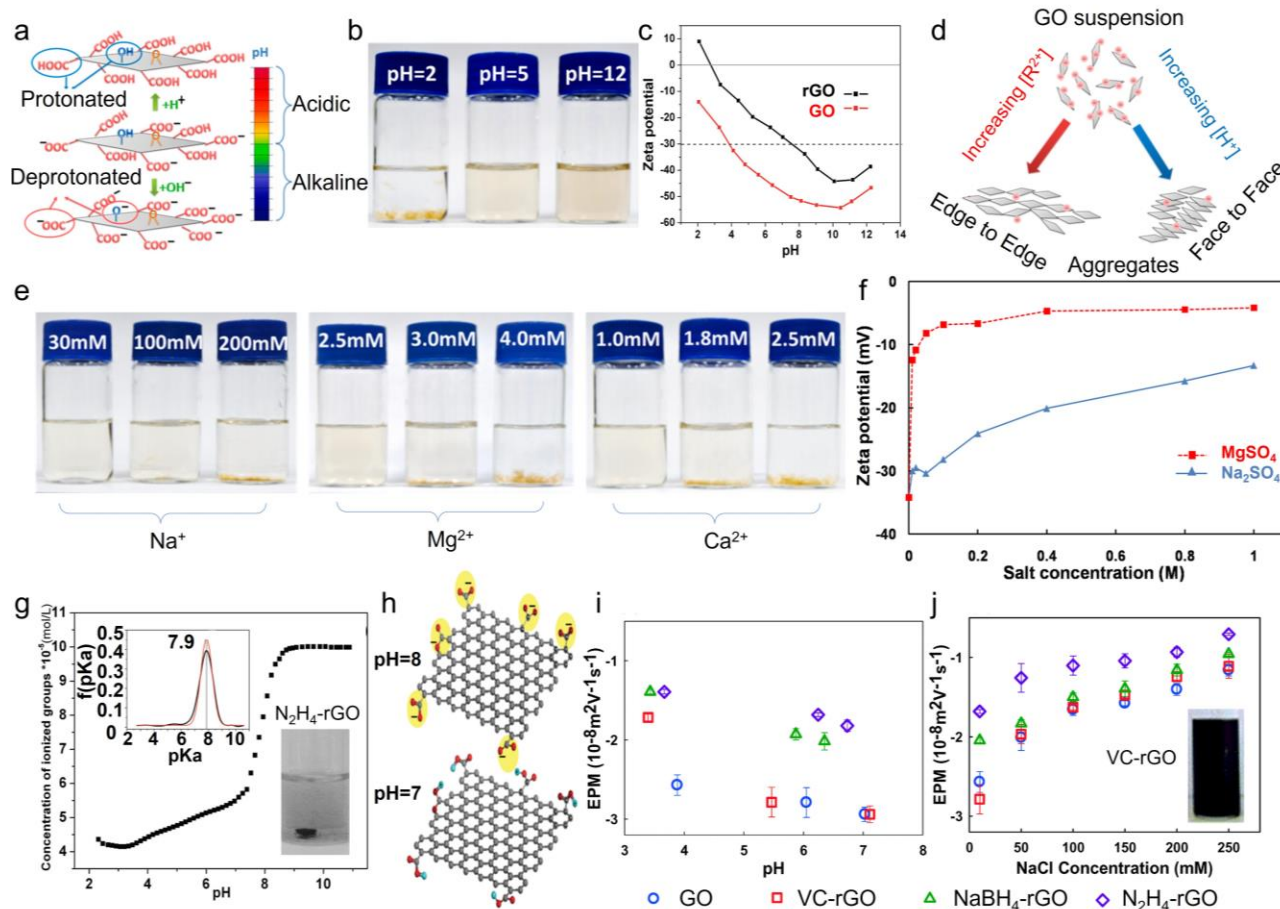


Figure 2.6. (a) GO deprotonation of the carboxylic acid groups at the edges and hydroxyl groups on plane as pH increases. Adapted with permission from Ref. [96]. Copyright 2013 American Chemical Society. (b) Photograph illustrating the influence of pH on the aggregation behaviors of GO suspension after 24 h. GO concentration = 0.01 g/L [96]. (c) Zeta potential of GO and rGO aqueous dispersion as a function of pH. The rGO was reduced by hydrazine (N_2H_4) from GO suspension. Adapted with permission from Ref. [90]. Copyright 2012 American Chemical Society. (d) Aggregation modes of GO [96]. (e) Photograph illustrating the influence of monovalence (Na^+) and divalence (Mg^{2+} and Ca^{2+}) on aggregation behaviors of GO after 2 h [96]. (f) Zeta potential of GO in different electrolytes (Na_2SO_4 , $MgSO_4$) as a function of salt concentration. GO concentration = 0.05 g/L. Adapted with permission from Ref. [97]. Copyright 2018 Elsevier B.V.. (g) Concentration of ionized groups measured by sodium binding isotherm as a function of pH for rGO. The inset graph shows the pK distribution of the oxygen-containing groups. The fitted curve is shown in red, and the individual Gaussian is shown in black. The rGO, namely N_2H_4 -rGO, was reduced by hydrazine from GO suspension. Adapted with permission from Ref. [90]. Copyright 2012 American Chemical Society. Inset photograph shows hydrazine reduced rGO in water. Adapted with permission from Ref. [100]. Copyright 2011 Elsevier Ltd.. (h) Cartoon representation (carbon, gray; oxygen, red; hydrogen, blue) of the ionization of carboxyl groups of rGO obtained by hydrazine reduction, at the indicated pH values. The ionized groups are highlighted [90]. (i) EPM as a function of pH. GO or rGO concentration = 0.01 g /L. The rGO named as VC-rGO, $NaBH_4$ -rGO, and N_2H_4 -rGO correspond to reduction of GO in water by ascorbic acid (VC), $NaBH_4$, and N_2H_4 , respectively. Reproduced from Ref. [101] with permission

from the Royal Society of Chemistry. (j) EPM as a function of NaCl concentration. pH was 5.6 ± 0.2 for GO, 5.5 ± 0.2 for VC-rGO, 6.0 ± 0.2 for NaBH₄-rGO, and 6.0 ± 0.2 for N₂H₄-rGO. Error bars indicate standard deviation of at least three measurements [101]. Inset: photograph of VC-rGO suspension in water. Reproduced from Ref. [102] with permission from the Royal Society of Chemistry.

As the oxygen content plays an important role in colloidal stability, rGO flakes, with few oxygen-containing groups and restored sp² domains, are less stable in water than GO, due to the lower electrostatic repulsion and higher van der Waals attractive forces [90],[94],[103]. In water, rGO obtained by hydrazine (N₂H₄) reduction of GO in suspension showed one distinct pK_a at 7.9, corresponding to the remaining carboxyl groups at the edge of rGO flakes (**Figure 2.6g** and h) [90], resulting in flake aggregation at pH below 7.9 (**Figure 2.6g**) [90],[101]. rGO flakes can be dispersed in water when GO is reduced by ascorbic acid (VC) [101],[102], polyphenols [104], sucrose [104] and glycine [105], because the resulting rGO contains more oxygen containing groups, such as carboxyl groups, than rGO reduced by hydrazine. As shown in **Figure 2.6i** and j, rGO obtained by VC reduction had an EPM similar to GO as pH and cation concentration increased, resulting in stable suspension in water [102].

The GO and rGO stabilities in organic solvents are different than in water. Because of the polar oxygen containing groups, GO flakes disperse well in water and other polar solvents, *e.g.*, dimethylformamide (DMF), N-methyl-2-pyrrolidone (NMP), tetrahydrofuran (THF) and ethylene glycol, while GO flakes form unstable suspensions in chloroform, acetone, isopropanol and dimethyl sulfoxide (DMSO) and can't be dispersed after sonification in methanol, dichloromethane (DCM), and n-hexane (**Figure 2.7a**) [106]. Several hypotheses were proposed to explain this phenomenon. Solvents with small electrical dipole moments (*e.g.*, n-hexane, 0.085 D) fail to disperse GO, but solvents with larger electrical dipole moments (*e.g.*, water, 1.82 D; NMP, 3.75 D) promote GO flake-solvent interactions [106]. However, some solvents with large electrical dipole moments (*e.g.*, DMSO, 4.09 D) can't provide GO with long term stability [106] likely

because of the lack of interactions between solvent and GO flakes, *e.g.*, electrostatic forces, hydrophobic interactions, and hydrogen bonding [94],[107],[108]. Van der Waals interactions between rGO and solvents enhance the flake stability in toluene, chlorobenzene (CB), *o*-dichlorobenzene (*o*-DCB) and 1-chloronaphthalene (CN) (**Figure 2.7b**) [91]. The similar surface tension in solvents and rGO (46 mN/m) are likely to contribute to the dispersion of rGO in ethylene glycol (47.7 mN/m) and NMP (40.1 mN/m) [110]–[112].

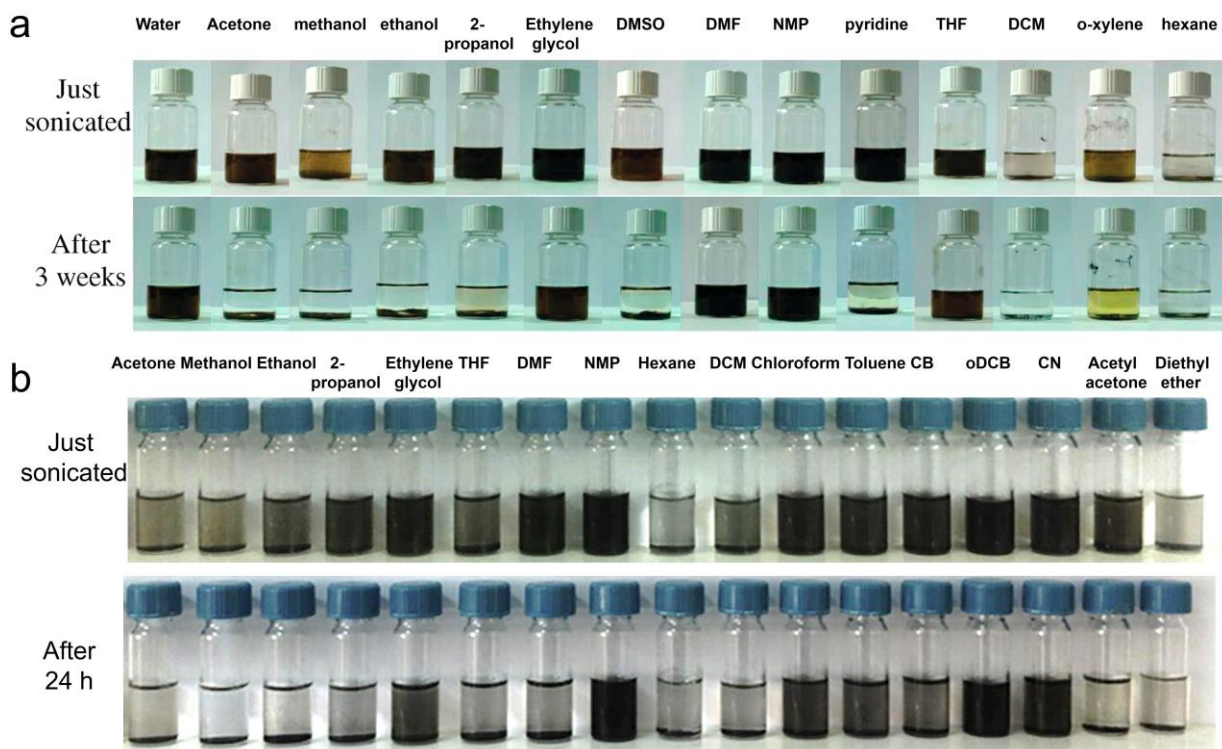


Figure 2.7. (a) Photographs of GO in water and organic solvents after ultrasonication for 1 h. Top: immediately after sonication. Bottom: 3 weeks after sonication. Adapted with permission from [106]. Copyright 2008 American Chemical Society. (b) Photographs of rGO in organic solvents after ultrasonication for 1 h. Top: immediately after sonication. Bottom: 24 h after sonication. Adapted with permission from Ref. [109]. Copyright 2014 Elsevier Inc..

2.1.4 Amphiphilicity of GO

As discussed, GO flakes are stable in water because the oxygen-containing groups provide hydrophilicity. However, the basal plane of sp^2 conjugated domains is hydrophobic. Thus, the GO flakes display amphiphilicity, like molecular surfactants with both hydrophilic and hydrophobic

regions. Studies showed that GO flakes can float at the water-air interface in a Langmuir-Blodgett (LB) trough and can stabilize air-in-liquid bubbles [113],[114], suggesting interfacial activity like molecular amphiphiles (**Figure 2.8a** and b) [8],[115]. Larger GO flakes (*e.g.*, $> 5 \mu\text{m}$) tend to assemble at the air-water interface, while the smaller flakes (*e.g.*, $< 1 \mu\text{m}$) remain in the water phase [8], because smaller GO flakes are more hydrophilic due to the higher density of carboxylic acid groups at the edges.

Due to the interfacial activity, GO can also assemble at oil-water interfaces to stabilize emulsion droplets (**Figure 2.8c**). Emulsions are the mixture of two immiscible phases (usually an oil phase and an aqueous phase), in which one phase forms droplets stabilized by emulsifiers and dispersed in the other phase [116]. Kim *et al.* reported the formation of GO emulsions for the first time [8]. As shown in **Figure 2.8c**, a phase separation between oil and GO suspension can be observed at a pH of 10, but toluene-in-water emulsion droplets formed as the pH decreased to 5, because the protonation of carboxylic acid groups drastically reduces the hydrophilicity of GO flakes, and GO flakes can move to the oil-water interfaces to stabilize oil droplets [8],[117]. Interfacial tension (γ) represents the force of attraction between the molecules of two fluids at the liquid-liquid interface, and low values of γ imply the two liquids are miscible [118]. The γ between a GO aqueous suspension and oil can be quantified via optical tensiometry by suspending a GO droplet with a certain volume in oil [117]. The GO droplet is extracted by a syringe, and as the droplet volume reduces, γ can be obtained by evaluating the tension resisting the extraction force. As shown in **Figure 2.8d**, γ between toluene and water decreased when GO was added to water at all pH values, but more so at lower pH, confirming that GO flakes can reduce interfacial free energy like surfactants do and that this varied based on the pH-dependent amphiphilicity of GO.

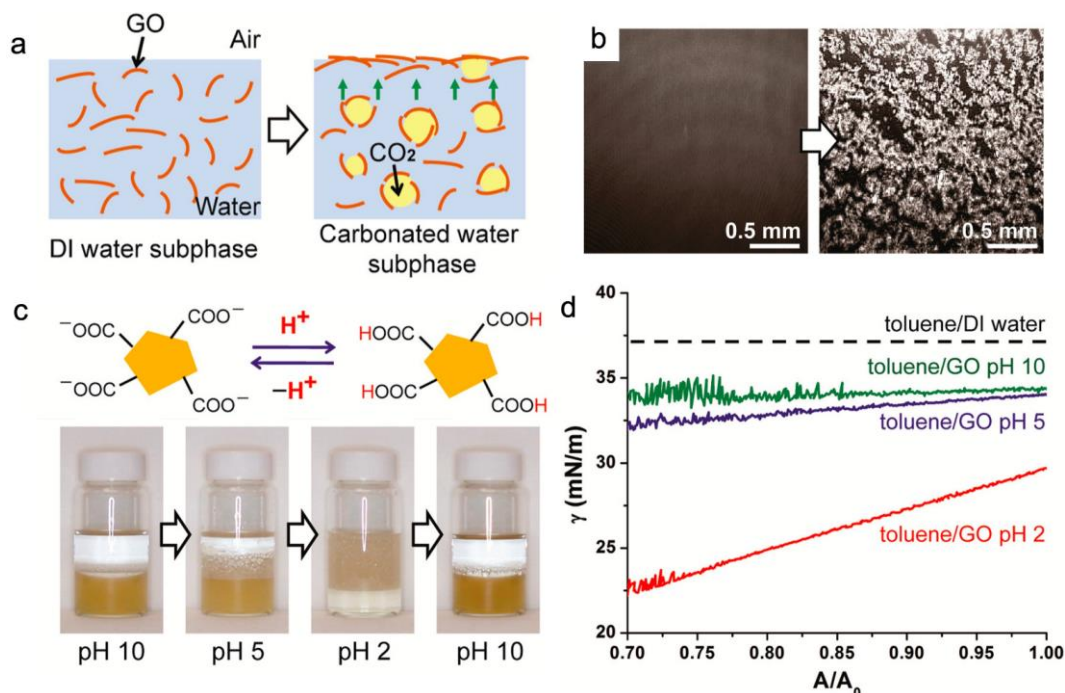


Figure 2.8. (a) Illustration showing the flotation of GO in carbonated water. GO was first captured by the rising CO₂ bubbles and then transported to the water surface. (b) Brewster angle microscopy (BAM) images without (left) and with (right) GO on the surface. As GO flakes floated up to the air-water interface, the surface refractive index changed, allowing the observation of GO through BAM. (c) The carboxyl groups can be reversibly protonated and charged, rendering pH-dependent amphiphilicity of GO. Photographs below show the toluene-GO suspension biphasic mixtures at different pH. At pH of 10, GO remained in aqueous phase as flakes were deprotonated and more hydrophilic. At pH of 5, GO preferred the oil-water interface to stabilize emulsion droplets as the flakes were protonated and more hydrophobic. At pH of 2, GO can be completely extracted from water to the oil-water interfaces and stabilize more emulsions. When the pH was back to 10, the emulsions were destabilized, and GO flakes were re-dispersed in the aqueous phase. (d) Interfacial tension between toluene and water, and between toluene and GO water dispersions at different pH. The interfacial tension was measured as the droplet was shrunk and the overall interfacial area decreased from an initial value of A_0 to a lower value of A . (a-d) Adapted with permission from [8]. Copyright 2010 American Chemical Society.

The amphiphilicity of GO also can be tuned by adjusting the ratio between hydrophilic and hydrophobic regions, *e.g.*, by restoring hydrophobic sp² domains [114],[119], changing the surface charge density of flakes [8],[117],[120], and adding hydrophobic molecules [121],[122]. Due to the large surface area, GO flakes are kinetically trapped at the interface, resulting in stable films, bubbles, or droplets [4]. Besides contributing to emulsion's long-term stability as stabilizers, GO

flakes can act as building blocks to prepare graphene-based materials with structure templated by emulsion droplets.

2.2 Pickering emulsions stabilized by GO

GO flakes can stabilize Pickering emulsions with high resistance to coalescence; this is crucial for producing graphene or graphene composite materials with different porous structures. The following sections summarize the mechanisms of Pickering emulsions stabilization, current research on GO stabilized Pickering emulsions, and studies on graphene and graphene composite materials prepared by GO emulsion templating.

2.2.1 First-principle study of emulsions stabilized by Pickering particles

Pickering emulsions are emulsions that are stabilized by particles rather than surfactants [123]. Previous studies have demonstrated that the resistance against coalescence of Pickering emulsions is due to the irreversible adsorption of particles at oil-water interface [124],[125]. Because Pickering emulsion templating is one of the main assembly methods in this thesis, the particle attachment energy at the oil-water interface and emulsion stabilization will be discussed in detail as established by pioneering studies [124]–[128]

Spherical particles are the most typical stabilizers in Pickering emulsions [126]. Considering a spherical particle with radius r adsorbing at the oil-water interface, a contact angle θ is the angle between the oil-water interface and a line tangent to the particle at the three-phase contact point, measured in the water phase [125] (**Figure 2.9a**). For hydrophilic particles, θ is $< 90^\circ$, whereas for hydrophobic particles $\theta > 90^\circ$. The depth of the particle immersed in water h is shown in **Figure 2.9a**. According to Young's equation, the relation between the interfacial tensions, including γ_{so} (between solid-oil interface), γ_{sw} (between solid-water interface), and γ_{ow} (between oil-water interface), and contact angle θ is shown as (**Figure 2.9b**):

$$\gamma_{so} - \gamma_{sw} = \gamma_{ow} \times \cos\theta \dots \dots \dots \text{Equation 2.1}$$

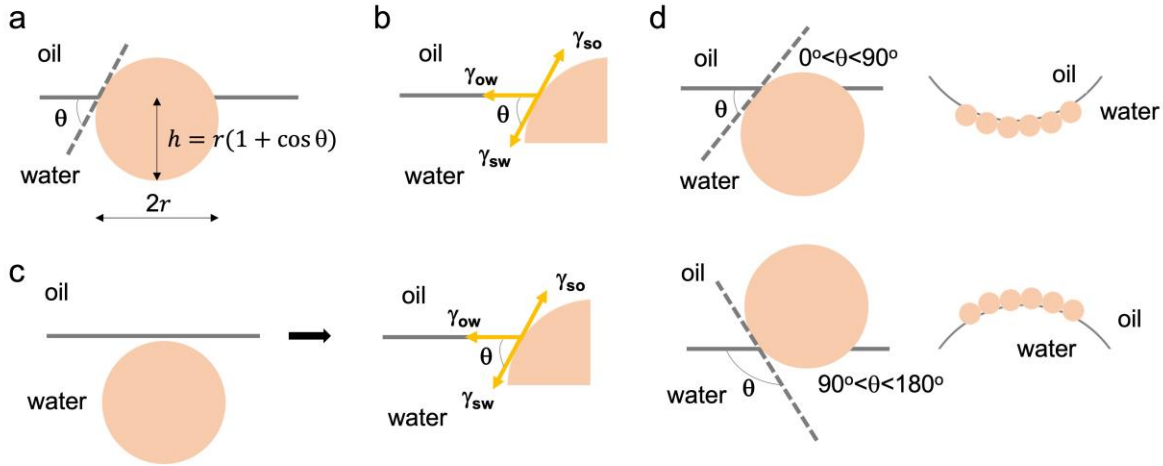


Figure 2.9. (a) Illustration of a spherical particle of radius (r) at a planar oil and water interface with a contact angle $\theta < 90^\circ$ measured through water phase. (b) Illustration of particle at oil-water interface with interfacial tensions: γ_{so} , γ_{sw} , and γ_{ow} , and the contact angle. (c) Illustration of a hydrophilic particle's adsorption process from water phase to the oil-water interface. (d) Positions of a hydrophilic (top) and a hydrophobic (down) spherical particle at a planar oil-water interface, and corresponding positioning of particle when stabilizing emulsion droplet interface.

Let us now define that the interfacial area of the oil-water interface without any particles is known as A_{ow} , the surface area of the particles is A_s , the interfacial area of the particles in contact with the oil interface is A_{so} , and the interfacial area of the particles in contact with the water interface is A_{sw} . A_s is thus the sum of A_{so} and A_{sw} . When the particle adsorbs at the oil-water interface, part of A_{ow} is replaced by the particle; we call this A_e . To evaluate the total energy associated with particle adsorption at the oil-water interface, we can calculate the interfacial free energy change as the particle moves from one phase to the oil-water interface. Here we assume gravity is negligible.

A hydrophilic particle will be initially immersed in water (**Figure 2.9c**, left), then it will bind to the oil-water interface. When the particle is in the water phase at the beginning, the interfacial free energy (E_w) is shown as:

$$E_w = \gamma_{sw} \times A_s + \gamma_{ow} \times A_{ow} \dots \dots \dots \text{Equation 2.2}$$

Accordingly, when the particle is bound to the oil-water interface, the interfacial free energy (E_{int}) is expressed as:

$$E_{int} = \gamma_{so} \times A_{so} + \gamma_{sw} \times A_{sw} + \gamma_{ow} \times (A_{ow} - A_e) \dots\dots\dots \text{Equation 2.3}$$

Therefore, the change of interfacial free energy when the particle adsorbs at the oil-water interface, ΔE_{ads} , is the difference between E_{int} and E_w :

$$\Delta E_{ads} = E_{int} - E_w = A_{so} \times (\gamma_{so} - \gamma_{sw}) - \gamma_{ow} \times A_e \dots\dots\dots \text{Equation 2.4}$$

Taking the Young's equation (**Equation 2.1**) into account, ΔE_{ads} can be expressed as:

$$\Delta E_{ads} = \gamma_{ow} \times (A_{so} \times \cos\theta - A_e) \dots\dots\dots \text{Equation 2.5}$$

For a hydrophilic particle, $h = r \times (1 + \cos\theta)$ (**Figure 2.9a**). We can easily derive the areas A_{so} and A_e from the particle radius and θ , assuming that the oil-water interface is planar up to the contact line:

$$A_{so} = 2\pi r \times (2r - h) = 2\pi r^2 \times (1 - \cos\theta) \dots\dots\dots \text{Equation 2.6}$$

$$A_e = \pi \times (r \times \sin\theta)^2 = \pi r^2 \times (1 - \cos^2\theta) \dots\dots\dots \text{Equation 2.7}$$

Therefore, we can obtain the adsorption energy for hydrophilic particle ($0^\circ < \theta < 90^\circ$):

$$\Delta E_{ads} = -\pi r^2 \times \gamma_{ow} \times (1 - \cos\theta)^2 \dots\dots\dots \text{Equation 2.8}$$

As we can see from **Equation 2.8**, for a hydrophilic particle ($\theta < 90^\circ$), the change in interfacial free energy when the particle adsorbs at the oil-water interface is below 0 ($\Delta E_{ads} < 0$). Accordingly, to remove or desorb the particle from the oil-water interface, the change in interfacial free energy for desorption $\Delta E_{desp} = -\Delta E_{ads} > 0$.

When the particle is hydrophobic ($90^\circ < \theta < 180^\circ$), the adsorption energy is expressed the same as **Equation 2.8**, except that sign in front of the $\cos\theta$ changes into (+) because the relative position of the center of the particle in relation to the oil-water interface is changed (**Figure 2.9d**): in this case, the hydrophobic particle starts from the oil phase before it binds to the oil-water interface.

Overall, ΔE_{desp} and ΔE_{ads} are a function of radius and contact angle of particle:

$$\Delta E_{desp} = -\Delta E_{ads} = \pi r^2 \times \gamma_{ow} \times (1 \pm \cos\theta)^2 \dots \dots \dots \mathbf{Equation\ 2.9}$$

where the sign is – if $\theta < 90^\circ$, and + if $90^\circ < \theta < 180^\circ$

According to **Equation 2.9**, when a particle adsorbs at the interface, the interfacial free energy decreases. After the particle is adsorbed at the interface, the energy needed to move the particle back to the phase where it would preferentially locate itself (water for hydrophilic particle, or oil for hydrophobic particles) is always greater than zero, meaning that the adsorption of the particle is irreversible, and the three-phase interface (oil-particle-water) is stable [124]–[128].

θ is a significant parameter in determining the emulsion type. During emulsification, the liquid that the particles have more affinity with usually becomes the continuous phase, and the other phase constitutes the dispersed phase (*i.e.*, emulsion droplets) [123],[125],[126]: this means that oil-in-water (o/w) emulsions are formed with hydrophilic particles ($\theta < 90^\circ$) (**Figure 2.9d**, upper), and water-in-oil (w/o) emulsions are formed with hydrophobic particles ($\theta > 90^\circ$) (**Figure 2.9d**, lower).

The water contact angle of GO is in the range of 30-70°, depending on the oxidization level, defect and sp^2 domain density of GO flakes [122],[129],[112],[130],[131]. Despite this variability, θ for GO flakes is always lower than 90°, and many studies have demonstrated that GO flakes stabilize o/w emulsions [8],[115],[122],[132],[133].

When a GO sheet is absorbed at the oil-water interface, the interfacial area A_{so} and replaced area A_e in **Equation 2.4** are equal to A_{GO} (length \gg thickness), therefore, the desorption and adsorption energy are derived as [133]:

$$\Delta E_{desp}^{GO} = -\Delta E_{ads}^{GO} = A_{GO} \times (\gamma_{ow} - \gamma_{so} + \gamma_{sw}) \dots \dots \dots \mathbf{Equation\ 2.10}$$

According to Young’s equation (**Equation 2.1**), the ΔE_{desp}^{GO} and ΔE_{ads}^{GO} are given by:

$$\Delta E_{desp}^{GO} = -\Delta E_{ads}^{GO} = A_{GO} \times \gamma_{ow} \times (1 - \cos\theta) \dots \dots \dots \text{Equation 2.11}$$

Considering that GO's water contact angle is lower than 90 ° and thus $\cos\theta < 1$, the ΔE_{desp}^{GO} is always above 0. Therefore, the GO sheets can irreversibly adsorb at oil-water interfaces to stabilize Pickering emulsions and decrease interfacial free energy of system.

GO sheets as 2D stabilizers exhibit different features compared to particles, as summarized in **Figure 2.10** [133]. As all the atoms of GO at oil-water interfaces directly contribute to stabilizing emulsions, GO flakes are more efficient than spherical particles at stabilizing emulsions, meaning that lower concentrations of GO is needed to obtain stable Pickering emulsion compared to nanoparticles (*e.g.*, 200 ppm of GO compared to 500 ppm of silica) [133]. Also, while spherical particles are likely to produce an imperfect surface coverage, resulting in molecular transport through voids, GO sheets can fully cover the oil droplet surface. Lastly, since the GO flakes can form multilayers, they can act as barriers for molecular transport between the oil and water phases [115],[134],[135].

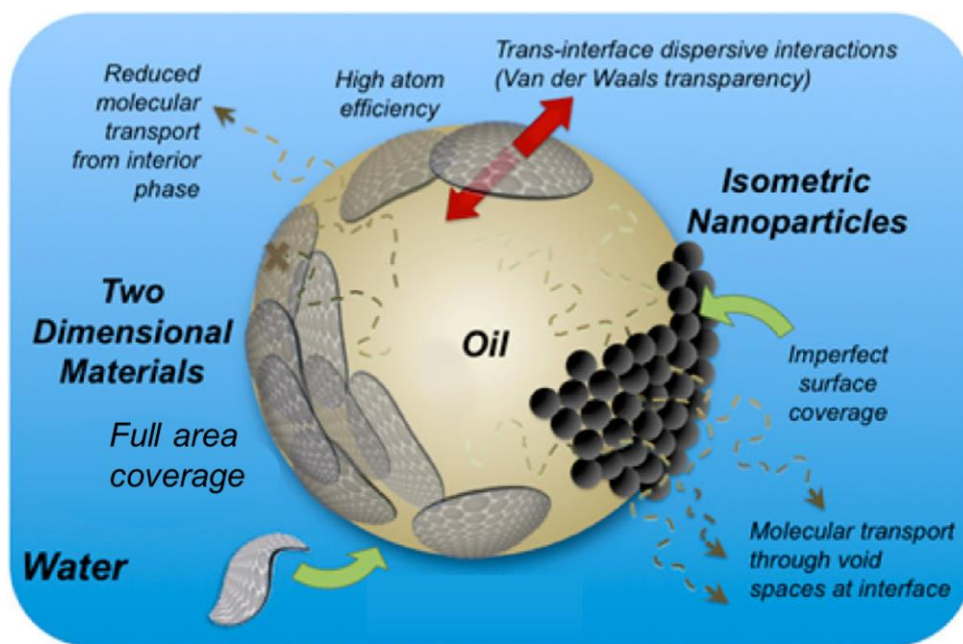


Figure 2.10. Schematic overview of the stabilizing features of GO compared with particles. Adapted with permission from Ref. [133]. Copyright 2014 American Chemical Society.

2.2.2 Factors affecting GO Pickering emulsions

In this section, we summarize the factors affecting GO Pickering emulsions, including the oil polarity, oil to water volume ratio, and features related to GO, *i.e.*, concentration and amphiphilicity.

2.2.2.1 Effect of oil phase

The choice of the organic liquid used as oil phase has an impact on GO emulsion formation and stability [136]. The π - π interaction between the sp^2 domains of GO with oil phase, *e.g.*, toluene, chlorobenzene, benzyl chloride, or chlorobenzene, reinforces the adsorption of GO flakes on the oil-water interface, and results in stable emulsions [115]. GO flakes can stabilize both emulsions with polar (*e.g.*, ethyl heptanoate [115]), and non-polar oils (*e.g.*, hexane [137], perfluorohexane [138], liquid paraffin [139], perfluorohexane [138]), while GO flakes modified by ions or hydrophobic components tends to stabilize emulsions only with non-polar oils [122],[140].

The oil to water volume ratio is also an important factor. Previous study showed that when the oil volume fraction (ϕ_o) was below 0.5, as ϕ_o increased, a higher stable emulsion fraction can be observed (**Figure 2.11**). However, when $\phi_o > 0.5$, the stable emulsion fraction decreased as ϕ_o increased, meaning not all the oil can be emulsified. Retaining higher fraction of internal phase in emulsions requires more GO flakes to stabilize the oil-water interfaces. If the GO flake concentration is not sufficient, the oil droplets become less stable and coalesce. Also, to fully emulsify the higher volume fractions of oil phase, an appropriate amphiphilicity of GO is required [122],[140],[141].

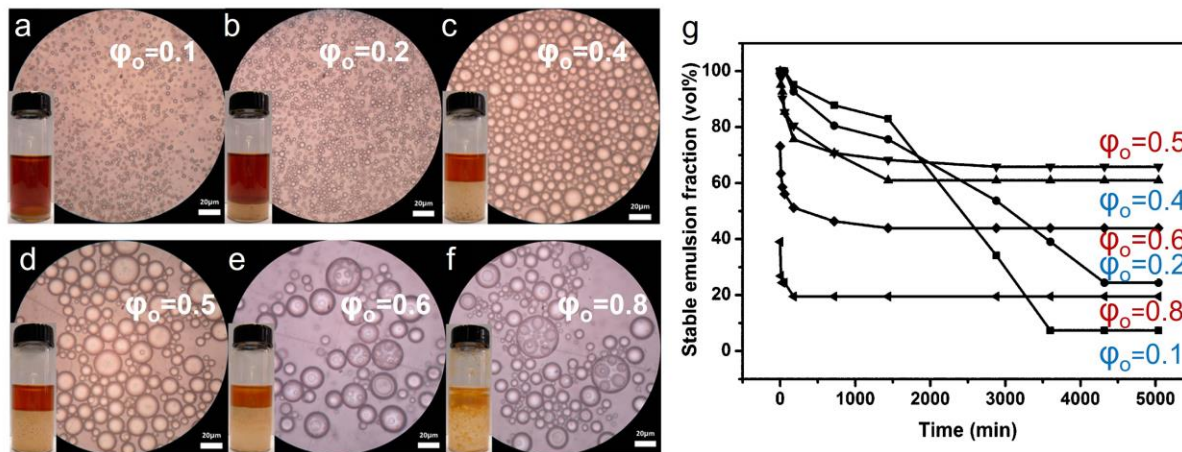


Figure 2.11. Optical microscope images and photos of benzyl chloride in water GO emulsions prepared with different oil volume fractions (ϕ_o). (a) 0.1, (b) 0.2, (c) 0.4, (d) 0.5, (e) 0.6, and (f) 0.8. Concentration of GO: 1 g/L. Scale bar=20 μm . (g) The stable emulsions volume fractions were monitored after preparation. Adapted with permission from Ref. [115]. Copyright 2013 American Chemical Society

2.2.2.2 HIPEs

Emulsions containing an internal phase volume fraction above 74% are called high internal phase emulsions (HIPEs) [142]–[144], as 74% represents the maximum volume fraction that uniform spheres can occupy in a space without being deformed. HIPEs can also be referred to as “gel-emulsions” [145],[146], since their behaviour is viscoelastic because of the compact packing of droplets. Due to higher internal phase volume fraction and more droplet formation compared to non-HIPEs [142],[147], HIPEs can be used as templates for porous monoliths with high porosity. The particles or flakes in Pickering HIPEs can act as mechanical barriers to prevent droplet destabilization and phase separation [148]. To date, studies have reported GO or rGO stabilized HIPEs with internal phase volume fraction up to 85% [122],[132],[140]. The amphiphilicity of GO strongly affects the formation of stable HIPEs, and can be adjusted by reduction of GO [132],[149],[150] or CTAB modification [122],[140]. Since GO features affect the properties of GO emulsions, and consequently determine the formation of HIPEs, studies on GO/rGO HIPEs will be covered in the following section.

2.2.2.2 Effect of GO flakes

Studies have reported that as GO concentration increases, more GO flakes can migrate to the o/w interface, stabilize more total o/w interfacial area, resulting in smaller droplet size and more stable emulsion (**Figure 2.12a**) [115],[151],[152].

Decreasing the pH (**Figure 2.12b**), reducing GO (**Figure 2.12c**), adding ions such as Na⁺ (**Figure 2.12d**) can enhance the hydrophobicity of GO [115],[151],[153]. Thus, the flakes can reach a proper amphiphilicity to assemble at o/w interface in emulsions, whereas pristine GO flakes remain in the water phase instead of migrating to the oil-water interface [115],[117],[122]. It has been reported that as pH increased, fewer emulsions formed, because the deprotonated GO flakes stay in the water phase instead of stabilizing the oil-water interfaces (**Figure 2.12b**) [115] and o/w HIPEs with ϕ_o of 75% can be obtained with GO suspensions at pH of to 2 ~3 [141].

When the GO was significantly reduced or a small amount of Na⁺ was added, the GO flakes can stabilize the o/w emulsions with a smaller average droplet size (first two images in **Figure 2.12c** and d). However, if the hydrophobicity was increased due to higher reduction degree or higher ion concentration (*e.g.*, >300 mM of Na⁺, or >100 mM of Mg²⁺), flocculation happened because of the drastically decreased surface charge of flakes, and emulsions were destabilized (see the last two images in **Figure 2.12c** and d). Multi-emulsion droplets, *i.e.*, water-in-oil-in-water emulsions, can be observed, meaning that oil droplets formed within the w/o emulsions. Studies have shown that w/o, instead of o/w emulsions, can be obtained with hydrophobic graphene [154],[155] and rGO flakes [149],[150],[156]. For example, Wong *et al.* prepared rGO flakes through thermal reduction at 800 °C of GO; the rGO flakes were able to stabilize w/o HIPEs with ϕ_w of 80 % water phase, using 0.2 g/L of rGO [150]. W/o emulsion are preferred when the oil phase needs to be the external, continuous phase to dissolve oil soluble additives, such as crosslinkers and polymers.

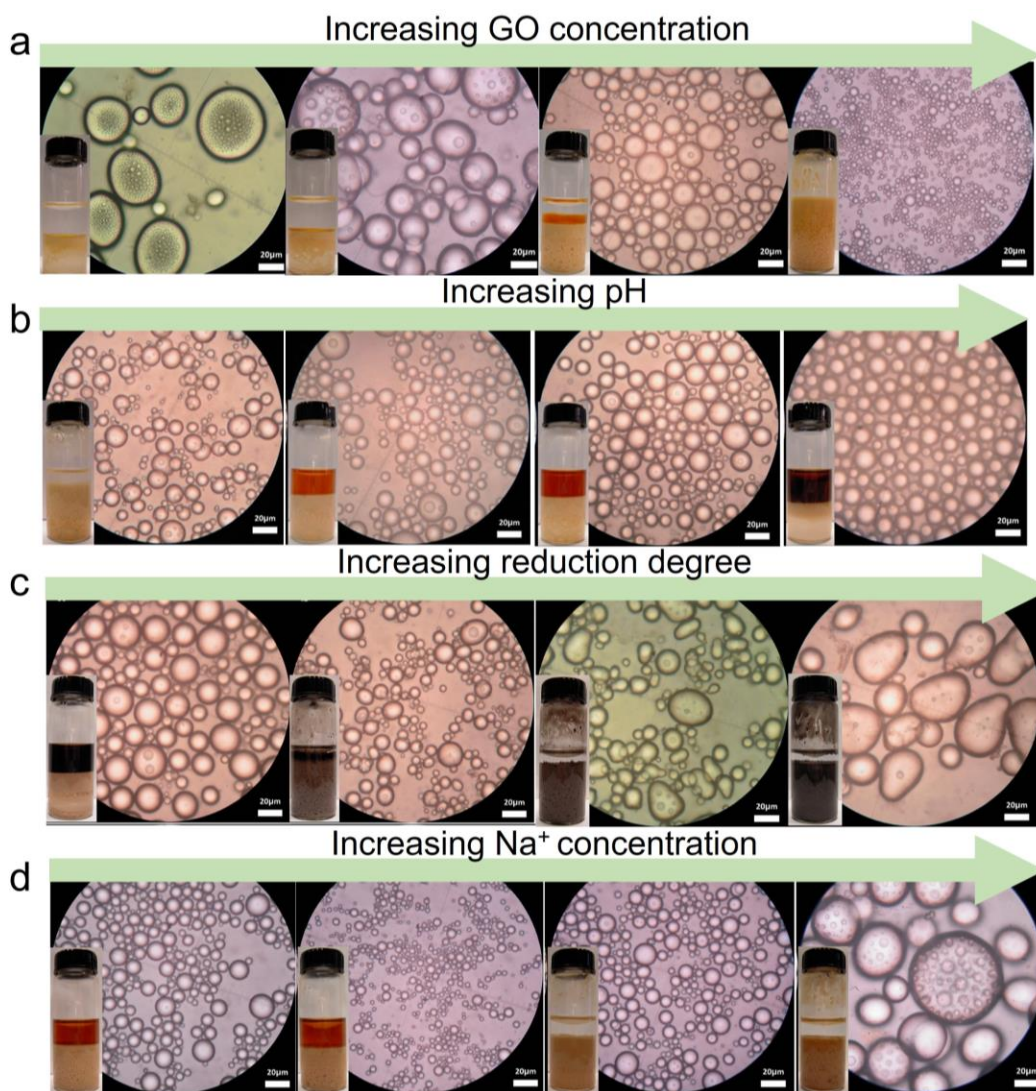


Figure 2.12. Optical microscope images and photos of benzyl chloride in water emulsions stabilized by GO, taken 72 hours after emulsification. The aqueous phase is the top and its color (transparent, light or dark brown) indicate that few or many GO flakes are present in it. Emulsions containing benzyl chloride droplets are shown in the bottom phase. Volume ratio of benzyl chloride: water = 1:1. Scale bar=20 μm . (a) GO emulsions with increasing concentrations, from left to right: 0.1, 0.5, 1, and 3 g/L. More stable emulsions formed, and smaller droplets were observed as GO concentration increased. (b) Emulsions stabilized by GO at various pH, from left to right: pH=1, 3, 6, and 11, GO concentration = 1 g/L. The upper aqueous phase became darker as pH increases, showing that more GO flakes stayed in the water phase rather than stabilizing o/w emulsions. (c) Emulsions stabilized by GO reduced by glucosamine at 80 $^{\circ}\text{C}$, concentration = 1 g/L. From left to right, the reduction degree increased, as indicated by the increasing maximum absorption peaks of rGO (234.8, 241.8, 252.6, and 257.8 nm) through UV-vis absorption spectroscopy measurements. (d) Emulsions stabilized by GO with different NaCl concentrations, from left to right: 0.1, 10, 100, and 1000 mM, GO concentration = 1 g/L. As shown in the last two images in the panels b and c, flocculation of flakes and destabilization of emulsion droplets can be observed. Panels a-d are adapted with permission from Ref. [115]. Copyright 2013 American Chemical Society.

Adjusting amphiphilicity of GO flakes with monovalent molecules (*e.g.*, CTAB [122],[140]) enhance the stability of emulsions and can be used to obtain HIPEs. Due to the hydrophobic alkyl chain, CTAB increases the hydrophobicity of GO more efficiently than Na^+ : a lower mass of CTAB is needed to stabilize similar emulsions ($\text{Na}^+:\text{GO}=36.5\sim 50$ wt% [151],[153], $\text{CTAB}:\text{GO}=2\sim 12$ wt% [122]). The addition of CTAB decreases the negative charge of GO flakes (**Figure 2.13a**), and increases the static contact angles of flakes against water (**Figure 2.13b**), thus enhancing the hydrophobicity of GO [122]. HIPEs were obtained using GO modified by CTAB [122],[140]. It has been showed that the droplet size of GO HIPEs can be adjusted by the extent of CTAB modification: larger CTAB concentrations decreased droplet size, as more hydrophobic GO flakes can stabilize more oil/water interfaces (**Figure 2.13c**) [122]. If, however CTAB content increased too much (*i.e.*, as high as 10% of the GO weight), the excessive GO hydrophobicity destabilized the emulsions, which was reflected by the larger variation in droplet size (**Figure 2.13c**). If the CTAB:GO mass ratio became very large (*e.g.*, >90 wt%), water-in-oil GO HIPEs can be obtained, since the GO flakes became hydrophobic, with static contact angle against water above 90° [140]. Water-in-oil emulsions can also be obtained when hydrophobic modifiers were added to GO (*e.g.*, poly(L-lactic acid) (PLLA) [157], stearyl trimethyl ammonium bromide [158]).

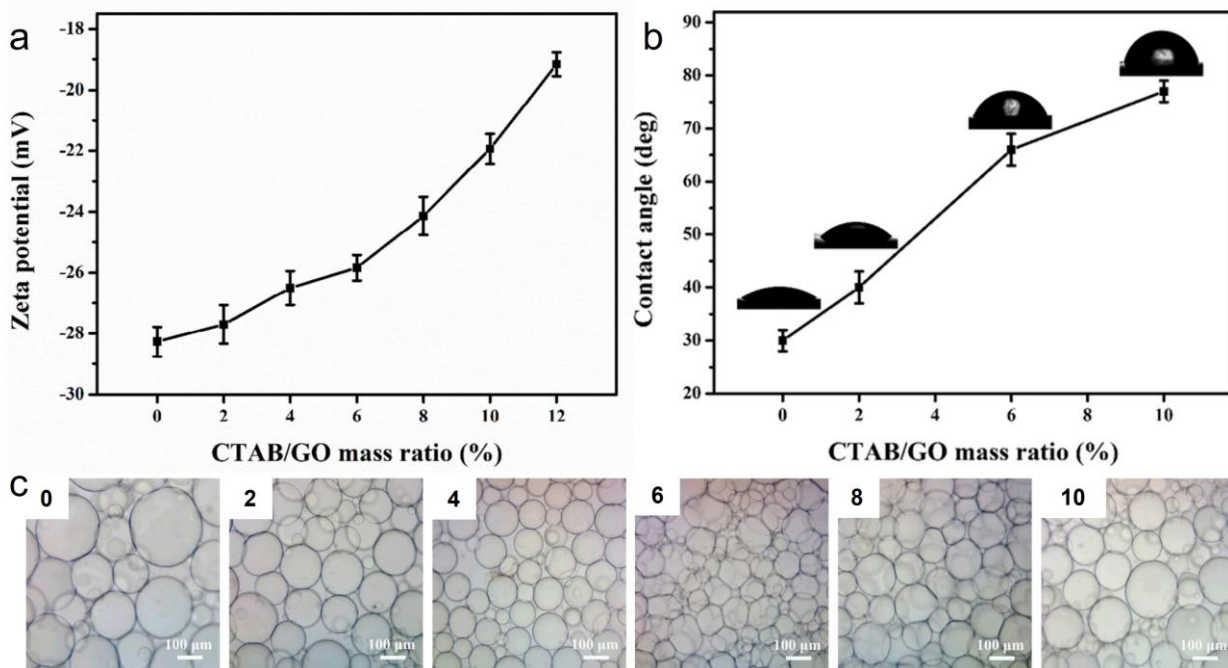


Figure 2.13. Surface modification of GO with CTAB for emulsion stabilization. (a) Zeta potential of GO modified with different amounts of CTAB. (b) Static contact angle against water of GO modified with different amount of CTAB. (c) Optical microscopy images of HIPEs stabilized by CTAB modified GO flakes. CTAB to GO mass fractions are 0, 2, 4, 6, 8 and 10 wt%. GO concentration = 0.8 g/L. Volume ratio of cyclohexane: water= 3:1. Adapted with permission from [122]. Copyright 2016 American Chemical Society.

In summary, as shown in **Equation 2.11**, the surface tension between water and the organic phase selected, as well as the contact angle between GO and water are important considerations to obtain stable GO emulsion. In practice, factors including oil type, oil-to-water volume ratio, concentration and amphiphilicity of GO should be considered together. Due to the polydisperse nature of GO, the conditions to form stable emulsions vary among specific systems, and often need be studied on a case-by-case basis.

2.3 Towards porous architectures: GO assembly templated by Pickering emulsions

Emulsion templating has been successfully used to synthesize 3D porous materials, thanks to the simplicity of template removal (*i.e.*, washing [152] and freeze-drying [141]) and the low cost

of the materials involved. GO stabilized Pickering emulsions have been used as templates to build graphene and graphene-composite 3D porous monoliths with controllable pore size, interconnectivity, electrical conductivity, and mechanical strength. Multiple steps are involved in achieving porous materials with the desired properties, including GO functionalization before emulsification, emulsion formation by adjusting factors (*e.g.*, pH, GO concentration), and treatment of the emulsions (*e.g.*, reduction, drying) to obtain solvent-free 3D monoliths. In this section, we will review the strategies used to synthesize 3D porous materials starting from GO-stabilized Pickering emulsions. As will become clear, the main challenge is to prepare stable emulsions with high oil content to fabricate highly porous materials while maintaining the stability of the network once the liquid phase is removed.

2.3.1 Preparation of GO Pickering emulsion templates for porous materials

When GO Pickering emulsions are used as templates for porous materials, the key step is to prepare stable emulsions with controlled size and composition. To achieve these purposes, besides following the general principles outlined in the previous section, additives are often added to the GO flakes or to the oil phase, aiming to enhance the stability of emulsions or to functionalize the porous materials.

A comprehensive review on all published reports on porous monoliths obtained by GO or rGO Pickering emulsion templating is summarized in **Table 2.2**. This table and the following discussion include both reports that use GO, rGO or modified flakes as the only emulsion stabilizers and those where surfactants or particles are added as co-emulsifiers together with GO or rGO flakes. A few reports discuss emulsions containing GO or rGO, but the droplets are stabilized only by surfactants, *e.g.*, w/o emulsions stabilized by span 80 with GO added to water phase, or emulsions with GO

added after emulsification [159],[160]. These are not discussed since they don't fit the scope of our review on emulsions stabilized by GO or rGO flakes.

Table 2.2. Summary of emulsion formation conditions and corresponding structural parameters of the 3D porous monoliths templated by GO Pickering emulsions.

*NA: not available

Stabilizer and modifications	Stabilizer concentration (g/L)	Oil to water volume ratio	Emulsions		Material of porous monolith	Structure	Pore size (μm)	Density (mg/cm^3)
			Type	Size (μm)				
Emulsions stabilized by GO, rGO or modified flakes								
GO [152]	2-7.5	1:2	o/w	~100	rGO	Closed pores	~100	6-12
GO with NaCl and VC, pH adjusted to 2, [153]	4 (GO); 1.46 (NaCl)	1:5 – 4:5	o/w	12-40	rGO	Open pores	12 – 42	4-9
GO added with VC [161]	7	1:2	o/w	*NA	rGO	Open pores	10-50	NA
GO/PVA, acrylic acid (AA) monomer in water phase, pH adjusted to 3 [162]	5 (GO); 1 (PVA)	0.9:1	o/w	38	GO/PVA/PAA	Open pores	40	NA
GO/PVA, with NaCl and ethanediamine added to GO[153]	8 (GO); 2 (PVA)	1:3 - 6:3	o/w	12-42	rGO/PVA	Open pores	13-45	4-10
GO modified with NaHSO_3 [151]	0.25-2 (GO); 8 (NaHSO_3)	1:1	o/w	60-100	rGO	Honeycomb network	70-100	1.1-2.8
GO liquid crystals crosslinked by poly(oxypropylene) diamine [163]	3	1:4 – 6:4	o/w	4-77	rGO	Closed pores	1-30	NA
GO modified with CTAB, AA monomer in water phase [122]	0.8-1.4 (GO); 0.016-0.096 (CTAB); 288 (AA); 160 (NaOH)	3:1	o/w	80-200	GO/PAA	Open or closed pores	80-170	NA
GO modified with CTAB in water; divinylbenzene (DVB) and styrene (monomers) as the oil [140]	1 (GO) 0.2-0.9 (CTAB)	1:4	w/o	50-400	rGO with amorphous carbon	Open pores	40-352	NA
GO, added with N_2H_4 , adjusting pH to 1, 1-hexadecano as oil phase [164]	4 (GO)	NA	o/w	100	rGO/1-hexadecano	Open pores	NA	NA
rGO, styrene and DVB monomers as oil phase [150]	0.1-5 (rGO)	1:1	w/o	~ 300	poly(styrene-co-divinylbenzene) /rGO	Closed pores	~300	~1000
Emulsion templates stabilized by GO or rGO with additives or co-emulsifiers								

GO/PVA [165]	2 (GO); 1 (PVA)	1:1	o/w	NA	rGO/PVA	Open pores	2	NA
GO/polyvinyl alcohol (PVA)/sucrose [141]	10 (GO); 6 PVA; 6 (sucrose)	3:1	o/w	<40	GO/PVA/sucrose, rGO	Open pores	7-30	~100
GO modified by PLLA/temperature responsive poly(D, L-lactic acid-co-trimethylene carbonate) (PLMC)/SiO ₂ particles [157]	20-80 (GO); 100 PLMC; 15 SiO ₂	2:3	w/o	<50	GO/PLMC/SiO ₂	Open, hierarchical pores <i>via</i> 3D printing	1.5 mm; 5-40 mm	70-87
GO/SDS/polystyrene (PS) particles [166]	7 (GO); 100 (SDS); 100-300 (PS)	1:3	o/w	NA	rGO/PS	Open pores	70	7.75-14.59
GO/PS nanoparticles Adjusting pH of GO suspension to 2 [167]	4 (GO) 2 (PS)	1:2	o/w	5-50	GO/PS	Dense pores	4-20	45.3
GO/PVA/SDS [168]	4 (GO); 25 (PVA); 50 SDS	NA	o/w	NA	rGO with amorphous carbon	Open pores	~ 5	NA
GO/PVA [169]	2 (GO) 1 (PVA)	1:1	w/o	NA	GO/PVA	Open pores	2-10	NA
GO/gelatin [170]	1-6 (GO) 220 (gelatin)	3:5	o/w	NA	GO/gelatin	Open pores	1-2	NA
GO/PVA/butanol, added with ethylenediamine (EDA) [171]	8.3 (GO); 0.5 (PVA); 0.04-0.17 (butanol)	5:12	o/w	20-50	rGO/PVA	Open pores	~50	5-50
GO/sodium dodecyl benzene sulfonate (SDBS)/CTAB, PDMS in oil [172]	1 (GO); 0.25 (SDBS); 0.25 (CTAB)	1:1	w/o	20-40	GO/PDMS	Open pores	~30	NA
GO/cellulose nanofibrils, PMMA dissolved in oil [173]	8 (GO); 8 (cellulose)	1:3-1:4	o/w	NA	rGO porous monoliths with amorphous carbon	Open pores	100	1-9
GO/PS, PS added to oil phase [174]	10 (GO); 1.5-6 (PS)	1:3	o/w	NA	rGO/PS	Closed pores	20-70	22
GO/Fe ₃ O ₄ particles in water, with drugs in oil phase [139]	1-5 (GO); 0-1.5 (Fe ₃ O ₄)	1:2	o/w	~100	rGO/Fe ₃ O ₄ loading drugs	Closed pores	~100	NA
GO/metal-organic framework (MOF) particles [175]	2(GO); 0.4~1 (MOFs)	1:1	o/w	2-30	GO/MOFs	Open pores	4-18	NA
GO/cellulose nanocrystals [176]	2-3.2 (GO); 2-0.8 (cellulose)	1:1	o/w	10-80	rGO/cellulose	Closed pores	5-60	NA
GO/hydroxyethyl cellulose, acrylamide (AA) monomers added to water [177]	2(GO); 10 (hydroxyethyl cellulose)	1:1	o/w	NA	GO/PAA/hydroxyethyl cellulose/	Closed pores	20-100	NA
GO/CNT/2-ethyl-4-methylimidazole (EMI)/span80,	2 (GO); 0.3 (CNT); 2	NA	w/o	<10	GO/CNT/PAN	Closed pores	< 10	NA

acrylonitrile (AN) monomers added to the oil phase [178]	(EMI);3.7 (span80)							
GO/polyvinylpyrrolidone (PVP)/span 80, monomers AA, DVB as oil phase [179]	3 (GO/PVP); 130 (span80)	1:4	w/o	NA	Poly(AA-DVB)/rGO/PVP	Open pores	~50	NA
GO/PVP/span 80, monomer hydrophilic acrylamide added to water, monomer DVB as oil phase [180]	3 (GO/PVP); 286 (span 80)	7:45	w/o	NA	Poly(Aam-DVB)/GO/PVP	Open pores	~700	NA
GO/span 80/DVB monomers [181]	5 (GO)	1:1	w/o	~30	rGO/PDVB	Open pores	~30	200
rGO/Hypermer 2296, DVB monomer as oil phase [149]	5 (GO)	1:3	w/o	NA	polyDVB and amorphous carbon form	Open pores	50-100	170-320
GO/Fe ₃ O ₄ /melamine formaldehyde (MF) added to water [132]	3 (GO); 22 (Fe ²⁺)	1:3	o/w	75-150	GO/Fe ₃ O ₄ /polyMF	Closed pores	~100	NA

When GO flakes serve as the main emulsifiers, the droplet size decreases as the GO concentration rises, and emulsion droplet size distribution narrows (**Figure 2.14a-c**) [122],[140],[151]. Consequently, the pores templated by the emulsion droplets become smaller (**Figure 2.14d-f**) [122],[140],[151] while the pore walls thicken, as shown by TEM diffraction patterns (**Figure 2.14g-i**) [151]. Higher GO concentrations increase the density of the resulting porous monoliths [150],[151], their compressive modulus [151],[152], and thermal and electrical conductivity after reduction [152],[164]. Higher concentration of GO leads to less opening, namely “pore throat”, between pores in HIPE templated porous monoliths (**Figure 2.14j-m**) as more barriers at o/w interfaces hinder the formation pore throats [122].

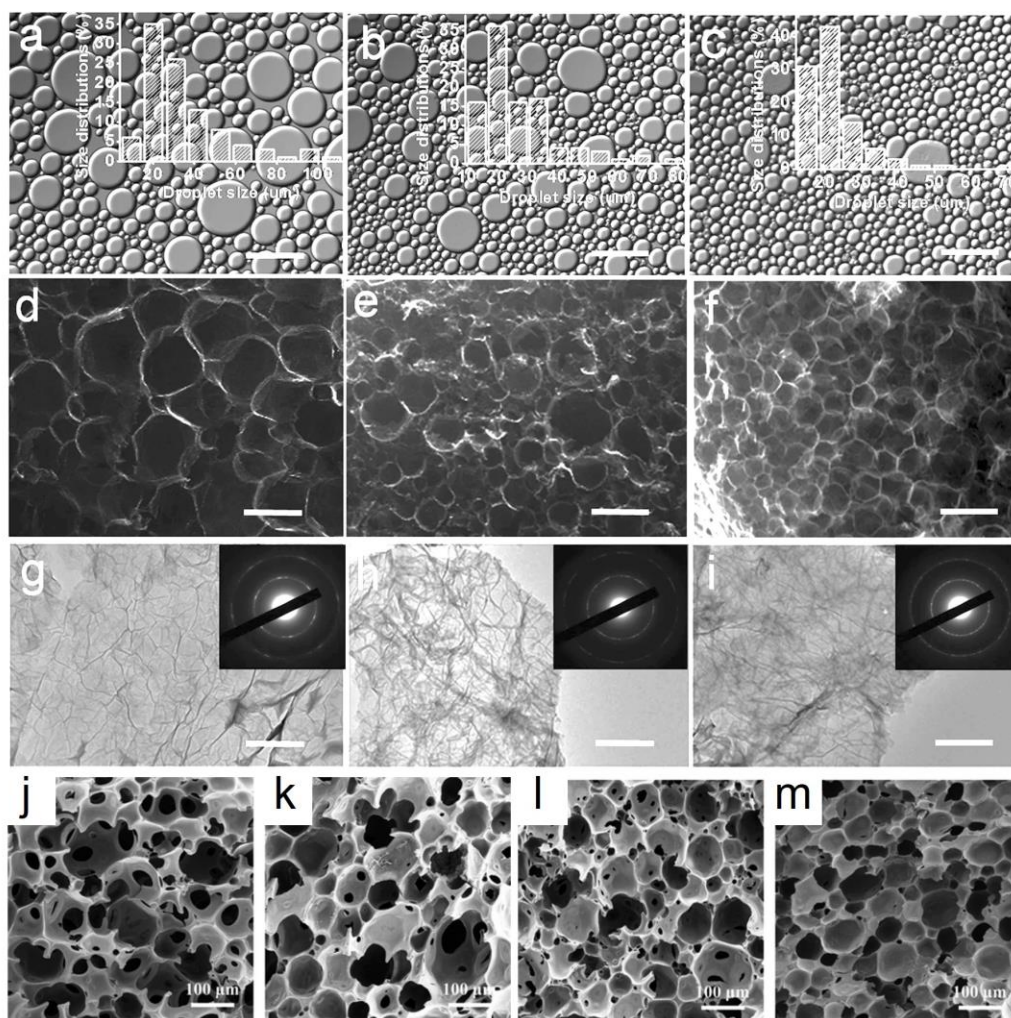


Figure 2.14. Controlling pore size and interconnectivity of monoliths by changing GO concentration. Note that the interconnectivity in the studies on GO emulsion templated porous monoliths was qualitative rather than quantitative. (a-c) Confocal laser scanning microscopy images of GO emulsions with GO concentrations of (a) 0.75 g/L, (b) 1.25 g/L, and (c) 2 g/L. Droplet size distributions of the emulsions are shown in the insets. (d-i) SEM and TEM images of porous rGO prepared by GO emulsions in panels a-c. The insets in g-i are the electron diffraction of the pore walls. The thickness of the wall increased with the increasing GO concentration. Cyclohexane-to-water volume ratio = 1:1. Scale bars, 100 μm in (a-f) and 1 μm in (g-i) [151]. (j-m) SEM images of GO/PAA porous monoliths prepared using GO stabilized o/w HIPE templates with different GO concentrations: (j) 0.8 g/L, (k) 1 g/L, (l) 1.2 g/L, (m) 1.4 g/L. Cyclohexane-to-water volume ratio = 3:1. Previous to emulsification, the GO flakes are modified with CTAB, with CTAB to GO mass fraction of 6 wt%. The scale bars for j-m are 100 μm . Adapted with permission from Ref. [122]. Copyright 2016 American Chemical Society.

When the ϕ_o reaches values $> 75\%$ in o/w HIPEs, the droplets are compact, and the thin barrier created by the flakes at the oil/water interface can easily break during internal phase evaporation, resulting in thinner pore walls and pore throats between the pores [141]. A higher internal phase

volume ratio leads to larger droplets in the emulsion and thus larger pores in the porous monoliths (**Figure 2.15**) with lower density [153],[163]. However, it has been shown that the emulsions became unstable, and the droplets as well as the pores became irregular as the internal phase volume increased (**Figure 2.15**) [163]. Besides increasing the concentration of stabilizers [157],[170], modifications of GO [122],[150], and the addition of additives and co-emulsifiers [141],[163],[176] [149] can enhance the emulsion stability.

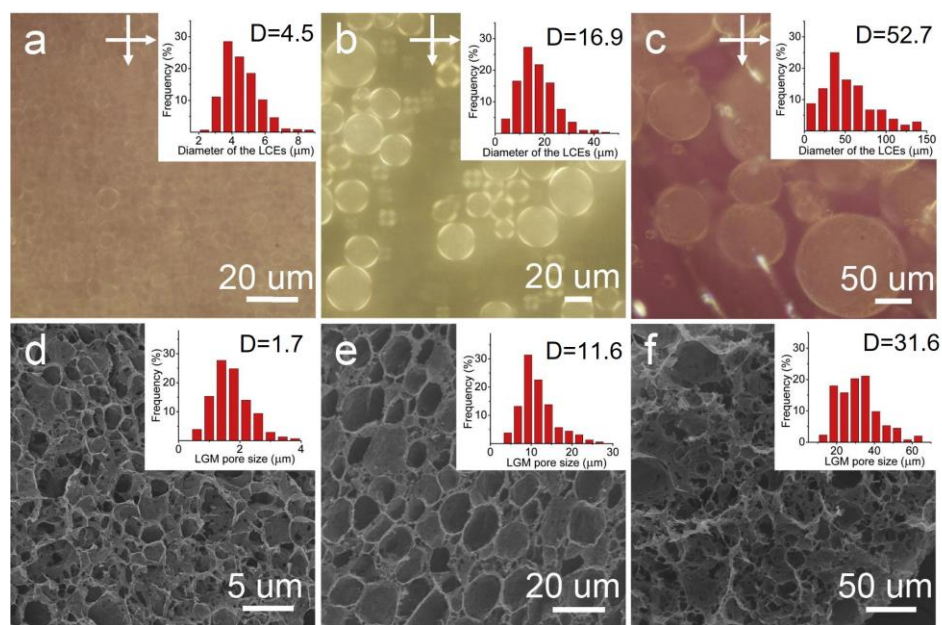


Figure 2.15. Influence of oil to water ratio on the GO emulsion droplet size and morphology of porous monoliths. (a-c) Polarized optical microscopy (POM) images of emulsions, and (d-f) SEM images of the corresponding rGO monoliths. Water to oil volume ratio: (a, d) 4:1, (b, e) 4:4, and (c, f) 4:6. Size distribution, average diameter of the emulsion droplets and diameter of the pores are inserted in each image. Cotton seed oil-to-water ratio =1:2. GO concentration = 3 g/L. Reproduced with permission from Ref. [163]. Copyright 2014 Elsevier Ltd..

Modifying the GO flakes before emulsification, *e.g.*, by changing the pH of GO suspensions, adding salt, and surface modification with hydrophobic molecules are effective methods to achieve stable emulsions and control the morphology of the resulting porous structure. Studies found that adjusting the pH of GO suspensions to 1-3 before the emulsification enhances the hydrophobicity of GO flakes, which in turn enhances the GO adsorption at oil/water interfaces to create stable emulsions [141],[153],[164],[167]. Chen *et al.* found GO/PVA (with concentration of GO at 5 g/L,

PVA at 1 g/L) stabilized o/w emulsion droplets can assemble into gel-like networks at a pH of 3, but dissociate and disperse at a pH of 14 [162]. The gel-like emulsions formed at a pH of 3 can be injected as 3D printing inks, and small, uniform pores were obtained in the resulting porous monoliths as opposed to those templated by emulsions formed at a pH of 14 [162]. As discussed, the addition of CTAB resulted in a decrease of droplet size and more o/w interfaces in GO stabilized HIPEs (**Figure 2.13c**, CTAB:GO mass fraction 0~6 wt%), leading to lower amount of GO flakes at interfaces, and thus thinner pore walls and more pore throats (**Figure 2.16**) [122]. When the hydrophobicity further increased with higher CTAB content, more closed pores were observed because larger emulsion droplets with less o/w interfaces formed, leaving larger amount of GO flakes at interfaces and closed pores (**Figure 2.16**) [122].

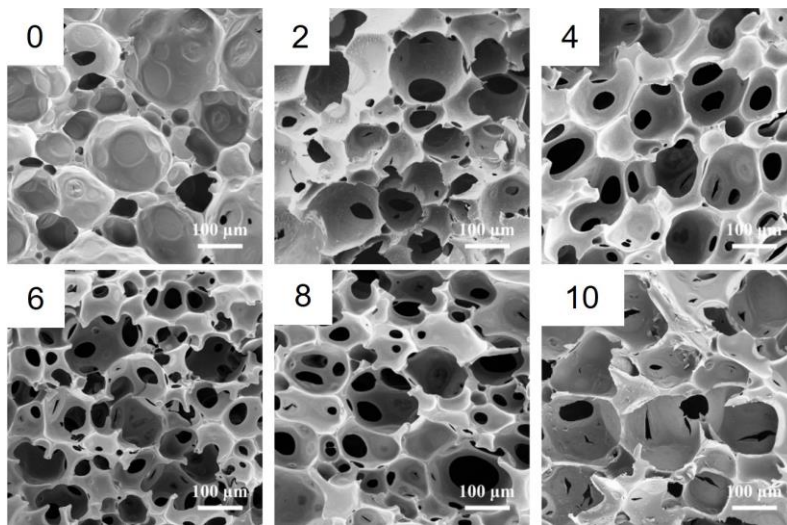


Figure 2.16. SEM images of porous monoliths templated by o/w GO HIPEs. GO was modified by CTAB. As CTAB to GO mass fraction increased from 0, 2, 4, to 6 wt%, more open pores were created. When CTAB to GO mass fraction further increased to 8 and 10 wt%, more closed pores appeared. GO concentration: 0.8 g/L. Volume ratio of cyclohexane: water = 3:1. Adapted with permission from [122]. Copyright 2016 American Chemical Society.

In addition to agents used to change the amphiphilicity of GO, a variety of additives can be added to GO for the purposes of crosslinking, co-emulsification, or functionalization. Crosslinkers such as poly(oxypropylene)diamine were added to the GO suspension before emulsification, in

order to improve the alignment of GO flakes and to enhance emulsion stability [163]. Co-emulsifiers, including particles (*e.g.*, Fe₃O₄ [139], SiO₂ [157], metal organic frameworks (MOFs) [175], cellulose nanocrystals [173],[176] and polystyrene (PS) [166],[167]), and surfactants (*e.g.*, PVA [141],[165],[168],[169] and sodium dodecyl sulfate (SDS) [168],[182]) can be added to water phase together with GO to stabilize emulsion droplets. The addition of co-emulsifiers decreases the size of the o/w emulsion droplets, and as a consequence the pore size of resulting porous monoliths, similar to the effect of increasing GO concentration [141]. Interactions between GO and co-emulsifiers (*e.g.*, hydrogen bonding [139] [175] and π - π interactions [166],[167]) enhance the stability of the emulsion droplets against coalescence during both emulsion formation and the post-emulsification treatments [176], which also contribute to the small pore size and narrow pore distribution (an example is shown in **Figure 2.17a-k**). Adding co-emulsifiers increases the viscosity of emulsions [141],[157], so that these can be used as 3D printing inks. An example is presented in **Figure 2.17l** and m: the resulting materials showed large pores (~ 1mm) created through the printing process and small pores (70-87 μ m) templated by the emulsion droplets. Temperature responsive additive poly(D, L-lactic acid-co-trimethylene carbonate) (PLMC) was added to oil phase for functionalization purpose, so that the porous monoliths had temperature responsiveness [157].

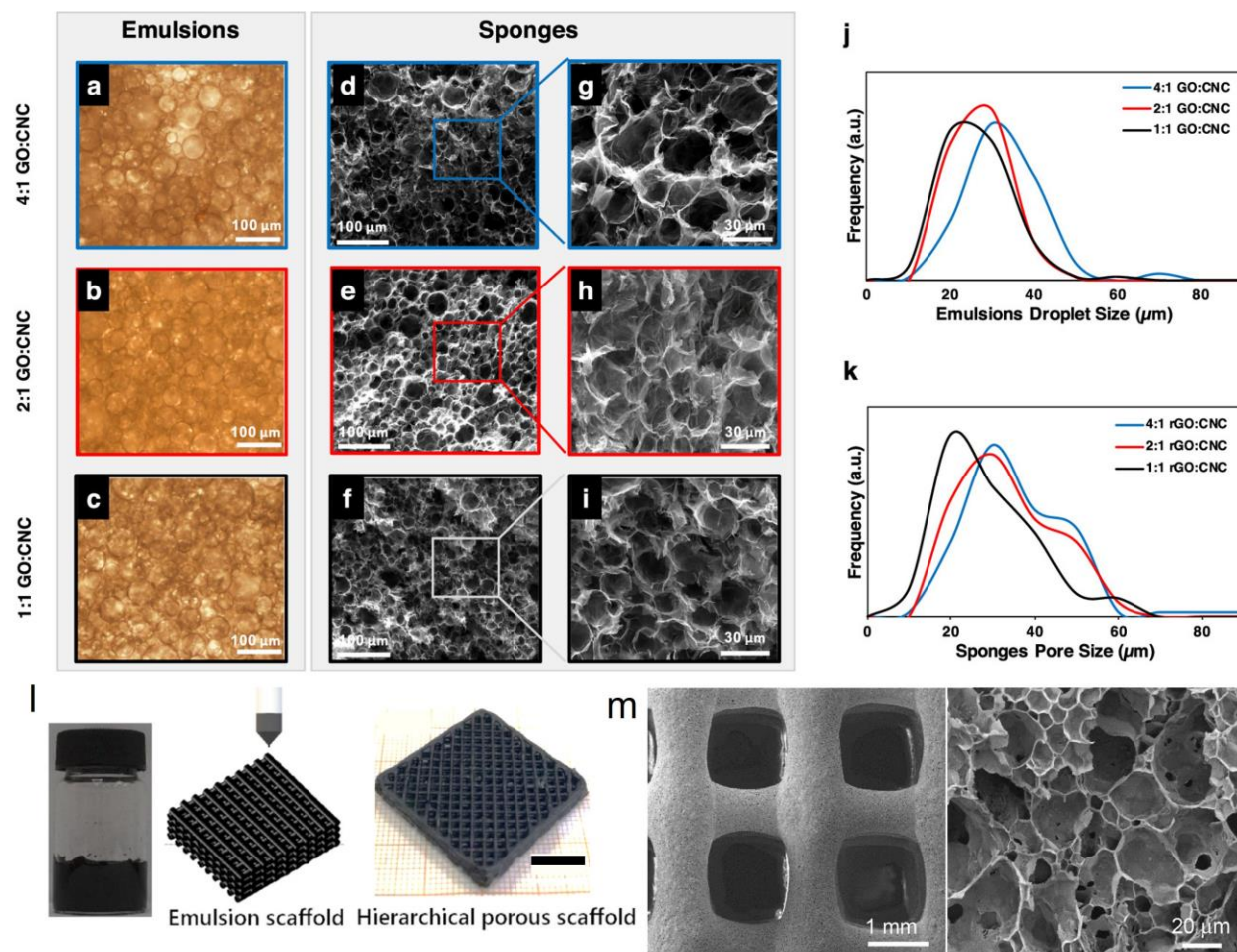


Figure 2.17. Morphology of porous monoliths templated by co-emulsifiers stabilized emulsions. (a-c) Optical microscopy images of o/w emulsions at different GO/nano-cellulose mass ratios. The total concentrations of GO and cellulose was 6 g/L in all cases. Cyclohexane-to-water volume ratio = 1:1. (d-i) SEM images of corresponding rGO/nano-cellulose porous monoliths. Droplet size (j) and pore size (k) distribution of the emulsions and porous monoliths. Adapted with permission from [176]. Copyright 2020 American Chemical Society. (l-m) Emulsion ink for 3D printing stabilized by GO/SiO₂ particles. GO was modified by PLLA-COOH so that the flakes can be dispersed in dichloromethane (CH₂Cl₂). CH₂Cl₂-to-water volume ratio = 2:3. Concentration are 40 g/L (GO), 100 g/L (PMLC), and 15 (SiO₂). (l) Photograph of emulsions (left), illustration of 3D printed emulsion scaffold (middle), and photograph of porous monolith (right) (scale bar = 1 cm). (m) SEM images showing the microstructure of the 3D printed scaffold with both large pores from 3D printing and small pores templated from emulsion droplets. Adapted with permission from Ref. [157]. Copyright 2021 Wiley Periodicals LLC..

2.3.2 Post-emulsification treatments: reduction and drying methods

After obtaining stable emulsions as templates, the next key step is to remove the solvents to obtain porous monoliths. For polymer-based monoliths templated by GO or rGO emulsions, the solvent removal doesn't lead to the collapse of structures because the polymeric structures are

fixed by crosslinkers. Therefore, the polymeric monoliths can be directly dried in air or in a vacuum [122],[132],[140],[149],[181]. However, for GO and rGO based porous monoliths, van der Waals interactions between flakes and solvent as well as capillary force cause the collapse of the porous networks [167],[170],[182]. Therefore, various treatments, including hydrothermal reduction of emulsions, chemical reduction, direct freezing of emulsions, and thermal reduction of porous monoliths have been tried.

During reduction, GO flakes are reduced and immobilized as they form networks. Since GO flakes must be used as the starting materials, these two reduction techniques can be applied only to o/w emulsions. To perform a hydrothermal reduction, the GO emulsions are sealed in an autoclave with a polytetrafluoroethylene (PTFE)-lined container and placed inside an oven. The GO flakes in water are reduced due to the high temperature and pressure, and crosslinked *via* hydrophobic and π - π interactions upon restoration of sp^2 domains [183],[184]. Li *et al.* first fabricated microporous rGO monoliths by hydrothermal reduction of hexane-in-water GO emulsions [152]. For comparison, they also prepared rGO porous monoliths *via* hydrothermal reduction of suspensions of GO in water, without emulsion templating. As shown in **Figure 2.18a**, the monoliths made by emulsion templating had closed, spherical pores templated by oil droplets. The porous monoliths made starting from a GO suspension showed irregular pores (**Figure 2.18b**) and had a higher density (24.2 mg/cm^3 , **Figure 2.18c**, right) compared to emulsion templated porous monoliths (8.6 mg/cm^3 , **Figure 2.18c**, left). The closed-cell porous networks contributed to the excellent mechanical elasticity (85% stress retention after 1000 compression cycles at 50% strain) as shown in **Figure 2.18d**.

Chemical reduction is achieved by adding reduction agents such as vitamin C [139],[161],[176], N_2H_4 [163],[164] or NaHSO_3 [151] to the GO-containing water phase. The process happens at

temperatures of 70-90 °C, *i.e.*, milder than hydrothermal reduction. After chemical reduction, several washings with water are performed to remove reduction agents. For example, rGO porous monoliths were obtained by NaHSO₃ reduction of GO emulsions, as shown in **Figure 2.18e-h** [151]. Highly ordered honeycomb-like structure with uniform polyhedral pores was shown in **Figure 2.18e-g**. The monoliths had a low density (2.8 mg/cm³) and excellent elasticity, being able to fully recover from 80% deformation after 10 cycles of compression (**Figure 2.18h**) [151].

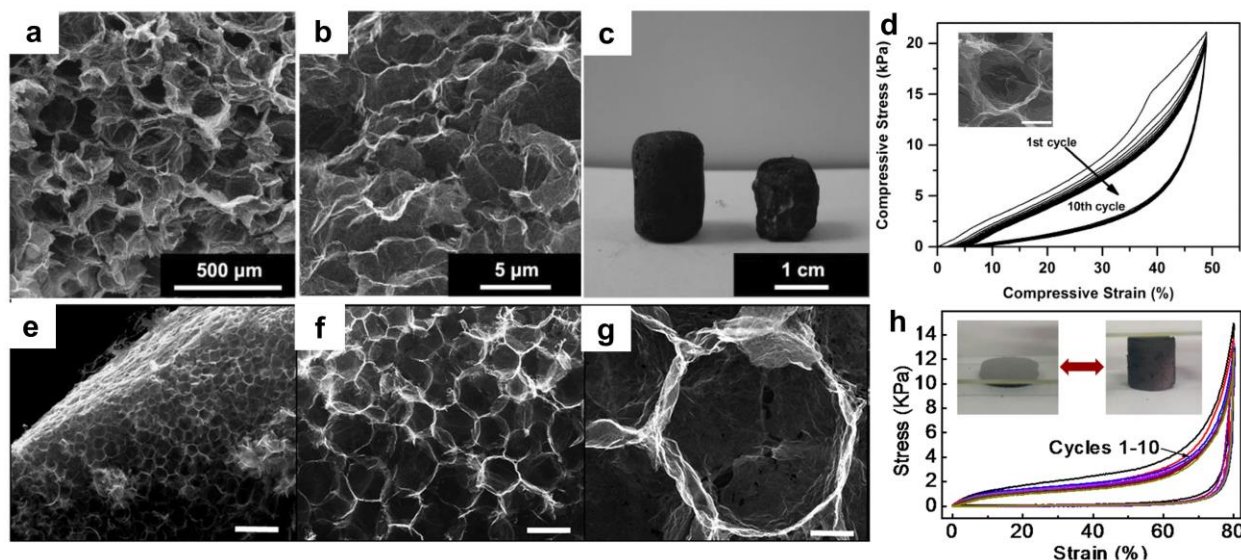


Figure 2.18. Reduction methods to prepare porous rGO monoliths. (a-d) Hydrothermal reduction: SEM images of porous rGO prepared with GO emulsion templating (a) and with GO suspension without emulsions (b). (c) Photographs of rGO monoliths prepared with (left) and without (right) emulsion templating. (d) Compressive stress-strain curves of the first 10 cycles of compression of rGO monoliths prepared by emulsion templating. The inset is an SEM image of a pore after the first compression to 50%, scale bar = 50 μm. Adapted with permission from Ref. [152]. Copyright 2014 WILEY - VCH Verlag GmbH & Co. KGaA, Weinheim. (e-h) rGO porous monoliths templated by GO emulsions reduced by NaHSO₃. (e-g) SEM images of a rGO porous monolith at lower (e) and higher magnification showing closely packed pores with polyhedral morphology (f), and a hexagonal pore sharing its boundaries with other six adjacent pores (g). Scale bar = 150 μm (e), 50 μm (f), 8 μm (g). (h) Stress-strain curves of 10 compression cycles on the rGO monolith shown in panel e, exhibiting elastic deformation. Inset, photographs of the monolith under compression and release [151].

The oil phase (*e.g.*, hexane, cyclohexane or cotton seed oil) and/or impurities can be removed by washing with water at 80 °C [152] or at room temperature [161], or with acetone/ethanol/water

step by step [153],[163], or even HCl [176]. The washing step is time consuming and can cause coalescence of oil droplets [176].

Freeze-drying can be performed after hydrothermal reduction [153] or after the washing step of chemical reduction [139],[151],[163],[176], which is to eliminate solvents and obtain rGO porous monoliths. During freeze-drying, ice crystals are directly sublimated into water vapor at low pressure, minimizing surface tension change and avoiding porous structure collapse. In addition, it's possible to obtain GO and GO composite porous monoliths by directly freeze-drying GO emulsions [141],[157],[168],[169],[175].

Studies have demonstrated that during freezing, ice nucleation and growth can affect GO [185] or rGO [186]–[188] porous structure, as flakes can assemble around the ice crystals. Specifically, the freezing direction (**Figure 2.19a**) and temperature (**Figure 2.19b**) are key parameters. When directionally frozen, ice crystals prefer to grow in the direction of the temperature gradient. As growing, ice crystals push away the rGO flakes, which become entrapped between neighboring ice and form ice-templated 3D networks. Following freeze-drying, ice crystals sublimate and parallel, elongated pores are generated [185],[188].

Temperature is another factor affecting the ice formation. Ice solidification has two consecutive phases: ice nucleation and growth. At lower freezing temperatures, nucleation prevails and results in formation of smaller ice crystals, which in turn results in smaller pore size. In contrast, at higher freezing temperature, crystal growth dominates, resulting in the formation of larger ice crystals and larger pores [186],[187].

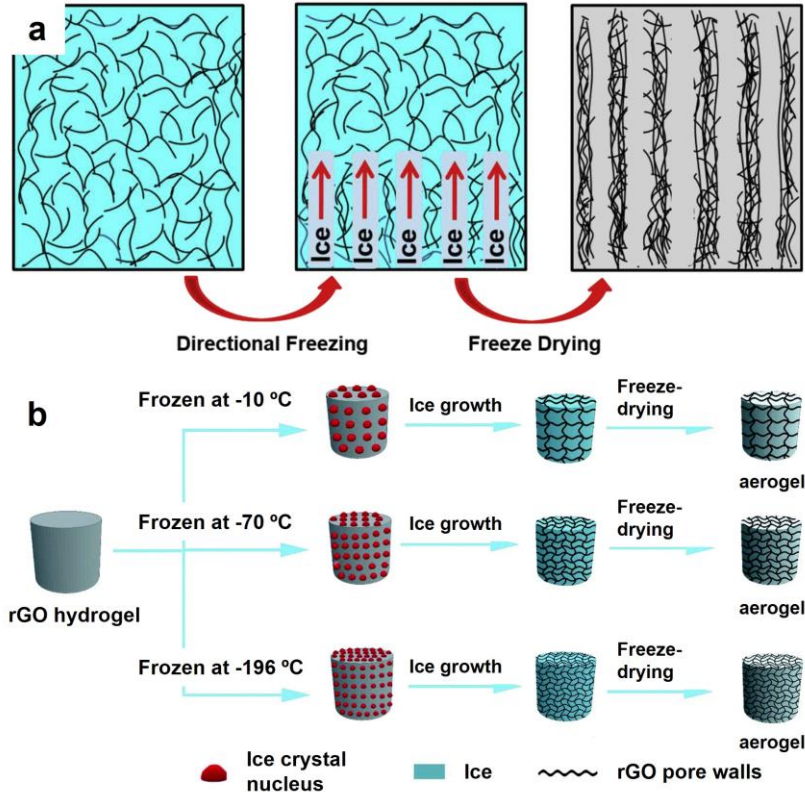


Figure 2.19. (a) Illustration of the directional freezing and pores oriented in parallel after drying. Reprinted with permission from Ref. [188]. Copyright 2016 Elsevier Ltd.. (b) Illustration of ice crystallization and growth under different freezing temperatures, and porous monoliths with different pore size obtained after drying. Reproduced from Ref. [187]. with permission from the Royal Society of Chemistry.

Directional freezing has been applied to GO emulsion systems. For example, Brag *et al.* froze GO emulsions unidirectionally to promote the growth of ice within the continuous water phase surrounding the emulsion droplets (**Figure 2.20a**) [141]. After eliminating the oil by drying in a vacuum, the GO pore walls at triple junctions between adjacent pores showed micro to nano sized patterns and wrinkles templated by ice crystals growth (**Figure 2.20b-e**).

It should be noted that the freezing temperatures haven't been studied to adjust the morphology of monoliths via GO emulsion templating. There is a gap that remains in obtaining complex architectures and compositions through the control of emulsion and ice templates.

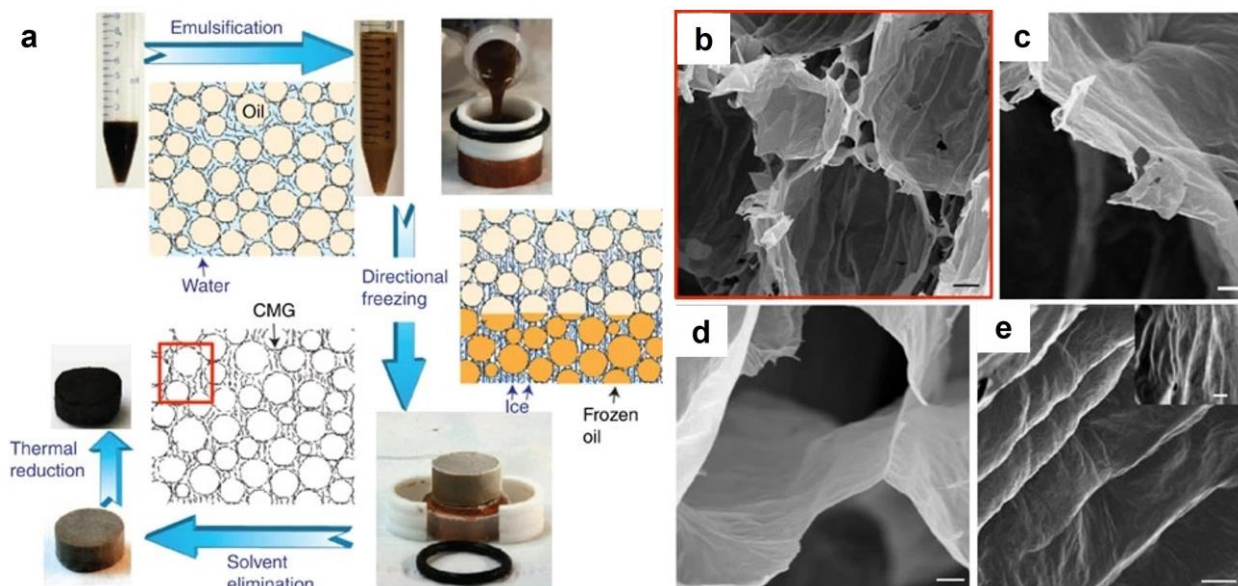


Figure 2.20. (a) Assembly process, including emulsification, unidirectional freezing, and freeze drying to obtain rGO monoliths. Following the arrows: emulsification with 75 vol% of the internal toluene phase, emulsions moulded and subsequently directionally frozen. While growing, ice crystals template the patterns and wrinkles on the GO pore walls. After eliminating the solvents by freeze-drying and reduction, porous rGO monoliths were obtained. (b-e) SEM images showing the architecture of porous rGO. Scale bars, 10 μm (b), 2 μm (c), 1 μm (d) and 2 μm (e) [141].

Thermal reduction is a common way to obtain rGO porous monoliths after freeze-drying GO emulsions. By heating the GO monoliths in inert atmosphere (*e.g.*, Ar or N₂) above 300 °C, the oxygen containing groups are removed and sp² networks are restored [141],[168],[173],[182]. Therefore, rGO monoliths are obtained preserving the morphology of porous GO but with significantly higher electrical conductivity [92]. Previous studies have shown that rGO monoliths obtained through thermal reduction of GO emulsions had carbon to oxygen atomic ratio up to 20, whereas monoliths obtained by hydrothermal reduction and chemical reduction showed carbon to oxygen atomic ratio below 7 [141],[152],[161],[163],[176]. The high reduction degree led to electrical conductivities nearly 100 times higher than those achieved on hydrothermally reduced rGO monoliths with a similar density [141],[152]. The post-emulsification treatments, properties and applications of porous GO and rGO based monoliths templated by GO/rGO emulsions are summarized in **Table 2.3**. The emulsion formation conditions have been shown in **Table 2.2**.

Table 2.3. Post-emulsification treatments, properties and proposed applications of GO and rGO based porous monoliths obtained by GO/rGO emulsion templating.

Stabilizer and modifications	Material of monolith	Post treatment(s)	SSA (m ² /g)	Compressive modulus (kPa)	Conductivity (S/m)	Proposed application
Hydrothermal reduction						
GO [152]	rGO	1. Hydrothermal reduction at 180 °C for 10 h 2. Remove hexane by washing with water at 80 °C 2. Annealing at 40 °C in 100% humidity	310 - 490	16-42	0.48-1.76	Pressure sensing
GO/PVA with NaCl and ethanediamine [153]	rGO/PVA	1. Hydrothermal reduction at 95 °C 2. Remove oil by washing with acetone-ethanol and water 3. Freeze-drying	NA	NA	NA	absorption of organics
GO/PVA/butanol [171]	rGO/PAA	1. Hydrothermal reduction at 95 °C for 6 h 2. Directional freezing at –33 °C for 12 h 3. Freeze-drying	NA	0.2 – 0.16	NA	absorption of organics
Chemical reduction						
GO and Fe ₃ O ₄ particles [139]	rGO/Fe ₃ O ₄ loading with drugs	1. Chemical reduction by vitamin C at 90 °C	NA	NA	0.14-0.26	drug delivery
GO [163]	rGO	1. Chemical reduction by N ₂ H ₄ at 90 °C 2. Remove cotton seed oil by washing with acetone/water and freeze drying	NA	NA	NA	NA
GO/1-hexadecanol [164]	rGO/1-hexadecanol	1. Chemical reduction by N ₂ H ₄ at 90 °C	NA	NA	1	energy storage and conversion as author proposed
GO [161]	rGO gel	Chemical reduction by vitamin C at 90 °C	NA	NA	NA	uranyl extraction
GO/cellulose nanocrystals [176]	rGO and rGO/cellulose	1. Chemical reduction with ascorbic acid at 70 °C 2. Wash with HCl and water 3. Freezing at -80 °C and freeze-drying	NA	30 (rGO); 100-400 (rGO/cellulose)	NA	absorption of organics
GO with NaHSO ₃ [151]	rGO	1. Chemical reduction at 70 °C 2. Freezing at -20 °C and freeze drying	NA	1.3-12.9	NA	absorption of organics
Freeze-drying						
GO/MOF particles [175]	GO/MOFs	Freezing in liquid nitrogen and freeze-drying	146	NA	NA	gas absorption

GO/PVA [169]	GO/PVA	Freeze-drying	22.3	NA	NA	NA
GO/PLMC/SiO ₂ [157]	GO/PLMC/SiO ₂	1. 3D printing with emulsion as inks 2. Freezing at -18 °C then freeze-drying	NA	NA	NA	shape memory, temperature-responsive drug release
GO/SDBS/CTAB [172]	GO/PDMS	1. Freezing at -20 °C then freeze drying	NA	NA	NA	gas barrier
GO/PVP/span 80, monomers AA, DVB as oil phase [179]	Poly(AA-DVB)/GO/PVP	Freeze-drying	NA	NA	NA	absorption of organics
Thermal reduction						
GO/PS [174]	rGO/PS	1. Freezing in liquid nitrogen and freeze drying 2. Thermal reduction at 200 °C	NA	31.75	4.33	pressure sensing
GO [141]	rGO	1. Directional freeze-drying 2. Thermal reduction ~ 1000 °C	431	1 kPa	NA	absorption of organics
GO/PVA [165]	rGO	1. Freezing in liquid nitrogen and freeze drying 2. Microwave irradiation reduction at 150 °C	127	NA	NA	absorption of organics
GO/cellulose nanofibrils/P MMA added to oil phase [173]	rGO/amorphous carbon	1. Freeze-drying 2. Thermal reduction at 800 °C	NA	9 - 32 KPa, at 80% stain%	NA	interference shielding material and flexible pressure sensor
GO/SDS/PS particles [166]	rGO/PS	1. Freezing in liquid nitrogen and freeze drying 2. Thermal reduction at 200 °C	NA	NA	1.28	pressure sensing
GO/PVA/SDS [168]	rGO	1. Freeze drying 2. Thermal reduction at 750 °C	325	NA	NA	immobilization of glucose oxidase

2.4 Stimuli-responsive GO systems

Stimuli-responsive materials exhibit responsiveness to external stimuli like pH, temperature, light, electrical current and moisture, through changing their properties, such as morphology, solubility, or mechanical strength, in a controlled and reversible manner. Research has been done on responsive materials for various applications such as sensors, actuators, and artificial muscles. GO and rGO have been used as components that directly respond to stimuli or as additives to

improve the conductivity, strength, or overall responsive performance of responsive materials [9]. In the next few sections, stimuli-responsive systems incorporating GO and rGO as active or passive components will be reviewed. The functionalization of GO and rGO for temperature responsive systems will be also introduced.

2.4.1 pH or light responsive GO and rGO systems

GO and rGO can directly respond to several stimuli by themselves, such as pH [30], light [189], and electric field [9]. This section will introduce examples of GO and rGO systems that can actively respond to pH and light.

2.4.1.1 pH responsive systems

Because GO colloidal stability is sensitive to pH, the protonation (at low pH) and deprotonation (at high pH) of GO flakes can be used to adjust the electrostatic forces and van de Waals interactions, resulting in the dispersion and self-assembly of flakes (*e.g.*, solution-gelation transition shown in **Figure 2.21a**). For instance, Bai *et al.* found that when the pH of a GO suspension was reduced from 4.6 to 0.6 (**Figure 2.21b**), the weakened electrostatic repulsion and enhanced hydrogen-bonding between flakes caused the GO to start interacting with each other, forming hydrogels, in which flakes bond into networks in aqueous medium [31].

For applications such as drug delivery, gels are needed to form in more basic rather than acidic conditions (*e.g.*, intestine pH \sim 6.8–7.4), polymers such as poly(ethylene oxide) (PEO) [31], cellulose [190], and PVA [191], chitosan [192] have been added as bonding agents to tune GO assembly under different pH. An example is shown in **Figure 2.21b**: at the same concentration, GO sheets mixed with PEO went through solution-gelation transition at a pH of 4, while pure GO sheets formed hydrogels at a pH of 0.6[31]. In another example, PAA was added to GO, leading to sol-gel transition at a pH of 7, which enabled the release of vitamin B₁₂ to the intestine [191].

Thanks to the large surface area of flakes and abundant interactions (*e.g.*, π - π and hydrophobic interactions) between flakes and the potential drug that is loaded, GO and rGO flakes serve as nano- or micro-carriers for pH-controlled drug delivery (**Figure 2.21c**). At an acidic pH, drugs protonate, weakening the interactions between drug and GO or rGO flakes, leading to drug release from the sheets. To avoid the aggregation of flakes in physiological condition because of the presence of ions and to improve the sensitivity to different pH, responsive molecules such as poly(2-(diethylamino) ethyl methacrylate) [193], poly(2-vinylpyridine) [194], and 2,3-dimethylmaleic anhydride [30] have been introduced to GO.

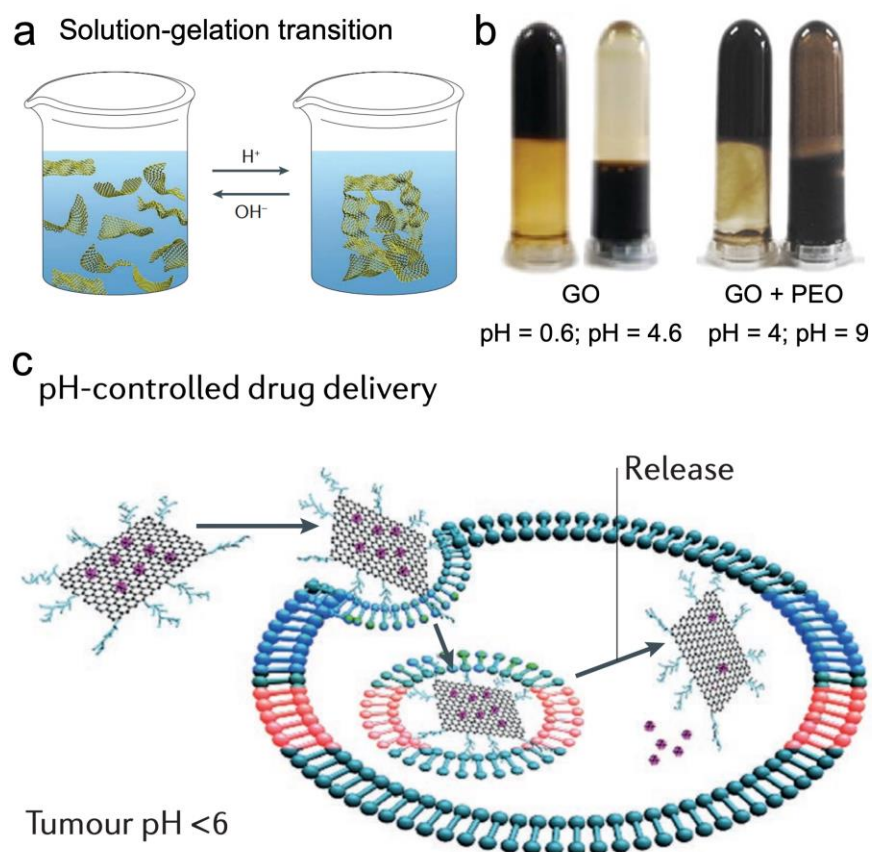


Figure 2.21. pH response of GO sheets. (a) Illustration of solution-gelation transition of GO sheets upon switching pH. Reproduced from Ref. [10] with permission from Nature. (b) Solution-gelation transition of GO (5 g/L) or GO (5 g/L) mixed with PEO (1 g/L). On the left: GO at pH of 0.6 or at pH of 4.6. On the right: GO/PEO at pH of 4 or at pH of 9. Reproduced with permission from Ref. [31]. Copyright 2011 American Chemical Society. (c) Illustration of pH controlled drug delivery of GO to tumour cell through cellular uptake [10].

2.4.1.2 Light responsive systems

GO and rGO sheets exhibit photothermal conversion, meaning they can absorb near infrared (NIR) radiation and convert the absorbed energy internally to heat [195]–[197]. This can happen by direct excitation of IR-active vibrational modes in GO and rGO followed by the conversion of vibrational energy to heat during relaxation, or by free carrier absorption followed by electron-phonon scattering in rGO [198]. Due to the excellent tissue penetration and the possibility to achieve spatiotemporal control, NIR light excitation has been exploited in GO and rGO drug delivery systems to induce drug delivery or generate hyperthermia in tumors for photothermal therapy (**Figure 2.22a**) [199]–[201].

The flakes have compatibility with polymers and enhances mechanical strength and thermal conductivity of composites [202]–[205]. Different from polymers, GO and rGO possess a negative thermal expansion coefficient (*e.g.*, GO $-68 \times 10^{-6}/\text{K}$ [206], rGO $-14.9 \times 10^{-6}/\text{K}$ [207]). Photothermal actuators, which can convert light stimuli into motions [10],[208],[209], have been developed based on this feature. Actuators are commonly designed as asymmetric layered films, where each layer has different thermal expansion coefficients [205],[210]–[214]. An example of a layered structure with rGO, PMMA, and gold nanorods is shown in **Figure 2.22b** [205]. Upon photothermal heating, the mismatch between the deformations of rGO (contraction) and PMMA (expansion) led to bending of the film; gold nanorods in different sizes gave the actuator wavelength-selectivity. A light responsive spider robot was fabricated with the actuators based on PMMA/rGO/Au (**Figure 2.22c**). When legs were irradiated by laser (808 nm), the local heating induced bending of the legs, leading to the displacement of the gravity center, thus the robot can move forward (**Figure 2.22c**). The negative thermal expansion coefficient, the flexibility, and the thermal conductivity of rGO sheets ensure the sensitivity and durability of actuators [205].

Photothermal effect can also be used to induce desorption of water molecules adsorbed on GO and rGO; since the desorption induces different deformations in GO and rGO [215]–[218], actuators made of GO/rGO bilayers have been obtained (**Figure 2.22d**) and the deformation was more noticeable as the reduction degree in rGO increases [216]. This effect was exploited to create GO/rGO ribbons mimicking the movement of mimosa leaves as well as the crawling and grasping behaviors of insects (**Figure 2.22e**).

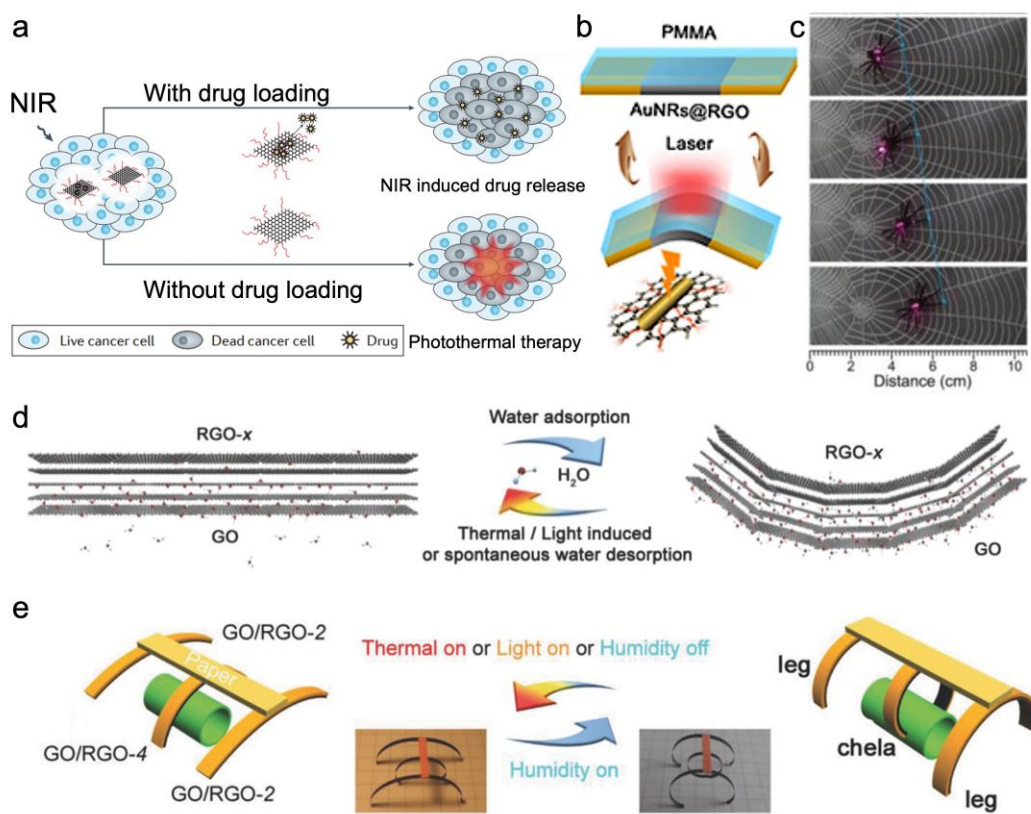


Figure 2.22. Light responsive systems based on GO or rGO. (a) Illustration of the use of NIR light in conjunction with GO and rGO flakes for light controlled drug release and photothermal therapy. Reproduced from Ref. [10] with permission from Nature. (b) Illustration of PMMA/rGO/Au nanorods layer-designed actuators and the light induced deformations. Reproduced with permission from Ref. [205]. Copyright 2018 WILEY - VCH Verlag GmbH & Co. KGaA, Weinheim. (c) Light-driven walking spider robot made with PMMA/rGO/Au nanorods actuators [205]. (d) Illustration of water adsorption/desorption between GO/rGO bilayers induced asymmetric volume changes. Reproduced with permission from Ref. [216]. Copyright 2018 WILEY - VCH Verlag GmbH & Co. KGaA, Weinheim. (e) Schemes for the graphene “insect” responding to surroundings humidity, temperature, and light changes. The “chela” for grasping was made with rGO at higher reduction degree than the “legs” [216].

GO and rGO flakes are also used to convert light to heat in temperature responsive systems; this will be covered in the section 2.4.3. Since temperature responsive behavior relies on temperature-responsive polymers (such as PNIPAM), in the next section we will introduce the responsive mechanism of temperature responsive polymers, using PNIPAM as an example.

2.4.2 Temperature responsive polymer: PNIPAM

Temperature is one of the most important stimuli in nature. Since the first report of temperature induced phase separation behavior of PNIPAM in 1968 [219], temperature-responsive polymers have been widely applied to develop responsive systems for applications such as drug delivery [220]–[223], separation [224]–[227], and tissue engineering [228]–[230]. Temperature responsive polymers can have either an upper critical solution temperature (UCST), meaning the polymer chains are non-soluble at temperatures lower than UCST and become completely soluble above UCST, or a lower critical solution temperature (LCST), implying the reverse phenomenon (**Figure 2.23a and b**) [231],[232].

PNIPAM is the first and most studied synthetic temperature-responsive polymer. At temperatures below its LCST (around 32 °C) [219],[233], PNIPAM chains interact with water through hydrogen bonds between the amide groups and water [32]–[34]. The hydrated chains have an extended coil conformation and are water soluble (**Figure 2.23c**). Upon heating to the LCST, hydrogen bonds between PNIPAM and water break, and hydrophobic isopropyl group and backbone partially dehydrate due to hydrophobic effect [32]–[37]. The hydrophobic interactions between PNIPAM chains predominate, and the polymer chains aggregate and phase-separate from water in a process called “coil-to-globule transition” [234],[235] (**Figure 2.23c**) [32]–[37]. Hydrogen bonds between PNIPAM and water can form again upon cooling to temperatures lower than LCST, reversing the phase transition [219]. The temperature-induced transition of PNIPAM

can be used to develop temperature responsive surfaces, vehicles and hydrogels that release drugs on demand [233].

From a thermodynamic point of view, below the LCST, the free energy of mixing ($\Delta G = \Delta H - T\Delta S$) of PNIPAM in water is negative: the enthalpy of mixing is negative due to the formation of hydrogen bonds; even though the entropy of mixing is negative because of an increase in order [236], the negative enthalpic term is predominant. As the temperature increases, hydrogen bonds between PNIPAM and water break; since this process is endothermic, the enthalpic term becomes less negative and the entropic term $T\Delta S$ starts to dominate [237]. Above LCST, the free energy of mixing becomes positive, leading to de-mixing and phase separation.

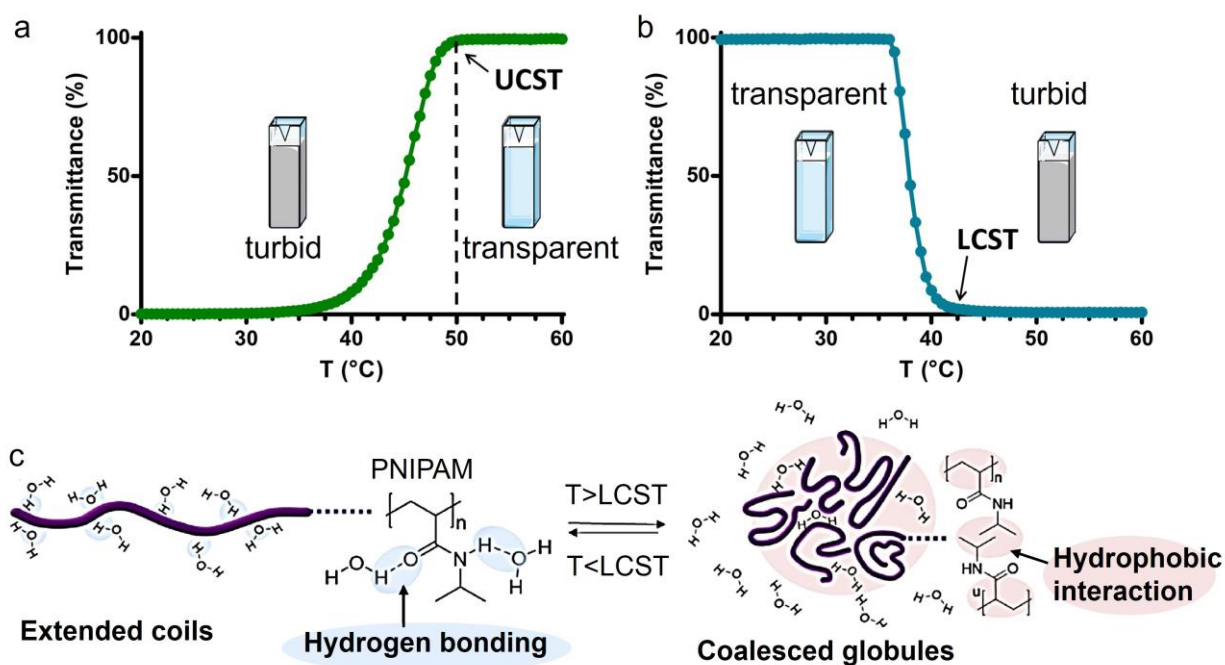


Figure 2.23. Illustrations of transmittance curves obtained with UV-vis spectrophotometry as a function of temperature for (a) UCST and (b) LCST polymers in solvent. The transmittance change of sample upon heating reflects the coil-globule transition. Reproduced with permission from Ref. [232]. Copyright 2011 Wiley Periodicals Inc.. (c) Schematic showing the coil-to-globule transition of PNIPAM: the polymer chains are extended coils below LCST and become coalesced globules due to hydrophobic interactions above LCST. Reproduced with permission from Ref. [233]. Copyright 2019 Wiley-VCH Verlag GmbH & Co. KGaA, Weinheim.

2.4.3 Functionalization of GO and rGO for temperature responsive systems

GO or rGO sheets have been integrated in temperature responsive polymers to enhance properties such as mechanical strength [238]–[240], electrical and thermal conductivity [241],[242], and drug loading efficiency [243]–[245] for applications including sensing [246],[247], catalysis [248]–[250], drug delivery [244],[245],[251], medical devices [228],[252], and pollutant removal [253]. In these systems, GO and rGO flakes serve as merely supportive and reinforcing components, and the temperature sensitivity is achieved through responsive polymers such as PNIPAM [238],[254],[255], poly(N-vinylcaprolactam) (PVCL) [256],[257], and poly(ethylene oxide) (PEO) [244]. The polymers can be bonded to GO or GO by initiating polymerizations of the monomers on the surface of flakes (**Figure 2.24a** and **b**) with methods such as reversible addition-fragmentation chain transfer (RAFT) polymerization [246],[254], atom transfer radical polymerization (ATRP) [243], click chemistry [245],[254], ring opening polymerization [258], and single electron transfer-living radical polymerization (SET-LRP) [259]. To ensure the covalent grafting of polymers on the sheets, the surface GO or rGO sheets needs to be activated by chemical modification to turn the sheets into polymerization initiators (**Figure 2.24b**) [255],[259] or crosslinkers [240],[242],[260]. Flake functionalization and further polymerization require multiple steps of synthesis and purification and, in some cases, need to be conducted in an inert atmosphere.

GO and rGO sheets surface modified with PNIPAM exhibit reversible dispersion-aggregation transition upon cooling-heating (**Figure 2.24c** of rGO and **d** of GO) [254],[255],[261]. PNIPAM functionalization stabilize both GO and rGO flakes in water below the LCST, thanks to the hydrogen bonds formed between PNIPAM and water. Aggregation occurs above the LCST as PNIPAM becomes hydrophobic, resulting in the assembly of sheets through hydrophobic

interactions [254],[255],[261]. The LCST of GO/PNIPAM or rGO/PNIPAM is different from study to study as reduction degree, functionalization method and flakes size change. Due to the poor stability of rGO in water, the LCST of rGO/PNIPAM was found to be lower than that of PNIPAM (*e.g.*, 24 °C in **Figure 2.24c** [261]). On the contrary, LCST shifted to a higher temperature in GO/PNIPMA systems (*e.g.*, 40 °C in **Figure 2.24d**), as a higher energy to disrupt hydrogen bonding is required for this system compared to PNIPAM [255]. The aggregated GO/PNIPAM or rGO/PNIPAM flakes can be re-dispersed again by cooling below LCST and mild shaking [254],[255],[258],[261]. The coil-to-globule transition of PNIPAM on the surface of the sheets results in a change in wettability of the flakes (**Figure 2.24e**). This can be exploited to tune the affinity between GO/PNIPAM sheets and different molecules [250],[262]. For example, electrodes including GO/PNIPAM became more hydrophobic and impeded the transfer of a hydrophilic coenzyme to the electrode, achieving temperature-responsive electrocatalysis (**Figure 2.24f**) [255]. Temperature responsive GO and rGO flakes are also applied as vehicles for drug delivery [243],[244],[263]. Below LCST, the drugs are confined on the flakes due to the hydrogen bonding between PNIPAM and drugs, whereas above LCST, the PNIPAM chains are hydrophobic and the hydrogen bonds break, leading to the drug release (**Figure 2.24g**) [243].

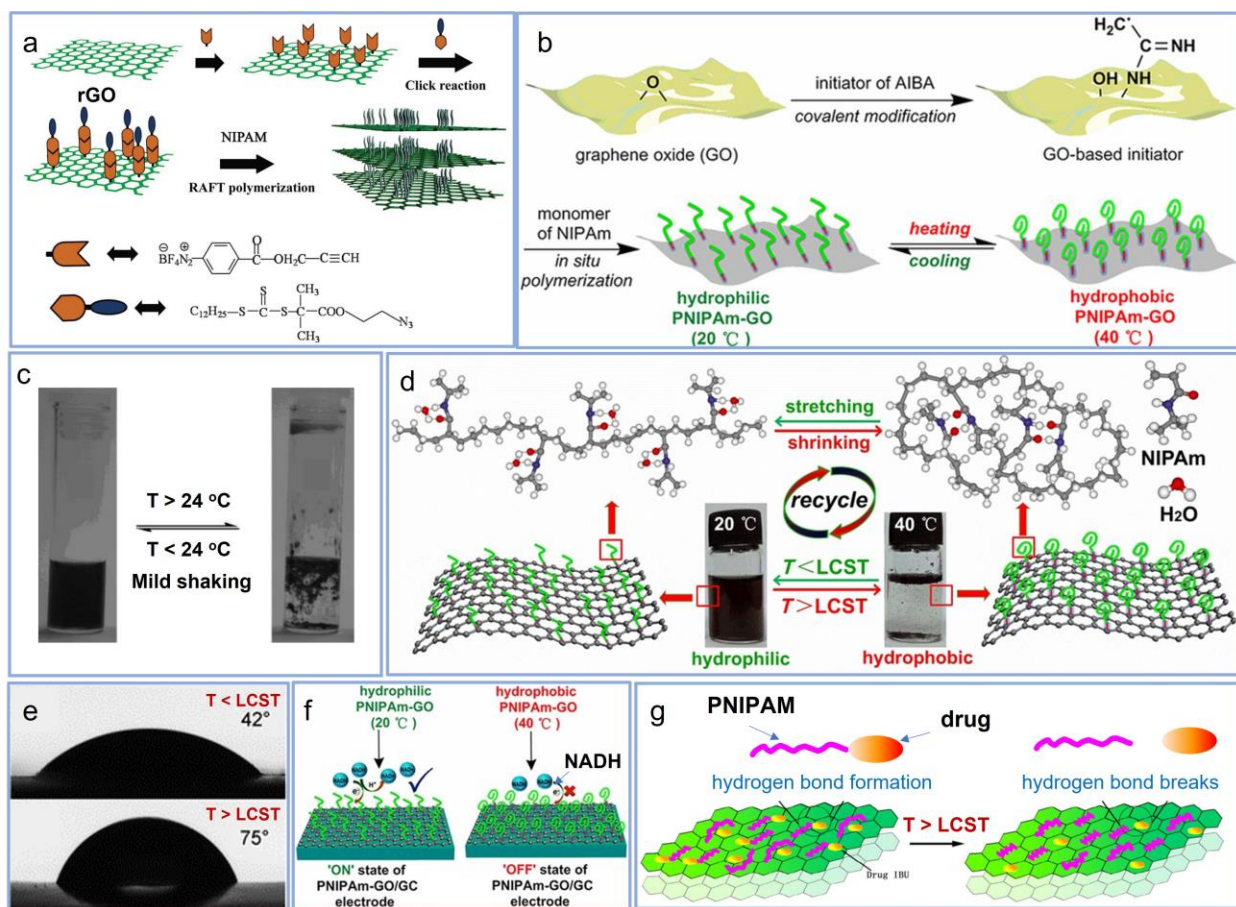


Figure 2.24. Surface functionalization of GO and rGO flakes with temperature responsive PNIPAM by covalently grafting: (a) rGO with PNIPAM brushes through click chemistry and RAFT polymerization. Reproduced from [254] with permission from Wiley Periodicals, Inc.. (b) GO surface modified with PNIPAM by turning GO into an initiator and *in situ* polymerization. Reproduced from Ref. [255] with permission from Wiley-VCH Verlag GmbH & Co. KGaA, Weinheim. (c) Reversible temperature responsive aggregation and dispersion of rGO/PNIPAM sheets in water. LCST = 24 °C. Reproduced from Ref. [261] with permission from Wiley Periodicals, Inc.. (d) Illustration and photos of reversible temperature responsive aggregation at 40 °C and dispersion at 20 °C of GO/PNIPAM flakes in aqueous solution [255]. (e) Static contact angles of water droplets on GO/PNIPAM films at temperatures lower and higher than LCST. Reproduced from Ref. [262] with permission from the Royal Society of Chemistry. (f) Temperature responsive “on” and “off” switchable electrocatalytic detection of 1,4-dihydro- β -nicotinamide adenine dinucleotide (NADH) using a glassy carbon electrode modified by GO/PNIPAM [255]. (g) Loading of ibuprofen drug on GO/PNIPAM through hydrogen bonding between ibuprofen and PNIPAM, and temperature responsive drug release due to the breakage of hydrogen bonding. Reproduced from Ref. [243] with permission from Springer Science Business Media B.V..

Temperature responsive hydrogels were obtained with GO or rGO and temperature responsive polymers, which showed swelling-to-shrinking transition at LCST due to the dehydration of the

polymeric networks (**Figure 2.25a**) [238]–[240],[260]. The GO or rGO flakes physically crosslink the polymer chains through hydrogen bonds and enhance the tensile strength of the resulting hydrogels (**Figure 2.25b**); however, increasing flake concentration decreases the volume change response to heat (an example is shown in **Figure 2.25c**) [204],[240],[264]. rGO flakes cannot be easily introduced in the hydrogels at the beginning of polymerization, resulting in an inhomogeneous distribution of flakes in the polymeric matrix [265]. Temperature-responsive hydrogels containing rGO were achieved by reducing the GO/polymer composites with *e.g.*, hydrazine reduction (**Figure 2.25d**) [266], or initiating polymerization within the rGO networks (**Figure 2.25e**) [267], resulting in hydrogels with high electrical and thermal conductivity.

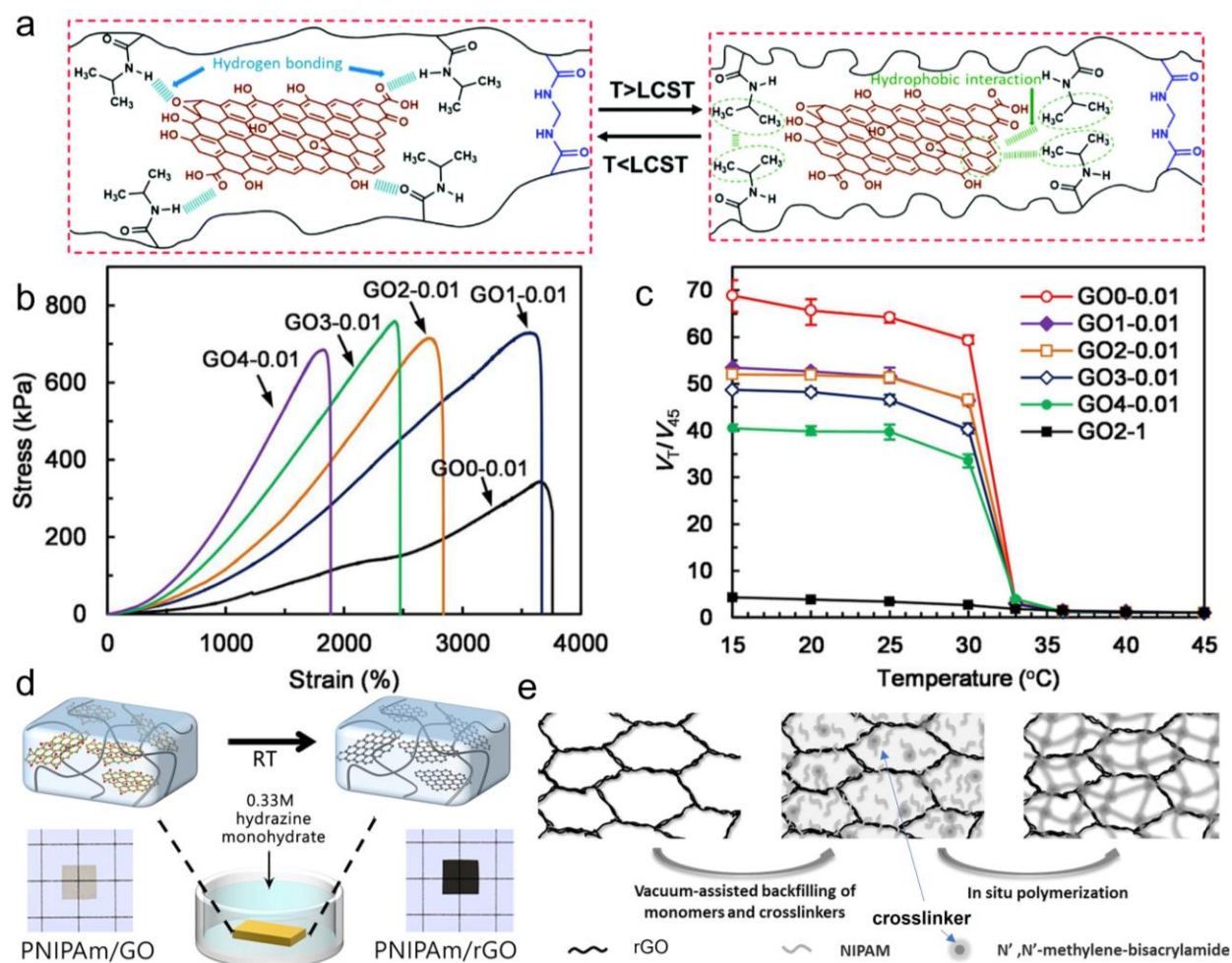


Figure 2.25 (a) Temperature-responsive swelling-to-shrinking transition of GO/PNIPAM networks. Reproduced from Ref. [264] with permission from Royal Society of Chemistry. (b) Typical stress–strain curves of GO/PNIPAM hydrogels with different contents of GO. The hydrogels named as “GOX-Y” have X wt% of GO and Y wt% of BIS, relative to NIPAM. Reproduced from Ref. [204] with permission from the Royal Society of Chemistry. (c) Temperature dependence of the equilibrium swelling ratios of GO/PNIPAM hydrogels with GO content from 0 to 4 wt% and BIS content between 0.01 wt% and 1 wt% [204]. Swelling ratio = V_T/V_{45} . V_T and V_{45} represent the equilibrium volumes of hydrogels at the temperature shown on the x axis for each point and $45^{\circ}C$, respectively [204]. (d) Illustration for the reduction of GO dispersed in the PNIPAM hydrogel. The GO/PNIPAM composites were immersed in aqueous hydrazine monohydrate to obtain GO/PNIPAM. Inset: photographs of rGO/PNIPAM hydrogels [266]. (e) Example of preparation of rGO/PNIPAM hydrogels. An rGO porous monolith was prepared by freezing a GO suspension and reduction. The NIPAM solution mixed with crosslinkers, and initiators was infiltrated in the rGO porous monolith. Then, polymerization was carried out for 12h. Reproduced with permission from Ref. [267]. Copy right 2014 WILEY-VCH Verlag GmbH & Co. KGaA, Weinheim.

The swelling-shrinking of temperature responsive GO and rGO 3D networks are exploited for microfluidic devices, drug delivery, photothermal therapy, and solar water evaporation

applications; and due to the photothermal conversion of GO and rGO flakes, light are commonly used to direct the deformation [242],[264],[268]–[273]. For example, NIR light has been applied to increase the local temperature of PNIPAM hydrogels containing GO or rGO, therefore, drugs loaded inside hydrogels can be released due to the increase in hydrophobicity of polymeric chains and the shrinkage/contraction of networks (**Figure 2.26a**) [243],[274]–[278]. The incorporation of GO and rGO enhances the drug loading efficiency compared to the pure polymers due to the high surface area of the sheets and non-covalent interactions between flakes and drugs [243]–[245]. To release drugs at physiological temperature (*i.e.*, 37 °C, higher than PNIPAM’s LCST around 32 °C), PNIPAM is copolymerized with hydrophilic components (*e.g.*, PAA [274]), which enhance the energy required to disrupt hydrogen bonding. Another example of reversible swelling-shrinking of GO/PNIPAM hydrogels is shown in **Figure 2.26b**, in which hydrophilic acrylamide (AAm) was introduced to increase the LCST to 39 °C [268]. GO increased the local temperature in response to NIR light, leading to a contraction of the PNIPAM chains and an overall shrinkage of the hydrogel (**Figure 2.26c** 1&2); when the NIR excitation was stopped, the hydrogel returned to its swollen state (**Figure 2.26c**, 3) [268]. In the swollen state, the large pores can capture cells, while under NIR light, the smaller pores resulted in the “on-demand” release of cells, allowing for *in vitro* cell collection and isolation (**Figure 2.26d**).

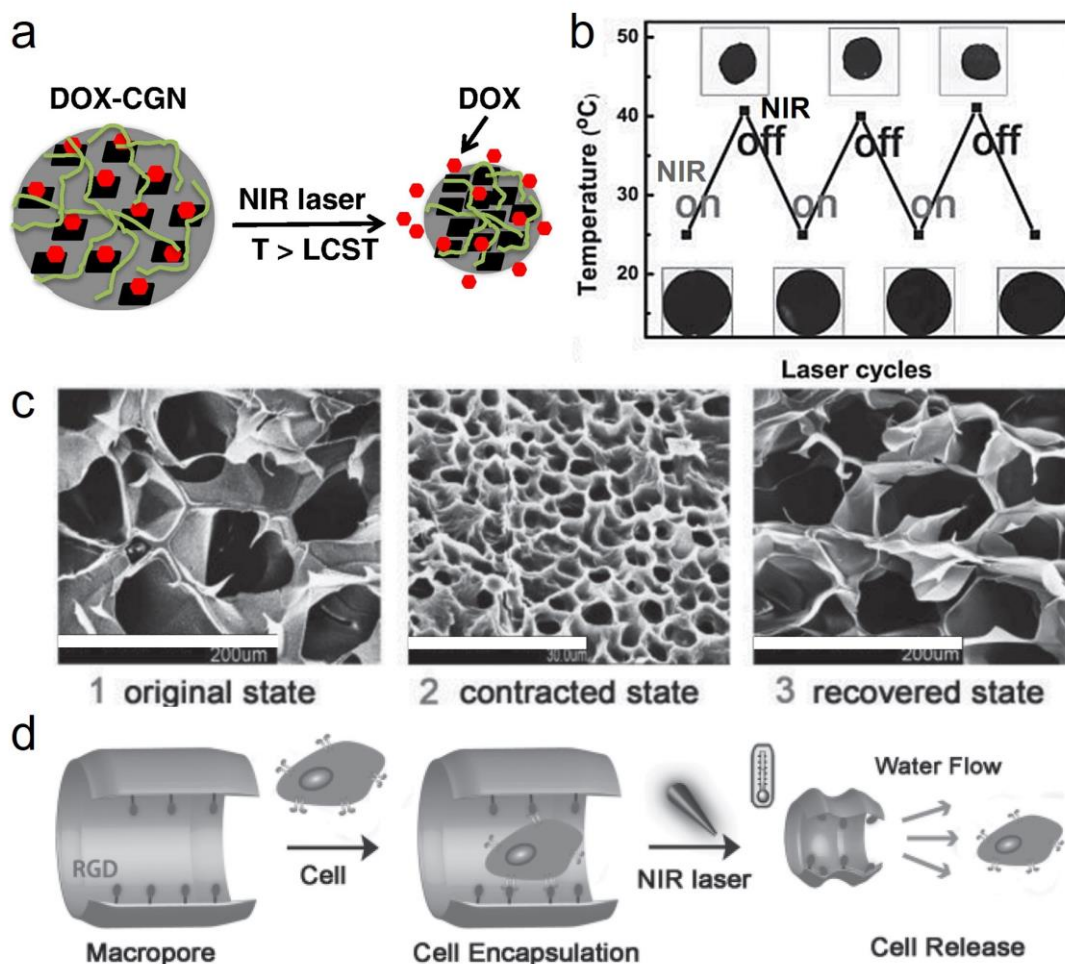


Figure 2.26 (a) Loading of doxorubicin hydrochloride (DOX) on GO/chitosan/PNIPAM composite nanospheres ($< LCST$) and NIR-induced temperature responsive release of DOX ($> LCST$) upon contraction of the nanospheres. Reproduced from Ref. [276] with permission from Elsevier Inc.. (b) GO/PNIPAM/PAAM hydrogel shrinking under NIR light and swelling when the NIR light was off. Temperature changed as a function of NIR laser on–off cycles. The insets show the corresponding photograph of the hydrogels; the sizes of squares are the same. Reproduced with permission from Ref. [268]. Copyright 2013 WILEY - VCH Verlag GmbH & Co. KGaA, Weinheim. (c) SEM images of freeze-dried GO/PNIPAM/PAAM hydrogels in different states: (1) the original swollen state before NIR light exposure; (2) NIR-induced contracted state; (3) the recovered swollen state after NIR laser was turned off. Scale bars are 200, 30, and 200 μm , respectively [268]. (d) Schematic of the encapsulation and NIR-induced cell release [268].

In summary, GO and rGO flakes contribute to the temperature-responsive polymeric systems as supportive components with the advantages such as mechanical strength, large surface area and conductivity; the flakes can also contribute to photothermal conversion in photothermal responsive systems. In these systems, deformation is achieved by responsive polymers, and it highly depends

on the change in amphiphilicity of polymers and the interactions between polymeric chains in response to temperature. However, composing GO/rGO with polymers requires a complex design and multiple steps of synthesis. Considering that GO and rGO flakes can be building blocks for scaffolds and gels, just like polymers, and these amphiphilic flakes exhibit direct response to stimuli such as pH, in this thesis, we have hypothesized that it's possible to achieve temperature responsiveness in the GO or rGO flakes without introducing responsive polymers, which is inspired by the mechanism of traditional temperature-responsive polymers.

2.5 Polydopamine functionalization of GO and rGO

In this work we will show the synthesis of a temperature responsive rGO system through functionalization of GO with PDA (Chapter 5). We provided some general information of what DA and PDA are in the general introduction chapter. In this section, we introduce concepts related to DA polymerization and the chemistry of PDA, formation of PDA on GO and rGO, and materials based on GO and rGO that are functionalized by PDA.

2.5.1 Dopamine polymerization and chemistry of PDA

Marine mussels, such as *Mytilus edulis*, attach to a variety of surfaces in aqueous environments using byssus threads and plaques (**Figure 2.27a**). Lee *et al.* discovered that mussel proteins found in the plaque-substrate interfaces, such as Mefp-5, are rich in catechol and amine moieties (**Figure 2.27b-d**), which synergistically contribute to mussel's universal adhesive property. They also identified DA as a small molecule compound that contains both functionalities (**Figure 2.27e**). They found DA can self-polymerize into PDA which has catechol and amine groups and adheres to a wide range of substrates (*e.g.*, Cu, SiO₂, and poly(tetrafluoroethylene) (PTFE)) [38]. It has been shown that PDA is spontaneously formed by pH-induced oxidative polymerization of dopamine-hydrochloride in an alkaline solution (pH > 7.5), commonly tri(hydroxymethyl)-

aminomethane (Tris) or phosphate buffer [41],[279]–[281]. PDA functionalization has generated great interest because of the applications in a broad variety of fields, such as drug delivery [282], tissue engineering [283], biomineralization [284], sensors [285], pollutant removal [286], batteries [287], and catalysts [288].

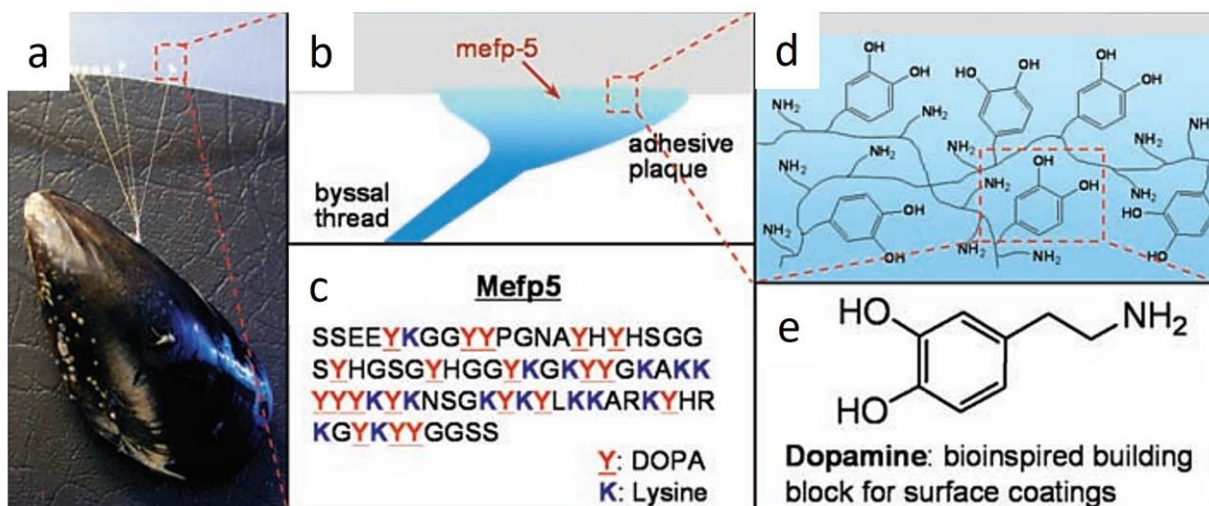


Figure 2.27. (a) Photo of a mussel attach to a PTFE substrate. (b) Schematic illustrations of the interfacial location and (c) the amino acid sequence of Mefp-5. S: serine, E: glutamate, Y: tyrosine, K: lysine, G: glycine, P: proline, N: asparagine, A: alanine, H: histidine, L: leucine, R: arginine. (d) A simplified molecular representation of characteristic amine and catechol groups from Mefp-5 shown in the red square. (e) Dopamine contains both amine and catechol functional groups found in Mefp-5 and was used as a molecular building block for polymer coatings. Reproduced with permission from Ref. [38]. Copyright 2007 The American Association for the Advancement of Science.

Despite the wide applications and numerous studies, the chemical structure of PDA and its polymerization mechanism are still under discussion, although it's commonly accepted that PDA is a mixture of covalently bonded and physically assembled units (**Figure 2.28**) [38],[279],[281],[289]–[291]. The polymerization of DA starts with the formation of 5,6-dihydroxyindole (DHI) through an oxidation pathway that includes the oxidation of dopamine to dopamine-quinone, the production of leukochrome through intramolecular cyclization oxidation, further oxidation into dopachrome and finally the formation of DHI through tautomerization [38],[281],[291] (**Figure 2.28a**). DHI molecules can form covalently bonded DHI dimers and

trimers which polymerize into PDA (**Figure 2.28a**, indicated in blue circles) [38],[281],[292]. Uncyclized forms of oxidized dopamine can react with themselves or with DHI through catechol-catechol coupling, resulting in the formation of primary amine groups on PDA (**Figure 2.28a** indicated in green circles) [289],[293],[294]. Liebscher *et al.* proposed a linear structure of PDA with DHI, 5,6-indolequinone, leukochrome, and uncyclized dopamine covalently bonded through benzene rings (**Figure 2.28b**) [289]. Pyrrolicarboxylic acid (PCA) moieties arising from the partial degradation of DHI can also bind to (DHI)₂/PCA through covalent bonds in the early stage of PDA formation (**Figure 2.28c**) [290],[292]–[294]. The use of Tris buffer also affects the PDA structure: Tris, which contains an amino group, can react with quinone groups in PDA and partially terminate the chain growth (**Figure 2.28d**), resulting in small fractal aggregates [290],[295]. Non-covalent interactions also contribute to PDA formation (**Figure 2.28e**): (dopamine)₂/DHI trimers are physically crosslinked through hydrogen bonds and π - π interactions [281],[290],[296], and aromatic structures can interact with each other through cation- π interactions mediated by nearby cations [297],[298].

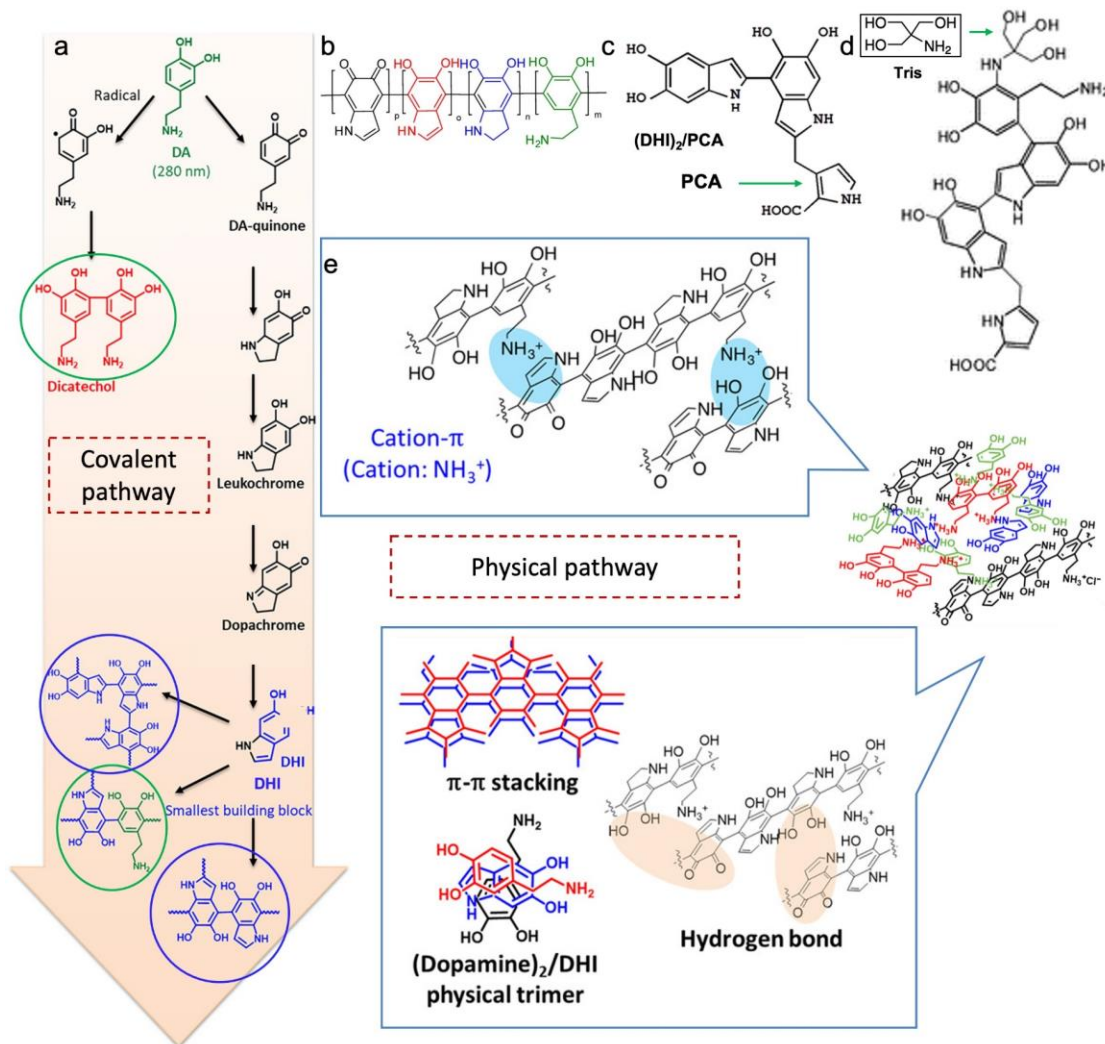


Figure 2.28. Representative covalent (chemical) and physical assembly pathways for PDA formation. (a) Covalent pathway: dopamine is sequentially oxidized to heterogeneous derivatives and polymerize *via* covalent bonds, adapted from reference [298] with permission from American Association for the Advancement of Science. (b) Proposed PDA structure with DHI and indole-dione units in different degrees of (un)saturation that are covalently linked by C–C bonds between the benzene rings. Reproduced with permission from Ref. [289]. Copyright 2013, American Chemical Society. (c) (DHI)₂/PCA trimer complex through covalent bonds, adapted from reference. Reproduced with permission from Ref. [292]. Copyright 2014, American Chemical Society. (d) Tris bonded to dopamine and DHI that ends the chain growth, adapted from reference. Reproduced with permission from Ref. [295]. Copyright 2014, American Chemical Society. (e) The oligomers physically assemble *via* hydrogen bond, π - π stacking, and cation- π interaction, adapted from reference [298].

2.5.2 PDA and surface modification of GO

Since PDA forms through DA oxidation, the reaction can be used to reduce GO [299]. Xu *et al.* first applied this strategy to reduce GO and functionalize rGO sheets with PDA in an Tris solution

(pH = 8.5) [300]. They obtained rGO/PDA flakes that showed electrical resistance 2 orders of magnitude lower than GO, indicating the reduction of GO. Hydrophilic groups from PDA enhance the dispersion of rGO in water [300] and allow further functionalization of rGO sheets in aqueous medium [301],[302].

The reduction of GO by DA and formation of PDA on the surface of rGO happen effectively at temperatures between 60 °C and 100 °C [42],[300],[303]–[306]. Carrying out the reaction at room temperature also enables formation of PDA, but results in a lower reaction rate and less reduced GO [307]–[309].

The mechanism of PDA-induced reduction of GO and the morphology of PDA on the surface of rGO sheets was studied by Cheng *et al.* [42]. They proposed that the reduction and coating process have three steps (**Figure 2.29a**). First, the catechol groups reduce GO by reacting with GO hydroxyl and epoxy groups, resulting in the restoration of sp² domains. Dopamine or oxidized intermediate species bind to rGO sheets *via* π - π interactions and covalent bonding, *i.e.*, aryl-aryl coupling. Next, dopamine and intermediate species undergo pH-induced polymerization into precursors that bind onto the rGO sheets. In the third step, the precursors become nucleation seeds for PDA growth. PDA morphology showed DA concentration dependence: when DA concentration was lower (0.15 g/L, 1.5 times that of GO), the seeds grew into nanosized PDA clusters (**Figure 2.29b**), agreeing with other reports that PDA can form into clusters on various of substrates [292],[310]–[312]. As DA concentration increased, PDA clusters became denser and thicker, and aggregated into films that fully covered rGO flakes when DA concentration reached 0.8 g/L (8 times that of GO) (**Figure 2.29c**).

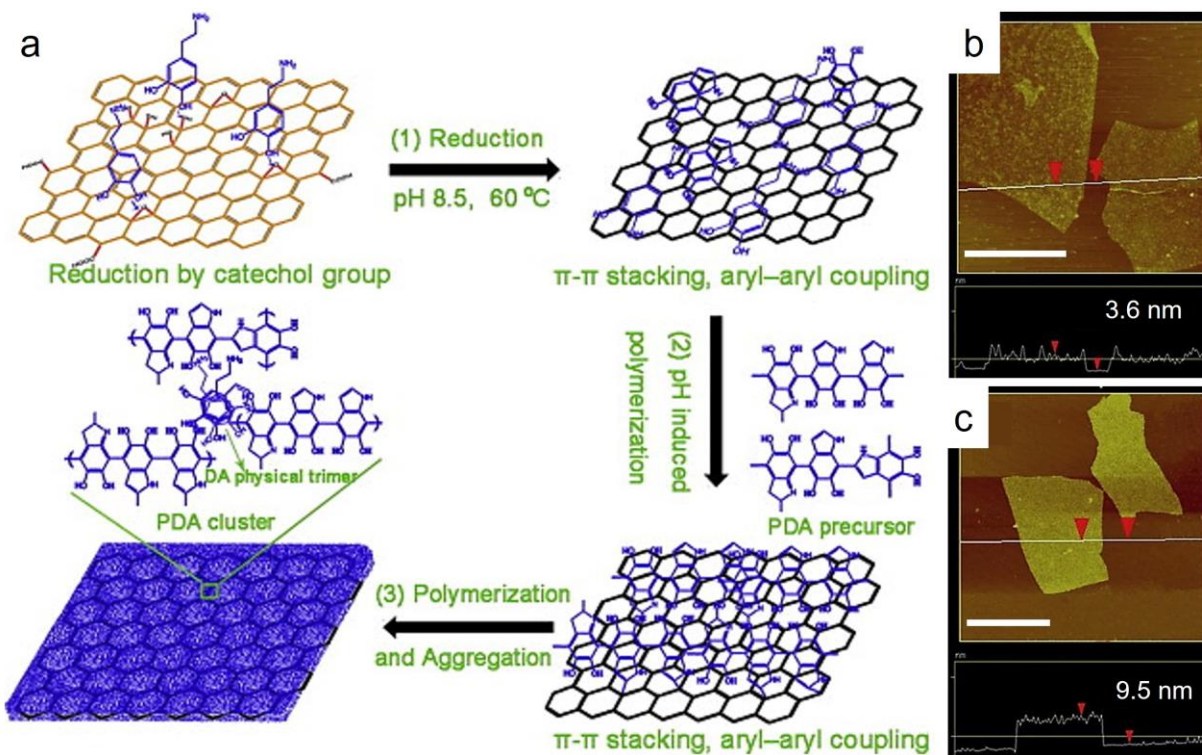


Figure 2.29. (a) Proposed mechanism for the reduction and surface modification of GO by DA. Reproduced with permission from Ref. [42]. Copyright 2013 Elsevier B.V.. (b-c) AFM images and cross-section height analyses for rGO/PDA obtained with 0.15 g/L DA (b) and 0.8 g/L DA (c). GO concentration = 0.1 g/L. Scale bar = 2 μ m. Adapted from reference [42].

2.5.3 PDA composites with GO or rGO

Taking advantage of the abundant functional groups and the adhesive properties of PDA, a great number of materials containing GO/PDA or rGO/PDA have been synthesized for a wide variety of applications. We will discuss a few examples in this section.

The rGO/PDA flakes can directly assemble into films through air drying or filtration [309],[313]–[317]. Air-drying involves the self-assembly of flakes at liquid-air interface [318]–[320]. Due to amphiphilicity, the flakes in suspension tend to move toward the liquid-air interfaces during liquid evaporation [4]. Therefore, during air drying, films are obtained as the flakes concentrate at the liquid-air interface. Filtration is essentially a flow-directed assembly method, in which a suspension is forced through a filter under high pressure [321],[322]. During the separation from liquid, the flakes assemble at the liquid-solid interface between the aqueous

suspension and the filter, stacking into layered structures [323]. The films can be obtained after filtration, drying and filter removal [324].

When assembled into films, rGO/PDA flakes form nacre-like structure. Nacre, or mother of pearl, is an organic-inorganic composite made of neatly stacked aragonite nanoplatelets sandwiching biopolymers in between the layers [325],[326]. This “brick-and-mortar” structure provides nacre with exceptionally high tensile strength [325],[326]. The rGO/PDA sheets are ideal for building nacre-mimicking films, due to the good mechanical strength of rGO sheets and the adhesive property of PDA. For example, Cui *et al.* obtained GO/PDA flakes, produced GO/PDA film by evaporation, and reduced the films *via* hydroiodic acid reduction, to prepare rGO/PDA films [309]. The tensile strength of rGO/PDA films increased significantly as the GO content increased in the GO/PDA films (**Figure 2.30a**). rGO/PDA films with PDA content lower than 9% showed higher tensile strength than films made of pure GO (**Figure 2.30a**). The authors proposed that PDA can act as a crosslinker for GO through both covalent and non-covalent interactions, thus increasing the energy required to break the films. However, an excess of PDA can act as intercalating impurities and reduce the mechanical properties. The original rGO/PDA films showed nacre-like layered structures (**Figure 2.30b**), and after tensile test, the edges showed fractures indicating slippage between the sheets before breakage due to the strong covalent crosslinking between sheets (**Figure 2.30c**) [309].

Taking advantage of the functional groups on PDA, additives such as branched aramid nanofibers [317], cellulose [315], PVA [313], and pyrimidinone [314] were mixed with GO/PVA or rGO/PDA to reinforce the interactions between flakes and further enhance flake packing in nacre-like films. For example, the rGO/PDA films showed air pockets between layers (**Figure 2.30d**), while the rGO/PDA/PVA films had a more compact lamellar microstructure (**Figure**

2.30e). The PVA served as extra “mortar” to fill the gaps between the flakes, and further crosslinked the sheets *via* hydrogen bonding between PVA and PDA, which significantly improved the tensile strength of films [313].

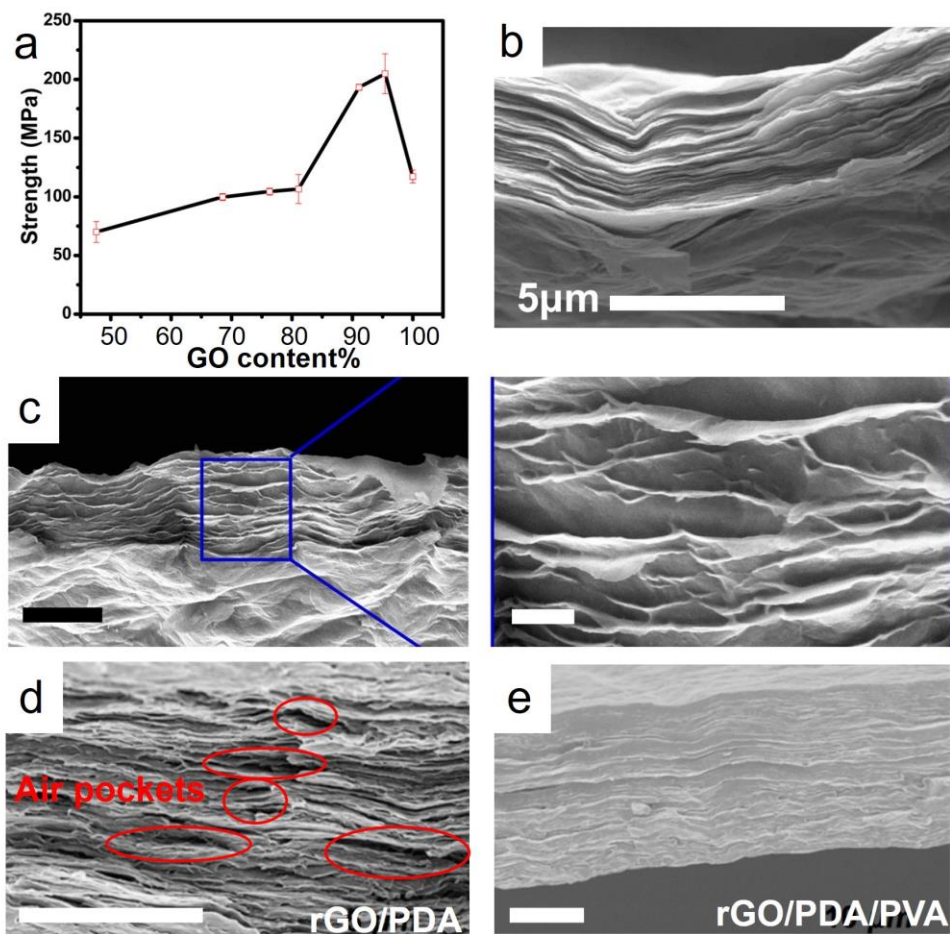


Figure 2.30. (a) Tensile strength of rGO/PDA films with different GO contents (wt%) [309]. (b) SEM cross-section morphology of the rGO/PDA nacre-like film with 95 wt% GO before break in tensile test. Reproduced with permission from Ref. [309]. Copyright 2014 American Chemical Society. (c) SEM surface morphology at different magnifications of the fractures of rGO/PDA (95 wt% GO) after tensile test [309]. (d-e) SEM images of rGO/PDA films (d) and rGO/PDA/PVA (e) films. Reproduced with permission from Ref. [313]. Copyright 2017 American Chemical Society.

The reduction of GO by DA in Tris solution (pH = 8.5) can yield hydrogels when the concentration of GO was higher than 2 g/L (**Figure 2.31a**) [42],[286]. The mechanism is similar to hydrothermal reduction, in which the gelation happens during the GO reduction process by DA and the rGO flakes are bonded into networks through π - π interactions [42],[286]. After freeze-

drying, rGO/PDA porous monoliths (**Figure 2.31b**) showed a porous morphology similar to hydrothermally synthesised rGO (**Figure 2.31c**), with interconnected pores formed by randomly cross-linked flakes [286].

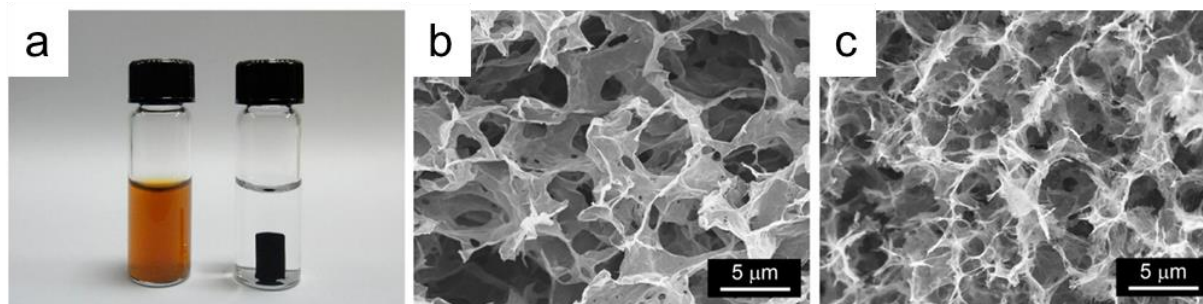


Figure 2.31. (a) Photographs of GO dispersions mixed with dopamine before reduction (left) and after reduction by DA, leading to an rGO/PDA hydrogel (right). (b-c) SEM images of rGO/PDA (b) and rGO (c) porous monoliths after freeze-drying. Reproduced with permission from Ref. [286]. Copyright 2013 American Chemical Society.

PDA layers have been also used to *in situ* deposit noble metal, metal oxide, and semiconductor nanoparticles on the surface of GO/PDA or rGO/PDA sheets for catalysis, sensor, pollutant removal, and lubrication applications (*e.g.*, **Figure 2.32**) [299],[301]–[303]. Polymers [307],[327]–[329], proteins [308],[330] and metal nanowires [331] can also be bonded to GO/PDA or rGO/PDA through non-covalent interactions with PDA, leading to the production of electrodes, sensors, tissue engineering scaffolds, and pollutant removal hydrogels.

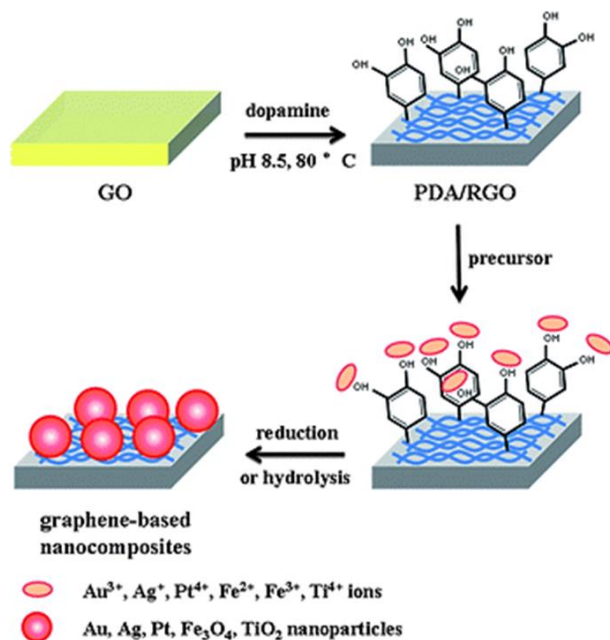


Figure 2.32. Illustration *in situ* deposition of noble metals, metal oxide and semiconductor nanoparticles on surfaces of rGO/PDA. Reprinted with permission from Ref. [303].

2.6 Summary

Since the discovery of graphene, GO has been viewed as an ideal precursor and building block to obtain graphene-based materials in efficient and sustainable ways. The synthesis, chemistry, and properties of GO have been intensively studied. Of these, colloidal stability and amphiphilicity are critical, as they explain and affect GO assembly at different interfaces or under specific stimuli.

GO can stabilize Pickering emulsions by irreversible adsorption at oil/water interfaces, reducing the interfacial free energy. The emulsion stability and droplet size are affected by factors such as pH, ionic strength, GO concentration, and oil-to-water volume ratio. Pickering emulsions, or HIPEs with variable droplet size and composition can be obtained by adding additives to adjust the amphiphilicity of GO or by adding co-emulsifiers. Post treatments of emulsions stabilized by GO ensure the removal of droplet templates while preserving GO porous networks, and can be used to control the chemical composition, morphology, and architecture of the resulting monoliths. It should be noted that, in most studies, GO or rGO only serve as stabilizers rather than building

materials. Scaffolds made only of GO templated by Pickering emulsions with controllable pore size and interconnectivity were never demonstrated, nor were complex architectural features such as hierarchical porosity ever achieved.

GO and rGO flakes can actively respond to stimuli such as pH, as the interactions between flakes are controlled, leading to aggregation, gelation, or deformation. Temperature response however can only be achieved by introducing temperature responsive polymers on the surface of GO or rGO, *e.g.*, PNIPAM, which induce a temperature-dependent response based on changes in hydrophilicity of polymer and in interactions between polymer chains. These facts underline the possibility of achieving temperature response in rGO by surface chemistry design, mimicking the amphiphilic structure of PNIPAM.

Even though the mechanism is still under discussion, it's well accepted that DA polymerization happen in alkaline solutions ($\text{pH} > 7.5$) through covalent bonding and physical bonding pathways, resulting in hydrophilic oxygen and nitrogen containing groups in PDA. rGO/PDA can be obtained by DA reduction of GO at reaction temperatures higher than 60 °C, and PDA clusters or coatings can form on rGO flakes depending on DA concentration. Through PDA modification, films and porous monoliths based on GO/PDA and rGO/PDA can be obtained. However, the colloidal properties and amphiphilic nature of GO/PDA or rGO/PDA flakes have never been discussed, nor has their responsive behavior been studied in the same manner as what has been done for GO and rGO flakes.

Bridging text

GO stabilized Pickering emulsions have been known for years and have been widely used as templates to prepare porous materials mainly based on polymers, rGO, their composites, and/or amorphous carbon. In most cases, additives have to be added to GO or rGO in order to improve the stability of emulsions, control the emulsion droplet size as well as adjust the architecture of the porous monoliths. In the first study, we were able to achieve GO Pickering emulsions with controllable droplet size, in which flakes served as both stabilizers and building blocks. We obtained GO, rGO and GO composite scaffolds with architecture tailored for BTE application. Specifically, we addressed the following objectives:

- I. To tune the amphiphilicity of GO flakes to stabilize o/w emulsions.
- II. To obtain stable GO HIPEs with controllable droplet size by tuning the oil to water ratio and GO concentration.
- III. To develop a dual-templating strategy to obtain GO scaffolds with interconnected pores in hierarchical size distribution.
- IV. To study their architecture by developing a methodology based on PCI.
- V. To obtain GO scaffolds that are stable in aqueous medium and investigate MSC proliferation and infiltration on GO scaffolds.
- VI. To evaluate the versatility of the dual-templating strategy to control not only the architecture, but also the composition of scaffolds.

The manuscript has been published in *Carbon* in 2021:

Chen, Y., Su, X., Esmail, D., Buck, E., Tran, S. D., Szkopek, T., & Cerruti, M. (2022). Dual-templating strategy for the fabrication of graphene oxide, reduced graphene oxide and composite scaffolds with hierarchical architectures. *Carbon*, 189, 186-198.

3 Dual-templating strategy for the fabrication of graphene oxide, reduced graphene oxide and composite scaffolds with hierarchical architectures

3.1 Abstract

The broad applications of graphene-based scaffolds demand fabrication methods that are simple and yet can create complex architectures. This is particularly true for bone tissue engineering, where interconnected, micro and macro porosity is required for cell penetration and nutrient exchange. Here, a dual-templating method is developed to produce graphene oxide (GO) scaffolds with interconnected hierarchical porosity: upon freezing and drying high internal phase emulsions exclusively stabilized by GO sheets, large pores are templated by the oil droplets, and small pores by ice crystals formed in the water phase, whose size can be controlled by freezing temperature. The resulting scaffolds are excellent substrates for mesenchymal stem cell penetration and growth. This method also enables the synthesis of complex hierarchical architectures in reduced graphene oxide (rGO) and GO composite scaffolds, through a single, versatile strategy.

3.2 Introduction

Graphene-based porous scaffolds have attracted tremendous attention for their broad applications [332],[23] as they combine the mechanical strength, electrical conductivity, and

thermal stability of graphene in three-dimensional (3D) structures with large surface area, high porosity, and accessibility to ions and molecules[1],[333].

Bone tissue engineering (BTE) stands out as a promising application for graphene-based scaffolds, since graphene and graphene oxide (GO) substrates promote the proliferation and osteogenic differentiation of mesenchymal stem cells (MSCs) [13],[14], and 3D scaffolds containing graphene and GO can provide the necessary space for cell proliferation and infiltration, and promote bone regeneration [23],[334]–[337].

Ideally, BTE scaffolds should have interconnected large pores with diameters above 100 μm to enable cell infiltration and osteogenic differentiation [19]. They should also provide small pores to facilitate growth factor and nutrient diffusion [20]. Complex architectures were achieved in polymeric BTE scaffolds through techniques such as fused deposition modeling, and 3D printing [338],[339]. However, new fabrication techniques are necessary to create graphene-based scaffolds that meet BTE requirements.

Initially produced by chemical vapor deposition (CVD), graphene-based scaffolds with pore diameters above 100 μm could support the proliferation and induce the osteogenic differentiation of MSCs [23]. A limitation of CVD is that it can only produce pristine graphene structures [340], while studies have shown that the oxygen content in GO or reduced GO (rGO) facilitates cell proliferation and osteogenic differentiation through non-covalent interactions with growth factors and proteins [16],[17]. Also, oxygen moieties allow for scaffold functionalization [341].

Different studies have shown the assembly of GO sheets from colloidal dispersions into GO or rGO based scaffolds, with methods including crosslinking [342], reduction [15],[22] or templating [343],[344]. However, all these methods can produce GO or rGO based scaffolds with pore diameters of several tens of microns, which would inhibit cell infiltration. Although templating

allows control over pore diameters upon the removal of templates with the desired size [345], no one has reported the synthesis of pure GO or rGO scaffolds with large pores (>100 μm) and an interconnected hierarchical architecture tailored to BTE.

In this study, we combine emulsion oil droplets and ice as dual templates to control GO assembly and produce 3D GO/rGO-based scaffolds with interconnected hierarchical porous architectures. Through a simple emulsification-freezing-drying process, we obtain GO scaffolds with large primary pores templated from organic solvent droplets in the oil phase of high internal phase emulsions (HIPEs), and small secondary pores from ice crystals formed in the water phase. Different from previous studies [140],[162], here, the GO sheets are both HIPE stabilizers and the building blocks for the self-standing scaffolds. Using synchrotron-based phase contrast X-ray imaging (PCI), we show that these scaffolds are fully interconnected with high porosity. After crosslinking with glutaraldehyde and mild thermal treatment, we obtain water-stable GO scaffolds which allow proliferation and infiltration of mouse bone marrow MSCs. Using the same, versatile strategy, we also synthesize 3D scaffolds with similar hierarchical architectures made of rGO with different reduction degrees, and GO composites, including GO/polyacrylic acid, GO/elastin, and GO/hydroxyapatite nanoparticles.

3.3 Material and methods

3.3.1 Materials

Graphene oxide paste (25 wt%) was purchased from Abalonyx which was synthesized by a modified Hummers' method (product number 1.2A). Glutaraldehyde solution (25%, in H_2O), hexane (HPLC grade) and toluene (HPLC grade) were purchased from Fisher Chemical. Cetyltrimethylammonium bromide (CTAB, 99%) was purchased from Bio Basic. Polyacrylic acid (PAA) (average $M_w \sim 1,800 \text{ g mol}^{-1}$), elastin (soluble from bovine neck ligament, 3–60 kDa),

calcium hydroxide (96%), phosphoric acid (99%), and citrate sodium (99%) were purchased from Sigma-Aldrich.

3.3.2 Preparation of GO/CTAB suspensions

We dispersed GO paste into GO suspension at different concentrations (5, 7.5, 10, 12.5 mg mL⁻¹) through stirring for 20 min following 20 min of sonification. We dissolved CTAB into deionized water (DI) water to make CTAB solution (10 mL) at different concentrations with variable weight ratios of CTAB to GO. To make GO/CTAB composite suspension, we added CTAB solution (10 mL) to GO suspension (40 mL) drop by drop under stirring at room temperature, followed by 5-min stirring.

3.3.3 Preparation of GO HIPEs

We named HIPEs as “HIPE XX-YY%”, where XX is the GO concentration in the water phase in mg mL⁻¹ and YY is the value of oil volume percentage. To make HIPE 4–75%, we added hexane (7.5 mL) and GO/CTAB suspension (2.5 mL in 4 mg mL⁻¹ GO and CTAB to GO ratio at 1 wt%) into a glass vial. We emulsified the mixture with a vortex shaker (Vortex-Genie®) (speed of 2,700 rpm, 1 min). We prepared other HIPEs following the same methods using corresponding concentrations of GO and hexane volume ratios. For comparison, we used toluene as the oil phase to make HIPE 10–75%. Also, we used GO suspensions (2.5 mL, 4 mg mL⁻¹, or 10 mg mL⁻¹), or CTAB solutions (2.5 mL, 0.04 mg mL⁻¹ and 0.1 mg mL⁻¹) and hexane (7.5 mL) for emulsification.

3.3.4 Preparation of GO scaffolds, 2D GO membranes and rGO scaffolds

We extracted the HIPEs using syringes of different sizes. Then we froze the syringes in a freezer (–20 °C, 12 h) or put them into liquid nitrogen (–190 °C, 5 min). After the freezing process, we immediately freeze-dried the frozen syringes at 0.22 mbar with collector temperature at –84 °C using Labconco FreeZone Freeze Dryer for 48 h to eliminate the water and oil to obtain GO

scaffolds that we then cut into different heights. For crosslinking, we placed GO scaffolds in a closed glass container with two glass vials of glutaraldehyde (GA) (10 mL, 25 wt%). We sealed the glass container and put it into an oven at 50 °C for 12 h. Finally, we thermally treated the crosslinked GO scaffolds, for 1 h of annealing at 100 °C in an oven and followed by an autoclave for 20 min at 120 °C. For comparison, we thermally treated GO scaffolds without crosslinking.

For the preparation of GO membranes, we drop-casted 0.25 mL GO suspension (12.5 mg mL⁻¹) on each glass slide in the dimensions of 2.5 × 2 cm² and air dried them. We crosslinked with GA and thermally treated the slides using the same method as described above. We peeled the GO membranes off the slides with a blade.

We further thermally reduced the GA crosslinked GO scaffolds that were made from HIPE 10–83% (froze at –190 °C or –20 °C) at two temperatures. We put GO scaffolds (prepared at –190 °C) inside a glass vial and placed the vial in an autoclave with water outside the vial. Then we kept the autoclave in an oven (180 °C, 6 h). Also, we reduced GO scaffolds (frozen at –20 °C) by putting the scaffolds in a quartz boat and placing the boats in a furnace (800 °C). The heating rate was 5 °C/min with 1-h plateau at 800 °C under argon (flowrate at 400 sccm).

3.3.5 Preparation of GO composite scaffolds

GO/PAA scaffolds:

We first prepared GO/CTAB suspension by adding CTAB aqueous solution (5 mL, 0.3 mg mL⁻¹) drop by drop into GO suspension (15 mL, 10 mg mL⁻¹) and let it stir for 5 min. Then, we prepared PAA solution (5 mL) by adding PAA (30 mg, average M_w = 1800 g mol⁻¹) into DI water and stirring until fully dissolved. Afterwards, we added PAA solution (5 mL, 6 mg mL⁻¹) to GO/CTAB suspension (20 mL) drop-by-drop to obtain a GO/PAA suspension (with final GO concentration of 6 mg mL⁻¹, CTAB to GO ratio at 1 wt% and PAA to GO ratio at 20 wt%). We let the

suspensions stir for another 5 min before use. Afterwards, we obtained GO/PAA HIPE by adding hexane (7.5 mL) and GO/PAA suspension (2.5 mL) into a glass vial and emulsified the mixture by using a vortex shaker Vortex-Genie® (speed of 2,700 rpm for 1 min). To make GO/PAA scaffolds, we extracted the HIPE using syringes, and we froze them (at $-20\text{ }^{\circ}\text{C}$ or $-190\text{ }^{\circ}\text{C}$) then freeze-dried the syringes containing HIPEs following the same procedure as described for GO scaffolds.

GO/hydroxyapatite (GO/HA) scaffolds:

We prepared hydroxyapatite (HA) nanoparticle suspensions following a procedure described in our former study [15]. We then diluted the obtained HA suspension (33.3 mg mL^{-1} to 7.2 mg mL^{-1}) and we added HA suspension (5 mL) to GO/CTAB suspension (20 mL, containing 7.5 mg mL^{-1} GO and 1% CTAB) drop-by-drop to obtain GO/HA suspension. We let the suspension stir for another 5 min before use. Similarly, we obtained GO/HA HIPEs by adding hexane (7.5 mL) and GO/HA suspension (2.5 mL) to a glass vial and emulsifying as described above. We obtained GO/HA scaffolds through freezing at $-20\text{ }^{\circ}\text{C}$ or $-190\text{ }^{\circ}\text{C}$ following the same procedures as described above.

GO/elastin scaffolds:

We prepared 7.5 mg mL^{-1} GO suspension as described. We dissolved soluble elastin from bovine neck ligament into DI water to make elastin solutions (3 mg mL^{-1}). We added elastin solution (1 mL) drop-by-drop to GO suspension (4 mL) to make GO/elastin suspension. We obtained GO/elastin emulsions by emulsifying the mixture of GO/elastin suspension (5 mL) and hexane (5 mL) following the same emulsification methods. We obtained GO/elastin scaffolds through freezing at $-20\text{ }^{\circ}\text{C}$ or $-190\text{ }^{\circ}\text{C}$ following the same procedures as described.

3.3.6 Cell proliferation, morphology and infiltration

The experimental details of the isolation of mouse bone marrow multipotent MSCs are provided in the supporting information section. For cell proliferation, we cut the autoclaved GO scaffolds (prepared from HIPE 10–75%, frozen at $-20\text{ }^{\circ}\text{C}$) into cylinders (thickness of 4 mm, diameter of 7 mm) and placed individual scaffolds in the wells of a 48-well plate. We seeded the MSCs onto the scaffolds at 10^5 cells per well with three replicates. For comparison, we placed individual square GO membranes (side length of 15 mm) in the wells of a 6-well plate. We seeded the MSCs onto the membranes at 10^5 cells per well with three replicates. We cultured the cells with normal stem cell growth medium, at $37\text{ }^{\circ}\text{C}$ in 5% humidified CO_2 . After cultured for 6 h (day 0), 1, 3, 7, 10 days, we washed the scaffolds/membranes with phosphate-buffered saline (PBS) 3 times to remove unattached cells. Then, we added trypsin-EDTA (0.5 mL, 0.25%, Thermo Fisher Scientific, Canada) solution to detach the adherent cells and counted the cells with a hemocytometer.

For cell morphology, we seeded cells as described above but at half density. At day 7, we fixed the cells using glutaraldehyde (2%, in PBS) for 2 days at $4\text{ }^{\circ}\text{C}$. After washing with PBS three times, we dehydrated the samples with graded ethanol solutions (30%, 50%, 70%, 80%, 90%, 95%, and 100%) for 20 min per solution. We further dried the samples on a critical point dryer (Leica EM CPD300, Leica Microsystems Inc., Wetzlar, Germany). We coated the samples with 4-nm-thick platinum for scanning electron microscope (SEM) observation.

For experiments on cell infiltration and attachment, we seeded and cultured cells as described in the cell morphology section. At day 7, we fixed the cells using cold paraformaldehyde (4%, in PBS) for 15 min at room temperature. We permeabilized the cells with Triton X-100 (0.1%, in PBS) for 5 min and blocked non-specific binding protein in fetal bovine serum (FBS) (5%, in PBS) for 1 h. For staining, we immersed the samples in a PBST solution (0.05% Tween20 in PBS)

containing 1:1000 dilution of Phalloidin iFluor594 (Abcam Inc., Ontario, Canada) and 1:10,000 dilution of DAPI (Sigma-Aldrich D9542, 5 mg mL⁻¹ stock, MilliporeSigma Canada Co., Ontario, Canada) and incubated for 30 min. After washing with PBS, we observed the samples with a confocal microscope (Zeiss LSM 800 Axio Observer Z.1, Carl Zeiss Canada Ltd., Ontario, Canada).

3.3.7 Characterization

Structural characterization

We captured images of emulsion droplets with an optical microscope (Olympus CKX41 connected with Canon EOS Rebel T3 single-lens reflex). We analyzed the size of the emulsion droplets with ImageJ.

The hydrodynamic diameter and zeta potential of GO and GO/CTAB in water were determined using the Zetasizer Nano ZS (Malvern Instruments) at 25 °C. We carried out dynamic light scattering (DLS) at a scattering angle of 173°, and reported the intensity weighted mean size (Z-average) as the hydrodynamic diameter [78],[346],[347]. The zeta potential that estimates the surface charge of GO and GO/CTAB was obtained from electrophoretic mobility measurements and calculated from the Smoluchowski model with Henry's equation [93].

For contact angle measurements, aqueous dispersions of pristine GO, and GO/CTAB were drop casted on cleaned glass substrates and dried at room temperature. The wettability was measured against water through static contact angle using the OCA 150 Goniometer (DataPhysics Instrument). The dosing volume is 5.00 µL, and the dosing rate is 1.00 µL/s.

We coated SEM samples with 4-nm thick platinum using a Leica EM ACE 600 high vacuum coater (Leica Microsystems Inc., Wetzlar, Germany). We observed the morphology of scaffolds

with a FEI Quanta 450 Field Emission Scanning Electron Microscope (FEI Company, Oregon, USA) under an accelerating voltage of 5 kV with spot size of 2 nm.

We visualized the internal microstructure of GO scaffolds using synchrotron-based PCI at the Biomedical Imaging Therapy Bending Magnet (BMIT-BM) beamline of the Canadian Light Source (Saskatchewan, Canada). The X-ray beam energy was 20 keV, and the X-ray radiation was absorbed by a LuAG:Ce scintillator (thickness of 50 μm) coupled to a PCO Edge5.5 detector, with sample-to-detector distance of 0.05 m. Samples were examined at 4.5x magnification using the WhiteBeam microscope. The resolution was set to 1.44 $\mu\text{m pixel}^{-1}$, and the field of view was 2560 pixel (H) * 2160 pixel (V). The samples were rotated to collect 3,000 projections with the exposure time of 250 ms per projection. We reconstructed the projected images to obtain slices with a volume of interest (1760*1760*720 voxels) using UFO-KIT (Karlsruhe Institute of Technology, Germany) and ImageJ. We used Avizo (Version 9.5, Thermo Fisher Scientific, USA) to set uniform thresholds through interactive thresholding and obtain binary images, thus, we discriminated the pores from the solid phase for 3D visualization, porosity and connectivity calculation.

We also measured porosity of GO scaffolds (with crosslinking and thermal treatments) through weighing method. We cut the GO scaffolds into cuboids, measured their dimensions and calculated their volume as V . Then we placed each scaffold in a centrifuge tube to minimize the error caused by the ultra-light weight of scaffolds. We weighed each tube with the scaffold inside as W_1 . Then we impregnated the scaffolds with DI water overnight. After that, we removed extra water and tenderly wiped the exceed liquid off the surface of scaffolds. Then, we weighed each tube with the wet scaffolds inside as W_2 . Pore volume can be calculated by the ratio of the difference in weight

($W_2 - W_1$) to the density of water ρ (0.998 g mL⁻¹ at 20 °C, 101.325 kPa). The porosity (P) was calculated according to the following equation:

$$P = \frac{[(W_2 - W_1) / \rho]}{V} \times 100\% \dots \dots \text{Equation 3.1}$$

We calculated the density of scaffolds by weighing them using a high-resolution scale (AB265-S/FACT, accuracy = 0.01 mg, Mettler Toledo, Mississauga, Canada) and measuring the diameter and height of scaffold cylinders using a digital caliper (DC02, accuracy = 0.01 mm, TACKLIFE, USA).

Chemical composition characterization

We performed energy dispersive X-ray spectroscopy (EDS) with the same SEM mentioned in the structural characterization section with an accelerating voltage of 10 kV and spot size of 3 nm.

We collected attenuated total reflection Fourier-transform infrared (ATR-FTIR) spectra with a Spectrum-Two IR spectrometer (PerkinElmer, Waltham, Massachusetts, USA) using an accumulation of 32 scans in the range of 400–4000 cm⁻¹ at a resolution of 4 cm⁻¹.

We analyzed elemental composition by X-ray photoelectron spectroscopy (XPS) on a Thermo Scientific K-Alpha photoelectron spectrometer (Thermo Fisher Scientific Inc., Waltham, Massachusetts, USA), equipped with an incident Ka X-ray source (1486.6eV, 0.843 nm) and an ultrahigh vacuum chamber (10⁻⁹ Torr). We used a flood gun of low energy electrons to prevent surface charging during the measurements. To detect elemental information and atomic content, we conducted survey scans in the step size of 1 eV and high-resolution scans for each detectable element in the step size of 0.1 eV. The analyzed spots were in 400 μ m in diameter. We used Avantage Software to analysis the survey and high-resolution spectra and fitted C1s curves with four components: C–C (C=C), C–O, C=O, and π - π^* shake up at 284.8, 286.5, 288.4 and 290.8 eV respectively.

We collected Raman spectra with a Bruker Senterra confocal Raman microscope (Bruker, Germany) using a 20 mW, 532 nm pump laser. We acquired the spectra with 120 s of integration time and 2 co-additions.

Measurements of compressive and thermal properties

We measured the compressive strength of the porous materials on a miniature loading stage (Ernest F. Fullam, Inc., New York, USA) equipped with a 20 g loading cell in a compression setup. The loading speed was 0.05 mm s⁻¹.

We carried out thermogravimetric analysis (TGA) using TGA 2500 Discovery (TA Instruments, Delaware, USA) and performed heating from room temperature to 800 °C at 10 °C min⁻¹ with nitrogen gas purged (20 mL min⁻¹).

3.4 Results and discussion

3.4.1 Strategy and formation of GO/CTAB HIPEs

Figure 3.1 shows our dual-templating strategy to obtain primary and secondary pores in GO scaffolds. GO sheets are amphiphilic due to the presence of both hydrophobic sp² bonded carbon atoms and oxygen-containing groups [8]. As a result, GO sheets can assemble at oil-in-water (o/w) interfaces, thus creating o/w Pickering emulsions [115]. When the internal oil phase volume fraction (ϕ_o) is above 74%, which is the maximum packing density of uniform spheres without deformation, the resulting emulsions are HIPEs [140]. In the first step, we create o/w HIPEs where the oil droplets become the templates for the primary pores. To achieve HIPEs, we adjust the amphiphilicity of GO with a cationic surfactant, CTAB (**Figure 3.1a**). Cationic CTAB molecules adsorb on negatively charged GO sheets (**Figure 3.1b**), and the hydrophobic alkyl chains of CTAB increase the hydrophobicity of GO [122],[348]. With an adjustable amphiphilicity, CTAB modified GO sheets can stabilize Pickering HIPEs [140]. After adding hexane to the GO/CTAB

suspension (**Figure 3.1c**) and emulsification through vortex mixing, we obtain GO/CTAB HIPEs (**Figure 3.1d**). The irreversible adsorption of GO sheets at the o/w interfaces hinders emulsion coalescence [115]. Because of the highly packed emulsion droplets, GO/CTAB HIPEs behave like gels and do not flow when inverted (**Figure 3.1d**).

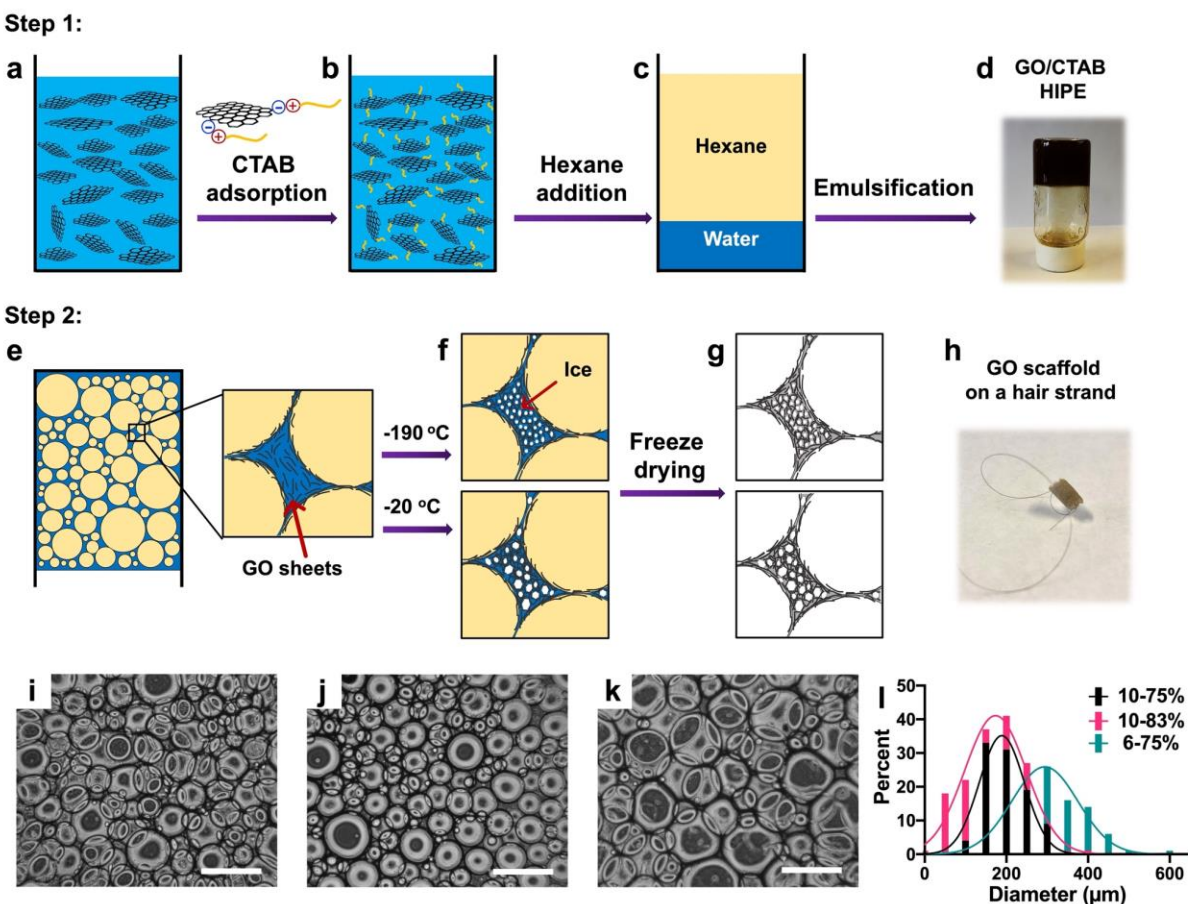


Figure 3.1. (a–h) Dual-templating strategy to create free-standing GO scaffolds with pores in bimodal diameter distributions. **Figure 3.1d** shows HIPEs in an inverted vial made with 10 mg/mL of GO modified by 1 wt% of CTAB, with $\phi_o = 80\%$ of hexane. **Figure 3.1h** shows a GO scaffold supported on a strand of hair. (i–k): Optical microscopy images of GO HIPEs: 10–75% (i), 10–83% (j), and 6–75% (k). Scale bar in all images = 500 μm . (l): emulsion droplet size distributions of HIPEs shown in i–k and nonlinear regression based on Gaussian model.

In the second step, we use this emulsion to create a porous scaffold upon freezing. The ice-templating method allows easy fabrication and control of hierarchical architectures [344],[349]. We start from highly packed HIPEs, where the GO sheets present in the aqueous phase (e) can assemble at the ice crystal boundaries through van der Waals interactions and hydrogen bonding

(**Figure 3.1f**) [185]. We then freeze the HIPEs at either $-190\text{ }^{\circ}\text{C}$ in liquid nitrogen, or $-20\text{ }^{\circ}\text{C}$ in a freezer to create different sizes of ice crystals in the water phase (**Figure 3.1f**). After freeze-drying and ice sublimation, we create secondary pores with different sizes depending on the freezing temperature (**Figure 3.1g**). With this strategy, we can fabricate highly porous and lightweight GO scaffolds (**Figure 3.1h**).

We modify the GO with CTAB using different CTAB to GO ratios of 0.1, 0.5, 1, 5 or 10 wt%. The ATR-FTIR spectrum of the GO/CTAB composite (**Figure 3.S1**) shows bands associated with GO, including ν_{OH} at 3408 cm^{-1} , $\nu_{\text{C=O}}$ at 1714 cm^{-1} , $\nu_{\text{C=C}}$ (aromatic) at 1630 cm^{-1} , and bands associated with CTAB, including ν_{CH} (methylene) at 2915 cm^{-1} and 2848 cm^{-1} , and the δ_{CH} at 1375 cm^{-1} . These results are consistent with previous studies and show that GO has been successfully modified with CTAB [350],[351].

Furthermore, we measure the zeta potential of GO and GO/CTAB to evaluate the change of surface charge. Before modification, the GO suspension exhibits a negative zeta potential (**Figure 3.S2**) due to the presence of carboxylic groups on the GO surface. The zeta potential gradually increases with increasing CTAB to GO weight percentage from 0.1% to 10%, which confirms the adsorption of the cationic CTAB on the negatively charged GO [347],[352]. Increasing CTAB to GO weight percentage also increases the hydrodynamic diameter of the modified GO flakes as observed by DLS measurements (**Figure 3.S2**), especially at CTAB equals to 10 wt% GO. This result suggests the formation of GO/CTAB aggregates due to hydrophobic interactions [348]. We further obtain the wettability of GO and GO/CTAB by static contact angle measurement (**Figure 3.S3**). The results confirm that the hydrophobicity increases with the increase of CTAB to GO weight percentage due to the presence of hydrophobic alkyl chains from CTAB [122],[348]. Still,

the contact angles measured remain below 90° for any of the GO/CTAB samples, implying that all these samples should be able to stabilize oil-in-water emulsions [8],[115].

The successful formation of GO/CTAB HIPEs primarily depends on the CTAB to GO ratio. Without modification, GO suspensions and hexane separate immediately after emulsification (**Figure 3.S4**). If GO is modified with 0.1 wt% or 0.5 wt% of CTAB, a small quantity of emulsion droplets forms because the GO sheets with enhanced hydrophobicity can move to the hexane/water interfaces, thus reducing the system free energy [140]. However, phase separation still occurs since not all the hexane is emulsified (**Figure 3.S4**). With 1 wt% of CTAB, a stable HIPE is formed (**Figure 3.S4**): GO sheets now have the optimum amphiphilicity and can fully stabilize the hexane/water emulsions. With $\phi_o = 75\%$, no hexane remains un-emulsified, and the HIPE system assumes a gel-like status. When modified with 5 wt% or 10 wt% of CTAB, the increased hydrophobicity causes emulsion aggregation and flocculation (**Figure 3.S4**). These results show that the modification of GO with 1 wt% CTAB provides the appropriate amphiphilicity to form GO HIPEs. We thus use 1 wt% CTAB for further experiments. The presence of GO is crucial for HIPE formation, since using only CTAB as the emulsifier is insufficient for emulsion formation (**Figure 3.S4**).

The stability of the HIPE is enhanced by increasing GO concentration (**Figure 3.S5**). At a GO concentration of 4 mg mL^{-1} , stable HIPEs can form with ϕ_o up to 75%. Higher GO concentrations of 10 mg mL^{-1} can stabilize HIPEs with ϕ_o as high as 83%, where more GO sheets with appropriate amphiphilicity are available to stabilize more hexane droplets [136]. We call the HIPEs “HIPE XX-YY%”, where XX is the GO concentration in the water phase in mg mL^{-1} and YY is the value of ϕ_o . For example, HIPE 10–75% corresponds to a HIPE made with a GO concentration of

10 mg mL⁻¹ and an oil-to-water ratio $\phi_o = 75\%$. The full range of HIPE compositions used in this paper is shown in **Table 3.S1**.

The emulsion droplet size is a crucial parameter since it determines the size of the primary pores of the GO scaffolds after freeze-drying. The HIPE 10–75% has a mean droplet diameter of $200 \pm 50 \mu\text{m}$ (**Figure 3.11i** and **l**). Increasing ϕ_o to 83% with a GO concentration of 10 mg mL⁻¹ (HIPE 10–83%) decreases the droplet size to $170 \pm 70 \mu\text{m}$ and increases the percentage of smaller droplets (**Figure 3.1j** and **l**). This likely occurs because the increase in oil phase volume destabilizes the emulsion and causes the collapse of the larger droplets. Decreasing the GO concentration significantly increases droplet size. The HIPE 6–75% has emulsion droplets with diameters of $300 \pm 80 \mu\text{m}$ (**Figure 3.1k** and **l**). In this case, fewer CTAB-modified GO sheets are available to stabilize hexane/water interfaces, and therefore larger droplets form. The type of solvent also affects the emulsion droplet size. HIPEs obtained using toluene as the oil phase have smaller droplets than those made in hexane (**Figure 3.S6**) due to the π - π interactions between the sp² domains on the GO basal plane and the aromatic ring of toluene [136].

3.4.2 GO based scaffolds

Figure 3.2a–f shows SEM images of the GO scaffolds obtained after freezing the hexane-in-water HIPEs at $-190 \text{ }^\circ\text{C}$ or $-20 \text{ }^\circ\text{C}$ and drying; a scaffold starting from a toluene-based emulsion is shown in **Figure 3.S7**. These scaffolds have large interconnected primary pores and smaller secondary pores formed within the walls of the primary pores.

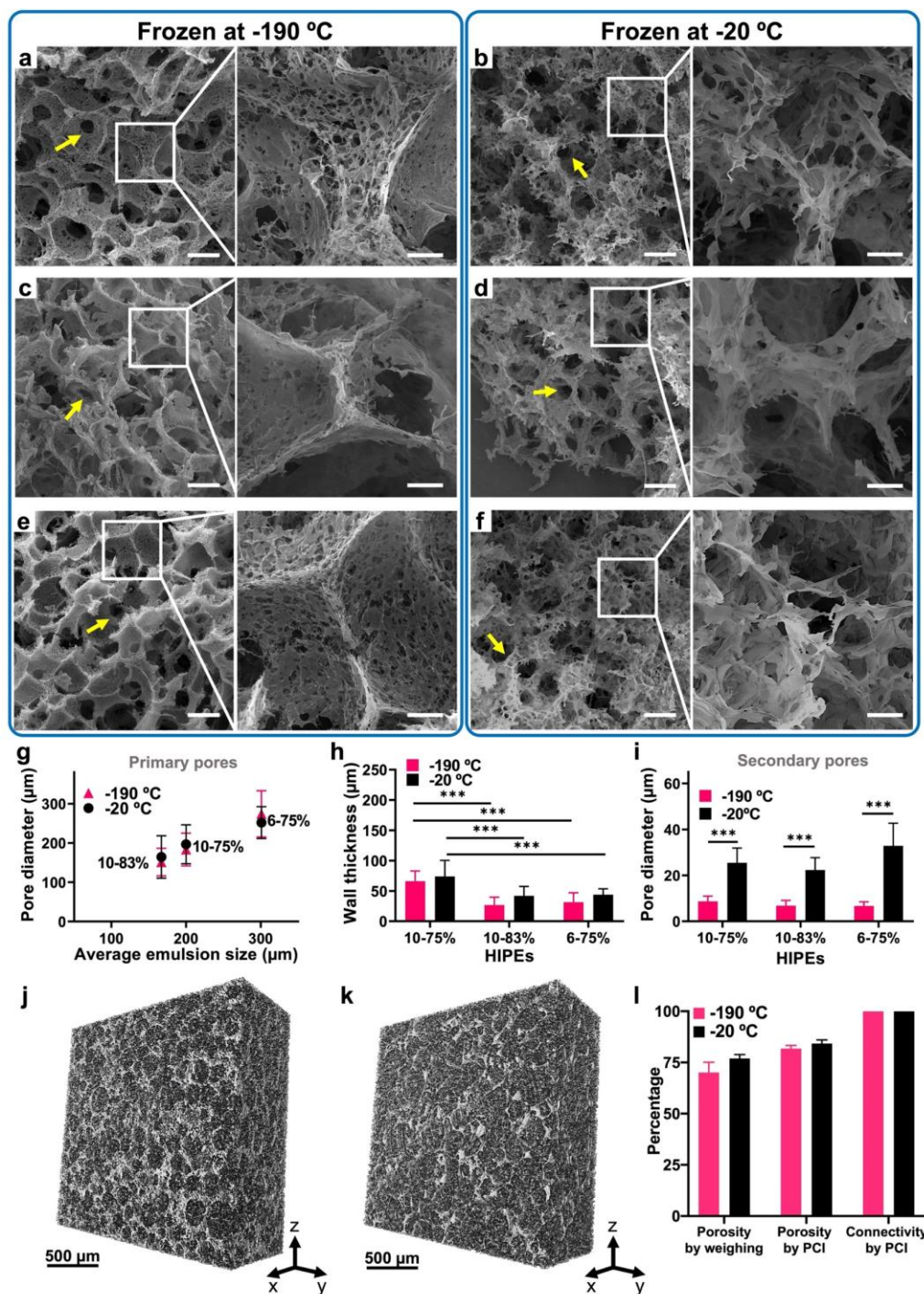


Figure 3.2. (a–f) SEM images of GO scaffolds prepared from HIPEs frozen at $-190\text{ }^{\circ}\text{C}$ (a, c and e) or $-20\text{ }^{\circ}\text{C}$ (b, d and f), corresponding to HIPE 10–75% (a, b), 10–83% (c, d) and 6–75% (e, f). In all panels the scale bars correspond to $200\text{ }\mu\text{m}$ for the images to the left and $50\text{ }\mu\text{m}$ for the zoomed-in images to the right. The yellow arrows point at some examples of openings between pores. (g) Primary pore diameter plotted against the corresponding HIPE droplet size ($n = 100$ from 3 independent experiments). (h) Wall thickness of the primary pores ($n = 50$ from 3 independent experiments), and (i) secondary pore diameter ($n = 100$ from 3 independent experiments). (j–k) 3D reconstruction images of GO scaffolds prepared from HIPE 10–75% frozen

at $-190\text{ }^{\circ}\text{C}$ (j) and $-20\text{ }^{\circ}\text{C}$ (k) through synchrotron-based PCI. (l) Porosity obtained through weighing measurement and PCI, and connectivity obtained through PCI of GO scaffolds prepared from HIPE 10–75% frozen at $-190\text{ }^{\circ}\text{C}$ or $-20\text{ }^{\circ}\text{C}$ ($n = 3$ independent experiments). The data represent the mean \pm standard deviation. The asterisks indicate statistically significant differences calculated by the two-tailed Student's t -test, with $***P < 0.001$.

The primary pores are templated from the emulsion droplets, as shown by the fact that their size corresponds to the original droplet size (**Figure 3.2g**). This correspondence is not 1:1, because of shrinkage during the drying process. The walls of the pores are made of layers of GO sheets, which function as oil droplet stabilizers in the HIPEs. The wall thickness can be adjusted by changing the aqueous phase volume or the GO concentration: if the hexane phase ϕ_0 is increased from 75% to 83%, the primary pore walls become thinner because of the smaller volume of continuous aqueous phase around the hexane droplets and thus the smaller quantity of GO (**Figure 3.2a–d** and **h**). With the same ϕ_0 at 75%, decreasing the GO concentration also reduces the wall thickness of the primary pores (**Figure 3.2a, b, e, f** and **h**).

All the scaffolds show openings between the primary pores (examples are indicated by yellow arrows in **Figure 3.2a–f**). This is likely due to the evaporation of hexane during the freeze-drying step, which ruptures the pore walls [122],[353],[354]. Because of the compact packing of HIPEs, the GO sheets form thin barriers at the contact area between the neighboring droplets. When frozen at $-20\text{ }^{\circ}\text{C}$, the hexane droplets remain in the liquid state. After sending to freeze-drying, the hexane is removed by evaporation in the vacuum. The mechanical force during the evaporation can break the thin GO barrier at the conjunction points, resulting in the openings between the pores. At $-190\text{ }^{\circ}\text{C}$, the hexane freezes, since its freezing temperature is $-95.3\text{ }^{\circ}\text{C}$. After sending to freeze-drying, the hexane firstly melts, then evaporates from the scaffolds. The evaporation also results in the opening of pores as observed at $-20\text{ }^{\circ}\text{C}$.

The freezing temperature strongly influences the size of the secondary pores (**Figure 3.2i**). The ice solidification has two competitive processes: nucleation and growth of ice crystals. When there

is a high-temperature gradient (at low freezing temperature, $-190\text{ }^{\circ}\text{C}$), ice crystal nucleation occurs rapidly throughout the scaffold and leaves limited time and space for ice crystal growth. This gives rise to small ice crystals and therefore small secondary pores (**Figure 3.2a**, c and e). At $-20\text{ }^{\circ}\text{C}$, the nucleation rate is lower, resulting in larger ice crystals and, after sublimation, larger secondary pores in the scaffold (**Figure 3.2b**, d and f).

With the help of PCI, we visualize the internal 3D microstructure of GO scaffolds prepared from HIPE 10–75% frozen at $-190\text{ }^{\circ}\text{C}$ and $-20\text{ }^{\circ}\text{C}$. Conventional absorption contrast X-ray tomography infers structure from the attenuation of X-rays transmitted through a sample. X-ray attenuation in materials composed of low-atomic number elements (such as carbon, oxygen and nitrogen) is comparatively low, leading to poor image contrast. A synchrotron provides access to the high brightness, spatially coherent beam, enabling the imaging of light elements in a sample based on the X-ray phase contrast. X-ray PCI infers sample structure by analyzing the distribution of transmitted X-ray not only from absorption but also from interference of the incident X-rays with the forward refracted phase-shifted X-rays, which makes it possible to image samples with low atomic number [355]. We apply this technique to gain insights into the internal microstructures of our scaffolds. The 3D reconstructed images show the interconnected porous architectures of GO scaffolds with both large and small pores, which agree well with our observation through SEM (**Figure 3.2a**, b, j and k, **Figure 3.S8**). We analyze the volume of the empty and solid phases in the 3D model and find that the scaffolds have high porosity (**Figure 3.2l**, the second set of bars) of $82 \pm 2\%$ (frozen at $-190\text{ }^{\circ}\text{C}$) and $84 \pm 2\%$ (frozen at $-20\text{ }^{\circ}\text{C}$). These results are similar to the porosities we obtain through weighing measurements, which show porosity of $70 \pm 5\%$ (scaffolds frozen at $-190\text{ }^{\circ}\text{C}$) and $77 \pm 2\%$ (scaffolds frozen at $-20\text{ }^{\circ}\text{C}$) (**Figure 3.2l**, the first set of bars).

Analysis of the 3D models from PCI also show that the pores in the scaffolds are highly interconnected (**Figure 3.21**, the third set of bars), which agree with SEM imaging.

3.4.3 Stabilization of GO scaffolds in aqueous medium and cell culture

The presence of interconnected large and small pores is favorable for BTE. For this application, scaffold stability in an aqueous medium is also crucial; however, the GO scaffolds produced thus far collapse and disperse in DI water (**Figure 3.3a**). GO sheets become negatively charged when immersed in water, and thus the scaffolds disintegrate easily due to electrostatic repulsion [356]. To improve stability, we crosslink the scaffolds by exposing them to glutaraldehyde (GA) vapor for 12 h at 50 °C (a process labeled as “+GA” from here on). The hydroxyl groups on the GO sheets can react with the aldehyde groups of GA through intermolecular acetalization, which leads to the crosslinking of GO sheets [357]; GA has been widely used as a crosslinker for biocompatible scaffolds in both *in vitro* and *in vivo* studies [358],[359]. We further anneal the scaffolds at 100 °C for 1 h to enhance π - π interactions between GO sheets [360]. Following autoclaving at 120 °C for 20 min, we obtain sterilized and water-stable GO scaffolds. Scaffolds that have been GA crosslinked, thermally annealed and autoclaved (thermal treatment and autoclaving will be referred as “+TT” from here on) maintain their integrity in aqueous environments for weeks (**Figure 3.3b**).

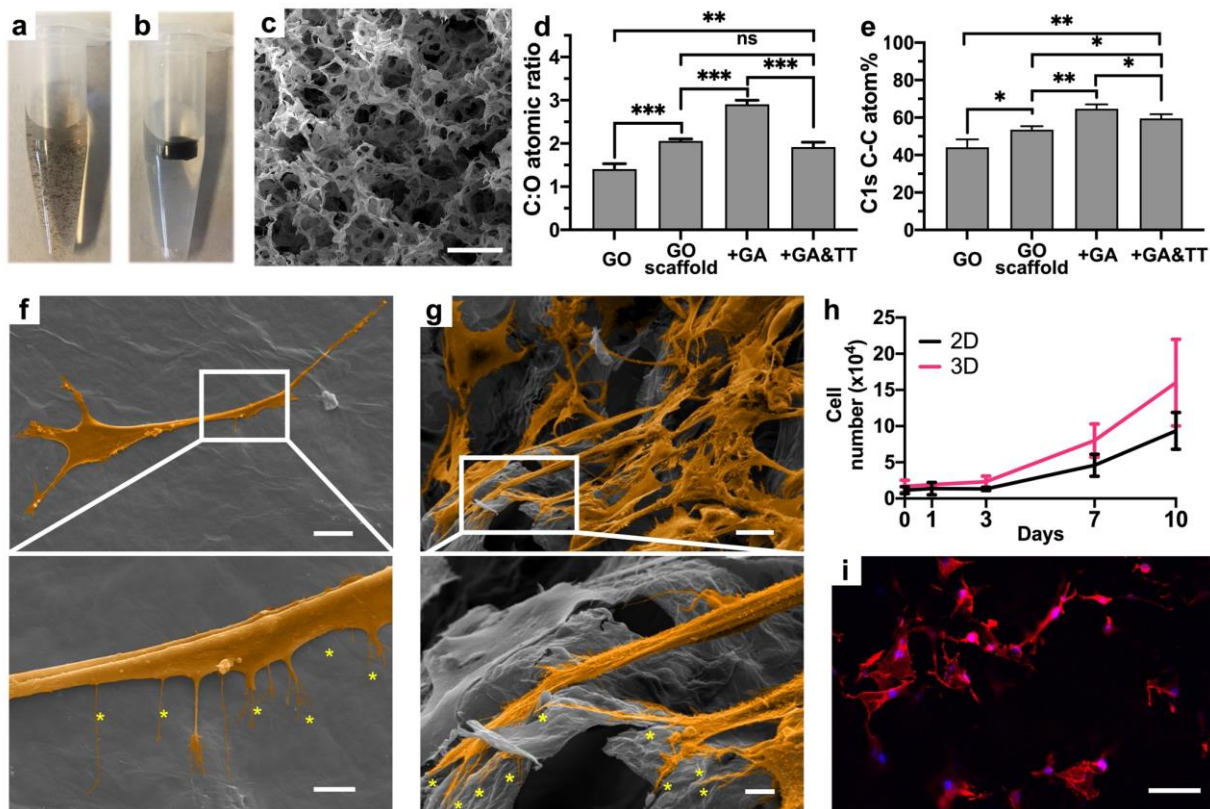


Figure 3.3. (a–b) Pictures showing an example of GO scaffolds before (a) and after (b) GA crosslinking and thermal treatment when immersed in DI water for 7 days. (c) SEM image of GO scaffold after crosslinking and thermal treatment. The scaffolds in (a–c) are prepared from hexane based HIPE 10–75% frozen at $-20\text{ }^{\circ}\text{C}$, scale bar = $200\text{ }\mu\text{m}$. (d) C:O atomic ratios from XPS survey scans and (e) percentage of C–C bonds from XPS high resolution C1s spectra (binding energy $\sim 284.8\text{ eV}$) of pristine GO, GO scaffolds, GO scaffolds with GA crosslinking (+GA), and GO scaffold after GA crosslinking and thermal treatment (+GA & +TT). $n = 3$ independent experiments. The data represent the mean \pm standard deviation. The asterisks indicate the statistical significance calculated by the two-tailed Student's t -test, where $*P < 0.05$, $**P < 0.01$, $***P < 0.001$ are considered to be significant difference. (f–g) SEM images of mouse MSCs after 7 days of culture on GO membrane (f) and GO scaffold (g). The cells are colored in orange; yellow stars label some of the cellular filamentous extensions interacting with the materials. The scale bars in panels f and g correspond to $20\text{ }\mu\text{m}$ for the images to the top and $5\text{ }\mu\text{m}$ for the zoomed-in images to the bottom. (h) MSC proliferation curves on 2D GO membrane and 3D GO scaffolds up to 10 days ($n = 3$ independent experiments). (i) Confocal microscopy image of MSCs inside a GO scaffold ($\sim 1\text{ mm}$ from the top) after 7 days of culture, with actin cytoskeleton in red (phalloidin staining labeled with Alexa Flour594) and nuclei in blue (DAPI staining), scale bar = $40\text{ }\mu\text{m}$.

Crosslinking and thermal treatment do not alter scaffold morphology (**Figure 3.3c**). We investigate the chemical structure evolution of GO scaffolds before and after crosslinking and thermal treatment by XPS. The initial GO flakes have a C:O atomic ratio of 1.4 ± 0.1 (**Figure**

3.3d; Table 3.S2, Figure 3.S9). After CTAB modification, the addition of alkyl chains significantly increases the C:O ratio to 2.10 ± 0.04 on GO scaffolds. High resolution C1s spectra also show an increase in C–C bonds on GO scaffolds upon CTAB addition (**Figure 3.3e** and **Figure 3.S10**). A very small amount of nitrogen (0.6 ± 0.7 atom%) is detected due to the presence of quaternary amines in CTAB (**Table 3.S2** and **Figure 3.S9**). After GA crosslinking, the C:O atomic ratio and C–C atom% further increase because of intermolecular acetalization with GA (**Figure 3.3d** and **e; Figure 3.S10**). However, following thermal treatment, the C–C atom% and C:O atomic ratio significantly decrease (**Figure 3.3d** and **e; Figure 3.S9** and **Figure 3.S10**), and no trace of nitrogen can be detected (**Table 3.S2, Figure 3.S9**). These two observations are evidence that thermal treatment may eliminate CTAB, with the disappearance of the alkyl chains and quaternary amines. The mild thermal treatment maintains the oxidized nature of GO scaffolds, as shown by the large amount of O still detected (**Table 3.S2**), and does not affect crosslinking, as shown by a C–C atom% significantly higher than the starting GO flakes and GO scaffolds (**Figure 3.3e**).

We confirm the importance of GA crosslinking to improve stability by testing the stability of scaffolds that are only thermally treated. These scaffolds dissociate after immersion in DI water for 7 days (**Figure 3.S11**); their C–C atom% is significantly lower than the percentage measured on the scaffolds that are also crosslinked with GA (**Figure 3.S10** and **Figure 3.S11**).

FTIR spectroscopy provides further evidence for the formation of crosslinks and the elimination of CTAB (**Figure 3.S12**). In addition to the peaks found in GO, the peaks assigned to ν_{CH} (methylene) at 2915 cm^{-1} and 2848 cm^{-1} , δ_{CH} at 1375 cm^{-1} (methyl group), ν_{CN} ($\text{N}(\text{CH}_3)_3$) at 920 cm^{-1} , and δ_{CH} (methylene chain) at 718 cm^{-1} in the GO/CTAB spectra arise from CTAB. After GA crosslinking, the peaks assigned to ν_{CH} , δ_{CH} , and ν_{COC} at 1050 cm^{-1} become more prominent

because of the addition of methylene chains in GA [357]. Following thermal treatment, the peaks relative to ν_{CH} and ν_{CN} almost disappear, which confirms the elimination of CTAB. The oxidized nature of GO scaffolds after GA and TT is also confirmed by the presence of oxygen containing groups in the FTIR spectra.

The GO-based, water-stable scaffolds with hierarchical, interconnected pores we produced are promising candidates to test the application of GO 3D substrates in BTE. Previous studies of cell behavior on GO substrates for BTE have only used 2D GO coatings on flat surfaces or membranes [16],[357], since there have been no reports to date of 3D pure GO scaffolds with hierarchical, interconnected pores. However, it is known that cells have different responses in terms of proliferation, attachment, differentiation and other cellular activities on 2D surfaces compared to 3D matrixes [361]–[363].

To evaluate the effect of the 3D structure of our scaffolds on cell proliferation and morphology, we also prepare water stable, free-standing 2D GO membranes (**Figure 3.S13**) by drop-casting the GO suspension on glass slides. After GA crosslinking and thermal treatment, we can peel the membranes off the slides. We culture mouse bone marrow MSCs on both the self-standing GO membranes and the GO scaffolds (+GA and +TT) (**Figure 3.3f and g**). As shown in SEM images, MSCs attach and spread on both 2D membranes and 3D GO scaffolds, showing elongated morphology on both surfaces. Different from what is observed on the 2D membranes, cells on 3D GO scaffolds create 3D networks spanning over the many pores of the scaffolds and connecting to the pore walls through filamentous extensions (**Figure 3.3g**).

By day 10, the cell number increases by approximately 8.5 and 7 folds compared to day 1 on 3D GO scaffolds and 2D GO membranes, respectively (**Figure 3.3h**). This trend is comparable with previous studies on graphene scaffolds [361],[363] and other widely applied polymeric [364],[365]

and ceramic [366],[367] scaffolds for BTE. For instance, Zhang et al. found that after 9 days of culture on 3D pristine graphene based scaffolds, human MSCs proliferated about 6 times than on day 1; like us, the same authors found that this increase was greater than that observed on 2D pristine graphene films [361]. Wu et al. found that on GO-containing silk fibroin-chitosan scaffolds, there were about 4 times more bone marrow MSCs after 7 days of culture compared to day 1 [368], which is very similar to what we find for the same period. Wu and many other researchers showed that the addition of GO in BTE scaffolds improves cell proliferation, attachment and osteogenic differentiation [369]–[371]. Our results showing GO scaffolds can support cell attachment and proliferation agree well with these studies.

The porous structure of 3D GO scaffolds not only enhances cell attachment; confocal microscopy images show that this architecture also facilitates cell infiltration through the primary pores all the way to the center of the scaffolds (**Figure 3.3i**). This result aligns with previous studies showing that an interconnected hierarchical porous architecture can offer a large surface area for cell attachment, while secondary pores can facilitate the diffusion of nutrients, therefore enhancing cell proliferation and infiltration [372],[373]. *In vivo* studies showed an interconnected hierarchical structure can enhance cell infiltration, metabolic exchange and blood vessel ingrowth for bone formation [374]–[376]. These results and our *in vitro* study show that our GO scaffolds with a hierarchical interconnected architecture are promising candidates for BTE.

3.4.4 Versatility of the dual-templating strategy

To test the versatility of this strategy, we also produce rGO porous scaffolds with different reduction degrees. Studies have shown that rGO scaffolds are promising candidates for BTE [22], and different reduction states of rGO induce different cell behavior [16]. Aiming to obtain rGO scaffolds with different reduction degrees, we thermally reduce the freeze-dried GO scaffolds in

different conditions through commonly used methods [16],[377], *i.e.*, hydrothermal reduction at 180 °C with water mist or thermal treatment at 800 °C in argon.

Through reduction, we obtain rGO scaffolds that maintain the hierarchical architectures of the parent GO scaffolds (**Figure 3.4a** and **e**). The thermal treatments successfully reduce GO to varying degrees as shown by a higher C:O ratio compared to pristine GO and reduced C=O and C–O peaks in high resolution C1s XPS spectra of rGO scaffolds (**Figure 3.4a** and **e**, **Figure 3.S14**). The degrees of reduction achieved are comparable to previous literature [7]. Also, the Raman spectra reveal increased D peak ($\sim 1340\text{ cm}^{-1}$) to G peak ($\sim 1580\text{ cm}^{-1}$) intensity ratio (I_D/I_G) with increasing reduction temperature, as compared with GO (**Figure 3.S14**). The G-peak is due to first-order Raman scattering involving the in-plane stretching phonon mode in sp^2 carbon materials, and the D-band is a second-order Raman scattering process involving the breathing mode of sp^2 carbon and symmetry breaking defects [378],[379]. During thermal reduction of GO, there is an increase in the I_D/I_G ratio compared to that measured on GO (**Figure 3.S14**) [380]–[382]. This can be explained by the fact that the I_D/I_G ratio of graphene, GO and rGO does not have a monotonic dependence on defect density [378],[383],[384]; in samples with high defect density such as GO and rGO the I_D/I_G ratio increases as the defect density decreases [383].

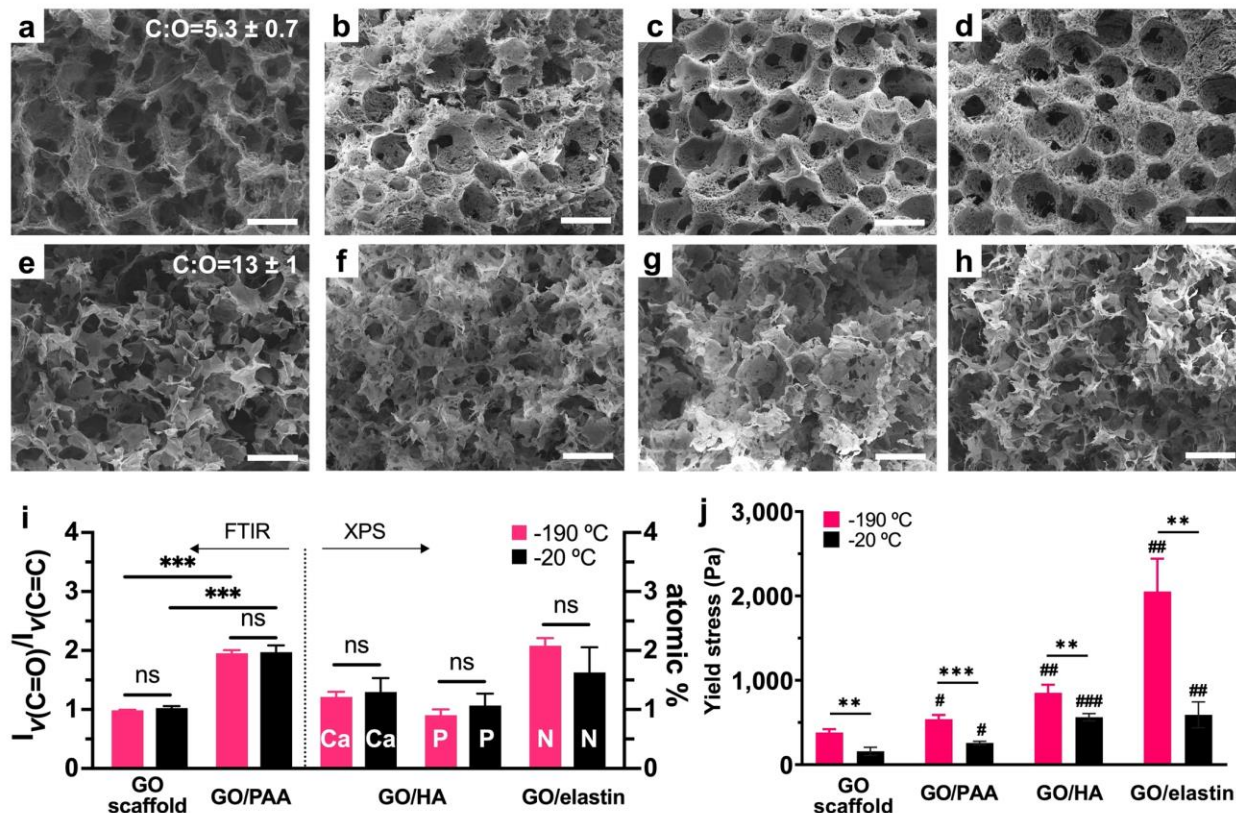


Figure 3.4. (a–h) SEM images of scaffolds produced with dual template strategy frozen at either $-190\text{ }^{\circ}\text{C}$ (a–d) or $-20\text{ }^{\circ}\text{C}$ (e–h) with different composition: rGO (a, e; C:O ratios from XPS survey data reported on the images), GO/PAA (b, f), GO/HA (c, g), GO/elastin (d, h). Scale bars in all panels are $200\text{ }\mu\text{m}$. (i) FTIR absorption intensity ratio between peaks relative to $\nu_{\text{C}=\text{O}}$ at 1714 cm^{-1} and $\nu_{\text{C}=\text{C}}$ at 1630 cm^{-1} for GO and GO/PAA scaffolds frozen at $-190\text{ }^{\circ}\text{C}$ and $-20\text{ }^{\circ}\text{C}$ (left y axis); atomic percentage of calcium and phosphorus on GO/HA scaffolds, and nitrogen on GO/elastin scaffolds, according to XPS survey scans (right y axis). (j) Yield stress for GO, GO/PAA, GO/HA and GO/elastin scaffolds prepared at $-190\text{ }^{\circ}\text{C}$ and $-20\text{ }^{\circ}\text{C}$. The data represent the mean \pm standard deviation. The pound signs indicate statistically significant differences between each scaffold and the corresponding GO scaffold frozen at the same temperature. The asterisks indicate statistically significant differences between scaffolds made at different temperatures. Statistical differences are calculated by the two-tailed Student's *t*-test, with * or # $P < 0.05$, ** or ## $P < 0.01$ and *** or ### $P < 0.001$, $n = 3$ independent experiments.

We then adapt the dual-templating strategy to synthesize GO composites by adding supplementary components into the initial GO suspension used as the aqueous phase for emulsion preparation. We test the versatility of our method using a synthetic polymer (polyacrylic acid, PAA), a biomolecule (soluble elastin from bovine neck ligament) and inorganic nanoparticles (hydroxyapatite, HA) as additives. PAA is a biocompatible polymer, and porous composites of

PAA and graphene-family materials have been applied in tissue engineering and water treatment [306],[385]. The synthesis of GO/PAA porous scaffolds usually starts with adding GO to acrylic acid monomers, initiators and crosslinkers and goes through polymerization under an inert atmosphere. In our method, we avoid the polymerization step by simply using a GO and PAA mixed suspension to produce GO/PAA composite HIPes. Elastin is a protein found in connective tissue that can improve the biocompatibility of graphene-based materials [386]. To the best of our knowledge, there have been no reports on the fabrication of GO/elastin composite porous materials. HA is the main component of bone and teeth and studies have shown that HA and rGO composite materials can enhance osteogenic differentiation of stem cells and promote new bone formation [15],[22]. To date, there have been no reports on 3D GO-based scaffolds composed with HA.

We can form homogeneous suspensions without visible aggregation with up to 20% of PAA and 24% of HA in GO/CTAB suspensions (expressed as a mass percent of additive with respect to the mass of GO). This is likely due to the negative charge of PAA and HA nanoparticles [15],[162]: the carboxylic groups present on PAA and the negative surface charge of HA nanoparticles can both increase GO hydrophilicity; by adding CTAB in controlled ratios to GO/PAA and GO/HA, we can tune GO amphiphilicity and create stable HIPes with hexane as the oil phase and $\phi_o = 75\%$ (**Figure 3.S15**). Because of the hydrophobic nature of elastin, we can directly add elastin to a GO suspension without CTAB (with 10% elastin respect to GO) and obtain homogenous mixed suspension, likely because elastin interacts with the hydrophobic domains of GO basal planes [386]. In this case, we can obtain emulsions with $\phi_o = 50\%$, while increasing ϕ_o to 75% results in excess non-emulsified hexane (**Figure 3.S15**).

After freeze-drying these emulsions at $-190\text{ }^\circ\text{C}$ or $-20\text{ }^\circ\text{C}$, we obtain scaffolds with primary large pores templated by the emulsion droplets, and secondary small pores templated by ice

(**Figure 3.4b–d, f-h**), as observed with emulsions containing only GO/CTAB. FTIR spectra show an increase in intensity of the peak assigned to $\nu_{C=O}$ peak at 1714 cm^{-1} compared to the $\nu_{C=C}$ peak at 1630 cm^{-1} , due to the addition of carboxylic groups from PAA in GO/PAA composite scaffolds (**Figure 3.S16**). The relative intensity ($I_{\nu(C=O)}/I_{\nu(C=C)}$) among GO/PAA scaffolds frozen at different temperatures are similar, but show a significant difference compared to pure GO scaffolds (**Figure 3.4i**). XPS survey spectra confirm the presence of calcium and phosphorus in GO/HA and nitrogen in GO/elastin scaffolds (**Figure 3.4i, Figure 3.S17**). The atomic percentage of the characteristic elements also shows no significant difference between different freezing temperatures. FTIR spectra show the characteristic bending vibration of PO_4^{3-} at 563 cm^{-1} indicating the presence of HA in GO/HA scaffolds (**Figure 3.S16**) [15]. TGA confirms the loading of HA in GO/HA composites (**Figure 3.S18**), and EDS mapping shows a uniform distribution of calcium and phosphorus in the GO/HA composites (**Figure 3.S19**).

The compressive stress-strain curves of all scaffolds include a linear elastic regime (controlled by cell wall bending), a plateau deformation regime (controlled by plastic cell wall buckling and collapse), and a densification regime (controlled by complete pore collapse) [387](**Figure 3.S20**). From these curves, it is possible to calculate the yield stress, corresponding to the onset of the bending-to-buckling deformation of cell walls, by linear regression of the linear elastic and plastic plateau regimes [387],[388] (see inset in **Figure 3.S20**). The results of this analysis (**Figure 3.4j**) show that by adding PAA, HA, or elastin to the GO scaffolds, the yield stress increases. Also, the scaffolds frozen at $-190\text{ }^\circ\text{C}$ show higher yield stress than the corresponding scaffolds frozen at $-20\text{ }^\circ\text{C}$. The GO/elastin scaffolds frozen at $-190\text{ }^\circ\text{C}$ show the highest yield stress of all samples. We observe a similar trend in a comparison of the compressive stress at 80% strain (**Figure 3.S21**).

Studies on porous carbon and hierarchical cellular materials show that an increase in scaffold density increases compressive strength [185],[389],[390]. Since all composite scaffolds studied here have a higher density than the corresponding pure GO scaffolds (**Figure 3.S21**), we infer that an increase in density contributes to the observed enhancement of yield stress and compressive stress at 80% strain for the composite scaffolds compared to the pure GO scaffolds.

We also find that the scaffolds frozen at $-190\text{ }^{\circ}\text{C}$ are denser than those frozen at $-20\text{ }^{\circ}\text{C}$; such an increase in density may thus also contribute to a higher yield stress and compressive stress at 80% strain of the scaffolds frozen at a lower temperature (**Figure 3.4j**; **Figure 3.S21**).

Another potential contribution to the observed differences in mechanical properties is the microscopic structure of the scaffolds. In the primary cell walls of scaffolds frozen at $-190\text{ }^{\circ}\text{C}$, there are uniformly distributed secondary pores with a small diameter (**Figure 3.2e** and **i**). These dense cell walls can better resist bending deformation and collapse of the primary pores under compressive load, leading to higher yield stress and densification stress [391].

To decouple other effects of additives beyond density on the compressive stress of the composite scaffolds, we prepare a pure GO scaffold with a density similar to that of the composite scaffolds. The resulting scaffolds are made from HIPE 7.2–75% (sample called “GO-7.2”) and have a density that is not significantly different from the GO/HA scaffolds, and approximately 2% and 5% higher than the GO/PAA scaffolds frozen at $-190\text{ }^{\circ}\text{C}$ and $-20\text{ }^{\circ}\text{C}$ respectively (**Figure 3.S22**).

Despite the small differences in density, when frozen at $-190\text{ }^{\circ}\text{C}$, the GO-7.2 scaffolds show significantly higher yield stress than both GO/PAA and GO/HA scaffolds. This result implies that the additives, which replace between 20% (in the PAA composites) and 24% (in the HA composites) of the GO sheets compared to the GO-7.2 scaffolds, are not able to create a porous network as stable as that created by the GO sheets. Thus, the resulting pore walls of the composite

scaffolds are less resistive to compression as compared to those of the pure GO-7.2 scaffold. This result is in line with our previous report [15]. We find a similar trend for the scaffolds frozen at $-20\text{ }^{\circ}\text{C}$, except that the differences are not significant for the GO/HA scaffolds.

Our method can produce GO, rGO and composite GO scaffolds with both large and small pores, interconnected to each other. No single previously reported method could achieve these results (**Figure 3.5**). **Figure 3.5a** shows an overview of the mean pore diameter in 3D porous scaffolds based on graphene, rGO or GO through different fabrication strategies reported to date. Our dual-templating method is able to prepare rGO and GO based scaffolds with larger pores than those achievable with assembly methods assisted by reduction [15],[22], crosslinking [342],[392]–[394] or emulsion-templating [141],[159],[162],[395], and is comparable to the pore range achieved with CVD and hard templating methods. CVD enables a wide range of pore diameters by selecting metal [340],[396] or metal oxide [397] templates with desirable architectures, but it is limited to the production of pristine graphene based scaffolds. The fabrication of GO and rGO based scaffolds with a wide range of pore diameters can be achieved by employing hard templates (**Figure 3.5a**) [343],[345],[398],[399]. Among these, ice crystal templating can lead to scaffolds with controllable pore size and different compositions [344],[400]–[402]. However, GO based scaffolds with large pores can be achieved only in composite scaffolds (*e.g.*, GO/cellulose or GO/boron nitride [398],[403]), whereas pure GO scaffolds can be synthesized only with small pores (up to few tens of microns) (**Figure 3.5b**) [404],[405]. Our dual templating method overcomes this limitation and enables the synthesis of pure GO, rGO and GO composite scaffolds with pore sizes ranging from several microns to hundreds of microns. This versatility arises from the combination of emulsion and ice dual-templating, control of the amphiphilicity of GO, as well as ice crystal size control by freezing at different temperatures. With this facile strategy, the dual-

templating method simultaneously expands the range of GO composite types and pore sizes that can be obtained through emulsion and ice templating methods (**Figure 3.5b**).

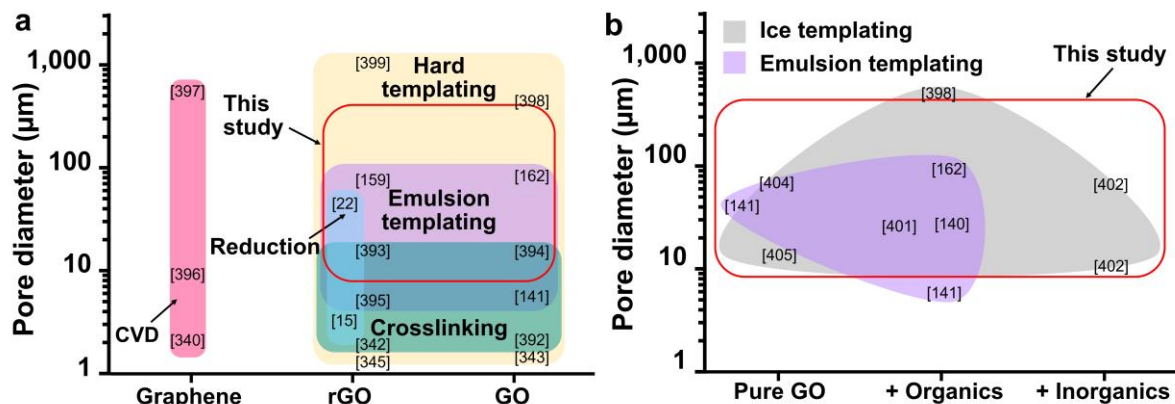


Figure 3.5. Comparison of pore diameters achieved so far with different fabrication methods for (a) scaffolds mainly based on graphene, rGO, GO or composite scaffolds and (b) Pure GO and GO composite scaffolds with organics or inorganics as additives. As indicated in the figure, light magenta, yellow, orchid, cyan, teal, and grey shading indicate CVD, hard templating, emulsion templating, reduction, crosslinking and ice templating methods, respectively. The y axis is shown as scaled logarithmically in both graphs. The sections circled in red refer to this study.

3.5 Conclusions

In summary, we have developed a dual-templating method to fabricate 3D porous GO, rGO, and GO composite scaffolds with interconnected porosity and hierarchical size distributions. We regulate the amphiphilicity of GO with a cationic surfactant, CTAB, to achieve stable HIPEs. In these HIPEs, the GO sheets are not only emulsion stabilizers but also the building blocks for dual-template assembly. The droplets containing the oil phase of the HIPEs become templates for interconnected primary large pores with mean diameters of 100–300 μm, and the ice crystals formed in the aqueous phase during freeze-drying become templates for the secondary pores with mean diameters around 10 or 20–60 μm, depending on the freezing temperature. For the first time, we apply synchrotron-based PCI to visualize GO scaffolds, and we find the scaffolds have high porosity and connectivity.

The GO scaffolds produced with this strategy can be easily made water-stable through crosslinking and thermal treatment. Using this strategy, we are able to use for the first time 3D GO scaffolds for MSC cell culture and show that cells can infiltrate through the scaffolds and grow in a 3D network as they proliferate and adhere to the interconnected primary pores. *In vivo*, the presence of GO should favor osteogenic differentiation and bone regeneration, and the hierarchical architecture should favor nutrient and metabolic exchange. This makes our scaffolds promising for non-load bearing BTE applications such as the repair of calvarial defects, where their relatively low compressive strength will not be detrimental. Future work including *in vivo* studies will be necessary to confirm this potential.

We thermally reduce the GO scaffolds to controllable reduction degrees while preserving the parent scaffold architectures, and by adding additives such as polymers (PAA), proteins (elastin) and inorganic nanoparticles (HA) in the emulsion fabrication step, we can generate composite scaffolds that maintain the hierarchical porous structures. The properties we achieved, including tunable hierarchical architectures, long-term water stability, diverse composition, and tunable reduction degrees (which correlates with electrical conductivity [7]), also make these scaffolds promising candidates for applications such as catalysis and water treatment [1].

3.6 Acknowledgement

The authors acknowledge the facilities, scientific and technical assistance of the McGill Institute for Advanced Materials, the Quebec Center for Advanced Materials and the Canadian Light Source. This work was supported by the McGill Engineering Doctoral Awards, the Canada Research Chair Program (CRC: 950–231239), Natural Sciences and Engineering Research Council of Canada (STPGP 506395–17), and the Fonds de Recherche du Québec–Nature et Technologies (Bourses de doctorat en recherche).

3.7 Supporting information

Isolation of mouse bone marrow multipotent MSCs

We isolated MSCs from the bone marrow of C57BL/6 male mice (6-8 weeks old, Charles River, Montreal, QC, Canada). The femurs and tibias were harvested, and the soft tissues were cleared from the bones. The epiphyseal heads were cut from each bone, and the bone marrow was flushed out of the cavities with ice-cold phosphate buffered saline (PBS). The cell suspension was filtered with a 70 μm cell strainer to remove large debris and then centrifuged (300 g force, 5 minutes). The cells were resuspended in α -MEM (Gibco BRL, NY, USA) supplemented with fetal bovine serum (FBS) (15%), penicillin (100 U mL^{-1}) and streptomycin (100 $\mu\text{g mL}^{-1}$), and they were cultured at 37 °C in a humidified atmosphere containing 5% CO_2 and 95% air with tissue-cultured treated plates (100-mm, Sarstedt Inc., North Carolina, USA). The cells were passaged upon reaching confluence with trypsin–EDTA (0.25%, Thermo Fisher Scientific Inc., USA) and split at a ratio of 1:3. The cells at passage 3 were characterized with flow cytometry. The results showed that cells were positive for mesenchymal stem cell markers (CD29+, CD105+, CD44+, Sca1+ and CD45- , >99%). The MSCs were used for experiments at passages 3-6 in normal stem cell growth medium, which is complete alpha-minimum essential medium (α -MEM supplemented with 10% FBS and 1% antibiotic-antimycotic, Gibco, USA).

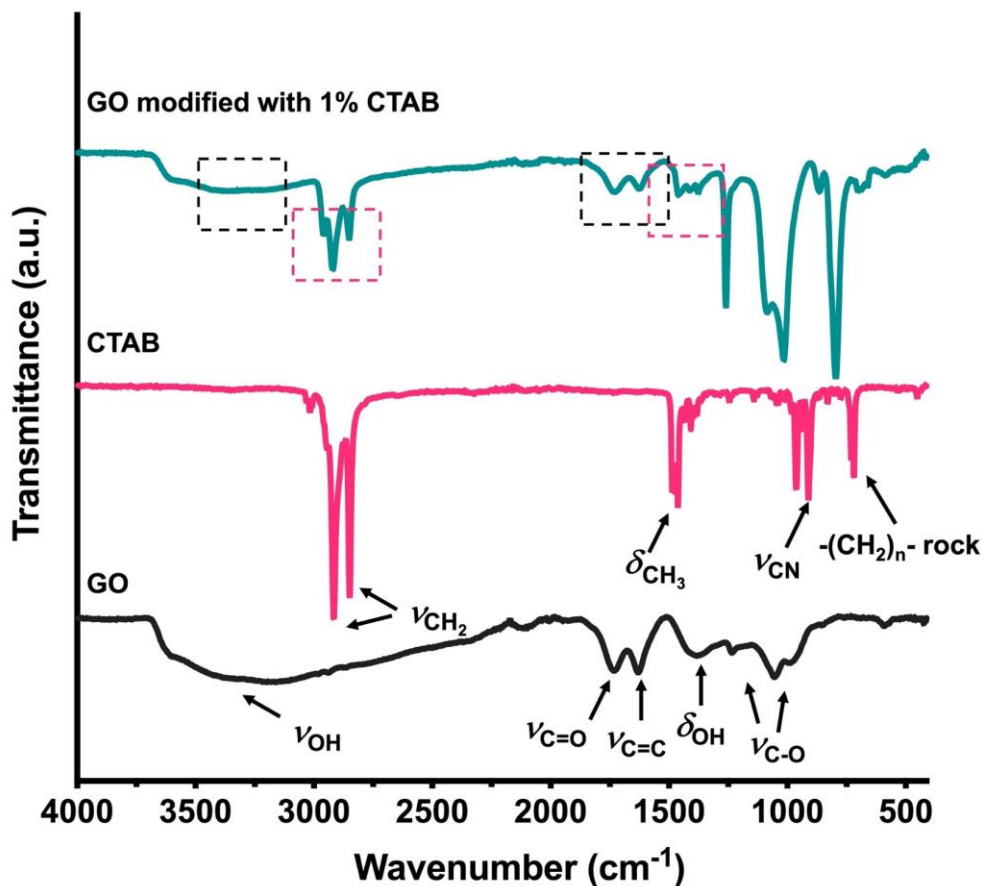


Figure 3.S1. FTIR spectra of GO, CTAB, and GO/CTAB (made from suspension with GO concentration of 4 mg mL^{-1} , and CTAB to GO ratio at 1wt%).

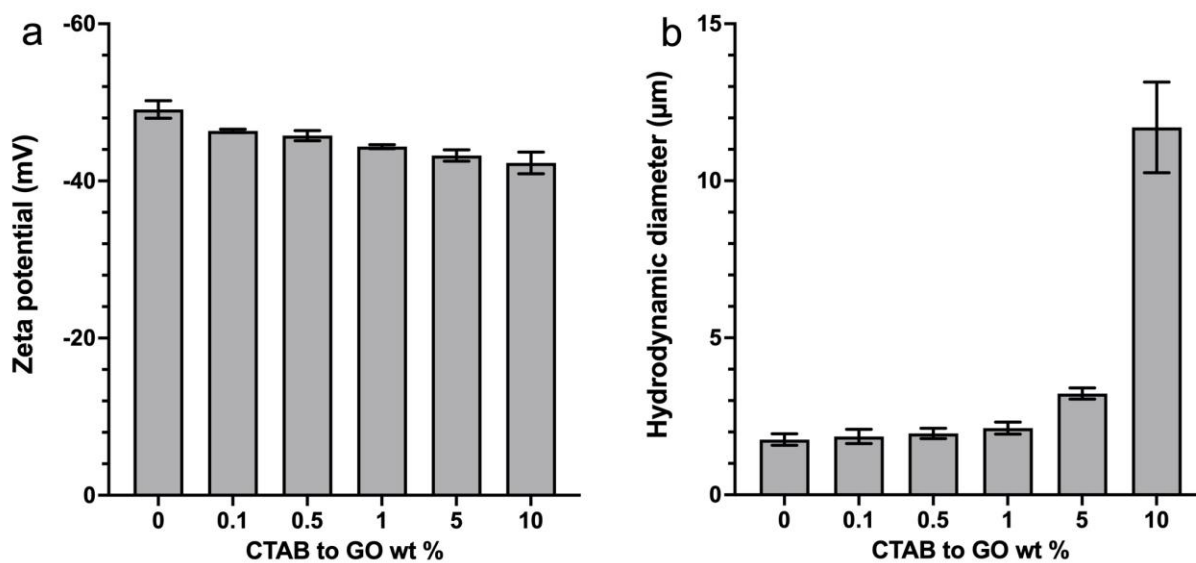


Figure 3.S2. Zeta potential and hydrodynamic diameter of pristine GO and GO/CTAB aqueous dispersions modified with different CTAB to GO weight percentage.

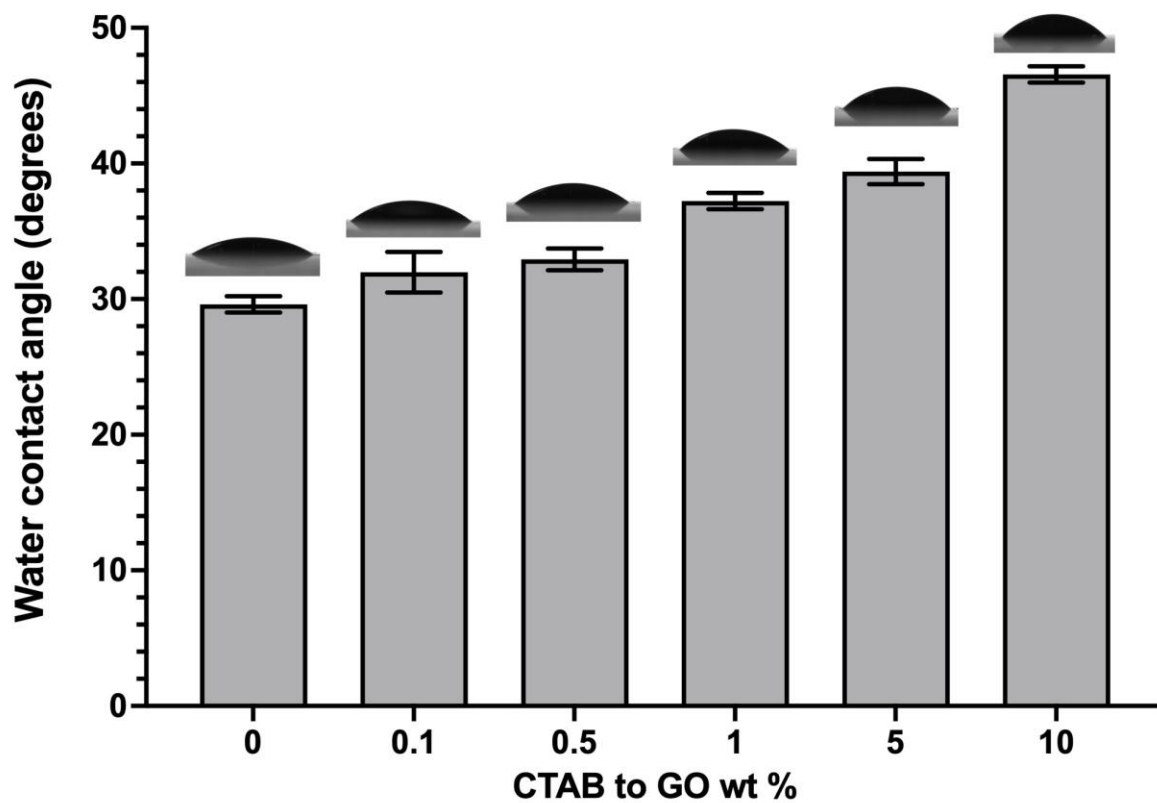


Figure 3.S3. Static water contact angle of pristine GO and GO/CTAB with different CTAB to GO weight percentage. Representative images showing water droplets spreading on the samples are shown on top of the bars.

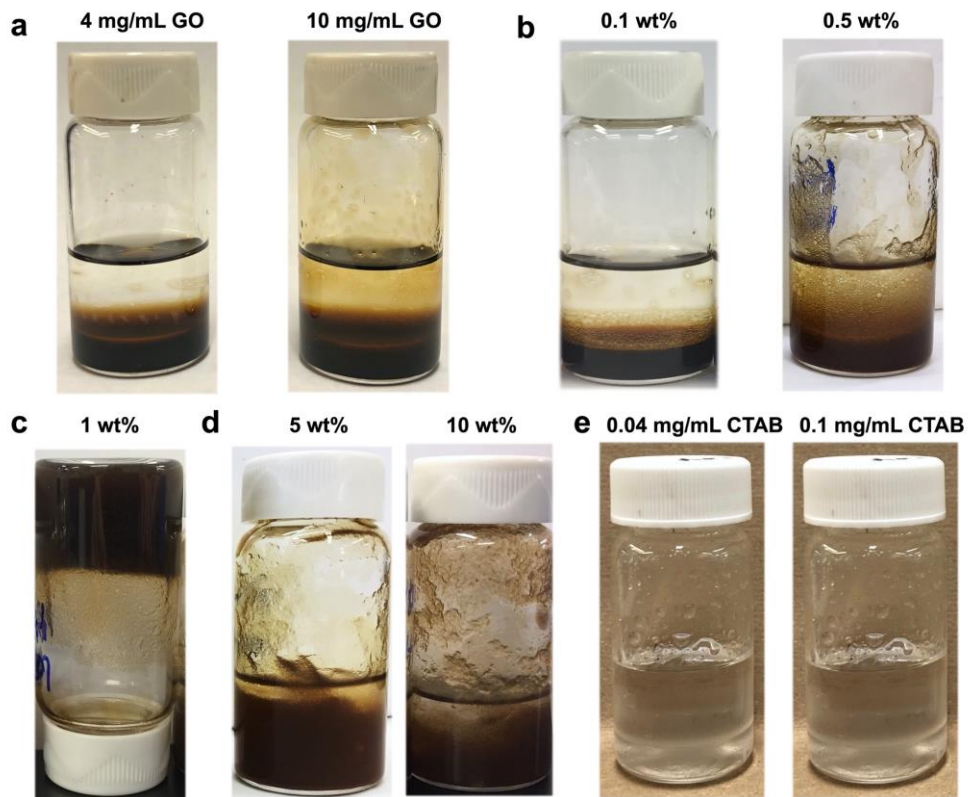


Figure 3.S4. Digital pictures showing (a) phase separation using 4 mg mL^{-1} , or 10 mg mL^{-1} GO suspensions as the aqueous phase; (b) phase separation using GO/CTAB suspensions, with CTAB to GO ratio at 0.1 wt% or 0.5 wt%; (c) formation of HIPE with CTAB to GO ratio at 1 wt%; (d) emulsion aggregation and flocculation with CTAB to GO ratio at 5 wt% or 10 wt%. The concentration of GO is 4 mg mL^{-1} in figures (b-d); (e) phase separation using 0.04 mg mL^{-1} , or 0.1 mg mL^{-1} CTAB solution as the aqueous phase (corresponding to the same concentration of CTAB when CTAB to GO ratio is at 1 wt% in 4 mg mL^{-1} or 10 mg mL^{-1} GO suspensions). All the samples in (a-e) have hexane as the oil phase with $\phi_o=75 \%$.

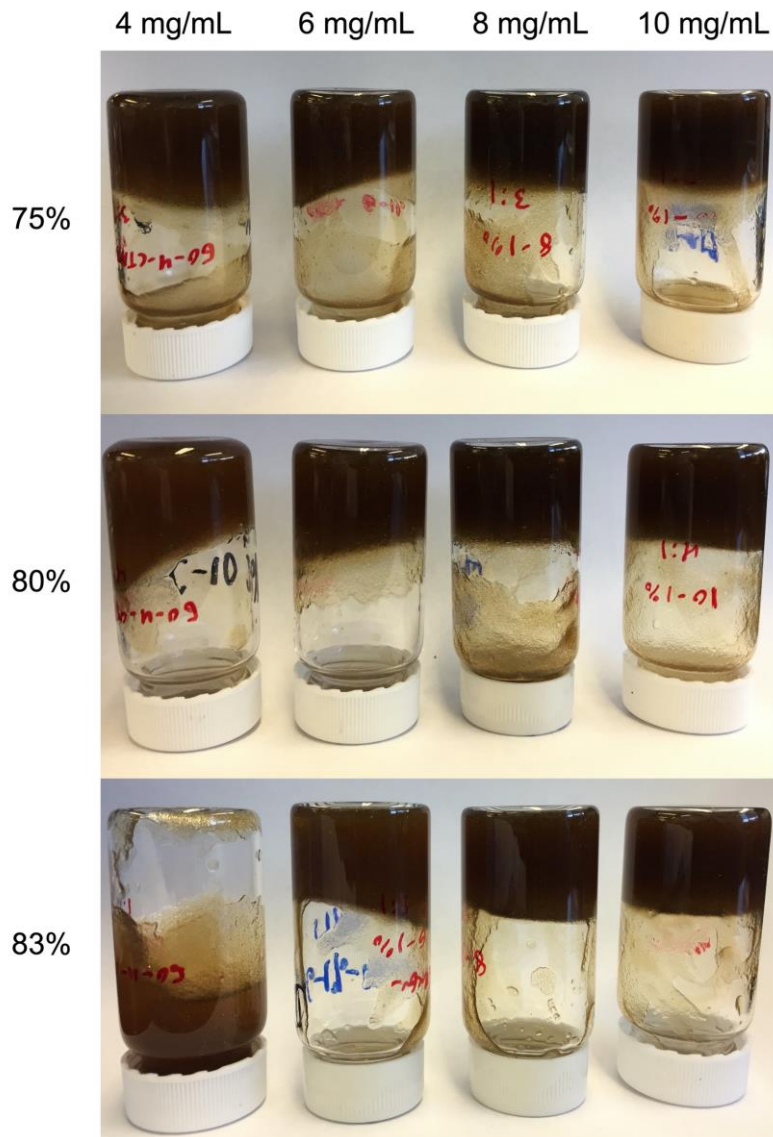


Figure 3.S5. Digital pictures showing HIEPs using hexane with $\phi_0=75\%$, 80% or 83% , when GO concentrations are 4, 6, 8, or 10 mg mL^{-1} in the GO/CTAB suspensions, with CTAB to GO ratio at 1wt%. The stability of HIEPs with gel-like status is enhanced by increasing the GO concentration.

Table 3.S1. Preparation of GO HIPEs. The HIPEs discussed in **Figure 3.1** are bolded.

Sample	GO concentration in the aqueous phase (mg/mL)	Weight percentage of CTAB to GO (%)	Hexane phase volume percentage (%)	Aqueous phase volume percentage (%)
4-75%	4	1	75	25
4-80%	4	1	80	20
4-83%	4	1	83	17
6-75%	6	1	75	25
6-80%	6	1	80	20
6-83%	6	1	83	17
10-75%	10	1	75	25
10-80%	10	1	80	20
10-83%	10	1	83	17

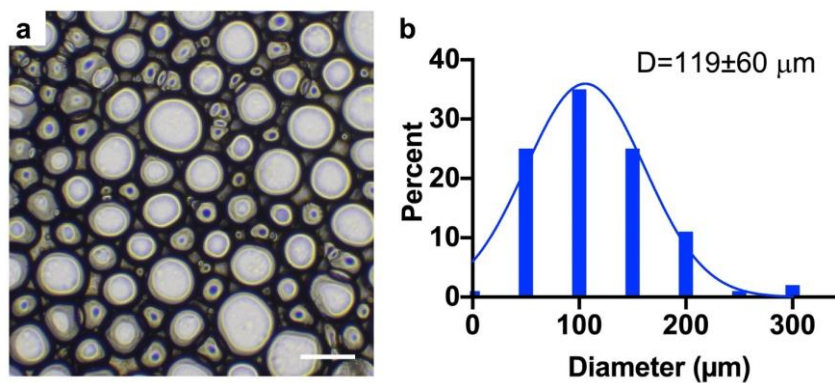


Figure 3.S6. Optical microscopy image (a) and droplet size distribution (b) of HIPE when CTAB to GO ratio is at 1 wt% with GO concentration of 10 mg mL⁻¹ and using toluene as the oil phase ($\phi_o = 75\%$). Scale bar=200 μm.

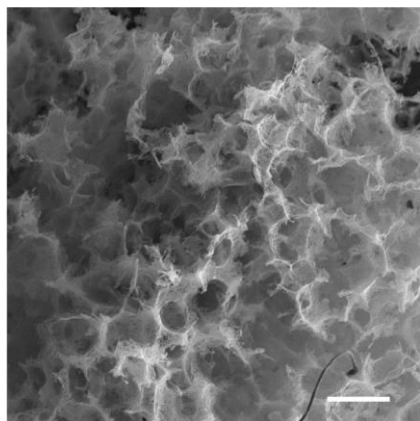


Figure 3.S7. SEM image of the GO scaffold prepared from toluene based HIPE with GO concentration of 10 mg mL^{-1} , and $\phi_0=75\%$ of toluene, frozen at $-190 \text{ }^\circ\text{C}$. Scale bar = $200 \text{ }\mu\text{m}$.

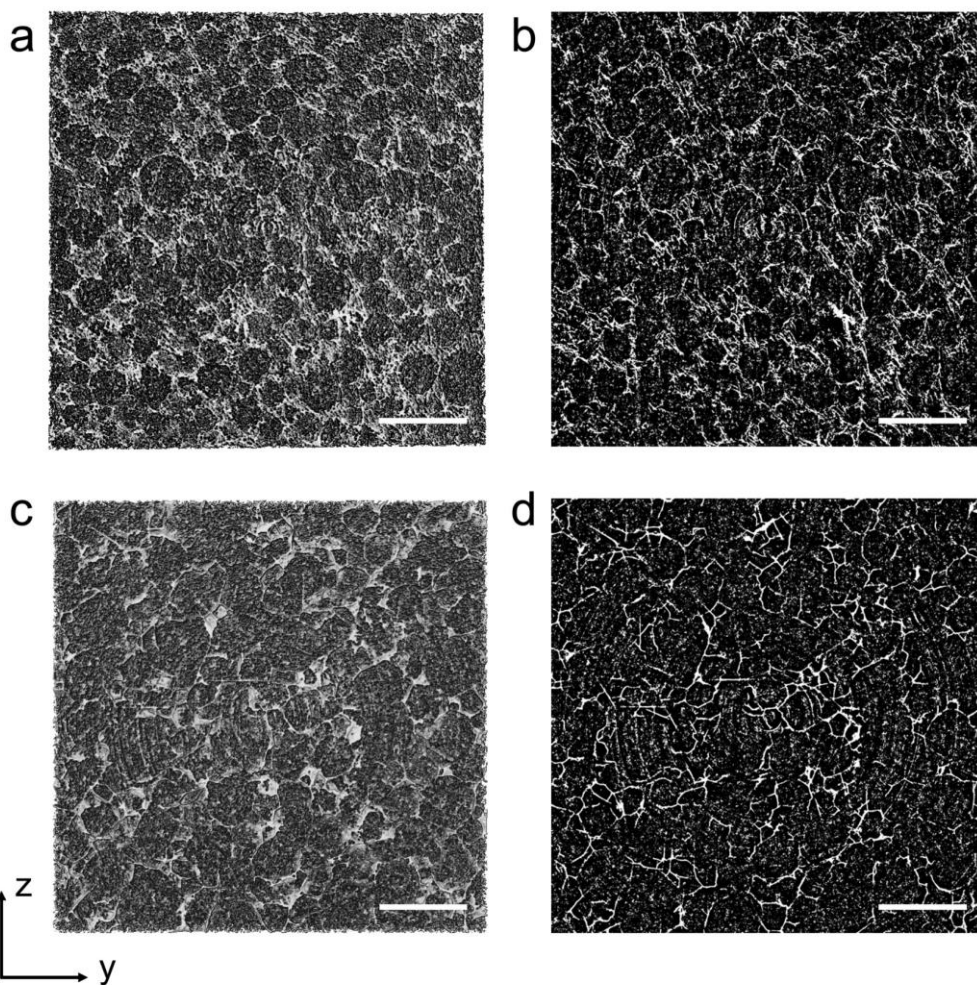


Figure 3.S8. Front view through x-axis of 3D reconstruction images (a and c) and corresponding segmented 2D cross section (b and d) of GO scaffolds prepared from HIPE 10-75% frozen at $-190 \text{ }^\circ\text{C}$ (a, b) and $-20 \text{ }^\circ\text{C}$ (c, d). Scale bar = $500 \text{ }\mu\text{m}$.

Table 3.S2. Surface chemistry from XPS survey data of GO, GO scaffolds, GO scaffolds with GA crosslinking (+GA) and GO scaffolds with GA crosslinking and thermal treatment (+GA & +TT) (n=3 independent experiments)

	GO	GO scaffolds	+ GA	+GA & +TT
C1s (atom%)	58±2	66±1	72.9±0.4	66±1
O1s (atom%)	41±2	32.2±0.1	25.1±0.7	34±1
N1s (atom%)	---	0.6±0.7	1.2±0.4	---
S2p (atom%) ^{a)}	0.4±0.8	0.7±0.6	0.74±0.07	---
C:O atomic ratio	1.4±0.1	2.10±0.04	2.90±0.09	1.9±0.1

^{a)} Sulfur is likely the impurity from Hammer's method in preparation method [88].

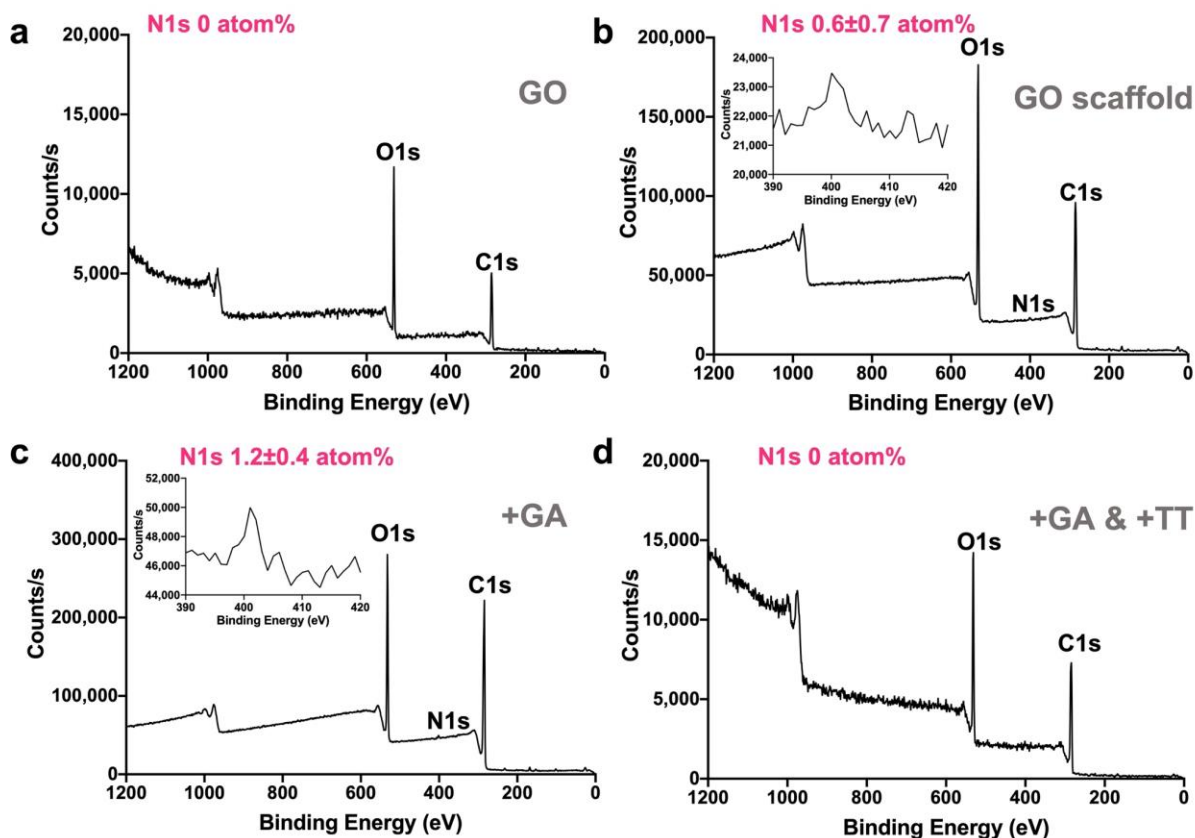


Figure 3.S9. XPS survey spectra of (a) pristine GO, (b) GO scaffold, (c) GO scaffold with GA crosslinking, and (d) GO scaffold with both crosslinking and thermal treatment, high resolution spectra of N1s inserted in (b-c).

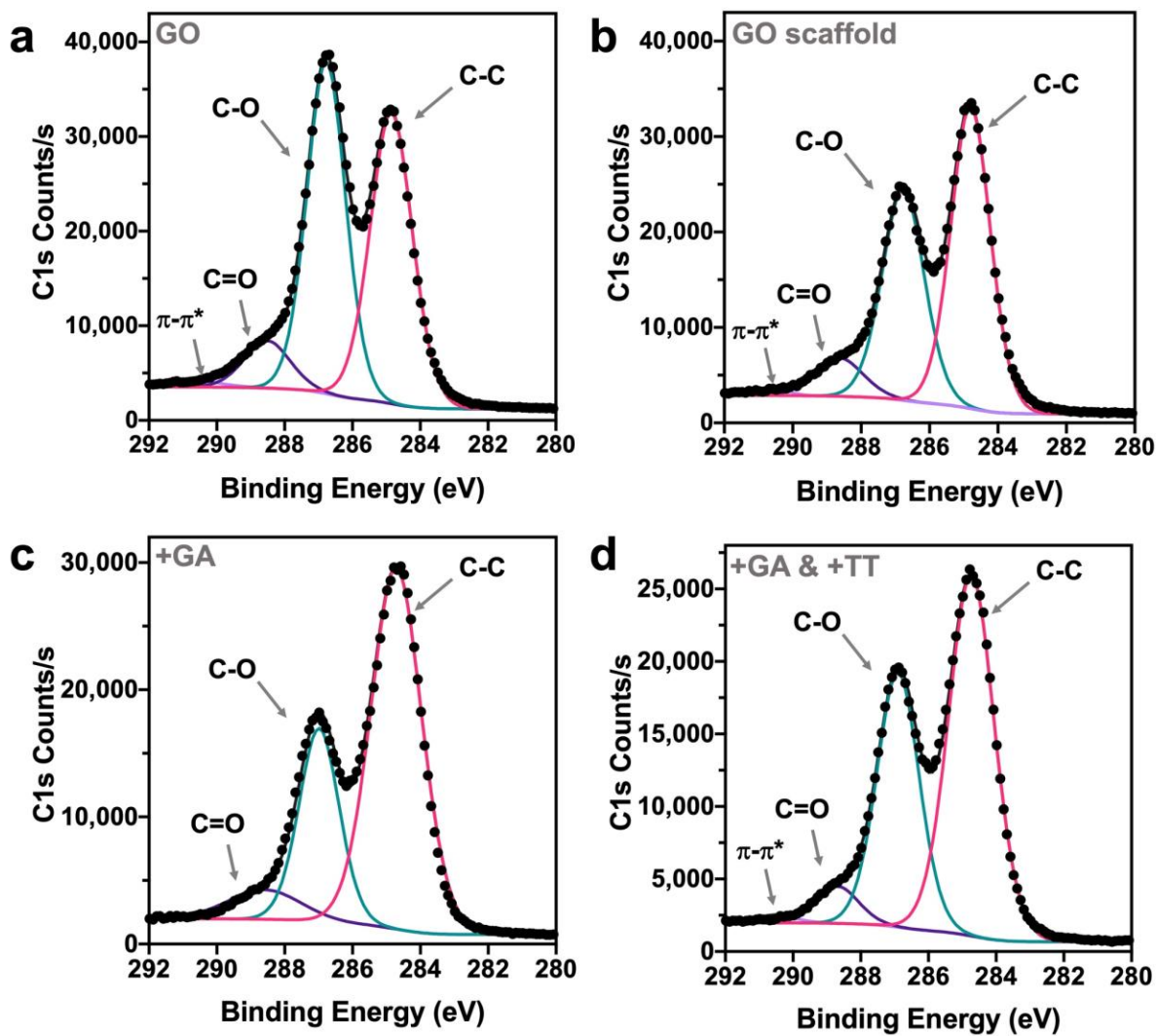


Figure 3.S10. XPS high resolution C1s spectra of (a) GO, (b) GO scaffold, (c) GO scaffold with GA crosslinking, and (d) GO scaffold with both crosslinking and thermal treatment.

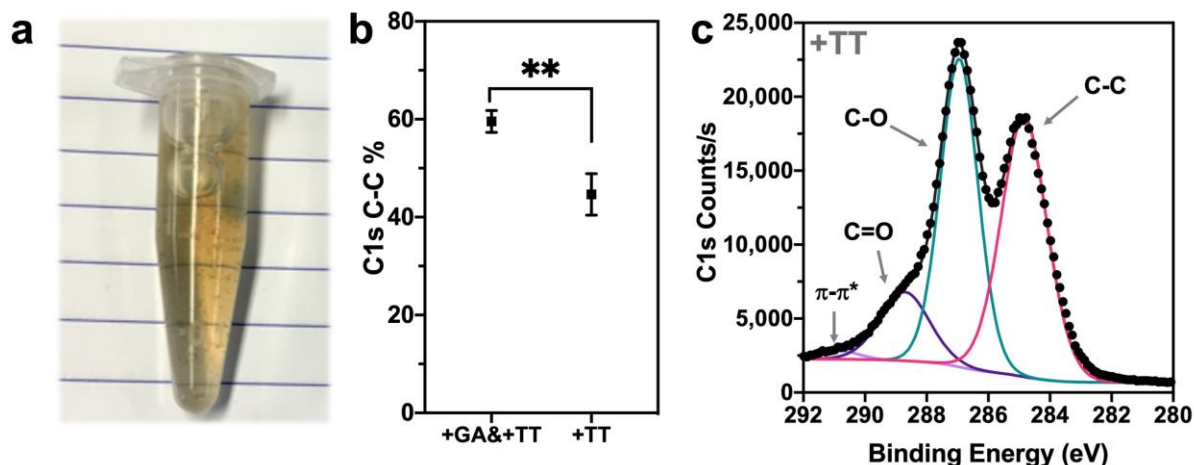


Figure 3.S11. (a) Digital picture showing thermal treated GO-C monolith without GA crosslinking immersed in DI water for 7 days. (b) Atomic percentages of C-C bonds measured from the high resolution C1s spectra (binding energy peak ~ 284.8 eV) of thermally treated scaffolds prepared with or without GA crosslinking. (c) XPS high resolution C1s spectrum of thermal treated GO scaffold without GA crosslinking. $n=3$ independent experiments, ** indicates significant difference with $0.001 < P < 0.01$.

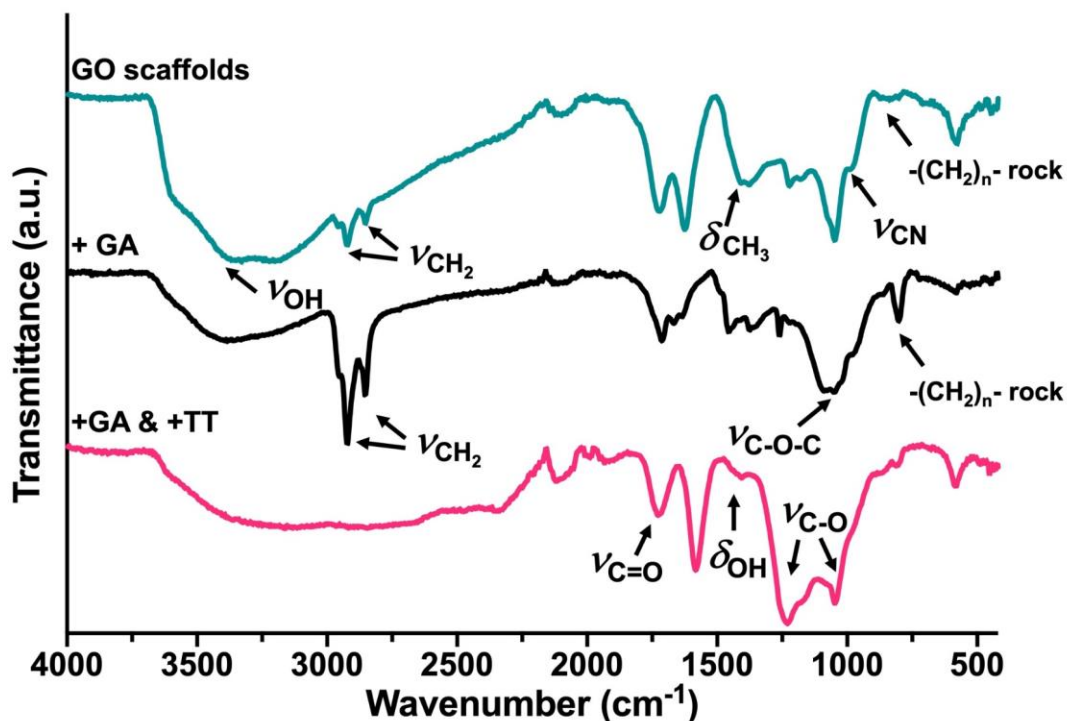


Figure 3.S12. FTIR spectra of GO scaffolds, GO scaffolds +GA, and GO scaffolds +GA & +TT.

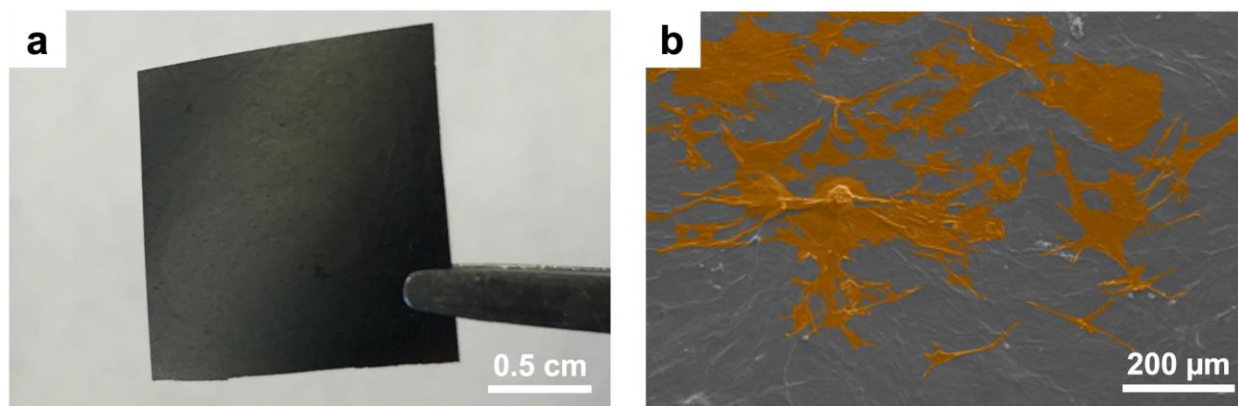


Figure 3.S13. (a) Digital photo of a 2D GO membrane. (b) SEM image of MSCs after 7 days of culture on a GO membrane. The cells are colored in orange.

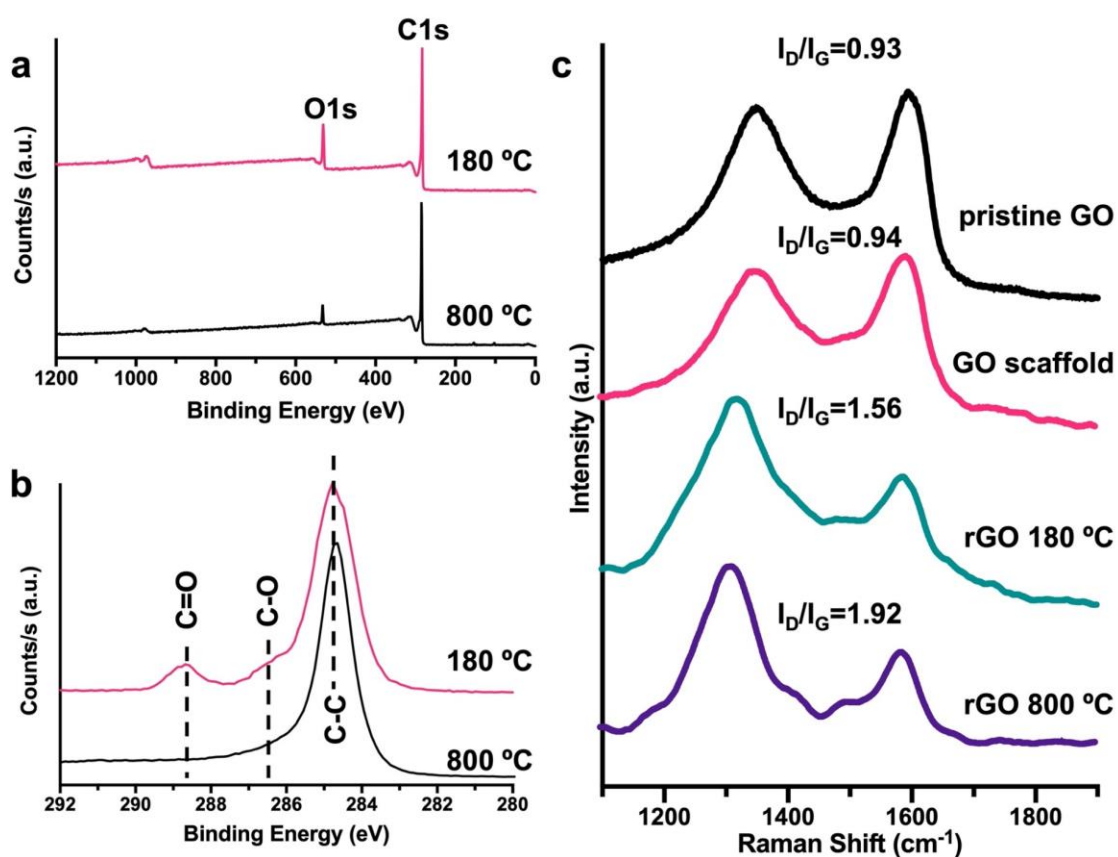


Figure 3.S14. (a) XPS survey spectra and (b) high resolution XPS C1s spectra of rGO scaffolds reduced at 180 °C and 800 °C. (c) Raman spectra of pristine GO, GO scaffold, and rGO scaffolds reduced at 180 °C or 800 °C.

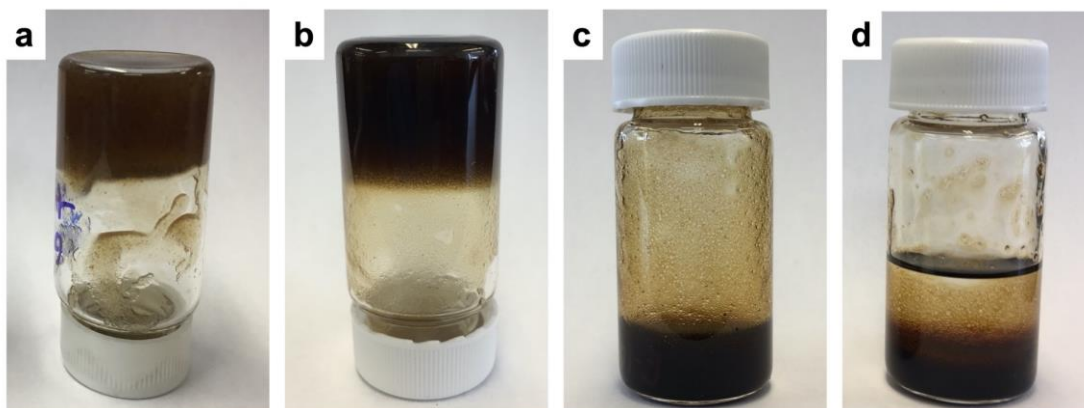


Figure 3.S15. Digital photos of GO based emulsions with 20 wt% PAA (a), 24 wt% HA (b), 10 wt% elastin (c-d), ratio respect to GO. The GO concentration in all composite aqueous suspensions is 6 mg mL^{-1} , the CTAB to GO ratio is 1 wt% in (a-b). Hexane is used in all samples, with $\phi_o=75\%$ (a, b and d) and $\phi_o=50\%$ (c).

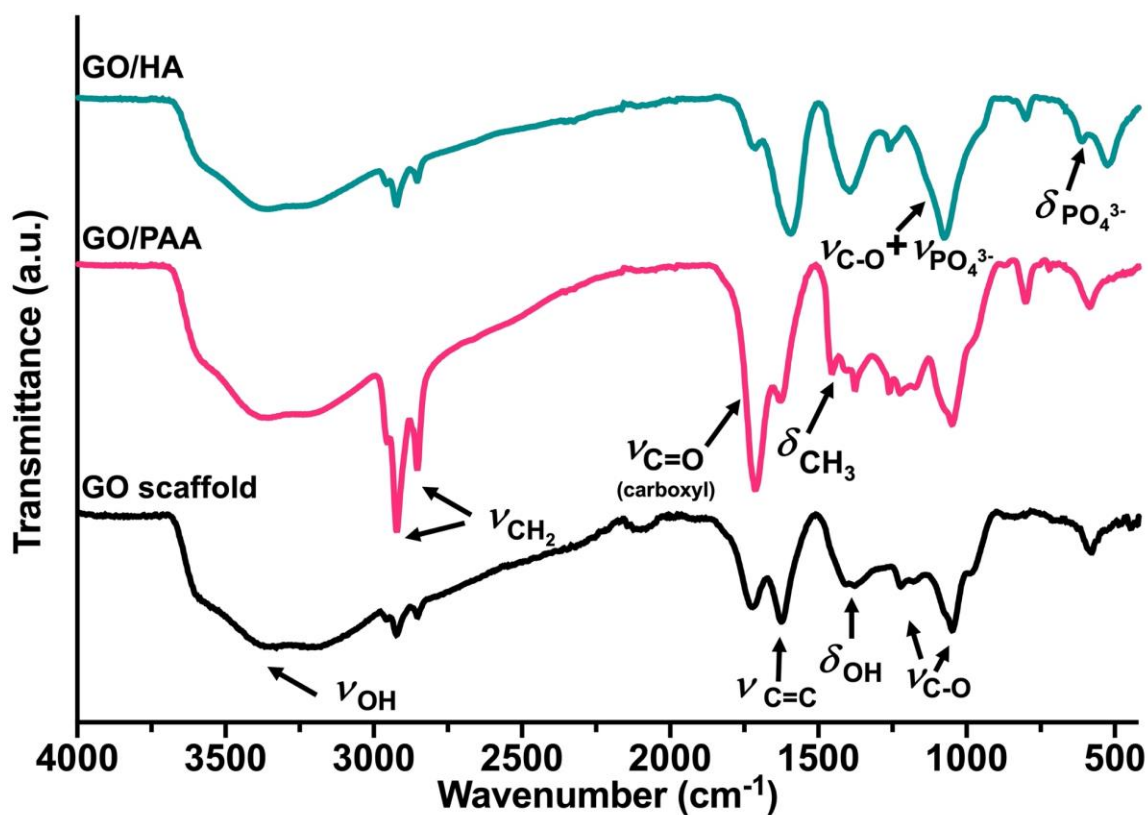


Figure 3.S16. ATR-FTIR spectra of scaffolds: GO, GO/PAA with 20 wt% PAA, and GO/HA with 24 wt% HA.

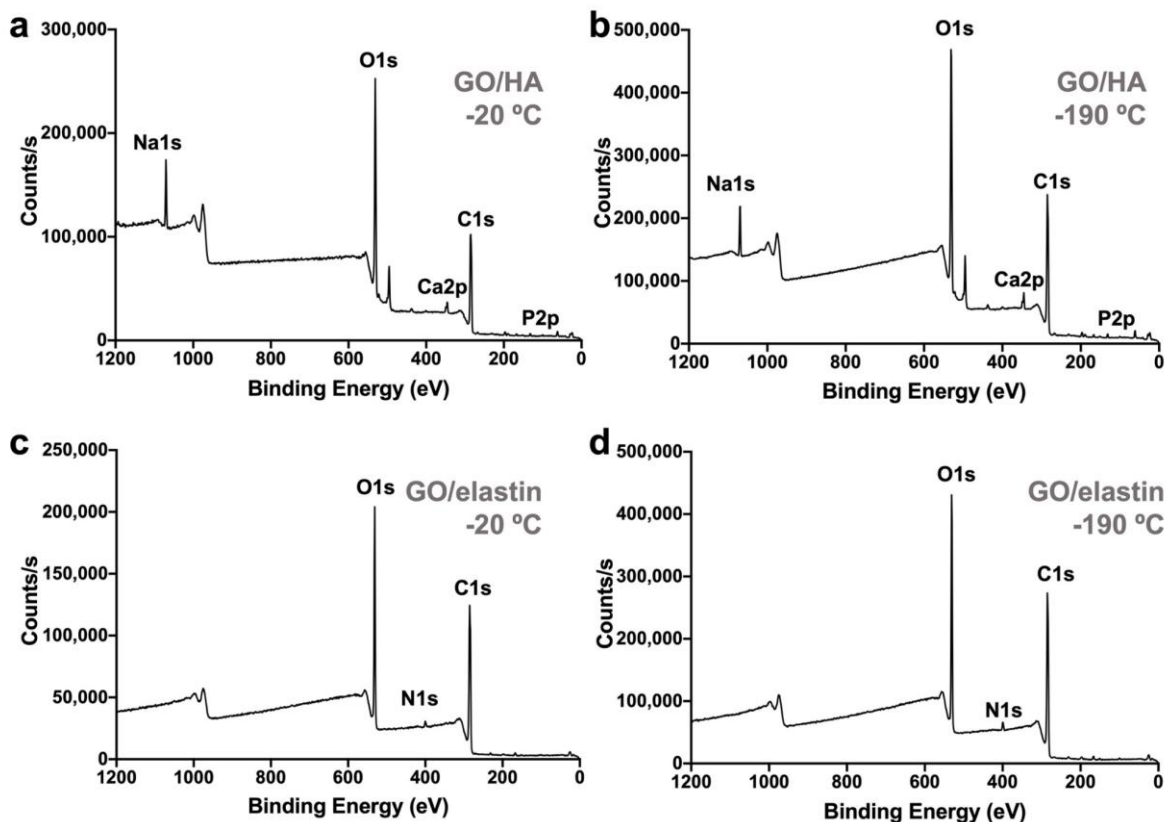


Figure 3.S17. XPS survey spectra of scaffolds: (a) GO/HA prepared at -20 °C, (b) GO/HA prepared at -190 °C, (c) GO/elastin prepared at -20 °C and (d) GO/elastin prepared at -190 °C. The presence of sodium is due to impurity from the HA preparation method [15].

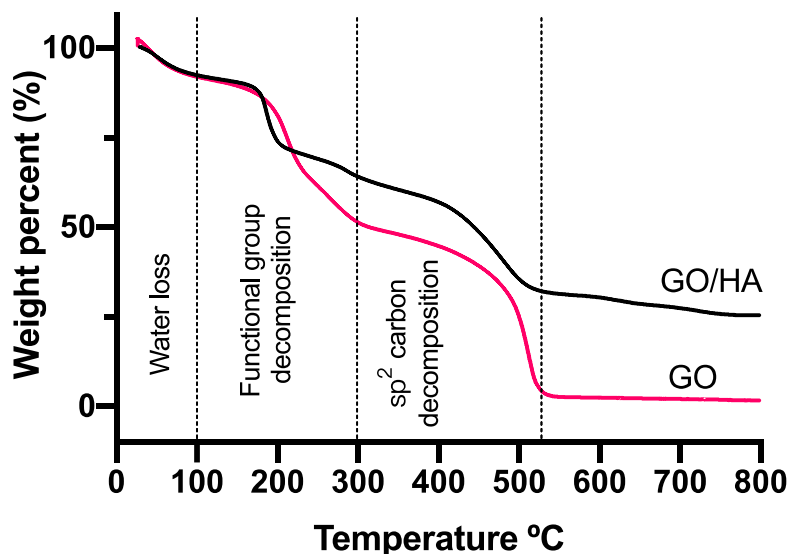


Figure 3.S18. TGA curves of GO and GO/HA scaffold under nitrogen atmosphere.

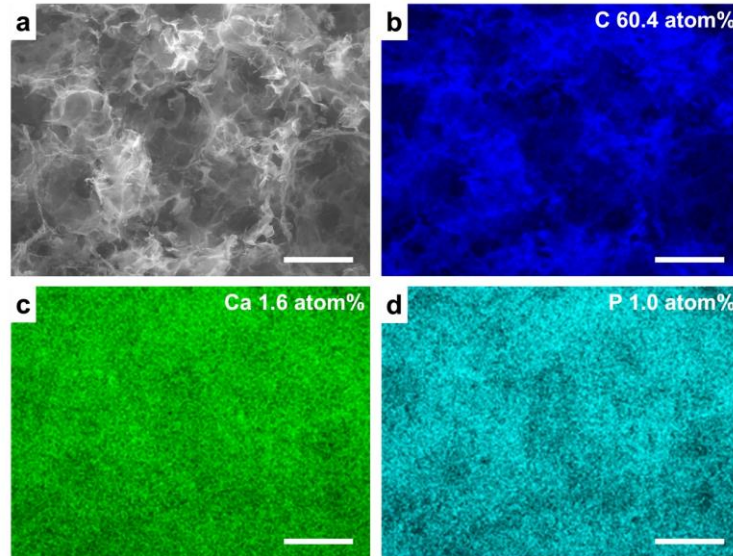


Figure 3.S19. SEM image (a) and EDS mappings of carbon (b), calcium (c) and phosphorus for GO/HA scaffold with 24 wt% HA relative to GO (prepared at $-20\text{ }^{\circ}\text{C}$). Scale bar=200 μm .

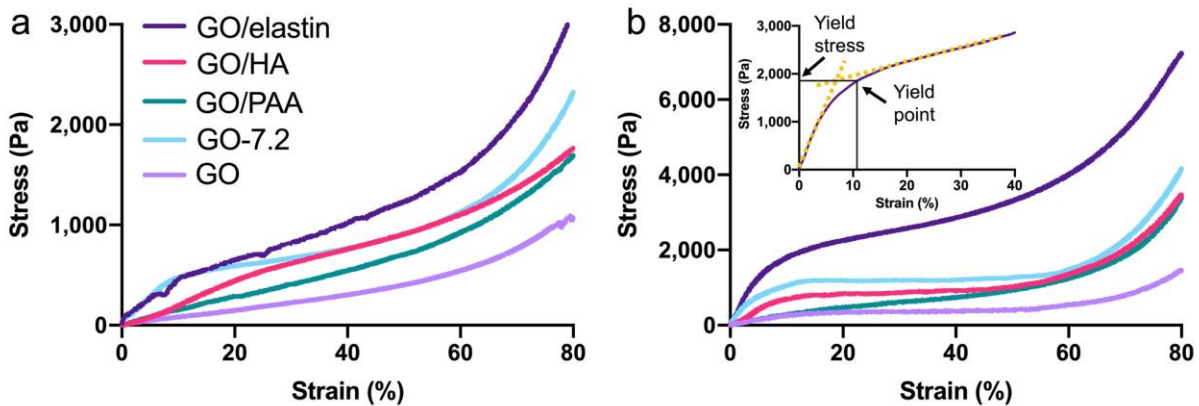


Figure 3.S20. Representative compressive stress-strain curves for GO (made from HIPE 6-75%) (orchid), GO-7.2 (made from HIPE 7.2-75%) (sky blue), GO/PAA (teal), GO/HA (magenta), and GO/elastin scaffolds (purple) prepared at (a) $-20\text{ }^{\circ}\text{C}$ and (b) $-190\text{ }^{\circ}\text{C}$. Linear regressions of the linear elastic and plastic plateau regimes are used to determine the yield point and yield stress (e.g., GO/elastin frozen at $-190\text{ }^{\circ}\text{C}$, inset).

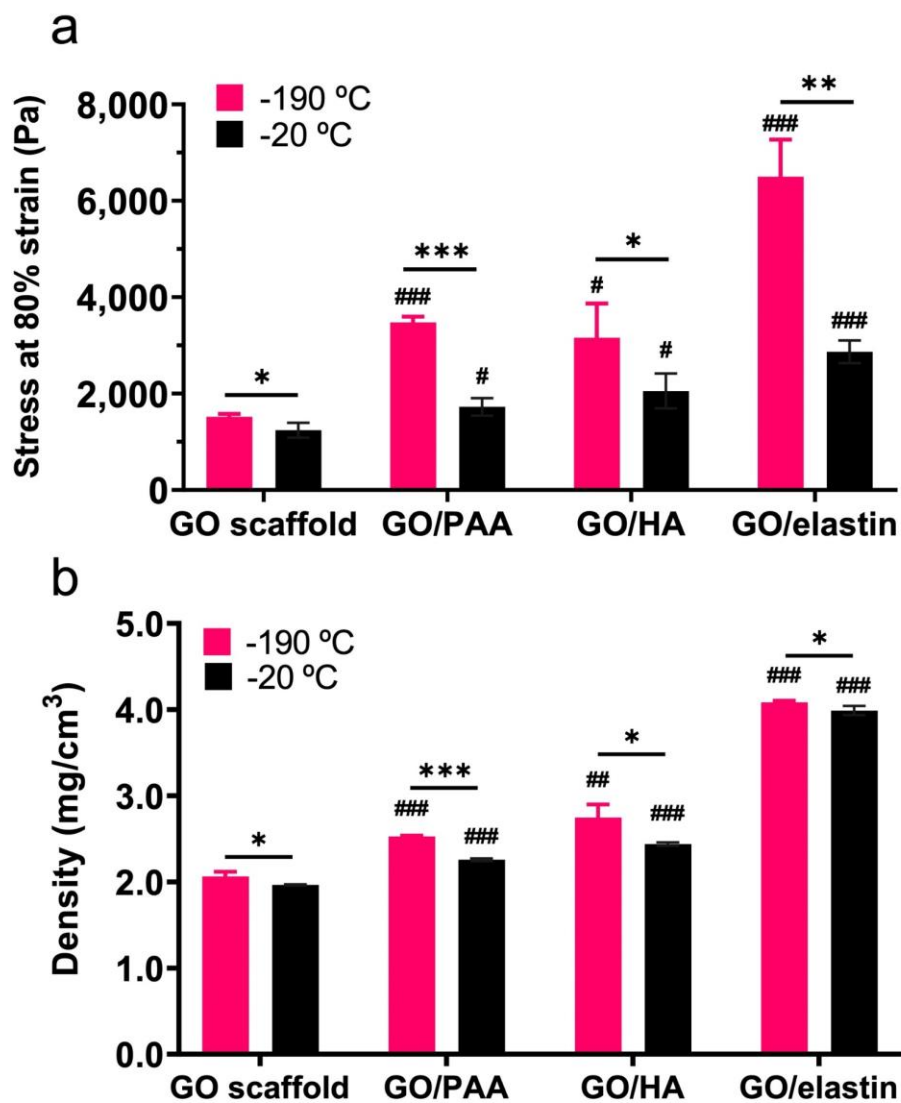


Figure 3.S21. Compressive stress at 80% strain (a) and density (b) of GO (made from HIPE 6-75%), GO/PAA, GO/HA and GO/elastin scaffolds frozen at -190 °C and -20 °C. The data represent the mean \pm standard deviation. The pound signs indicate statistically significant differences between the composite scaffolds and the corresponding GO scaffold frozen at the same temperature. The asterisks indicate statistically significant differences between the same type of scaffolds made at different temperatures. Statistical differences are calculated by the two-tailed Student's *t*-test, with * or #*P* < 0.05, ** or ##*P* < 0.01 and *** or ###*P* < 0.001, n = 3 independent experiments.

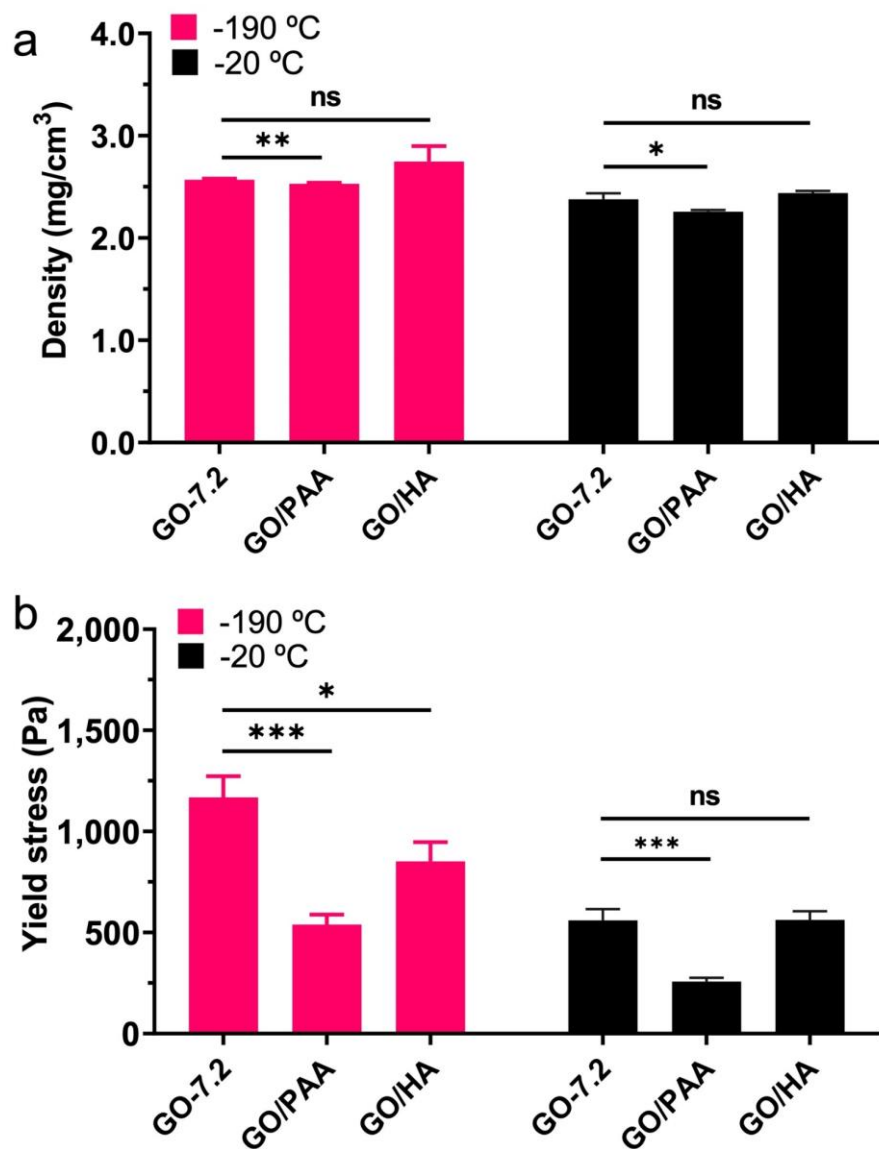


Figure 3.S22. Density (a) and yield stress (b) of GO-7.2 (made from HIPE 7.2-75%), GO/PAA, and GO/HA scaffolds frozen at -190 °C and -20 °C. The data represent the mean \pm standard deviation. The asterisks indicate statistically significant differences calculated by the two-tailed Student's *t*-test, with * $P < 0.05$, ** $P < 0.01$ and *** $P < 0.001$, $n = 3$ independent experiments.

Bridging text

In the previous chapter, we developed Pickering emulsion systems mainly based on GO and demonstrated that GO BTE scaffolds with interconnected pores in hierarchical size distributions can be obtained by a dual-templating strategy. In the next chapter, we further developed the GO Pickering emulsion systems, to obtain porous rGO with closed pores including catalytic cobalt oxide particles deposited inside the pores for selective seawater electro-oxidation. Our specific objectives were:

- I. To modify Co_3O_4 particles so that they can be stabilized in the oil phase of emulsions.
- II. To develop stable Pickering emulsions stabilized by GO containing Co_3O_4 particles in the oil droplets.
- VII. To obtain rGO/cobalt oxide electrodes through hydrothermal reduction, and characterize their physicochemical properties.
- VIII. To further develop the PCI-based methodology to visualize the pores and study the particle distribution inside the electrodes.
- III. To evaluate the selective electrocatalytic water oxidation performance of the rGO/cobalt oxide electrodes.

The findings of this study were published in *ACS Nano* in 2022:

Capilli, G.[§], **Chen, Y.**[§], Szkopek, T., & Cerruti, M. (2022). Selective Catalytic Electro-oxidation of Water with Cobalt Oxide in Ion Impermeable Reduced Graphene Oxide Porous Electrodes. *ACS nano*, 16(8), 12488-12499. [§]Authors contributed equally to this work.

4 Selective catalytic electro-oxidation of water with cobalt oxide in ion impermeable reduced graphene oxide porous electrodes

4.1 Abstract

The direct electrolysis of seawater is greatly inhibited by the oxidation of Cl^- to free chlorine, an undesirable, corrosive byproduct. To suppress the parasitic interference of Cl^- and any other ion, we developed a freestanding, electrically conducting, 3D macroporous reduced graphene oxide (rGO) scaffold with cobalt oxide particles selectively deposited on the internal walls of its closed pores (with an average diameter of $\sim 180 \mu\text{m}$). The pore walls act as membranes composed of stacked rGO flakes; the nanochannels between rGO layers (size $< 1 \text{ nm}$) are permeable to water and gases while preventing the diffusion of dissolved ions such as Cl^- . Due to this, the catalytic particles are selectively accessible to water molecules but not to ions, allowing electrolysis to occur without chlorine evolution. The electrodes developed exhibit a stable generation of O_2 from simulated seawater at pH 14, reaching a specific current density of up to 25 A g^{-1} during continuous electrolysis with 89–98% Faradaic efficiency, while chlorine generation is below 6 ppm h^{-1} , the sensitivity limit of the detection method employed. The strategy here proposed can be generalized to build electrodes that are inherently selective thanks to their architecture, with catalytically active particles loaded into closed pores with selective ion transport properties.

4.2 Introduction

The electro-oxidation of H_2O to O_2 is a crucial reaction to store energy as a green fuel such as H_2 [406]. This technology has not been widely applied yet because of its low efficiency. Its intrinsically high kinetic barrier requires the use of a catalyst to lower the applied potential [406]. Also, to generate H_2 sustainably on a large scale, abundant natural resources such as seawater must be employed as the electrolyte for water electrolysis. However, water electro-oxidation suffers from the competition of side reactions such as the oxidation of Cl^- to corrosive byproducts such as Cl_2 , HOCl , or ClO^- depending on the pH, hindering the direct use of seawater for water electrolysis [24],[25] and limiting this technology to water treated after energy-intensive desalinization processes.

The benchmark electrocatalysts based on noble metals (Pt, IrO_2) are not selective toward Cl^- , and their scarcity precludes their practical large-scale application [407]. Earth-abundant oxides and (oxy)hydroxides of first-row transition metals (FeOOH , NiOOH , Co_3O_4) are robust and show even higher catalytic performances in comparison to Pt/ IrO_2 [24],[408]. However, they too are not selective against Cl^- oxidation [24].

Non-precious-metal, heterogeneous electrocatalytic phases recently developed for selective seawater splitting include transition-metal hexacyanometalates [26] and oxidic metalates, such as cobalt phosphate and borate [25], which still require overly high overpotentials for large current densities and do not show long-term stability.

Under alkaline conditions, Cl^- oxidation in seawater occurs at a higher thermodynamic potential (+0.48 V) relative to that of water oxidation. A recent approach to prevent Cl^- (and Br^-) competition and catalyst poisoning in seawater consists of developing highly active catalytic phases for the oxygen evolution reaction that can reach large current densities at small

overpotentials ($\eta < 0.48$ V) and working in buffered alkaline media in a small range of potentials where chlorine evolution is thermodynamically impossible or kinetically disfavored against O₂ evolution [409]–[412]. These catalytic phases include layered bi-/trimetallic phosphides, hydroxides, sulfides, and nitrides grown in situ on Ni foam, such as Ni₂P–Fe₂P nanoplates [409], Fe–Ni(OH)₂/Ni₃S₂ nanoplates [410], core–shell NiFe/NiS_x [411], and core–shell NiMoN@NiFeN nanorods [412], which achieved record current densities (up to 1 A cm⁻²) at low applied voltages and long-term stability in alkaline seawater.

Another approach involves coating the catalyst with a thin layer of a negatively charged metal oxide, which significantly reduces Cl⁻ permeation toward the underlying catalytic sites [407],[413]. Other major challenges in seawater splitting are the presence of particulate, microbes and ions that are corrosive (Cl⁻) or that form insoluble precipitates (Mg²⁺), which can dissolve the catalyst or decrease its activity over time [24]. All of these factors are at the origin of the small number of electrocatalysts for seawater splitting reported so far.

In this work, we enhance the selectivity of water oxidation by preventing the transport of competitive species such as chloride ions to the catalytic sites of the electrode. We achieve selectivity by building a 3D rGO scaffold characterized by isolated pores with diameters of up to hundreds of micrometers that are internally decorated with an electrocatalyst for water oxidation, such as cobalt oxide nanoparticles [414], where the rGO pore walls act as selective membranes. We choose reduced graphene oxide (rGO) to build our porous electrode scaffold because it is electrically conductive and because the nanochannels between multiple stacked rGO flakes are permeable to water and gases but hinder the permeation of dissolved ions such as Cl⁻. The size of hydrated ions such as Cl⁻ is larger than the interplanar spacing between stacked rGO sheets

[27],[28]. This allows the electro-oxidation of water molecules to occur without competition from dissolved ions, thus avoiding the drawbacks of catalyst poisoning and corrosion.

To achieve this architecture, we use a combination of emulsion templating and hydrothermal reduction [152],[171]. GO flakes can stabilize emulsions due to their amphiphilicity arising from the presence of both hydrophobic sp^2 domains and hydrophilic oxygen-containing functional groups [8]. The GO flakes act as emulsifiers that assemble at the surface of the emulsion droplets; upon hydrothermal treatment, the GO-stabilized emulsions are transformed into self-standing rGO monoliths with pores of tunable size and interconnectivity [152],[171]. This combination allows achieving rGO scaffolds with closed pores and cobalt oxide nanoparticles loaded inside the pores. These features are crucial to achieve the selective electro-oxidation of water.

4.3 Results and discussion

4.3.1 General procedure of rGO/cobalt oxide electrode fabrication

We employ GO-stabilized hexane-in-water emulsion droplets to synthesize a macroporous rGO structure, where the cobalt oxide particles are introduced as a suspension in the hexane phase that templates the pores and the rGO flakes form a multilayer structure for the pore walls, endowing them with filtering capabilities.

To ensure the enclosure of Co_3O_4 particles inside the pores, we first functionalize the surface of Co_3O_4 particles with stearic acid (SA) to achieve Co_3O_4/SA nanoparticles with enhanced stability in the hexane phase. This is shown in **Figure 4.1a** and **Figure 4.S1**, where the Tyndall effect obtained upon shining a laser through the Co_3O_4/SA -hexane suspension indicates the presence of a stable dispersion of Co_3O_4 particles. Then, stable hexane-in-water emulsions of GO are generated by adjusting the amphiphilicity of GO with cetyltrimethylammonium bromide (CTAB). CTAB is a cationic surfactant that adsorbs on the negatively charged GO flakes and increases GO

hydrophobicity due to its alkyl chain [348], as shown in our previous study [46]. We then emulsify the $\text{Co}_3\text{O}_4/\text{SA}$ -containing hexane and the GO/CTAB-containing water. The resulting emulsions are stable (**Figure 4.1b**). The GO flakes stabilize the hexane/water interfaces, forming a layered GO wrapping around the emulsion droplets, while the $\text{Co}_3\text{O}_4/\text{SA}$ particles are trapped inside the hexane droplets. The subsequent hydrothermal treatment (HT) of the emulsion results in a freestanding rGO cobalt oxide hydrogel with macropores templated by the hexane droplets, containing Co_3O_4 particles inside (**Figure 4.1c**).

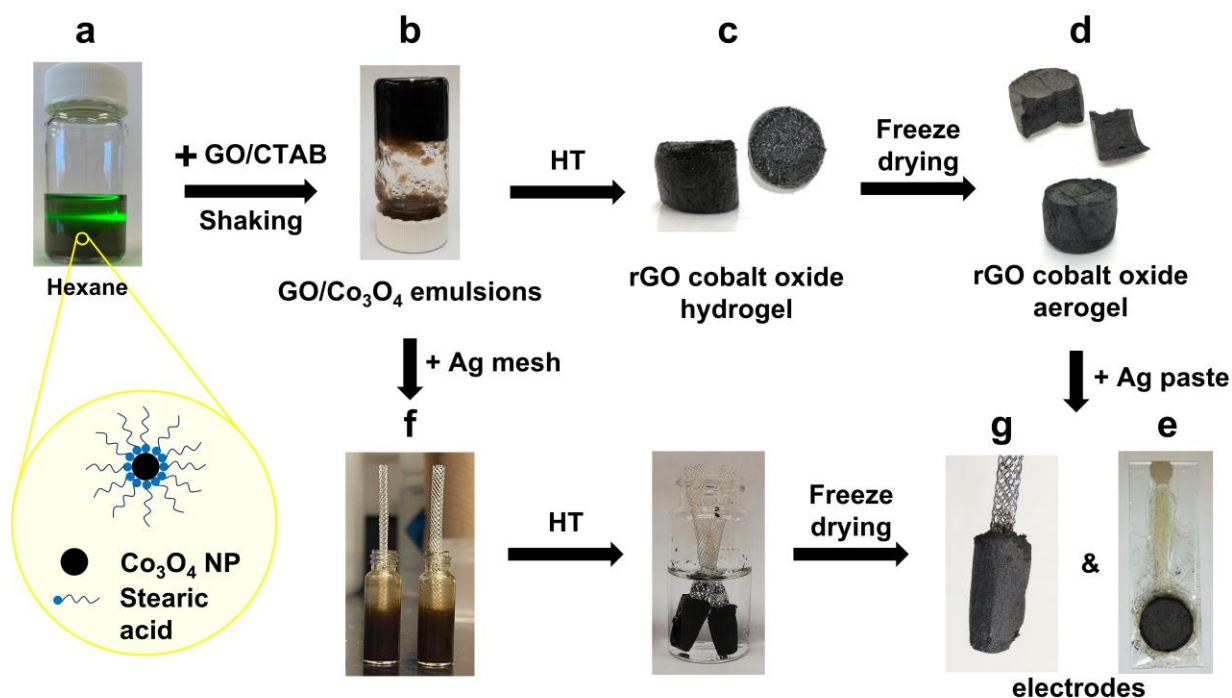


Figure 4.1. Overview of electrode fabrication. (a) Dispersion of $\text{Co}_3\text{O}_4/\text{SA}$ in hexane. The scattered green light shows the strong Tyndall effect of the dispersion. (b) Photograph of GO/ Co_3O_4 emulsions. (c) Photographs of rGO cobalt oxide hydrogels prepared after the HT of GO/ Co_3O_4 emulsions. (d) Photographs of rGO/cobalt oxide aerogels after freeze-drying the hydrogel in (c). (e) Electrode prepared by impregnating the bottom of the aerogel with Ag paint supported on glass. (f) Preparation of electrodes with integrated Ag mesh. The final result is shown in (g).

We fabricate two types of electrodes based on the same rGO microstructure. For the first type, we freeze-dry the rGO cobalt oxide hydrogel (**Figure 4.1d**) and then impregnate the bottom of the resulting aerogel with Ag paint supported on glass (**Figure 4.1e**), to connect it to the voltage source

for water electrolysis. The second type of electrode is obtained by placing an Ag mesh inside the GO/Co₃O₄ emulsions (**Figure 4.1f**) followed by HT and freeze-drying (**Figure 4.1g**). In this case, the tight contact formed between the Ag and the scaffold during the HT treatment allows the direct connection of a portion of exposed Ag mesh on top of the electrode to the voltage source. For comparison, we also prepare rGO electrodes supported by Ag paste excluding Co₃O₄ particles.

4.3.2 Modification and characterization of Co₃O₄ and GO emulsions

The surface of Co₃O₄ particles is modified with SA to enhance their stability in hexane. The functionalization with fatty acids, such as SA, increases the dispersion of nanoparticles in organic media [415]–[417]. The carboxylic acid heads of the SA can interact with Co₃O₄ through hydrogen bonding, and the alkyl chain of SA can facilitate the stabilization of Co₃O₄/SA in the hexane.

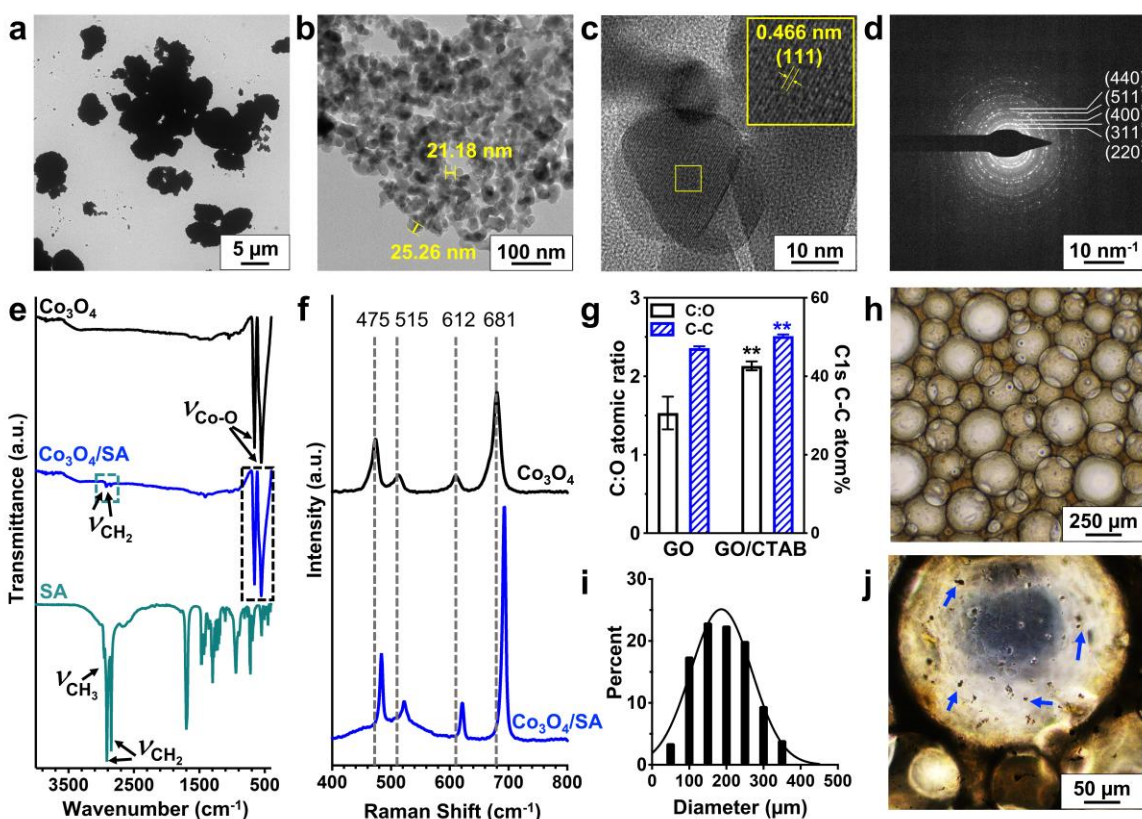


Figure 4.2. Characterization on Co₃O₄ and GO modifications, as well as GO emulsions. (a–c) TEM images of Co₃O₄/SA particles at different magnifications. In (b), the diameter of representative Co₃O₄ particles is indicated. Inset in (c): magnification of the area highlighted by the yellow square from an HRTEM analysis. (d) SAED patterns obtained from Co₃O₄/SA particles

reflecting the diffraction bands of the cubic Co_3O_4 lattice, whose most prominent zone axes are labeled and indicated by solid lines. (e) FTIR spectra of Co_3O_4 , $\text{Co}_3\text{O}_4/\text{SA}$, and SA. (f) Raman spectra of Co_3O_4 and $\text{Co}_3\text{O}_4/\text{SA}$ particles. (g) C:O atomic ratios from XPS survey scans and atomic percentage of C–C bonds (binding energy ~ 284.8 eV) from XPS high-resolution C 1s spectra of GO and GO/CTAB. The asterisks indicate statistically significant differences between GO and GO/CTAB calculated by the two-tailed Student's t test (** $P < 0.01$). (h) Optical microscopy image of hexane-in-water $\text{GO}/\text{Co}_3\text{O}_4$ emulsions. (i) Emulsion droplet size distribution of $\text{GO}/\text{Co}_3\text{O}_4$ emulsions ($n = 200$ droplets) and nonlinear regression based on a Gaussian model. (j) Optical microscopy image of $\text{GO}/\text{Co}_3\text{O}_4$ emulsions at higher magnification, with aggregates of $\text{Co}_3\text{O}_4/\text{SA}$ particles being highlighted by blue arrows.

We use transmission electron microscopy (TEM) to observe the pristine Co_3O_4 particles in water and the $\text{Co}_3\text{O}_4/\text{SA}$ particles in hexane (**Figure 4.2a–d** and **Figure 4.S2**). Both samples show micrometer-sized aggregates composed of nanoparticles, and the modification does not change the morphology of the nanoparticles (**Figure 4.2a–c** and **Figure 4.S2a–c**). An high-resolution TEM (HRTEM) analysis of Co_3O_4 and $\text{Co}_3\text{O}_4/\text{SA}$ particles (**Figure 4.2c** and **Figure 4.S2c**) shows that they are both composed of nanocrystallites in a so-called preoctahedral shape [418], with (220) and (111) diffraction planes relative to the Co_3O_4 cubic phase being readily identifiable (JCPDS 00-42-1467). The selected area electron diffraction (SAED) patterns (**Figure 4.2d** and **Figure 4.S2d**) confirm that the Co_3O_4 crystalline domains are not affected by the surface modification process.

The attenuated total reflection Fourier-transform infrared (ATR-FTIR) spectra of Co_3O_4 , SA, and $\text{Co}_3\text{O}_4/\text{SA}$ (**Figure 4.2e**) further confirm the successful modification of Co_3O_4 . The spectrum of $\text{Co}_3\text{O}_4/\text{SA}$ shows two bands associated with stearic acid, i.e. $\nu_{\text{as}}(\text{CH}_2)$ at 2917 cm^{-1} and $\nu_{\text{s}}(\text{CH}_2)$ at 2848 cm^{-1} [417],[419], along with the $\nu(\text{Co–O})$ bands related to Co_3O_4 at 560 and 660 cm^{-1} (the first band is attributed to an OB_3 vibration, while the second is ascribed to an ABO_3 vibration, where A denotes Co^{2+} ions with tetrahedral coordination and B denotes Co^{3+} ions with octahedral coordination) [420]–[422]. The Raman spectrum of Co_3O_4 particles (**Figure 4.2f**) shows the characteristic bands of Co_3O_4 at 515 and 612 cm^{-1} and broad bands associated with Co_3O_4 from

460 to 482 cm^{-1} and from 672 to 690 cm^{-1} , which are consistent with agglomerated Co_3O_4 nanoparticles [423],[424]. After SA modification, a blue shift of all the Raman peaks is observed (**Figure 4.2f**). This phenomenon was previously observed on metal oxide nanoparticles coated by a surfactant such as SA [425] and explained by the surface strain caused by the surfactant resulting in closer packing of the surface atoms and higher vibrational frequencies [425]. This further confirms that the surface modification of Co_3O_4 with SA is successful. We also use X-ray photoelectron spectroscopy (XPS) to obtain high-resolution spectra of Co 2p and characterize the oxidation state of Co_3O_4 particles. This will be discussed in the following section.

In summary, these results show that our first objective to create a stable suspension of Co_3O_4 particles in hexane is achieved, and the $\text{Co}_3\text{O}_4/\text{SA}$ particles can be used for the preparation of GO/ Co_3O_4 emulsions.

The GO flakes were characterized through scanning electron microscopy (SEM) (**Figure 4.S3a**). The lateral dimensions of the flakes are presented as the effective diameter of a circle with an area equal to the flake area in the range between 5 and 40 μm (**Figure 4.S3**). To obtain stable emulsions, the GO is modified with CTAB (CTAB mass equal to 1.5 wt % of GO) [46]. The surface composition of GO and GO/CTAB measured by XPS are shown in **Figure 4.2g**, **Table 4.S1** and **Figure 4.S4**. The initial GO flakes have a C:O atomic ratio of 1.5 ± 0.2 . After modification, the C:O ratio significantly increases to 2.10 ± 0.05 (** $P < 0.01$), which confirms the addition of alkyl chains from CTAB. High-resolution C 1s spectra also show a significant increase in C–C bonds on the GO/CTAB (50.2 ± 0.4 atom %) in comparison to GO (47.2 ± 0.5 atom %) (** $P < 0.01$) (**Figure 4.2g** and **Figure 4.S4**). These results are consistent with our previous study, showing the successful modification of GO with CTAB [46]. We have also analyzed the Raman spectra of GO; this will be discussed in the following section.

The GO/Co₃O₄ emulsions are prepared by mixing the Co₃O₄/SA-containing hexane phase and the GO/CTAB-containing water phase, with an oil to water volume ratio of 2:1. The resulting emulsions are stable without a phase separation of oil and water (**Figure 4.2h**). On the basis of an analysis of optical microscopy images, the GO/Co₃O₄ emulsions have a mean droplet diameter of $190 \pm 70 \mu\text{m}$ (**Figure 4.2i**). Aggregates of Co₃O₄/SA particles are visible as well, suggesting that the particles are present inside the emulsion droplets (**Figure 4.2j**).

4.3.3 Structural and physicochemical characterization of rGO/CoOx aerogels

After the HT process and freeze-drying, we obtain freestanding aerogels based on rGO and cobalt oxide: namely, rGO/CoOx aerogels. We use the nomenclature “CoOx” to indicate that the oxide phase after HT may differ from that of the pristine Co₃O₄ particles. SEM images of these aerogels (**Figure 4.3a,b**) show the pores templated from the GO emulsion droplets. The pores have a mean diameter of $177 \pm 65 \mu\text{m}$, in good agreement with the emulsion droplet diameter (**Figure 4.S5** and **Figure 4.2i**), as expected. The CoOx particles are present mostly as aggregates on the pore walls of the rGO network, as shown in **Figure 4.3b,c**. X-ray energy-dispersive spectroscopy (EDS) maps of the distribution of carbon, oxygen, and cobalt (**Figure 4.S6**) indicate that these elements are homogeneously present in the sample and confirm the presence of cobalt–oxygen-containing particles throughout the rGO scaffolds. Although the particles seem to be especially present along the pore walls, their exact location is difficult to determine with precision by EDS. The rGO aerogels produced from GO emulsions without Co₃O₄/SA particles in the hexane phase have a similar porous structure but there is no evidence of cobalt-containing particles (**Figure 4.S7**).

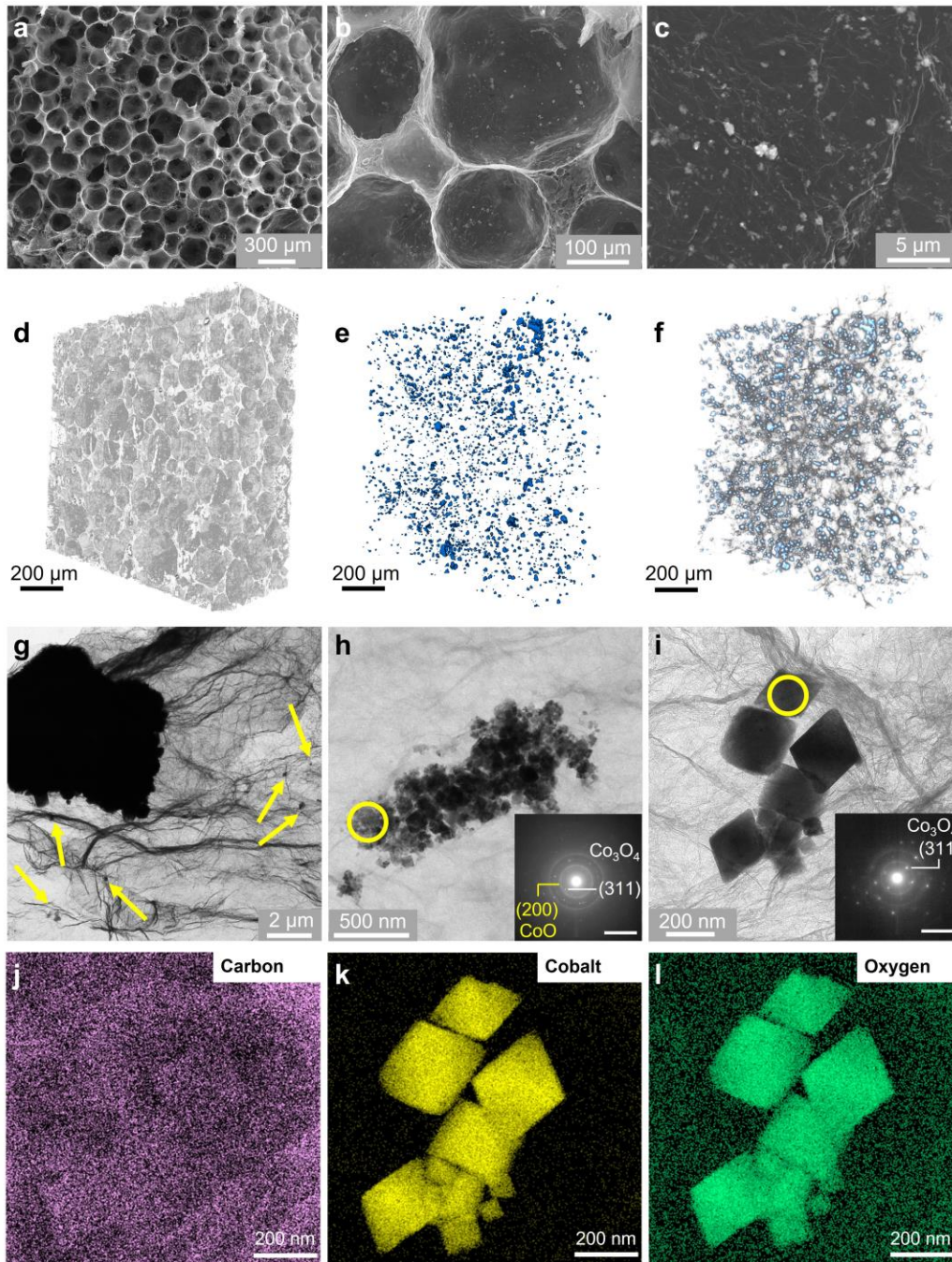


Figure 4.3. Structural characterization of the rGO/CoOx scaffold through SEM, PCI, and TEM. (a–c) SEM images of rGO/CoOx aerogels at different magnifications. (d–f) 3D reconstruction maps of rGO/CoOx aerogel obtained through synchrotron-based PCI, showing (d) the overall structure, (e) the CoOx particles (blue), and (f) the distribution of CoOx particles (blue) at the boundaries of rGO pores (gray), on the basis of the color mapping. (g–i) TEM images of the rGO/CoOx aerogel showing CoOx particles of different sizes embedded in rGO flakes. CoOx particles with sizes in the nanometer range are indicated by yellow arrows. Insets: SAED patterns of the areas highlighted by yellow circles in (h) and (i). A detailed identification is shown in **Figure 4.S9**. Scale bars: 10 nm^{-1} . (j–l) EDS elemental maps of the CoOx particles shown in (i).

To better understand the spatial relationship between the CoOx particles and rGO, we employed phase contrast X-ray imaging (PCI) with a synchrotron light source (see Methods) to further investigate the internal microstructure of the rGO/CoOx aerogels. This technique analyzes the distribution of transmitted X-rays including both the absorption and the interference between incident X-rays and forward-scattered X-rays at the boundary of materials. PCI is well suited to image light (i.e., low atomic number) objects that cannot be analyzed with traditional X-ray absorption techniques such as computed tomography [46],[355].

Due to the higher X-ray absorption of cobalt oxide in comparison to rGO, the CoOx particles generate a contrast higher than that of the rGO network (see **Figure 4.3d,e** and **Figure 4.S8** and a related description for a detailed explanation of this method). PCI image analysis is performed to construct false color maps with rGO pore boundaries shown in gray and CoOx particles shown in blue. The resulting image (**Figure 4.3f**) shows that the particles surround the pore walls of the rGO network, which agrees with the SEM images (**Figure 4.3b,c** and **Figure 4.S6c**) as well as the optical images of the emulsion (**Figure 4.2j**). This successful enclosure of CoOx particles inside rGO pores throughout the entire aerogel is an important feature for the selectivity of the electrodes.

By analyzing over 12000 CoOx particles visualized through PCI, we calculate the equivalent sphere diameter of the particle aggregates (see **Figure 4.S8** and a related description for a detailed explanation of this method) and find values ranging from a few micrometers up to 25 μm (**Figure 4.S8**). This result further confirms optical microscopy and SEM images showing that the particles are present as aggregates (**Figure 4.2a,b,j** and **Figure 4.3b,c**).

Because of the resolution limitation of SEM and PCI, TEM is employed to analyze nanoscale details of the CoOx particles in rGO/CoOx scaffolds. TEM images reveal that, along with the large aggregates, there are smaller aggregates in the sub-micrometer size range (**Figure 4.3g-i**). These

aggregates are composed of both nanoparticles like those found in the pristine Co_3O_4 sample (compare **Figure 4.S2b** and **Figure 4.3h**) and octahedral nanoparticles (**Figure 4.3i**). The SAED patterns of the two types of aggregates, reported as insets of **Figure 4.3h,i** and **Figure 4.S9**, reveal different crystal structures. The d spacings obtained from the most intense diffraction bands in the SAED patterns of the aggregate in **Figure 4.3h** are consistent with the coexistence of cubic Co_3O_4 (JCPDS 00-42-1467) and cubic CoO (JCPDS 00-043-1004) crystalline phases, while those of the nanoscopic octahedra in **Figure 4.3i** are indexed to the pure cubic phase of Co_3O_4 (more details are given in **Figure 4.S9**). Under a high-angle annular dark-field imaging mode (HAADF), the particles appear brighter in comparison to the rGO flakes in the background (**Figure 4.S10a, b**), since Co has an atomic number larger than those of C and O. EDS mapping of these two types of aggregates confirm carbon, cobalt, and oxygen as the main elemental components and the particle deposition on the rGO flakes (**Figure 4.3j-l** and **Figure 4.S10**).

We further characterize the rGO/CoOx aerogel by XPS to understand the composition of the CoOx particles and the degree of reduction of GO upon HT. XPS surveys of rGO/CoOx first confirm the presence of cobalt (2.0 ± 0.2 atom %, **Table 4.S2** and **Figure 4.S11**). After HT, the carbon atomic percentage significantly increases from $60 \pm 2\%$ (**Table 4.S1**) in GO to $82 \pm 2\%$ in rGO ($***P < 0.001$), and $79 \pm 2\%$ in rGO/CoOx ($***P < 0.001$) (**Table 4.S2** and **Figure 4.S11**), while the C atom % between rGO and rGO/CoOx shows no significant difference (**Figure 4.4a**). These XPS survey results confirm the reduction of GO and show a similar reduction degree between rGO and rGO/CoOx. Given the presence of oxygen in the cobalt oxide particles in rGO/CoOx after HT, the C:O ratio of pristine GO is compared with that of the control rGO aerogels without CoOx particles to evaluate the reduction degree, and it significantly increases from 1.5 ± 0.2 to 11 ± 2 , respectively ($***P < 0.001$) (**Figure 4.2g** and **Figure 4.4a**). The high-resolution C

1s XPS spectra of rGO and rGO/CoO_x (**Figure 4.S11**) confirm the removal of oxygen-containing groups during the HT, showing a significant reduction of C=O and C–O peaks in comparison to pristine GO (**Figure 4.S4**) and a significant increase in C–C bonds on the rGO (68 ± 2 atom %, $***P < 0.001$) and rGO/CoO_x (65 ± 1 atom %, $***P < 0.001$) in comparison to GO (**Figure 4.2g**, **Figure 4.S4** and **Figure 4.S11**); again, no significant differences are found between rGO and rGO/CoO_x (**Figure 4.4a**). These results are comparable to those in previous work, confirming successful reduction through HT [426],[427].

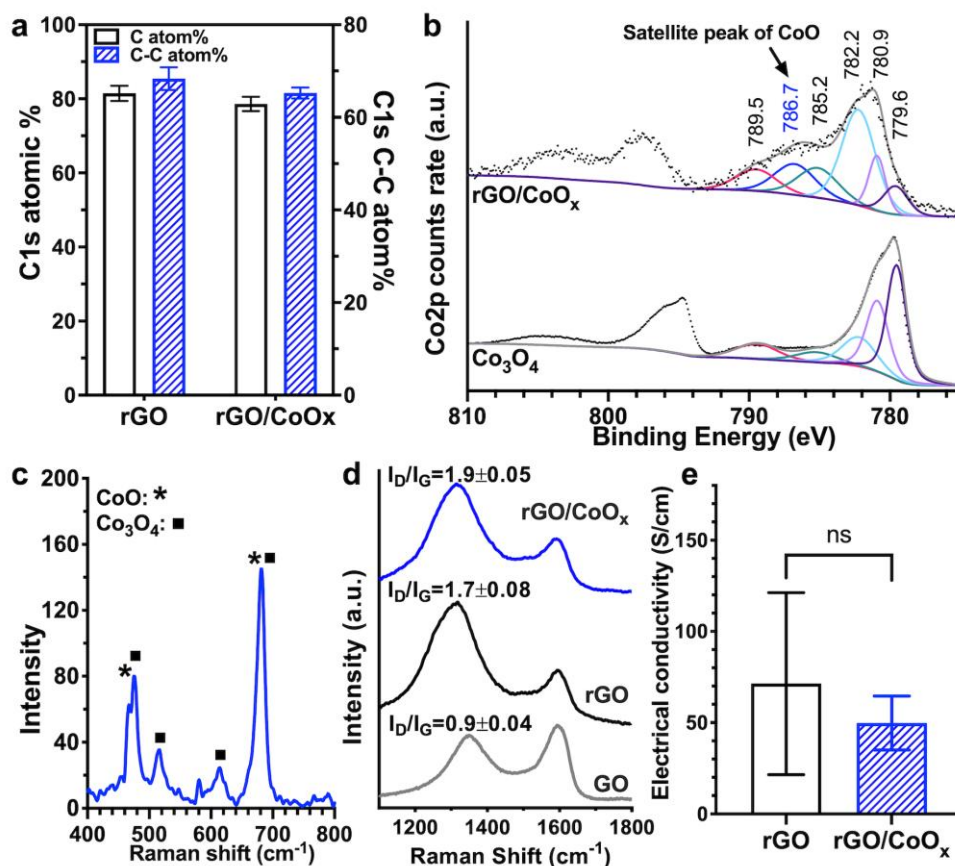


Figure 4.4. Physicochemical characterization of the electrodes. (a) Atomic percentage of C from XPS survey scans and atomic percentage of C–C bonds from XPS high-resolution C 1s spectra (binding energy ~ 284.8 eV) of rGO and rGO/CoO_x. No significant differences are found between the two samples ($P > 0.05$). (b) High-resolution XPS Co 2p spectra of the Co₃O₄ particles and rGO/CoO_x. (c) Raman spectrum of rGO/CoO_x showing peaks from both CoO and Co₃O₄. (d) Raman spectra of GO, rGO, and rGO/CoO_x with the corresponding I_D/I_G values. (e) Electrical conductivity of rGO and rGO/CoO_x aerogels. No statistically significant difference is found between rGO/CoO_x and rGO aerogels, as calculated by a two-tailed Student's *t* test.

The high-resolution XPS Co 2p spectra of pristine Co₃O₄ particles and rGO/CoO_x are characterized by spin-orbit-split 2p_{1/2} and 2p_{3/2} components (**Figure 4.4b**), which both contain the same chemical information; thus, we only fit the Co 2p_{3/2} component. The spectra of the pristine Co₃O₄ particles show the characteristic components at binding energies of 779.6, 780.9, 782.2, 785.2, and 789.5 eV, with the component at 779.6 eV being the most intense. This profile agrees with the Co 2p spectra of Co₃O₄ in the NIST XPS database [428] and previous literature [429].

Similar components are found in the rGO/CoO_x spectrum; however, the most intense peak is that at 782.2 eV. Moreover, an additional satellite peak appears at 786.7 eV. This peak was attributed to Co(II) in CoO by Biesinger *et al* [429]. Even though the satellite peak of CoO was reported at different binding energies by other authors, in all cases the presence of CoO was always indicated by a pronounced peak between 786 and 789 eV [428]–[431], as we find in the rGO/CoO_x spectra. These results are in agreement with those of TEM (**Figure 4.3h** and **Figure 4.S9**), showing the presence of some CoO after HT in the rGO/CoO_x samples, and are further confirmed by FTIR (**Figure 4.S12**) and Raman (**Figure 4.4c**, showing not only the same bands found in pristine Co₃O₄ particles but also an additional band at 468 cm⁻¹ that is typical of the CoO phase [420],[424]).

The Raman spectra of rGO and rGO/CoO_x in the higher-wavenumber region (**Figure 4.4d**) both exhibit increased D band (~1340 cm⁻¹) to G band (~1580 cm⁻¹) intensity ratios in comparison to that of GO. During the hydrothermal reduction of GO, the removal of oxygen-containing groups restores the sp² domains and decreases the defect density. The I_D/I_G ratio has a nonmonotonic dependence with point defect density [380],[384], and in samples with high defect density such as GO and rGO, the I_D/I_G ratio increases as the defect density decreases [381]–[383].

When they are taken together, Raman, XPS, and FTIR results confirm the successful reduction of GO in rGO/CoO_x and rGO samples and the restoration of sp² domains to increase the electrical

conductivity of these electrodes. Electrical conductivities measured using a four-point van der Pauw method are equal to $70 \pm 50 \text{ S cm}^{-1}$ for rGO and $50 \pm 20 \text{ S cm}^{-1}$ for rGO/CoOx samples (**Figure 4.4e**), comparable with those in previous reports [432],[433].

4.3.4 Selective electrocatalytic water oxidation on rGO/CoOx electrodes

The CoOx particles loaded inside the rGO scaffolds are catalysts for multistep electrochemical oxidations, such as that of water to O_2 in alkaline media [406],[434]. We investigate the two types of cylindrical rGO/CoOx electrodes described in **Figure 4.1**. The first type is connected to a potentiostat through a thin layer of Ag paste and will be referred to as Ag_p/rGO/CoOx; the second type is connected through a cylindrical Ag mesh and will be referred to as Ag_m/rGO/CoOx. The performance of the rGO/CoOx electrodes as catalysts for water oxidation is shown in **Figure 4.5**.

The two rGO/CoOx electrodes and two control electrodes, i.e. the bare Ag support and a rGO aerogel deposited on the Ag support, are immersed in simulated seawater buffered at pH 14 (NaCl 0.5 M + KOH 1 M) and polarized between 0.0 and +1.4 V vs Ag/AgCl at a scan rate of 10 mV s^{-1} , to first assess their electrocatalytic behavior under a positive bias (**Figure 4.5a**). Linear sweep voltammetry (LSV) scans recorded on the bare Ag support show a first peak centered at +0.3 V vs Ag/AgCl, due to Ag oxidation to Ag_2O , followed by an anodic current onset between +0.7 and +0.8 V, which results from the progressive oxidation to the Ag_2O_3 phase. In the potential range explored, there is no clear onset for the water or Cl^- oxidation reactions, which are shifted toward a more positive bias. The thermodynamic onsets for the oxidation of OH^- to O_2 and of Cl^- to ClO^- at pH 14 are 0.20 and 0.69 V vs Ag/AgCl, respectively. The high overpotential observed indicates that silver oxide is not an efficient catalyst for either of these reactions. Anodic sweeps of the rGO aerogel deposited on the Ag support show a capacitive behavior with no evidence of Faradaic

processes related to either water or Cl^- oxidation. No evolution of gas bubbles is observed on either control electrode during the anodic sweeps.

LSV scans of both rGO/CoOx electrodes are characterized by two small broad peaks centered at +0.15 and +0.55 V vs Ag/AgCl (indicated by arrows in **Figure 4.5a**), superimposed on the capacitive background of the rGO scaffold. These peaks are ascribed to the oxidation of the Co(II) oxide phase to the Co(III) oxide and CoOOH phases and to the formation of Co(IV) centers (CoO₂/CoOOH redox couple), respectively [406],[435]–[438], which are crucial intermediates during catalytic water oxidation to O₂. In both electrodes, the significant increase in the anodic current density at +0.75 V vs Ag/AgCl corresponds to the onset of the water oxidation reaction and is accompanied by the evolution of gas bubbles on the electrode surface.

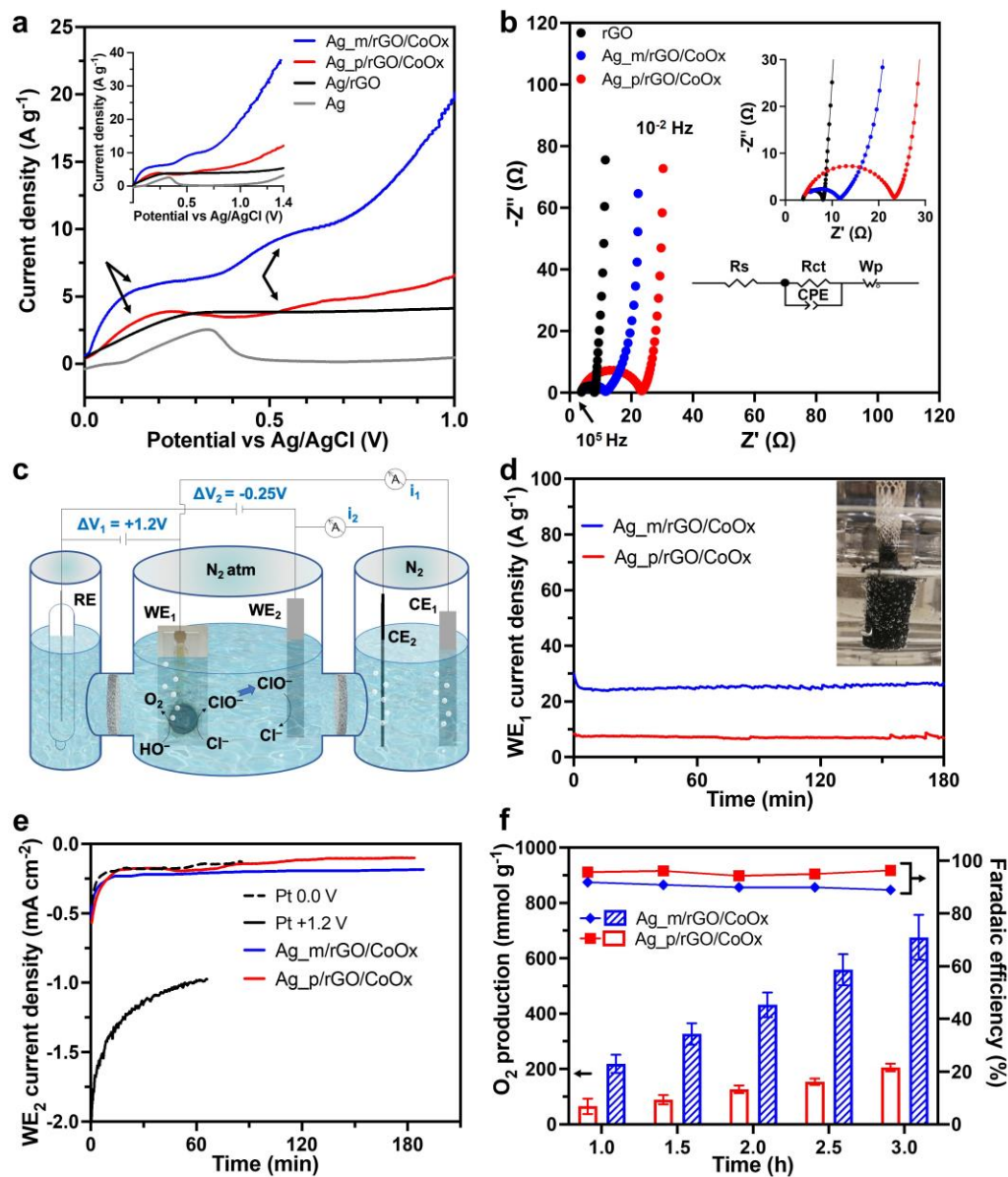


Figure 4.5. Electrochemical performance of rGO/CoOx electrodes for selective water oxidation. Measurements are performed in NaCl 0.5 M + KOH 1 M aqueous electrolyte, versus Ag/AgCl. (a) Linear sweep voltammetry scans of the Ag support (conducting Ag-coated glass substrate, gray), rGO on Ag support (black), rGO/CoOx on Ag support (red), rGO/CoOx incorporating an Ag mesh (blue) at a scan rate of 10 mV s^{-1} . Inset: detail of the scans from 0.0 to +1.4 V vs Ag/AgCl. (b) Nyquist plots of rGO and rGO/CoOx electrodes at +0.85 V vs Ag/AgCl and equivalent circuit used to fit the experimental data. (c) Schematic of the cell used to perform water electrolysis and assess the selectivity of the rGO/CoOx electrodes. (d) Chronoamperometry scans recorded during bulk electrolysis of simulated seawater at rGO/CoOx electrodes (WE₁) biased at +1.2 V vs Ag/AgCl. Inset: digital photograph showing the evolution of O_2 bubbles on the surface of an Ag_m/rGO/CoOx electrode during bulk water electrolysis. (e) Chronoamperometry scans recorded on WE₂ (Pt sheet biased at -0.25 V vs Ag/AgCl) during water bulk electrolysis at rGO/CoOx (WE₁), corresponding to the generation of free chlorine (*i.e.*, ClO^-) at WE₁. (f) O_2

generated by the two types of rGO/CoOx electrodes during water bulk electrolysis shown in (d), measured through gas chromatography. Error bars indicate the SD values based on the results from three electrodes. The graph also shows the calculated Faradaic efficiencies for the two catalysts (values on the right y axis).

The Ag_m/rGO/CoOx electrodes show higher current densities in comparison to the Ag_p/rGO/CoOx electrodes, most likely due to the shorter distance for electrical conduction between the Ag mesh and the bulk electrolyte. The rGO layer is thinner in the electrode in contact with the Ag mesh, resulting in a smaller Ohmic voltage drop across the electrode structure at the same current density.

In both types of rGO/CoOx electrodes, the kinetics of the Faradaic process is dominated by the transport of bulk water/OH⁻ to the cobalt sites inside the rGO structure and vice versa for the electrogenerated O₂, water, or protons. The closed macroporous electrode morphology of our scaffolds, which is necessary to achieve catalytic selectivity, also results in increased impedance to mass transport of the bulk electrolyte to the catalytic sites.

The electrochemical activity of these materials and electrolyte permeation inside their pores is assessed through electrochemical impedance spectroscopy (EIS), performed in buffered simulated seawater electrolyte (pH 14). The EIS spectra of rGO and both rGO/CoOx electrodes are presented in the Nyquist plots in **Figure 4.5b**, with the negative imaginary impedance $-Z''$ versus real impedance Z' and frequency f as a parameter from 10 mHz to 100 kHz. All spectra consist of a depressed semicircle in the high-frequency limit and a steep tail at the low-frequency limit, which we fit with a $R_s(R_{ct}Q)W_o$ equivalent circuit, illustrated in **Figure 4.5b**.

The zero imaginary impedance asymptote of the Nyquist semicircle at the high-frequency side represents the equivalent series resistance R_s , which arises from the sum of various Ohmic losses throughout the cell, including the resistance of the bulk electrolyte, electrode, and current collector

[439]. R_s has almost the same value for the three electrodes ($\sim 3.8 \Omega$), the rGO scaffold, and the electrical contacts (Ag).

The semicircle is ascribed to the impedance of the charge transfer (a resistance, R_{ct} , in parallel with a phase constant element, Q), Faradaic and capacitive, at the electrode–electrolyte interface, which includes both the external surface of the electrode and the surface inside the pores [439],[440]. The impedances of the charge transfers between the current collector and electrode and between the electrode and catalyst particles are also included in this model element.

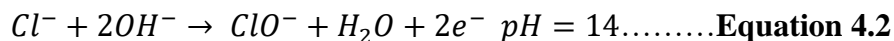
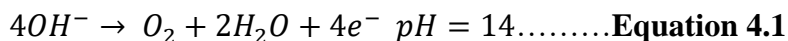
The diameter of the semicircle corresponds to the value of R_{ct} . In the case of rGO, the Faradaic charge transfer resistance is comparatively small (as will be seen), $R_{ct} = 4.2 \Omega$, and is dominated by ion transport processes, as has been observed previously for similar materials [439]–[441]. The semicircle diameter is larger for rGO/CoOx electrodes; R_{ct} values measured for Ag_m/rGO/CoOx and Ag_p/rGO/CoOx electrodes are equal to 7.7 and 19.3 Ω , respectively, and are mostly due to a Faradaic process (oxidation of water) at the cobalt particle–solution interface. The smaller resistance of Ag_m/rGO/CoOx is likely due to the thinner rGO/CoOx layer surrounding the Ag contact (~ 2 mm) in comparison to Ag_p/rGO/CoOx (~ 6 mm). The difference in thickness is likely responsible for a lower Ohmic potential drop across the rGO scaffold of Ag_m/rGO/CoOx, resulting in a more energy efficient electron transfer for the oxygen evolution reaction at the same potential due to the higher overpotential at the catalytic site.

The diverging imaginary impedance at low frequencies is a result of the low admittance of electrolyte species through the (sub)nanometer channels of the macropore walls of the working electrode [439]–[443]. At low frequencies, the diffusion of ions through the electrode microstructure enhances the imaginary component of the impedance. We model this part of the EIS curve with an open Warburg (W_o) or finite space Warburg equivalent circuit element, which

is usually adopted to describe diffusion through porous materials where one of the boundaries is impermeable [440],[442].

While the rGO electrode exhibits an ideal capacitive behavior (an almost vertical line in the Nyquist plot, corresponding to double-layer formation without the involvement of any Faradaic process), the low-frequency tails of the Nyquist plots of rGO/CoOx electrode impedance are slanted, indicating the presence of a Faradaic process limited by the permeation of reagents and products through the rGO structure. The greater deviation from an ideal vertical line in the low-frequency regime of Ag_m/rGO/CoOx electrodes in comparison to that of Ag_p/rGO/CoOx suggests an enhanced diffusive transport through the rGO structure as a consequence of the higher Faradaic performance previously described.

To assess both the electrocatalytic activity and selectivity of the rGO/CoOx electrodes toward simulated seawater oxidation to O₂, we use a cell composed of three compartments and a five-electrode setup (**Figure 4.5c**). Two working electrodes, the rGO/CoOx catalyst (WE₁) and a Pt sheet (WE₂), are hosted in the same compartment, while both counter electrodes, a Pt sheet (CE₁) and a glassy-carbon rod (CE₂), are placed in a second compartment, and the reference electrode (RE) Ag/AgCl is hosted in the third compartment. WE₁ (rGO/CoOx) is kept at +1.2 V vs Ag/AgCl. The electronic current flowing between WE₁ and CE₁ (*i*₁) can originate from two competitive reactions:



WE₂ (a Pt sheet) is kept at -0.25 V vs Ag/AgCl, a potential insufficiently negative to reduce the O₂ evolved from WE₁ but sufficient to reduce ClO⁻ back to Cl⁻. The electronic current flowing

between WE₂ and CE₂ (i_2) is proportional to the free chlorine generated by WE₁ during water electrolysis and thus allows us to evaluate the selectivity of WE₁.

This setup exhibits two major advantages over a standard one-compartment, three-electrode setup, which are necessary for the concurrent measurement of activity and selectivity of an electrocatalyst. The separation of working and counter electrodes in different compartments prevents the reoxidation/reduction of the species generated at one electrode on the corresponding counter electrode: i.e., the reduction of O₂ or ClO⁻ generated at WE₁ on the surface of CE₁ (and the oxidation of H₂ generated at CE₁ on WE₁). This phenomenon typically occurs during long experiments carried out with continuous stirring and can result in a significant overestimation of the catalytic current measured on the working electrodes. Also, the two working electrodes in the same compartment are required to directly quantify the catalyst selectivity. The amperometric determination of ClO⁻ evolved at WE₁ (i_2) has sensitivity comparable to that of the standard colorimetric *N,N*-diethyl-*p*-phenylenediamine assay [444], and it allows a continuous determination as opposed to both colorimetric and chromatographic methods, which require periodical sampling of the electrolyte. The ClO⁻ detection limit with our setup is approximately 9 μmol h⁻¹ (6 ppm h⁻¹; a detailed description is given in the Supporting information), which is far below the quantity of O₂ electrogenerated by the catalysts, as reported in **Figure 4.5f** and the related discussion.

The time profiles of the current (chronoamperometry) recorded on both types of rGO/CoOx electrodes (WE₁) and on WE₂ during the bulk electrolysis of simulated seawater are shown in **Figure 4.5d,e**, respectively. Both electrodes exhibit high activity toward water oxidation as well as catalytic durability, as demonstrated by the constant current values (i_1) recorded during the entire measurement (**Figure 4.5d**). The durability of the Ag_m/rGO/CoOx electrode for at least

25 h has been further confirmed by performing a longer chronoamperometric test (**Figure 4.S13**) under the same conditions, and its porous structure and physicochemical composition are not altered noticeably by the electrolysis (**Figure 4.S14 - Figure 4.S16**).

The Ag_m/rGO/CoOx electrode achieves a larger anodic current density (i_1) in comparison to Ag_p/rGO/CoOx, namely $25 \pm 5 \text{ A g}^{-1}$ versus $9 \pm 4 \text{ A g}^{-1}$, in agreement with comparisons of LSV and EIS spectra (**Figure 4.5a,b**). Here, the current values are normalized by the mass of the rGO/CoOx, i.e. the mass of the Ag collector is excluded, to allow comparison with other catalysts in the literature. The Faradaic current on both electrodes is accompanied by a copious evolution of gas bubbles, as shown in the inset of **Figure 4.5d**.

We now consider the currents measured at WE₂ (i_2) to estimate the fraction of the current measured at WE₁ that is related to water or chloride oxidation. The i_2 values recorded for both rGO/CoOx electrodes (**Figure 4.5e**) coincide with the current measured, in the same solution, using a Pt WE₁ biased at 0.0 V vs Ag/AgCl (dotted line). Under these conditions Pt is unable to oxidize either water or Cl⁻; therefore, this current can be taken as a reference level with an absence of Faradaic processes on WE₁. As a comparison, i_2 measured using a Pt WE₁ biased at +1.2 V vs Ag/AgCl (black line) is significantly higher and indicates electrogeneration of free chlorine on the Pt surface, together with water oxidation. These results imply that the rGO/CoOx electrodes are selective toward water oxidation and that the bubbles observed during electrolysis on the rGO/CoOx electrodes are indeed O₂.

The O₂ evolved from the rGO/CoOx electrodes is periodically quantified by means of gas chromatography (**Figure 4.5f**), to estimate the catalytic Faradaic efficiency by comparison with the current density recorded on WE₁ (i_1). The catalyst Faradaic efficiencies are calculated by dividing the moles of O₂ generated by the moles of electronic charge (e⁻) passed through WE₁. In

1 h of activity, 1 mg of Ag_m/rGO/CoOx and Ag_p/rGO/CoOx electrodes generate, on average, 207 and 62 μmol (46 and 14 mL) of O₂, respectively. Both electrodes show Faradaic efficiencies of between 89% and 98% during 3 h of continuous electrolysis.

The activity of the Ag_m/rGO/CoOx electrode is comparable to that of the recently developed, best-performing electrocatalysts for selective electrolysis of alkaline simulated seawater [409]–[412]: we can achieve a record current density of 25 A g⁻¹ while applying a potential of 1.2 V vs Ag/AgCl, i.e. comparable to the value measured at 1.15 V vs Ag/AgCl on the best Ni-based catalyst reported (**Table 4.S3**). The higher potential required by our system is due to the closed-pore microarchitecture of rGO/CoOx, which is crucial for electrode selectivity against Cl₂ evolution but slows down the transport of water/OH⁻ to the catalytic sites. At the same time, this architecture enables selective O₂ evolution in a much larger range of operational potentials in comparison to Ni-based catalysts, which avoid chlorine evolution by working in conditions where chloride oxidation is thermodynamically hindered, *i.e.*, under strongly alkaline conditions, over a limited applied potential range.

4.4 Conclusions

We achieve high selectivity in the catalytic water electro-oxidation process by designing a 3D rGO electrode with closed macropores functionalized on the inner side with catalytic cobalt oxide (CoOx) particles. The rGO pore walls selectively prevent the transport of dissolved ions while retaining the high permeability of gases and water molecules. Selective transport through the rGO nanochannels is crucial to catalytic selectivity: water and OH⁻ ions from the bulk solution can access the catalyst surface, and the electrogenerated O₂ and water molecules can easily leave the pores, but the Cl⁻ ions are kept outside the pores because their hydrated size is larger than the rGO interlayer distance. This architecture allows the rGO/CoOx electrode to be used as the anode in a

cell for water electrolysis employing seawater as the electrolyte, without suffering from Cl^- competition. Future research may involve preventing or slowing down the aggregation of the catalytic nanoparticles with different surfactant or solvent mixtures to further increase the electrocatalytic performance.

This work introduces an electrode architecture as a means that can be used to achieve selectivity in water electro-oxidation, different from previously reported systems that rely on external filtering membranes (dialysis) or optimized (co)catalyst phases that can operate only under restricted chemical conditions (i.e., a specific potential and pH).

This concept is flexible and can be extended to other scenarios beyond the suppression of Cl^- interference in seawater electrooxidation. The closed-pore structure is likely to selectively inhibit the transport of most solvated ions, since chloride ions are among the smallest hydrated anions. This feature would be particularly useful to prevent catalyst poisoning, which often occurs due to the presence of sulfur-rich compounds, microbes, corrosive ions, and particulate typically present in any natural water source.

Also, the proposed electrode structure may be successfully adapted to other electrocatalytic reactions requiring selectivity against interfering species or ions. Some examples include the electrooxidation of methanol in a raw fuel mixture or the electroreduction of water in the presence of anions such as sulfates and nitrates, as well as most dissolved transition-metal impurities.

The flexibility of our concept arises from the possibility of changing the catalytic particles that are loaded into the pores. The catalytic particles, as long as they are surface-modified to achieve a stable oil emulsion and are loaded inside the pores of the rGO host, can range from noble metals to first-row transition metals and their corresponding oxides, nitrides, sulfides, and phosphates, depending on the electrochemical reaction of interest.

4.5 Methods

4.5.1 Chemicals and materials

Graphene oxide paste (25 wt %, from Abalonyx, Norway) was synthesized by a modified Hummers method (product number 1.2A). Cobalt (II,III) oxide powder (Product No. 637025, particle size <50 nm, referred to as “Co₃O₄ particles”), stearic acid (95%), ammonium hydroxide solution in water (28.0–30.0% v/v), potassium hydroxide (99.99%), and sodium chloride (98%) were obtained from Sigma-Aldrich. Hexane (HPLC grade) was purchased from Fisher Scientific, ethanol anhydrous from Commercial Alcohols, cetyltrimethylammonium bromide (99%) from Bio Basic (Canada), the Ag paint from Ted Pella (USA), and Ag mesh 99.99% from Ofolan (China). Nitrogen and argon (Alphagaz-1 grade 99.999%) were purchased from Air Liquide. All chemicals were used without further purification.

4.5.2 Cobalt oxide-in-hexane dispersion

A 0.332 g portion of SA was dissolved in 40 mL of ethanol with stirring for 30 min. Then, a 20 mg portion of Co₃O₄ particles was dispersed in this solution with stirring, for 30 min. To rinse the Co₃O₄/SA particles, the suspension was centrifuged (300g force, 10 min) and the supernatant was discarded, followed by the addition of 40 mL of ethanol and ultrasonication for 5 min. This rinsing procedure was repeated three times. The so-obtained solid was dried in air and redispersed in 15 mL of hexane by ultrasonication for 20 min.

4.5.3 Graphene oxide dispersion and GO/Co₃O₄ emulsions

The GO suspension (12 g L⁻¹) was prepared by dispersing GO paste in water with stirring for 20 min followed by ultrasonication for 20 min and again stirring for 20 min. To obtain a GO/CTAB suspension, an aqueous CTAB solution (0.9 g L⁻¹, 6 mL) was added to the 30 mL GO suspension drop by drop, with stirring at room temperature, followed by 5 min of stirring.

Then, 3 mL of the GO/CTAB suspension and 6 mL of Co_3O_4 particles-in-hexane dispersion were placed in a glass vial and the mixture emulsified with a vortex shaker (Vortex-Genie, speed of 2700 rpm, 1 min).

Control GO emulsions without Co_3O_4 particles were also prepared by following the same procedure described above and adding pure hexane as the oil phase instead of the Co_3O_4 suspension in hexane.

4.5.4 rGO and rGO/CoOx macroporous aerogels

The glass vial containing the emulsion (without the cap) was sealed in a Teflon-lined autoclave (50 mL) and 3 mL of concentrated ammonium hydroxide solution were placed in the Teflon liner, outside the glass vial. The autoclave was heated at a rate of $0.5\text{ }^\circ\text{C min}^{-1}$ until it reached $250\text{ }^\circ\text{C}$, and this temperature was maintained for 5 h, followed by cooling to room temperature. The hydrogels obtained after the hydrothermal process were frozen with liquid N_2 and lyophilized them using a Freeze-Dryer (Labconco FreeZone) for 48 h to eliminate the water and residual hexane inside the scaffolds, giving either rGO or rGO/CoOx aerogels depending on the starting emulsions.

4.5.5 rGO and rGO/CoOx electrodes

To prepare the first type of electrode, a thin conducting layer of Ag paint was deposited on a glass slide and stuck on the cylindrical rGO or rGO/CoOx aerogels described previously. The aerogel must be attached right after the deposition of the Ag paint: i.e., when the paint is still liquid. The aerogel was gently deposited on the Ag layer, which instantly adhered to the macroporous aerogel surface. The exposed portion of the Ag layer was coated with epoxy resin to prevent the evolution of gases from this component when the electrode was immersed in the electrolyte and under bias. Finally, a conducting wire was soldered on the upper corner of the Ag layer, and this joint was covered with epoxy resin, to easily connect the electrode to the voltage supply

(potentiostat) during the electrocatalytic measurements. The second type of electrode was prepared by sticking a thin and long cylindrical Ag mesh inside the emulsions described above and following the same synthetic steps as above to obtain the aerogels. The aerogels resulting after freeze-drying were directly used for selective water electrolysis, by immersing in the electrolyte just the portion of the electrode corresponding to the rGO scaffold, to avoid electrochemical reactions on the exposed Ag mesh, which was connected to the potentiostat through an alligator clip. The two electrodes are referred to as Ag_p/rGO/CoO_x and Ag_m/rGO/CoO_x, respectively.

4.5.6 Physicochemical and structural characterization

TEM and HRTEM observations were performed with a Thermo Scientific Talos F200X G2 S/TEM instrument equipped with a Schottky field emission source, operating at an accelerating voltage of 200 kV. The samples were prepared by dropping a diluted suspension of material onto a standard carbon-coated copper grid. SAED was performed with the same instrument.

ATR-FTIR spectra were collected with a Spectrum-Two IR spectrometer with a LiTaO₃ (lithium tantalate) MIR detector (PerkinElmer, Waltham, USA). Each spectrum was generated by the accumulation of 32 scans in the range of 400–4000 cm⁻¹ at a resolution of 4 cm⁻¹.

The images of emulsion droplets were captured with an optical microscope (Olympus CKX41 connected with a Canon EOS Rebel T3 single-lens reflex, objective lenses magnification in 4× and 20×). The diameters of the emulsion droplets were analyzed with ImageJ software.

The samples for the SEM investigation were coated with a 4 nm thick platinum layer using a Leica EM ACE 600 high-vacuum coater (Leica Microsystems Inc., Wetzlar, Germany). The morphologies of the GO flakes and the aerogels were observed with a FEI Quanta 450 field emission scanning electron microscope (FEI Company, USA) under an accelerating voltage of 10 kV with a spot size of 2 nm. EDS was performed with the same equipment with an accelerating

voltage of 10 kV and a spot size of 3 nm. The equivalent diameter of the GO flakes and the pore diameter were analyzed with ImageJ.

The internal microstructures of rGO/CoOx aerogels were visualized by using synchrotron-based PCI at the Biomedical Imaging Therapy Bending Magnet (BMIT-BM) beamline of the Canadian Light Source (Saskatchewan, Canada). The X-ray beam energy was 20 keV, and the X-ray radiation was absorbed by a LuAG:Ce scintillator (thickness of 50 μm) coupled to a PCO Edge5.5 detector, with a sample to detector distance of 0.05 m. Samples were examined at 9 \times magnification using a WhiteBeam microscope. The resolution was set to 0.72 $\mu\text{m pixel}^{-1}$, and the field of view was 2560 pixels (H) \times 2160 pixels (V). The samples were rotated to collect 3000 projections with 50 ms exposure time per projection. The projected images were reconstructed to obtain slices with a volume of interest (1760 \times 1760 \times 720 voxels) using UFO-KIT (Karlsruhe Institute of Technology, Germany) and ImageJ software. The interactive thresholding module of Avizo software (Version 9.5, Thermo Fisher Scientific, USA) allowed us to obtain binary images and discriminate the cobalt oxide particles from the solid phase for their 3D visualization. The equivalent sphere diameters of the visualized particles were calculated through the Avizo label analysis module.

The sample elemental composition was analyzed by means of XPS on a Thermo Scientific K-Alpha photoelectron spectrometer (Thermo Fisher Scientific Inc., Waltham, USA), equipped with an incident $\text{K}\alpha$ X-ray source (1486.6 eV, 0.843 nm). A flood gun of low-energy electrons was employed to prevent surface charging during the measurements. To analyze the sample atomic composition, we conducted survey scans with a 1 eV step size (resolution) and high-resolution scans, for each detected element, with a step size of 0.1 eV. XPS analysis was carried out on the interior structure of purposely broken rGO and rGO/CoOx aerogels, to ensure that the results were

representative of the bulk electrodes. Even though the XPS probe depth was <10 nm [445], the spot analyzed with XPS was 400 μm in diameter and included not only the surface of CoOx particles but also that of several rGO pores. Avantage software was used to analyze the survey and high-resolution spectra. The high-resolution C 1s bands were fitted with four components: C–C (C=C), C–O, C=O, and π – π^* shake up at 284.8, 286.5, 288.4, and 290.8 eV, respectively.

The Raman spectra were collected with a Bruker Senterra confocal Raman microscope (Bruker, Germany) using a 10 mW 785 nm pump laser. The spectra were acquired after 120 s of integration time and 2 coadditions.

The electrical conductivity of the aerogels was measured through a four-point setup and the Van der Pauw method. The aerogel samples were cut into thin films with a square shape and fixed on a glass slide by gluing each corner of the square with a drop of Ag paint. The distance between each vertex and the film thickness was measured with a digital caliper (DC02, accuracy 0.01 mm, TACKLIFE, USA). The measurements were carried out at ambient temperature.

4.5.7 Electrochemical characterization

The rGO and rGO/CoOx electrodes (or the bare Ag layer as a control) were characterized by using a computer-controlled potentiostat/ZRA (Interface 1000E, Gamry Instruments, USA) and a conventional three-electrode cell in aqueous NaCl 0.5 M + KOH 1 M and a simulated seawater electrolyte buffered at pH 14, in air. The measurements were performed by using a Pt sheet as a counter electrode (CE) and Ag/AgCl/KCl 3.5 M as a reference electrode (RE). The electrode performance for electrocatalytic water oxidation was assessed through linear sweep voltammetry. All polarization curves were iR compensated (90%). The working electrodes (WE) were equilibrated at the initially applied potential for 30 s before starting the measurements and then polarized at a scan rate of 10 mV s^{-1} . The impedances of the electrodes were measured by applying

a sinusoidal potential centered at +0.85 V vs Ag/AgCl with 10 mV root-mean-square (rms) amplitude, in the frequency range between 100 kHz and 10 mHz. The geometrical factors of the measurement cell were interelectrode distance 10 mm, electrode area 50 mm² for Ag_m/rGO/CoOx (5 × 10 mm) and 80 mm² for Ag_p/rGO/CoOx (circle with diameter of 10 mm), and electrode thickness 2 mm for Ag_m/rGO/CoOx and 6 mm for Ag_p/rGO/CoOx.

4.5.8 Selective electrocatalytic water oxidation by rGO and rGO/CoOx electrodes

The bulk electrolysis of water was performed by using a computer-controlled potentiostat (Interface 1000E, Gamry) and a cell composed of five electrodes hosted in three compartments connected to each other through two microporous glass frit filters and sealed on top by airtight silicone caps (**Figure 4.5a**). One lateral compartment hosted the Ag/AgCl/KCl 3.5 M RE. In the central compartment we placed one of the rGO/CoOx electrodes previously described, referred to as WE₁, held at +1.2 V vs RE, and a Pt sheet, referred to as WE₂, held at -0.25 V vs RE and 1 cm away from WE₁. In the second lateral compartment we placed the two CEs of WE₁ and WE₂, respectively a Pt sheet (CE₁) and a glassy-carbon (GC) rod (CE₂). All of the electrodes were immersed in aqueous NaCl 0.5 M + KOH 1 M electrolyte (pH = 14), and each compartment was purged with N₂ for 5 min before starting the measurements. During the measurements, the electrolytic solution of the WE compartment was continuously purged with a flux of N₂ (30 mL min⁻¹). All data were reported with *iR* compensation (90%). A few milliliters of water was periodically added to the WE compartment, to keep the electrolyte volume constant. The electrolyte volume and the headspace of the WE compartment were both 30 mL. To quantify the O₂ evolution from WE₁, 1 mL of a gas sample was withdrawn from the headspace of the WE compartment every 30 min, using a glass syringe with a metal Luer-lock tip. The gas samples were analyzed with a GC-8A gas chromatograph (Shimadzu) equipped with a thermal conductivity

detector and an Alltech 5A molecular sieve column (10 ft, 80/100 mesh, washed). The injector temperature and column temperature were set respectively at 100 and 70 °C, and the Ar carrier flow rate was set at 5 mL min⁻¹. O₂ and N₂ were eluted after 3.33 and 4.83 min, respectively.

The setup used to carry out the water oxidation experiment and to measure the amount of O₂ evolved corresponded to a so-called a “continuously stirred tank reactor under flow”. This configuration exhibits several advantages, such as reducing the continuous increase of O₂ inside the cell that originates from small leaks and would increase the error in the measurement of the net O₂ electrogenerated. Also, working under steady-state conditions allows direct conversion of the O₂ concentration measured to the rate of O₂ production, without needing corrections for the O₂ partition between the liquid and the gas phases (Henry’s law) [446]. The lowest O₂ concentration detectable with our GC method was 5 ppm (5 μL L⁻¹ = 210 nmol L⁻¹ under standard conditions, according to the ideal gas law $PV = nRT$). Under an N₂ flow of 30 mL min⁻¹, this value corresponded to a minimum O₂ production rate of 0.15 μL min⁻¹. The O₂ production rates recorded during the chronoamperometric measurements were in the range of 50–200 μL min⁻¹, far above the detection limit. The amount of O₂ produced over time (**Figure 4.5f**) was calculated by integrating over time the O₂ production rates measured every 30 min. The O₂ production rate was calculated by the following formula: $v_{O_2} (\mu\text{mol min}^{-1} \text{ g}^{-1}) = C_{O_2} (\mu\text{L L}^{-1}) \times 10^{-3} (\text{L mL}^{-1}) \times j (\text{mL min}^{-1}) / (m (\text{g}) \times 22.4 (\mu\text{L } \mu\text{mol}^{-1}))$, where C_{O_2} was the measured O₂ concentration, j the N₂ flux (30 mL min⁻¹), and m the mass of the electrode. The masses of the whole rGO/CoOx samples tested ranged between 4 and 5 mg. These values were used to derive the current density values. The Faradaic efficiency was calculated as the ratio $(4 \times \text{mol}_{O_2} \text{ generated}) / (\text{mol}_{e^-} \text{ flowed through the circuit}) = (4 \times v_{O_2} (\text{mol s}^{-1} \text{ g}^{-1}) \times m (\text{g})) / (i (\text{C s}^{-1}) / F (\text{C mol}^{-1}))$, where v_{O_2} was the O₂ production

rate, m the mass of the electrode, F the Faraday constant, and i the current measured during the chronoamperometry (**Figure 4.5d**).

4.6 Acknowledgement

We gratefully acknowledge the support from the Canada Research Chair Foundation, the Natural Sciences and Engineering Research Council of Canada (NSERC), the Fonds de Recherche du Québec - Nature et Technologie (Postdoctoral research scholarship B3X, project number: 305938 and Doctoral research scholarship B2X), and the Quebec Centre for Advanced Materials. Part of the research described in this paper was performed using beamline BMIT-BM at the Canadian Light Source (CLS), the national synchrotron facility of the University of Saskatchewan, which is supported by the Canada Foundation for Innovation (CFI), the NSERC, the National Research Council (NRC), the Canadian Institutes of Health Research (CIHR), the Government of Saskatchewan, and the University of Saskatchewan. We gratefully acknowledge the generous support of the CLS staff.

4.7 Supporting information

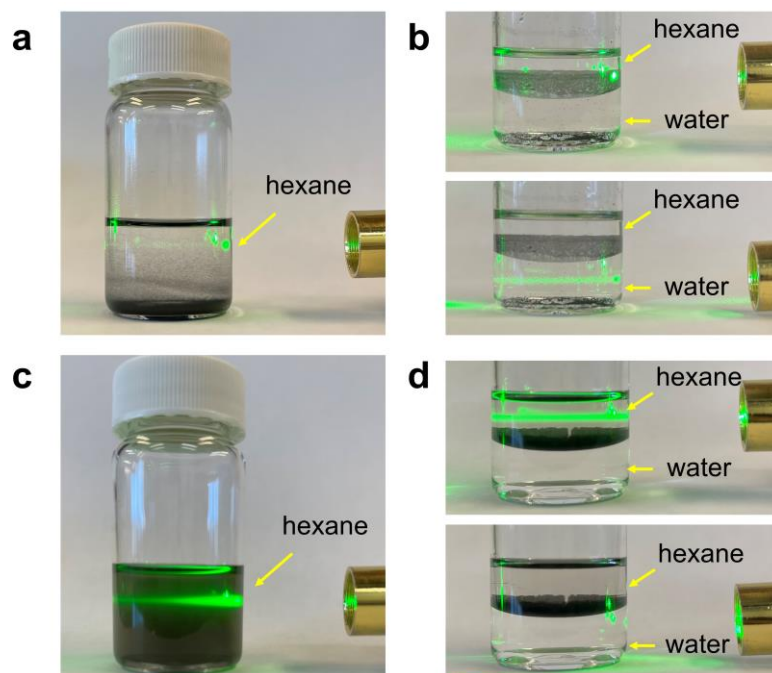


Figure 4.S1. Digital photographs showing (a) pristine Co_3O_4 particles in hexane, (b) pristine Co_3O_4 particles in hexane (top) and water (bottom) after shaking, (c) $\text{Co}_3\text{O}_4/\text{SA}$ particles in hexane, (d) $\text{Co}_3\text{O}_4/\text{SA}$ particles in hexane (top) and water (bottom) after shaking. A green laser is pointed at the vials to evaluate the Tyndall effect in the dispersions. A clear solution without suspended particles shows no light scattering. In panel b, the absence of light scattering in the hexane phase (top) suggests the absence of dispersed Co_3O_4 particles in this medium after shaking. In panel d, the strong Tyndall effect observed in the hexane phase together with the absence of the Tyndall effect in the water phase after shaking suggests that the dispersion of $\text{Co}_3\text{O}_4/\text{SA}$ particles in the hexane phase and at the hexane/water interface.

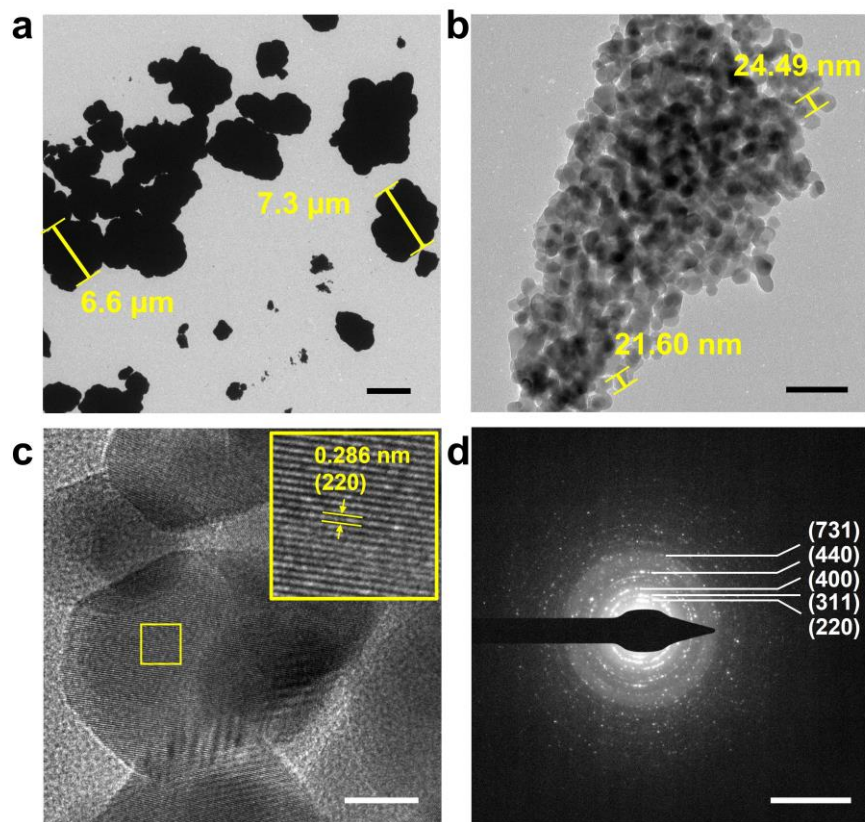


Figure 4.S2. (a-b) Representative TEM images of aggregates of pristine Co_3O_4 particles. (c) HRTEM analysis of Co_3O_4 particles. The magnification of the area highlighted by the yellow square, shown as an inset figure, allows to measure the d -spacing and identify the (220) diffraction planes of the Co_3O_4 cubic phase (JCPDS 00-42-1467). (d) The selected area electron diffraction (SAED) patterns obtained from Co_3O_4 particles reflect the diffraction bands of the cubic Co_3O_4 lattice, whose most prominent zone axes are labelled and indicated by solid lines. The SAED patterns in panel (d) and **Figure 4.2d** are identical within the experimental error. Scale bars: 5 μm (a), 100 nm (b), 10 nm (c), and 10 nm^{-1} (d).

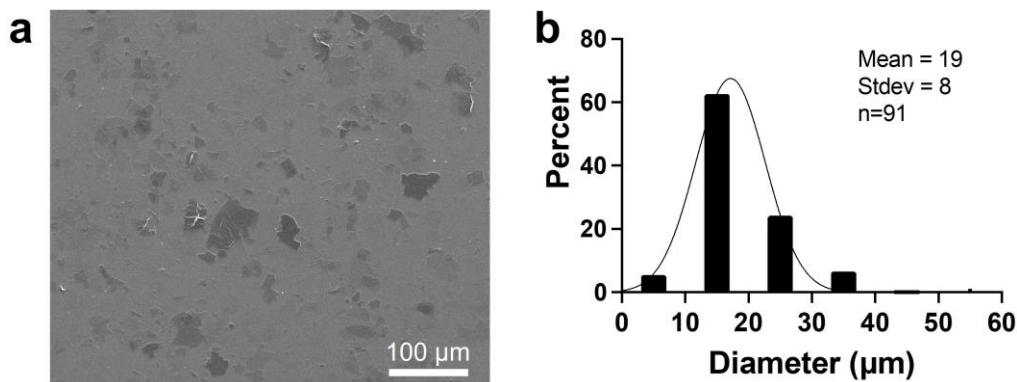


Figure 4.S3. (a) SEM image of the GO flakes used in this study. (b) GO flake size distribution and nonlinear regression based on a Gaussian model. The flake size is shown as the effective diameter of a circle that has the same area as the GO flake, as observed in the SEM.

Table 4.S1. Surface chemistry from XPS survey data of GO and GO/CTAB (n=3 experiment points)

	GO	GO/CTAB
O1s (atom%)	39±3	31.5±0.5**
C1s (atom%)	60±2	66.7±0.4**
N1s (atom%) ^{a)}	1.3±1.2	1.8±0.2

^{a)} Nitrogen on the original GO is the trace impurity from the sodium nitrate in the Hummers' method for GO preparation.

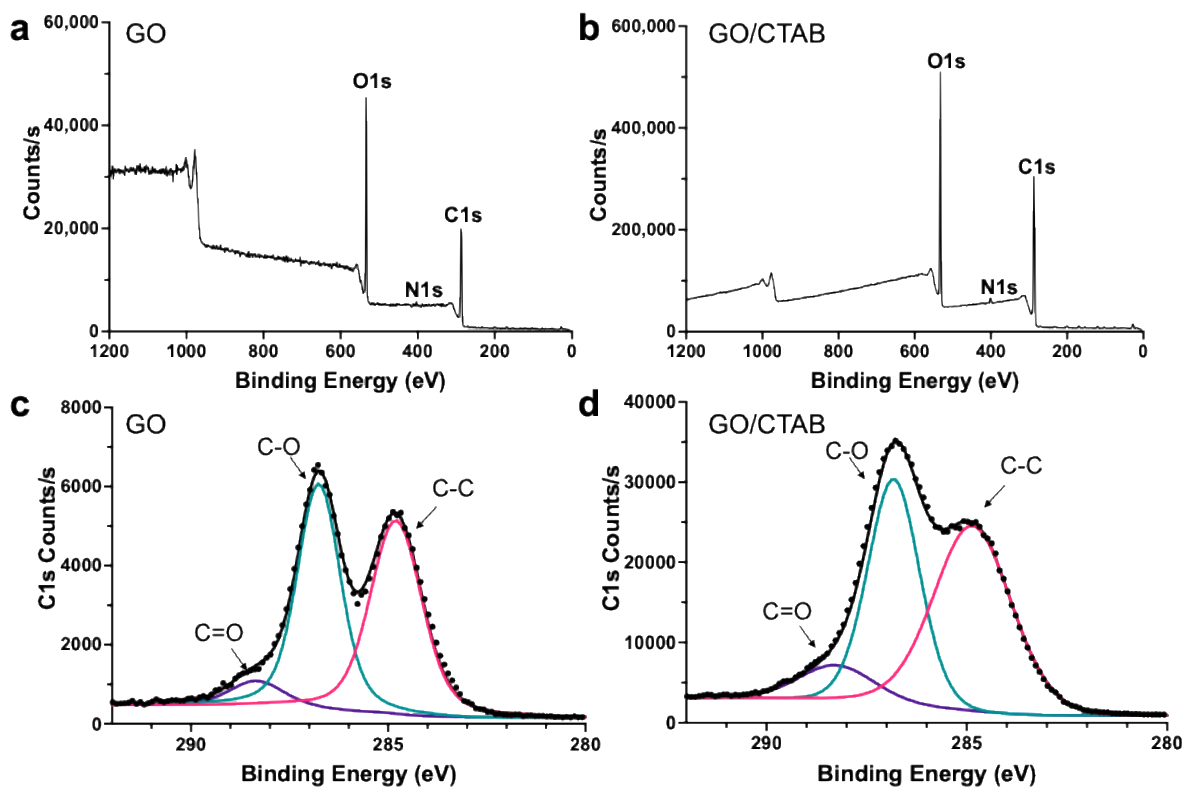


Figure 4.S4. Representative XPS survey spectra of (a) GO and (b) GO/CTAB. XPS high-resolution C1s spectra of (c) GO and (d) GO/CTAB.

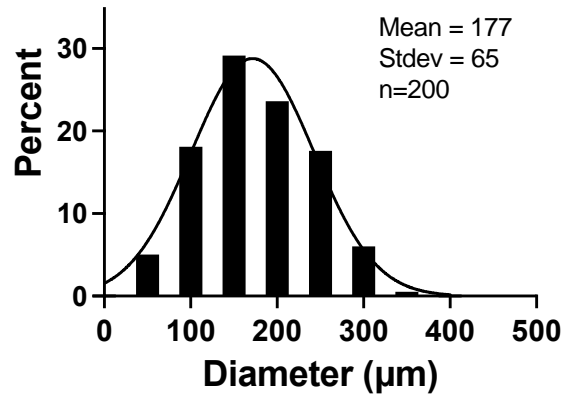


Figure 4.S5. Pore diameter distribution of rGO/CoOx aerogels and nonlinear regression based on Gaussian model. The pore diameter is calculated based on the analysis of 200 pores observed in SEM images.

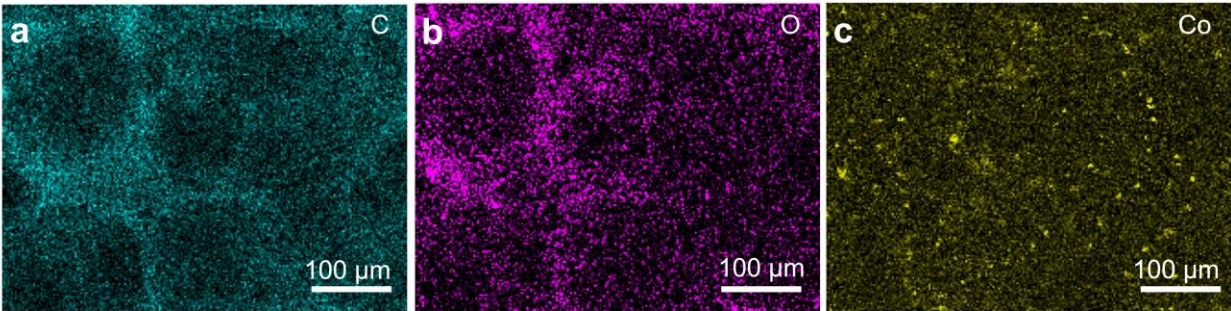


Figure 4.S6. (a-c) EDS mapping of carbon and oxygen of the SEM image of rGO/CoOx aerogel shown in **Figure 4.3b**.

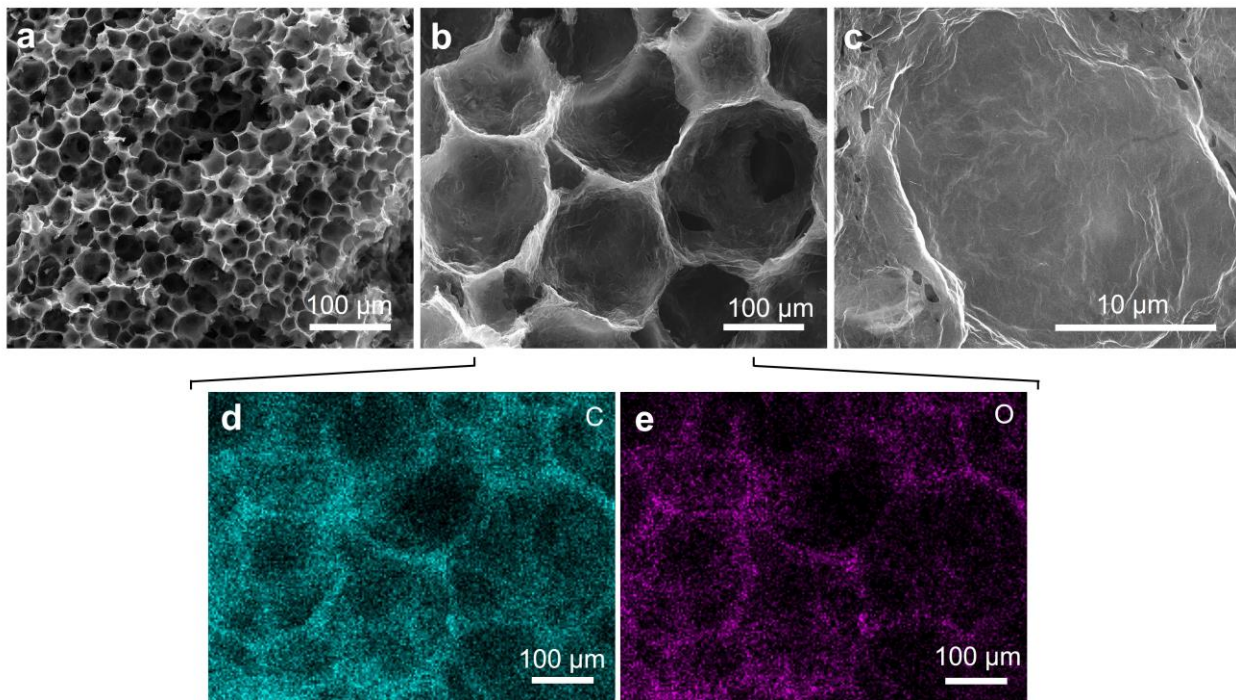


Figure 4.S7. (a-c) SEM images of rGO aerogel synthesized without Co_3O_4 particles (control sample) at different magnifications. (d, e) EDS mapping of carbon and oxygen.

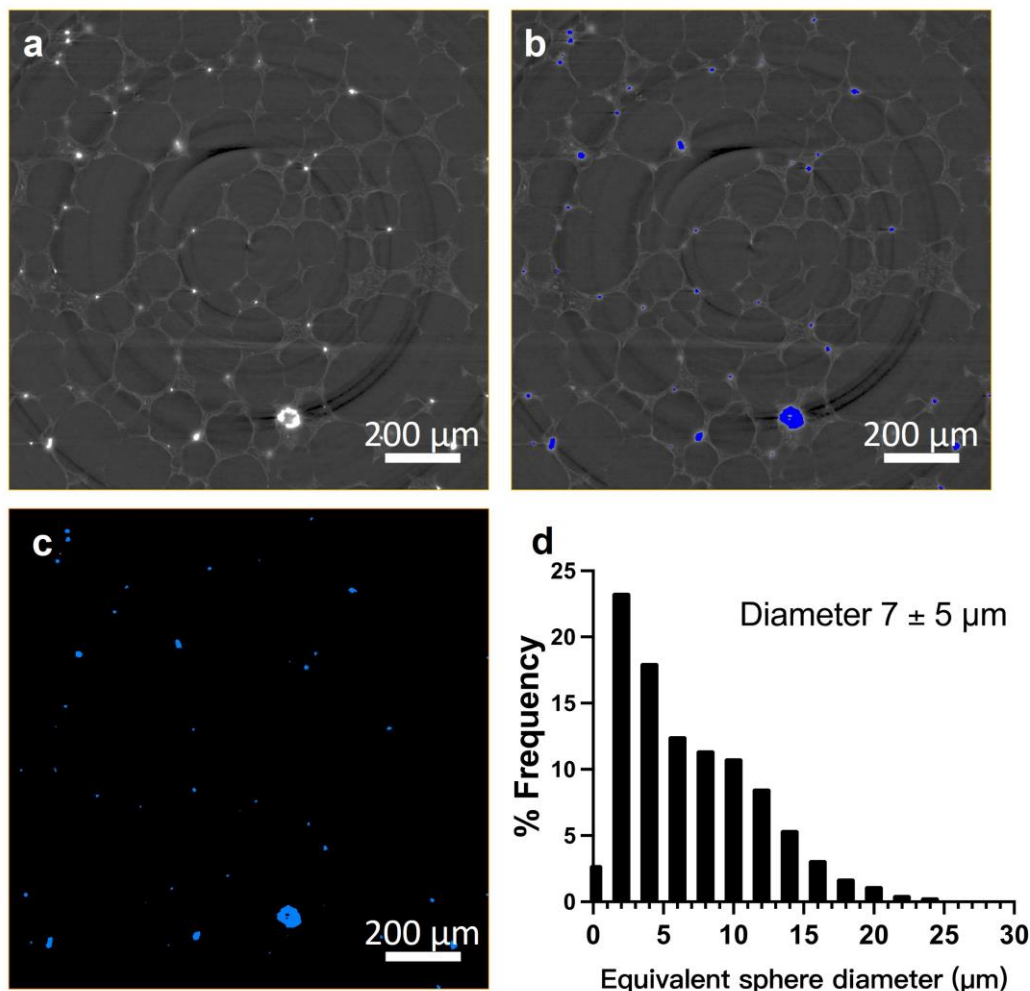


Figure 4.S8. Phase contrast image (PCI) analysis of rGO/CoOx scaffolds. (a) Greyscale reconstruction slice (8-bit) showing the rGO pores as grey contour and CoOx particles as bright dots. Because of the higher X-ray absorption of cobalt oxide, the CoOx particles show with higher contrast. (b) With the interactive thresholding module in Avizo software, we set a certain grey level range (200-255) as a threshold (highlighted in blue) that only includes bright particles in the greyscale image. (c) After applying the interactive thresholding, the greyscale image is transformed into a binary image showing the CoOx in light blue. (d) With the label analysis module in Avizo, we obtain the volume of visualized particles, and thus the equivalent sphere diameter of particles. The equivalent diameter is equal to the diameter of a sphere that has the same volume of the particle.

We do not report X-ray powder diffraction (XRD) results because the diffraction pattern of rGO-CoOx samples varied from one measurement to another and we were not able to define a “representative” measurement. The isolated cobalt oxide particles in the scaffold behave as single crystals, each one immobilized in a particular random orientation. The result is not a powder XRD pattern – where all the possible grain orientations are statistically sampled throughout the

compressed powder – nor a single crystal XRD, where the crystal orientation is controlled. XRD revealed a limited number of diffraction peaks, and often their relative peak intensities did not match the reference patterns in the literature. For this reason, we performed high resolution TEM characterization coupled with selected area electron diffraction (SAED) to clarify the composition and phases of the particles present in the electrodes.

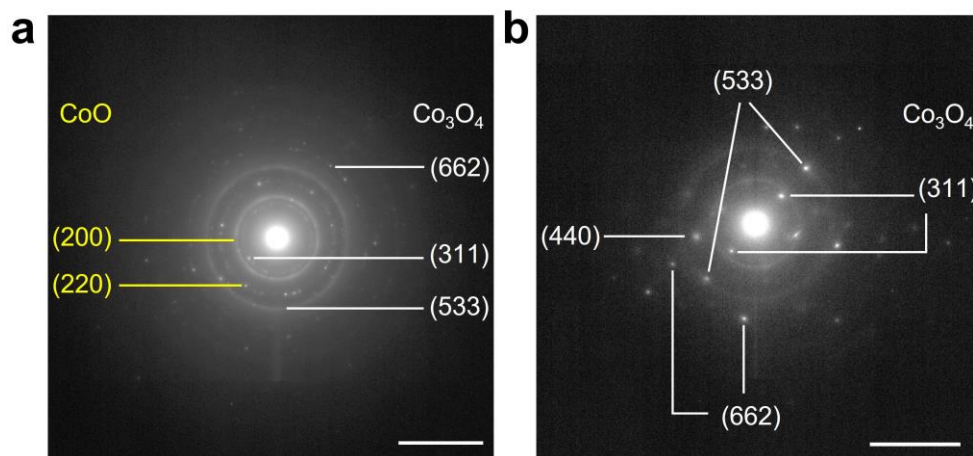


Figure 4.S9. SAED patterns and the most prominent diffraction bands obtained from CoOx particles inside the rGO/CoOx aerogel shown in **Figure 4.3h** (a) and **3i** (b) of the main text. (a) The SAED pattern of the aggregate highlighted with a yellow circle in **Figure 4.3h** contains the most prominent diffraction bands of both the cubic Co_3O_4 (JCPDS 00-42-1467) and cubic CoO (JCPDS 00-043-1004) crystalline phases, indicated by the white and yellow labels, respectively. (b) The SAED pattern of the octahedral particles highlighted with a yellow circle in **Figure 4.3i** matches the interlayer spacing of a single-crystal Co_3O_4 cubic phase, and its four most intense diffraction planes are indexed in white. Scale bars: 10 nm^{-1} .

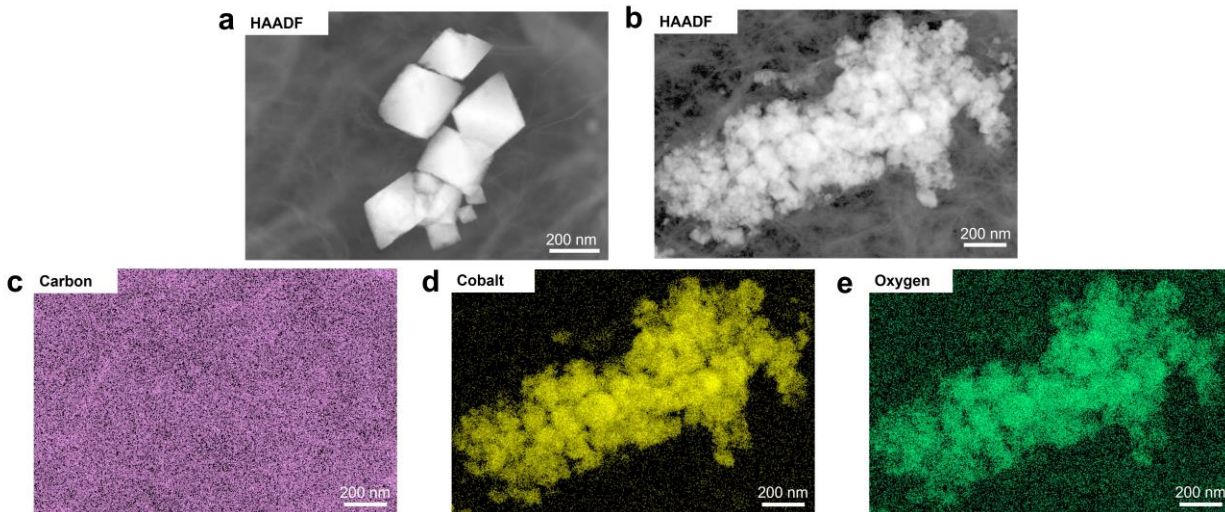


Figure 4.S10. (a) HAADF image the CoOx particles shown in **Figure 4.3i**. (b) HAADF image and (c-e) the corresponding EDS elemental maps of CoOx particles shown in **Figure 4.3h**.

Table 4.S2. Surface chemistry from XPS survey data of rGO and rGO/CoOx (n=3 experiment points). XPS analysis was carried out on the interior structure of purposely broken rGO and rGO/CoOx aerogels, to ensure that the results are representative of the bulk electrodes. Even though the XPS probe depth is <10 nm [445], the spot analysed with XPS is 400 μm in diameter and includes not only the surface of CoOx particles but also that of several rGO pores.

	rGO	rGO/CoOx
O1s (atom%)	7.3 \pm 0.9	10 \pm 1
C1s (atom%)	82 \pm 2	79 \pm 2
N1s (atom%)	11 \pm 1	9 \pm 2
Co2p (atom%) ^a	---	2.0 \pm 0.2

^a The high nitrogen content arises from the reaction of ammonia vapors with the CO₂ generated from GO reduction during the hydrothermal treatment. It is likely present in the form of ammonium carbonate nanoparticles inside the rGO scaffold rather than as a doping element of the rGO sheets, as the temperature of the hydrothermal treatment is far below the one required to achieve nitrogen doping of graphitic materials.

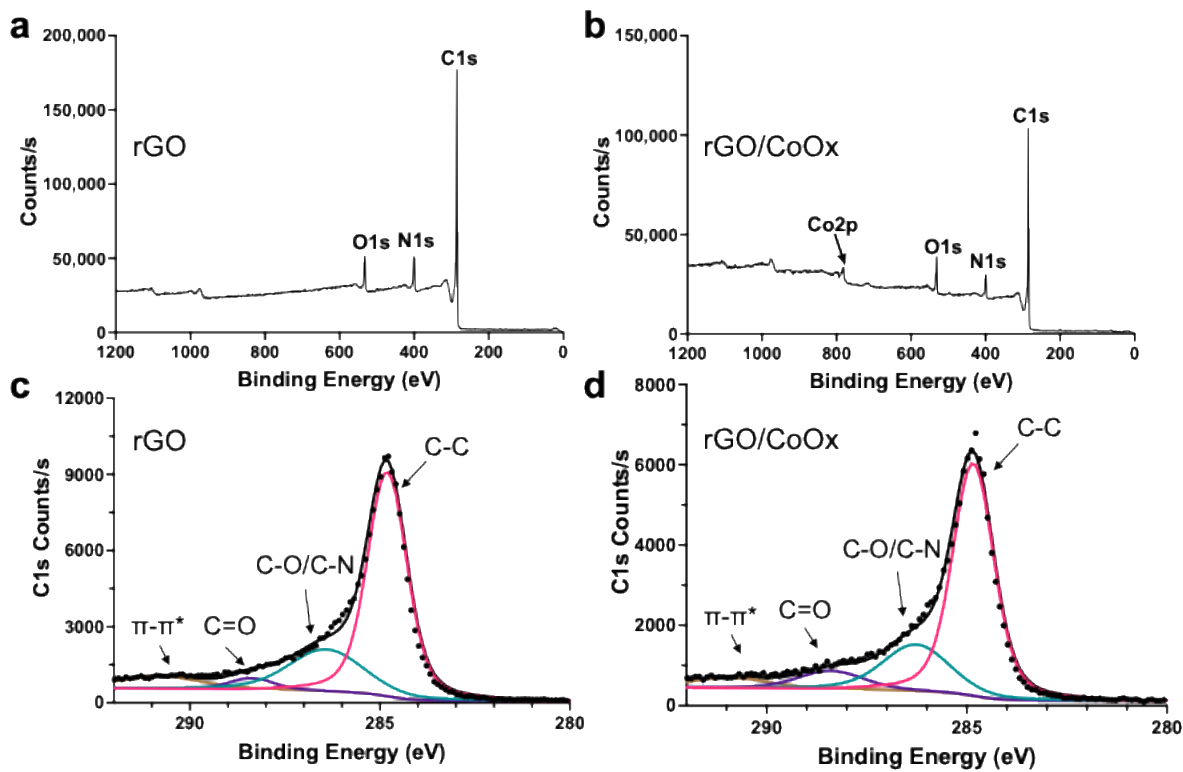


Figure 4.S11. Representative XPS survey spectra of (a) rGO and (b) rGO/CoOx. XPS high-resolution C1s spectra of (c) rGO and (d) rGO/CoOx.

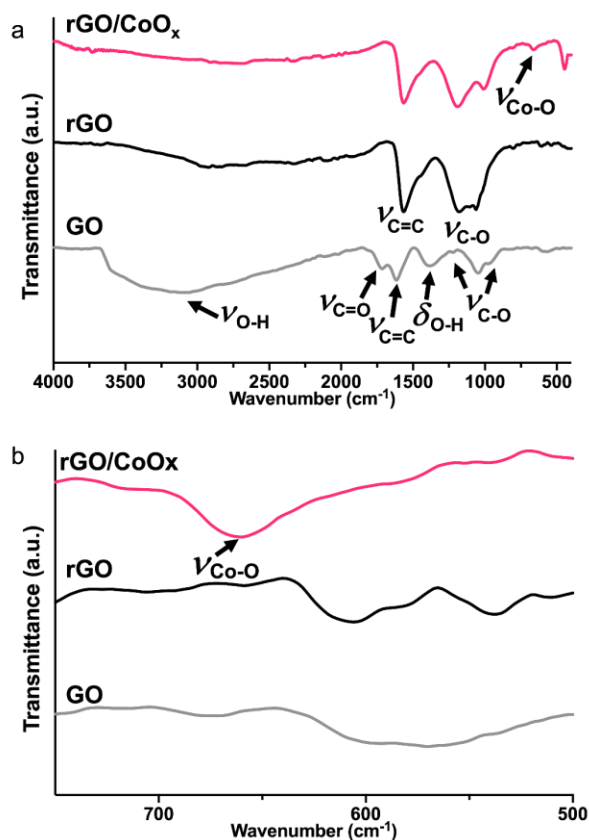


Figure 4.S12. (a) FTIR spectra of pristine GO, rGO, and rGO/CoO_x aerogels; (b) zoom-in into the low wavenumber region where the Co–O vibrations are visible. These spectra provide further evidence of the reduction of GO after the HT and the presence of cobalt oxide. After HT, the peaks assigned to $\nu(\text{C}=\text{O})$ and $\delta(\text{O}-\text{H})$ disappear, and the broad peak related to $\nu(\text{O}-\text{H})$ decreases. A broad band spanning from 560 to 660 cm^{-1} , which corresponds to $\nu(\text{Co}-\text{O})$, appears in the rGO/CoO_x aerogel spectra [420]–[422].

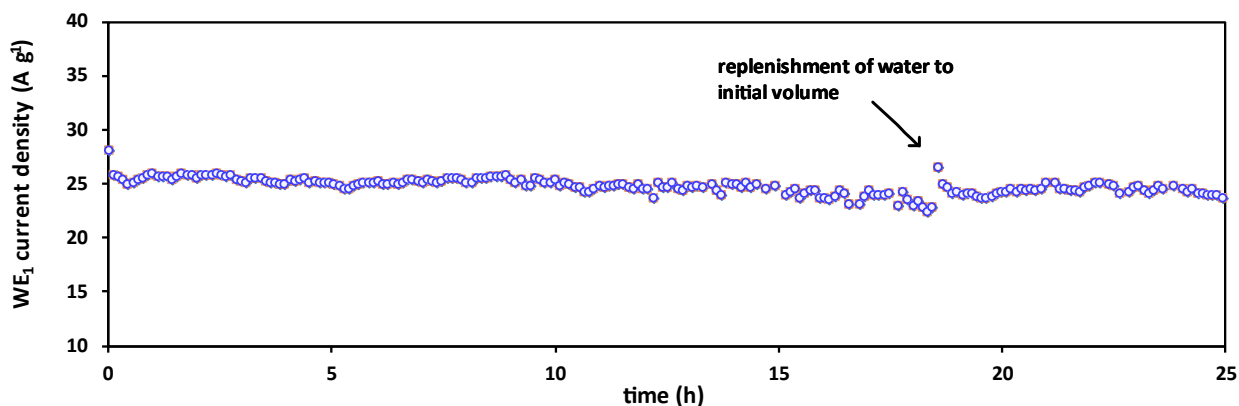


Figure 4.S13. Durability test of Ag_m/rGO/CoO_x electrode during selective water oxidation of simulated seawater, consisting of NaCl 0.5 M + KOH 1 M electrolyte. The chronoamperometric measurement is performed at room temperature, with the working electrode biased at +1.2 V vs Ag/AgCl.

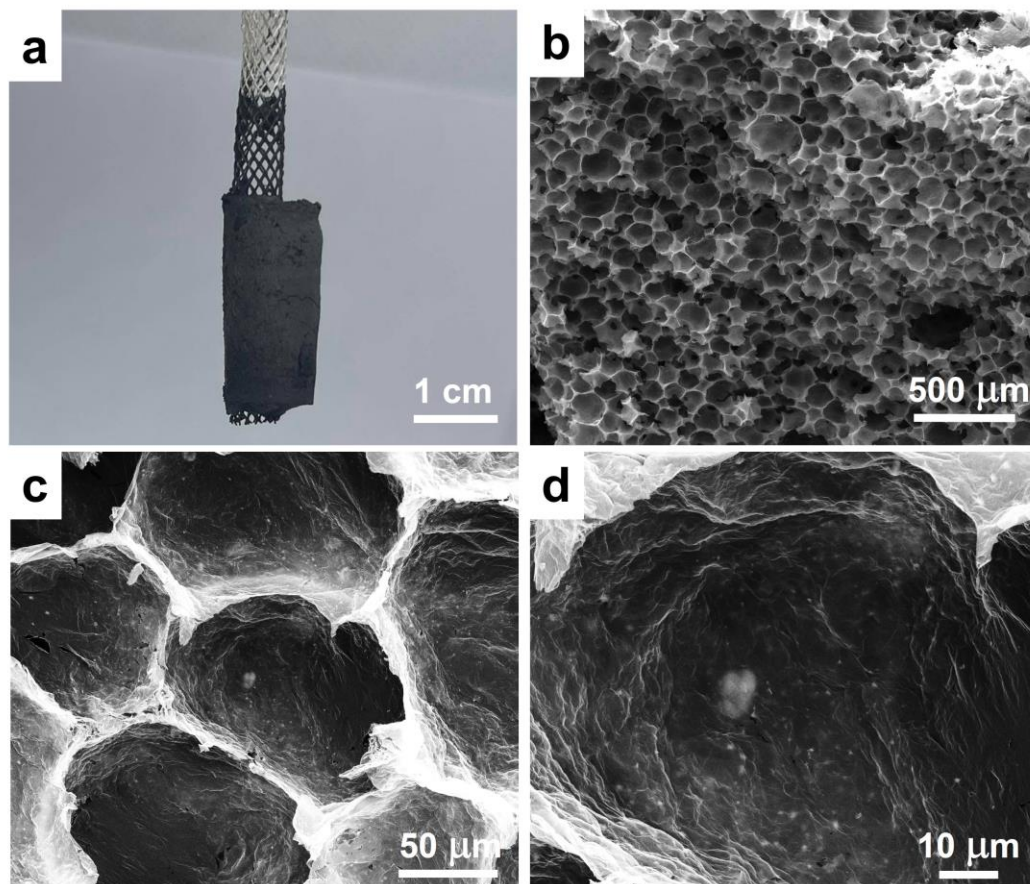


Figure 4.S14. Structural characterization of Ag_m/rGO/CoO_x electrode after selective water oxidation of simulated seawater for 25 hours, and subsequent washing in DI water before analysis. (a) Photograph and (b-d) SEM images of the electrode at different magnifications. The intact electrode porous structure and the particles embedded in the rGO pore walls closely resemble those recorded before electrolysis (**Figure 4.3**).

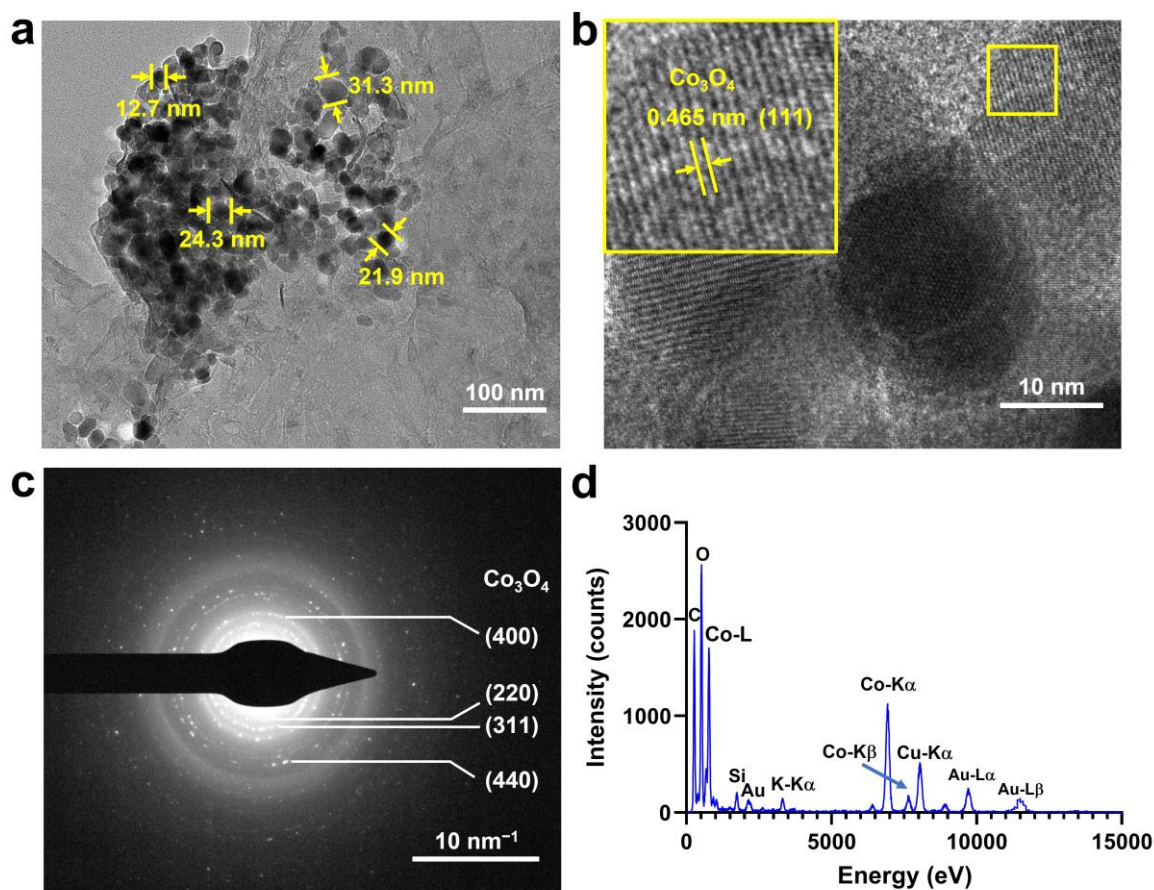


Figure 4.S15. Characterization of the catalytic particles inside the $\text{Ag}_m/\text{rGO}/\text{CoO}_x$ structure after selective water oxidation of simulated seawater for 25 hours, and subsequent washing in DI water before analysis. (a) TEM image of representative aggregates of cobalt oxide nanoparticles embedded in the rGO flakes. These sub-micrometric aggregates are similar to those imaged before electrolysis (**Figure 4.3** and **Figure 4.S10**). (b) HRTEM analysis of the cobalt oxide particles shown in panel a. The magnification of the area highlighted by the yellow square, shown as the inset figure, allows to measure the d -spacing of the nanoparticle and identify the (111) diffraction planes of the Co_3O_4 phase (JCPDS 00-42-1467). (c) The SAED patterns obtained from the particles in panel b reflect the most prominent diffraction bands of the cubic Co_3O_4 lattice. (d) EDS spectrum of the particles shown in panel a. The Au and Cu signals arise from the TEM grids utilized. After the electrolytic process, the physicochemical composition and morphology of the cobalt oxide catalytic particles in the electrode appear substantially unchanged.

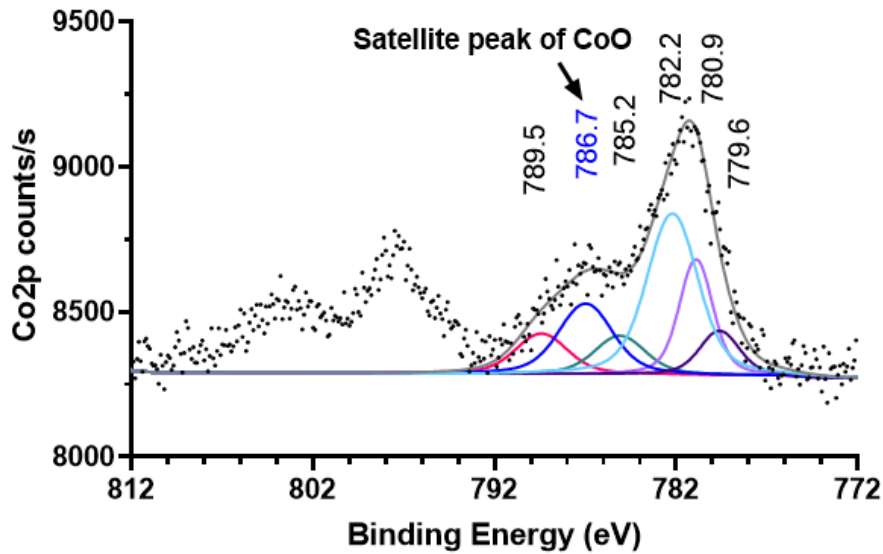


Figure 4.S16. High-resolution XPS Co2p spectrum of the Ag_m/rGO/CoO_x electrode after selective water oxidation of simulated seawater for 25 hours. The satellite peak at 786.7 eV indicates the presence of CoO, as it has been observed prior to electrolysis (**Figure 4.4b**), suggesting that the electrolytic process does not affect the composition and phases of the catalyst particles.

To estimate the limit of detection of free chlorine with our method, we conservatively assume an electric current of -0.5 mA cm^{-2} recorded on the electrode WE₂ to be the smallest that can be significantly distinguished from the background current recorded in the absence of free chlorine, i.e. -0.25 mA cm^{-2} (**Figure 4.5e**). The ClO⁻ production/detection rate can be calculated as:

$\nu_{\text{ClO}^-} [\text{mol h}^{-1}] = j [\text{C s}^{-1} \text{ cm}^{-2}] \times A [\text{cm}^2] \times 3600 [\text{s h}^{-1}] / n \times F [\text{C mol}^{-1}]$, where j is the net current density measured on WE₂ during the chronoamperometry (the reference current measured in the absence of free chlorine being subtracted), A is the area of WE₂ immersed in the electrolyte solution, n is the number of moles of e^- exchanged per mole of reactant (ClO⁻), and F is the Faraday constant. In our experiment, $j = 0.25 \text{ mA}$, $A = 2 \text{ cm}^2$, and $n = 2$ (the reduction of ClO⁻ to Cl⁻ is a bielectronic process, see equation 2 in the main article), which results in $\nu_{\text{ClO}^-} = 9.3 \text{ } \mu\text{mol h}^{-1}$.

The ClO^- detection rate can be expressed in ppm as follows: $v_{\text{ClO}^-} [\text{ppm h}^{-1}] = v_{\text{ClO}^-} [\text{mol h}^{-1}] \times 10^6 / \text{mol}_{\text{H}_2\text{O}} [\text{mol}]$, where water molecules alone are considered as reference. In our setup, the working electrode compartment contains 30 ml of electrolyte, which approximately corresponds to 1.67 mol of water ($MW_{\text{H}_2\text{O}} = 18 \text{ Da}$). In these conditions, the lowest ClO^- concentration detectable with our amperometric method (v_{ClO^-}) is 5.6 ppm h^{-1} .

Table 4.S3. Comparison between rGO/CoOx and the most active electrocatalysts reported for selective oxidation of alkaline simulated seawater (KOH 1 M + NaCl 0.5 M, pH = 14), at room temperature. Most of the catalytic activities in the literature are reported normalized by electrode area, but in the case of an extended 3D GO structure, it is more appropriate to compare specific activity per unit mass. All the catalysts chosen for this comparison are supported on thin sheets of nickel foam (1-1.5 mm thick) with areal density ranging from 35 to 45 g cm^{-2} .

The operational potentials of all the catalysts for comparison were iR compensated (85-95%) and referenced to the reversible hydrogen electrode (RHE) or reported as overpotentials (η) for the O_2 evolution reaction. At pH 14, the potentials of the RHE and Ag/AgCl/KCl 3.5 M reference electrodes are -0.827 and $+0.205 \text{ V vs SHE}$, respectively, and the thermodynamic onset of the OH^- oxidation to O_2 is $+0.402 \text{ V vs SHE}$. The values here reported (second column) are calibrated to the Ag/AgCl/KCl 3.5 M electrode using either one of the following equations: $E_{\text{Ag/AgCl}} = E_{\text{RHE}} - 0.827 - 0.205$ or $E_{\text{Ag/AgCl}} = \eta + 0.402 - 0.205$.

Catalyst	E vs Ag/AgCl (V)	j (mA cm^{-2})	Areal density (g cm^{-2})	j (A g^{-1})	Reference
Fe-Ni(OH) ₂ /Ni ₃ S ₂	+0.52	100	0.035-0.045*	2.2-2.9	[410]
Ni ₂ P-Fe ₂ P	+0.49	100	0.035	2.9	[409]
	+0.54	500	0.035	14.3	
NiMoN@Ni FeN	+0.48	100	0.035	2.9	[412]
	+0.54	500	0.035	14.3	
NiFe/NiS _x - Ni (Ni ³⁺)	+0.80	400	0.042	9.5	[411]
	+1.00	800	0.042	19.0	
	+1.15	1000	0.042	23.8	
Ag _m /rGO/ CoOx	+0.54	-	-	~9 ^a	This work
	+1.00	-	-	~19.5 ^a	
	+1.20	-	-	25 ± 5	

*As the value of catalyst areal density was not reported in this work, we calculated two values of current density per mass of catalyst, based on the lowest and the highest areal densities of commercial nickel foams.

^aThese values of current density per mass of catalyst do not result from chronoamperometric measurements and are rather estimated from the sweep voltammetric profile of the electrode.

At a low overpotential of 0.34 V, corresponding to 0.54 V vs Ag/AgCl, benchmark electrocatalysts such as Ni₂P-Fe₂P and NiMoN@NiFeN show superior specific activity compared to rGO/CoO_x, 14.3 (both catalysts) versus ~9 A g⁻¹, respectively. Also, the closed-pore structure of rGO/CoO_x is responsible for a smaller rate of current increase versus applied potential as compared to Ni foam-based catalysts, for example, from ~9 to 25 A g⁻¹ over 0.65 V for rGO/CoO_x versus a comparable 9.5 to ~24 A g⁻¹ over a 0.35 V change for NiFe/NiS_x-Ni. However, Ni foam-based catalysts are not intrinsically selective against chloride competition, which limits their application to a small potential range, while rGO/CoO_x electrodes can work in a wider potential range and pH window, thanks to the intrinsic selectivity resulting from their pore structure, as also discussed in the main article.

Bridging text

The assembly of GO or rGO flakes can be controlled at interfaces or in response to environmental stimuli. In the previous chapters, we have shown that emulsion and ice templating can be used to control the assembly of GO flakes. In the next chapter, we explored the self-assembly in response to changes in temperature. Since amphiphilicity is a critical factor for achieving the assembly of flakes at interfaces, we investigated in this chapter whether amphiphilicity can induce temperature responsiveness to GO or rGO flakes. We achieved this by mimicking the amphiphilic structure of PNIPAM in rGO flakes through surface functionalization with PDA, and attempted to achieve the following objectives:

- i. To introduce hydrophobic rGO domains and hydrophilic moieties with a one-step surface modification method using DA.
- ii. To control the surface chemistry, including the PDA modification and GO reduction degree, by varying reaction conditions.
- iii. To investigate the amphiphilicity and the colloidal properties of rGO/PDA flakes.
- iv. To study the rGO/PDA self-assembly in response to temperature change.
- v. To control the architecture of rGO/PDA based materials by temperature responsive self-assembly.

Chen, Y., Szkopek, T., & Cerruti, M.. Temperature Responsive Self-assembly of Polydopamine Reduced Graphene Oxide. Under revision.

5 Temperature responsive self-assembly of polydopamine reduced graphene oxide

5.1 Abstract

Graphene, graphene oxide (GO), and reduced graphene oxide (rGO) can respond to environmental stimuli such as pH, ionic strength and light by themselves, but not to temperature. Here we show that surface modification of rGO with polydopamine (PDA) leads to a temperature-responsive composite material, even though neither rGO nor PDA have intrinsic temperature responsiveness. Reducing GO with dopamine resulted in rGO/PDA flakes with hydrophilic PDA clusters attached to hydrophobic rGO domains, which mimics the amphiphilic structure of temperature responsive poly(N-isopropylacrylamide) (PNIPAM). The rGO/PDA flakes self-assemble at temperature higher than 30 °C, causing flake aggregation and precipitation in suspensions with concentration of 1 g/L, which is reversible upon cooling, shaking, and re-heating. A solution-to-gelation transition occurs upon heating suspensions with concentration of 10 g/L. Nacre-like films and porous monoliths are obtained by drying rGO/PDA suspensions at different concentrations. Films and porous monoliths obtained by drying suspensions that are previously self-assembled through heat have more compact structures compared to those obtained with suspensions that are not heated. Overall, this work introduces PDA modification of rGO as a one-step supramolecular strategy to enable temperature response in rGO without introducing intrinsically temperature-responsive components. A similar strategy could be applied to create amphiphilic structures in other hydrophobic nanomaterials, such as boron nitride, and develop

responsive systems whose self-assembly in suspension and architectural features realized upon drying can be controlled by temperature.

5.2 Introduction

As a two-dimensional (2D) form of sp^2 hybridized carbon atoms in a hexagonal lattice, graphene has attracted tremendous attention for its electrical [2],[447], mechanical [448], and thermal properties [449]. Graphene oxide (GO) and reduced graphene oxide (rGO) are two derivatives of graphene. Because of the abundant oxygen-containing groups present on the basal plane and edges, GO flakes can be dispersed in water with excellent colloidal stability. By removing oxygen-containing groups, rGO can be obtained with restored hydrophobic sp^2 domains with mechanical, thermal and electrical properties similar to graphene [7]. Sol-gel transition and assembly at interfaces are commonly used self-assembly-based methods to build graphene-based materials starting from GO and rGO flakes [4].

The self-assembly of GO and rGO can be induced by external triggers [31],[91],[450]–[453]. The flakes in suspensions can assemble into aggregates or hydrogels responding to changes in pH [91],[451], and ionic strength [31],[452]. For example, due to the surface chemistry of GO, the deprotonation at high pH and protonation at low pH of oxygen containing groups can cause a transition from suspended GO flakes to a GO hydrogel, due to changes in electrostatic and van der Waals interactions between the flakes [8],[96],[454], leading to responsive systems for applications such as drug delivery [455],[456], filtration [457], and sensing [458].

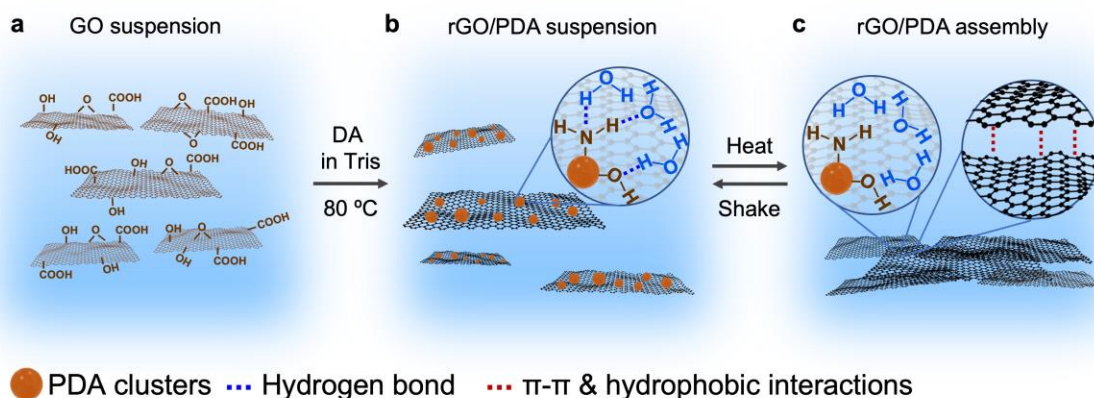
The self-assembly of GO and rGO cannot directly respond to temperature. The only temperature responsive systems shown so far had the GO or rGO flakes modified with temperature-responsive polymers, such as poly(N-isopropylacrylamide) (PNIPAM) [238],[254], poly(N-vinylcaprolactam) [256], and poly(ethylene oxide) [459]. For instance, when grafted with PNIPAM, GO flakes in

suspension can aggregate upon heating because of increased hydrophobicity of PNIPAM at temperatures higher than 30-33 °C [240],[254]. At lower temperature, PNIPAM chains in water display an expanded coil conformation because of hydrogen bonding between hydrophilic amide side groups and water [460]. These chains go through coil-globule transitions at the lower critical solution temperature (LCST) because hydrogen bonds between hydrophilic groups and water break [219],[234], and the hydrophobic isopropyl groups and hydrocarbon backbone in PNIPAM dehydrate while hydrophobic interactions prevail [32]–[37]. The functionalization of GO or rGO with temperature-responsive polymers requires multi-step synthesis and purification process, *e.g.*, click chemistry, free-radical polymerization, atom transfer radical polymerization, or reversible addition-fragmentation chain-transfer polymerization [245],[461]. In the resulting systems, GO and rGO flakes serve merely as passive, supporting platforms to improve the conductivity or mechanical strength of the temperature responsive materials [9],[238]. These systems do not exploit interactions between GO flakes to achieve temperature responsiveness of GO or rGO, like in pH-sensitive systems.

In this work, we take inspiration from the most studied temperature responsive polymer, PNIPAM, to achieve an rGO-based temperature responsive system that does not include any element that is temperature responsive on its own. To mimic the amphiphilic structure of PNIPAM, we aim to exploit the hydrophobic rGO domains to provide hydrophobic and π - π interactions to drive self-assembly and introduce on rGO hydrophilic groups that can stabilize the flakes in water. We hypothesize that upon heating, hydrogen bonds between the hydrophilic groups and water break and the hydrophobic and π - π interactions between rGO flakes dominate, therefore causing temperature-induced self-assembly.

To create this structure, we turn to a biomimetic surface functionalization approach using polydopamine (PDA). Dopamine (DA) is a relative of 3,4-dihydroxyphenylalanine (DOPA), an amino acid highly expressed in marine mussel foot proteins, responsible for the strong adhesion of mussels on a variety of surfaces [38]. Under alkaline conditions ($\text{pH} > 7.5$), DA oxidizes and polymerizes into PDA, a layer that sticks onto almost any material and has been used to enhance the hydrophilicity of surfaces [39],[40].

By heating DA in alkaline conditions in the presence of GO, PDA clusters can be formed on the surface of the flakes [42]–[45], and GO can be reduced to rGO due to the release of electrons during DA polymerization (Scheme 1a) [42],[300],[303]–[306]. Here we show that by optimizing the ratio between GO and DA, we control the surface chemistry of rGO/PDA flakes. The resulting rGO flakes functionalized with PDA clusters can respond to heat like PNIPAM: at room temperature, the rGO/PDA flakes are well dispersed in water thanks to the hydrophilicity of the PDA clusters (**Scheme 5.1**); upon heating to as low as 30 °C, the hydrogen bonds between PDA and water are weakened, and hydrophobic and π - π interactions between rGO/PDA flakes prevail, resulting in self-assembly of the flakes (**Scheme 5.1**). The process is reversible by cooling and shaking. This work thus introduces a mussel-inspired surface modification strategy to induce temperature responsiveness in rGO without any element that is temperature-responsive on its own.



Scheme 5.1. Schematic illustrations of (a) GO in water suspension, (b) transformation of the GO suspension into an rGO/PDA suspension where rGO flakes are modified with PDA clusters. The flakes are stable in water due to the formation of hydrogen bonds between PDA and water. (c) Temperature-induced self-assembly of rGO/PDA in water due to weakening of hydrogen bonds and predominance of π - π and hydrophobic interactions.

5.3 Results and discussion

5.3.1 Fabrication and characterization of rGO modified with PDA

We first studied the surface chemistry of the pristine GO flakes through X-ray photoelectron spectroscopy (XPS). Results showed a C:O atomic ratio of 1.5 ± 0.1 and the presence of C-O and C=O oxygen-containing groups on GO (**Figure 5.S1**) Atomic force microscopy (AFM) of GO flakes (**Figure 5.S1**) showed a thickness of ~ 1 nm, corresponding to single layer GO flakes [318],[462]. Results concerning the hydrodynamic diameter and surface zeta potential of GO will be discussed in the following section.

GO/DA dispersions in basic condition (pH=8.5, Tris buffer) were prepared with different weight percentage (wt.%) of DA relative to GO, and heated at 80 °C for 24 hours with stirring [300],[303]. In these conditions, as we will show below, GO was reduced to rGO while DA was polymerized. As such, these samples will be named RP10, RP50, and RP90, where R refers to rGO, P to PDA, and the number to the DA wt.% relative to GO. For comparison, samples with 50 wt.% DA relative to GO were prepared at 25 °C; PDA can still form in these conditions and bind to GO, but the

resulting GO is less reduced [43],[279],[309],[307],[308]. Therefore, these samples will be called GP50, where G stands for GO, to differentiate from the more reduced rGO obtained when the reaction is performed at 80 °C. After synthesis, all RP samples and the GP50 sample were well dispersed and stable in water thanks to PDA's affinity to water (**Figure 5.1a**) [300].

The Raman characteristic peaks of PDA overlap with the D and G bands of rGO [44], therefore, the reduction of GO by dopamine was evaluated via ultraviolet-visible (UV-vis) spectrophotometry. The absorbance peak at 230 ± 1 nm (**Figure 5.1.b**) of GO is attributed to the π - π^* transition of aromatic carbon bonds. A peak in the same position is found for GP50, suggesting GO remained oxidized in GP50. This peak significantly red-shifted to 251 ± 0.5 nm on RP10, 267 ± 1 nm on RP50, and 269 ± 1 nm on RP90, which indicates the reduction of GO by DA [463] and showed the increase in GO reduction degree with increasing DA amount (**Figure 5.S2**) [300],[464],[465]. This was also confirmed by the significant increase in absorbance in the spectral region above 230 nm due to the restoration of electronic π -conjugation (**Figure 5.S2** and **Figure 5.1b**) [92].

XPS survey results showed that the atomic percentage (atom%) of nitrogen on RP significantly increased compared to GO, proportionally to the amount of DA added (**Figure 5.1c**, **Table 5.S1** and **Figure 5.S3**), thus confirming the presence of PDA on the rGO surface [286]. The GP50 also showed significantly higher atom% of nitrogen compared to GO due to the formation of PDA (**Figure 5.1c**). High resolution spectra of C1s were used to quantify relative amounts of hydrophilic groups on the surface of GO, RP and GP. Primary and secondary amine, catechol, and quinone groups from PDA, as well as the remaining oxygen containing groups from rGO, contribute to the overall atom% of C-N (~ 285.8 eV), C-O (~ 286.6 eV) and C=O (288.4 eV) bonds (**Figure 5.1d**, **Table 5.S2** and **Figure 5.S3**) [300],[309],[466],[467]. The total atom% of C-N, C-

O and C=O on RP samples were significantly lower than on GO and GP, suggesting the reduction of GO in the RP samples, in agreement with UV-vis results. RP50 showed the lowest total atom% of C-N, C-O and C=O because of reduction and the moderate amount of PDA present on this sample.

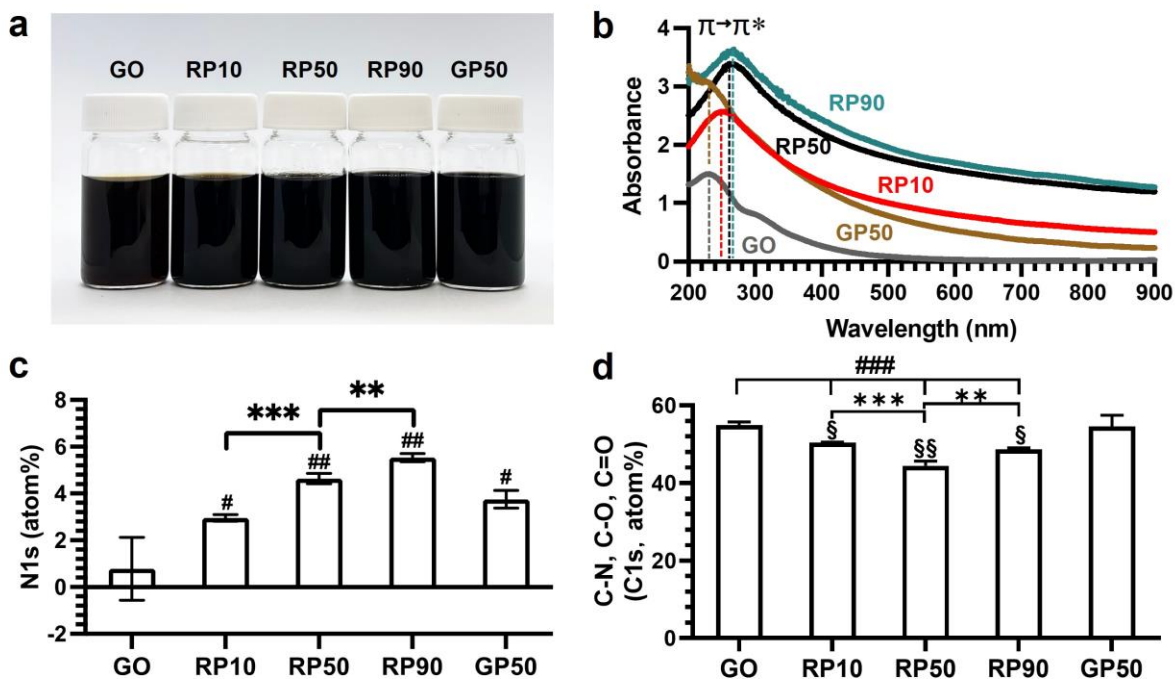


Figure 5.1. Characterization of GO, RP and GP. (a) Digital photographs showing GO, RP and GP suspensions in water (1 g/L). Pictures were taken 3 months after suspension preparation. (b) Representative UV-vis absorption spectra of GO, RP10, RP50, RP90 and GP50. (c) Atomic percentage of N1s from XPS survey scans measured on GO, RP10, RP50, RP90 and GP50. (d) The total atomic percentage of C-N, C-O and C=O bonds (binding energy \sim 285.8, 286.6 and 288.4 eV respectively), evaluated from high resolution C1s XPS spectra. $n = 3$ independent experiments. The data are represented as the mean \pm standard deviation. The #, * and § signs indicate statistically significant differences, #: between GO and RP10, RP50, RP90; *: between RP10 and RP50, RP50 and RP90; §: between GP50 and RP10, RP50, RP90. Differences are based on Student's t -test (§ $P < 0.05$, ** and §§ $P < 0.01$, ### and *** $P < 0.001$).

5.3.2 Temperature induced self-assembly

The GO, GP and RP dispersions (1.5 mL, 0.05 g/L) were kept at different temperatures for 30 mins, ranging between 25 and 70 °C. The digital photographs (Figure 5.2a) and optical microscopy images showed that flakes of RP10 (Figure 5.S4), RP90 (Figure 5.S4) and GP50 (Figure 5.2b)

remained well dispersed at all temperatures, whereas the RP50 flakes started to aggregate at 30 °C and aggregated further at 70 °C (**Figure 5.2c** and **Figure 5.S4**).

The aggregation was further confirmed by measuring the UV-vis transmittance of the samples at 750 nm. The GO, RP and GP samples had no absorbance peak at 750 nm (**Figure 5.1b**), indicating the flakes don't emit or absorb light at this wavelength, thus, we can measure the transmittance change only due to the aggregation as function of temperature (**Figure 5.2d**). The recorded transmittance values were constant for all samples except for RP50, which instead showed an increase in transmittance as the flakes assembled and sedimented upon heating. The transmittance increased continuously, without sudden changes over the course of the experiment. The lack of a dramatic change in transmittance at a certain temperature implies that, different from PNIPAM, the temperature-induced assembly is a continuous process for RP50 flakes.

Zeta potential measurements, estimating the surface charge of flakes [468], showed no significant change for the GO, RP10, RP90 and GP50 suspensions at 25 and 70 °C (**Figure 5.2e**), which confirmed their stability in water. On the other hand, the zeta potential of RP50 significantly decreased in magnitude when measured at 30 °C, and further decreased at 70 °C, indicating weakened electrostatic repulsions and hence decreased stability of sheets. The lower zeta potential value of RP compared to GO and GP can be attributed to the presence of pyrrole carboxylic acid moieties in PDA [310]–[312].

Static water contact angle measurements similarly showed a significant increase at 70 °C only for RP50 (**Figure 5.2f**), indicating the RP50 flakes became more hydrophobic upon heating, which confirms the importance of hydrophobicity increase in the separation of flakes from water.

Dynamic light scattering (DLS) results showed that the hydrodynamic diameter (D_h) of the original GO flakes was $2.0 \pm 0.1 \mu\text{m}$. The D_h of RP50 increased as the temperature rose (**Figure**

5.S5), while the Dh of RP10, RP90 and GP50 remained stable, confirming visual and optical microscopy observations.

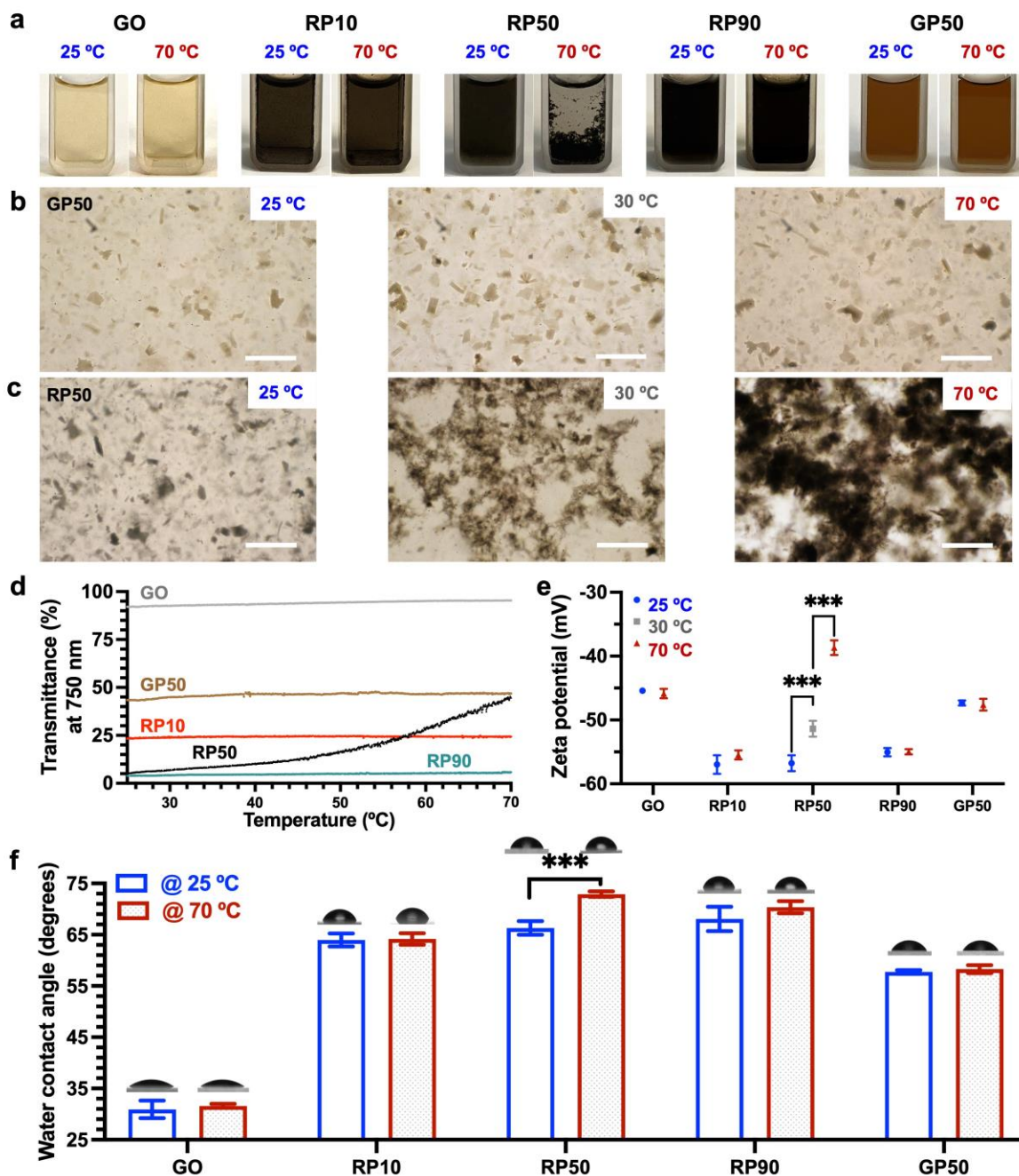


Figure 5.2. Temperature responsive self-assembly of RP. (a) Digital photographs showing the suspensions or aggregations of RP50 and GP50 at 25 and 70°C (1.5 mL, 0.05 g/L). Optical microscopy images of GP50 (b) and RP50 (c) in water at 25 °C, 30 °C, and 70 °C. Scale bar = 100 μ m. The liquid samples were carefully added onto petri dishes and the images were taken without covers. (d) Representative UV-vis transmittance values measured at 750 nm for GO, RP10, RP50, RP90 and GP50 (concentration 0.05 g/L) as the temperature gradually increased from 25 °C to 70

°C at a speed of 0.5 °C/min. (e) Zeta potential of GO, RP10, RP50, RP90 and GP50 flakes at 25 °C and 70 °C. Zeta potential of RP50 was also measured at 30 °C to explain the assembly observed at a lower temperature. (f) Static water contact angle of pristine GO, RP10, RP50, RP90 and GP50 at 25 °C and 70 °C. Representative images showing water droplets spreading on the air-dried flakes on glass slides are shown on top of the bars. $n = 3$ independent experiments. The data are represented as mean \pm standard deviation. Asterisks indicate statistically significant differences calculated by the Student's t -test ($***P < 0.001$).

Transmittance electron microscopy (TEM) and selected area electron diffraction (SAED) confirmed RP50 flake stacking during the gradual assembly process upon heating. At 25 °C, the RP50 flakes were composed of few layers (**Figure 5.3a**) as the SAED pattern showed distinct diffraction spots in a six-fold pattern, typical of crystalline graphene regions with one or two layers [84],[102]. More stacked layers were found at 30 °C, and both six-fold spots and rings were visible in the SAED pattern, indicating merging of diffraction spots due to the greater number of layers of rGO in the aggregates (**Figure 5.3b**). At 70 °C, only rings were visible in the SAED pattern, indicating further aggregation and superposition of multiple layers of RP50 (**Figure 5.3c**). AFM revealed single- and two- layered flakes with thickness approximately 1~2 nm at 25 °C, and clusters on flakes with average height of 3 nm that can be ascribed to PDA (**Figure 5.S6**), agreeing with previous studies that dopamine can assemble into PDA clusters on rGO and other substrates [42],[292],[310]–[312]. The topography of flakes at different temperature and corresponding histogram of counts versus height are shown in **Figure 5.3d-f**. The first peak (labeled as *) shown in the histograms refers to the height of the silicon substrate used for AFM observation (purple in the AFM topography images in **Figure 5.3d-f**). The overall height of most flakes, corresponding to the second peak in the histograms (labeled as \blacklozenge), shifted to higher values as the temperature increased to 30 °C (**Figure 5.3e**). At 70 °C, the two peaks were not visible, and instead a broad peak was shown, indicating the overall increased height due to the further assembly of sheets (**Figure 5.3f**).

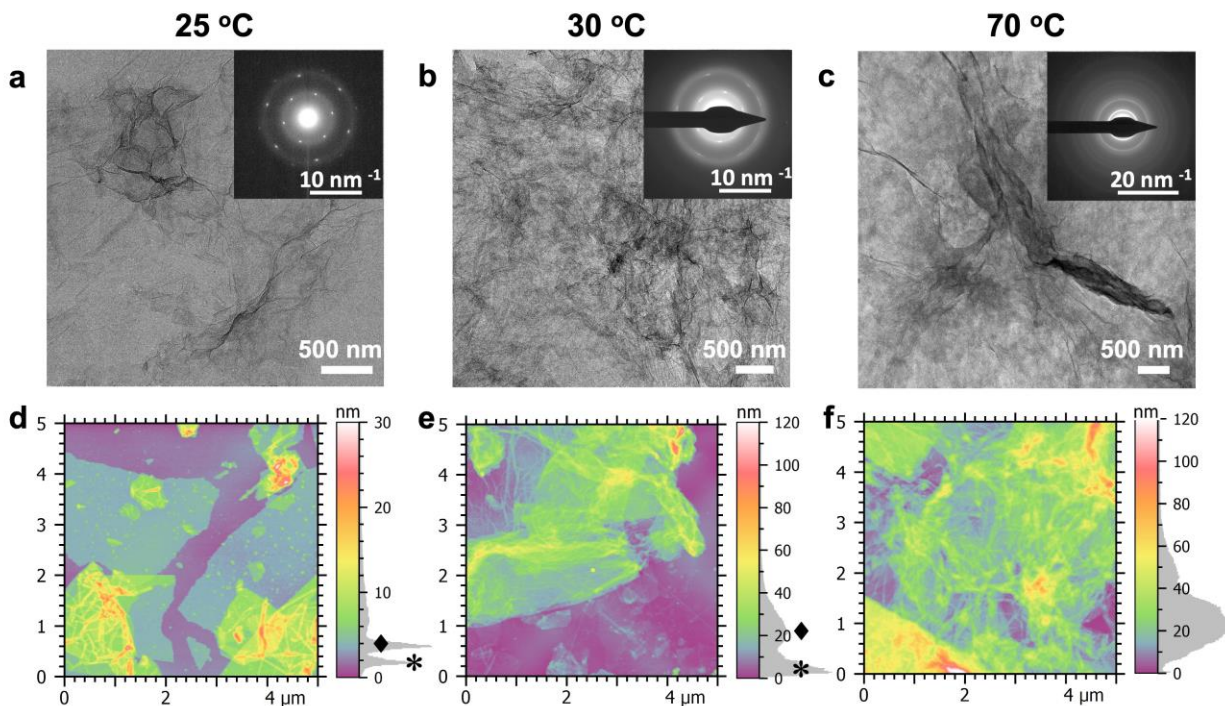


Figure 5.3. TEM and AFM visualization of temperature-induced self-assembly of RP50. (a-c) TEM images of RP50 flakes at 25 °C (a), 30 °C (b), and 70 °C (c). Insets: corresponding SAED patterns. (d-f) AFM images and corresponding histogram of counts versus height of RP50 at 25 °C (d), 30 °C (e), and 70 °C (f).

These results confirm that rGO/PDA can respond to temperature increase with a mechanism similar to that of PNIPAM. Upon heating, the hydrophilic PDA clusters dehydrate and hydrogen bonding between PDA and water weaken. Hydrophobic and π - π interactions between sp^2 domains on RP50 prevail, causing the RP50 flakes to stack as their stability in water decreases. As a result, the PDA clusters are enclosed within the aggregates and cause the overall zeta potential to become less negative compared to that measured on dispersed flakes at 25 °C. The increase in zeta potential weakens the electrostatic repulsion between RP50 flakes and further promotes the assembly. As the temperature increases, more PDA clusters dehydrate, and more flakes assemble into larger aggregates, until eventually the aggregates phase separate and sediment rapidly.

The other GP and RP samples, obtained by varying DA to GO ratio and reaction temperatures, are stable upon heating because of their different surface chemistry compared to RP50. GP50 and

RP10 are more oxidized than RP50 and have more hydrophilic groups on their surface. This ensures their stability in water even as the temperature rises, due to the lack of hydrophobic and π - π interactions that would otherwise drive the temperature-dependent assembly process. Even though RP90 is more reduced than RP50 (**Figure 5.1b**), the larger amount of PDA formed homogenous coatings on RP90 (**Figure 5.S7**) with significantly more hydrophilic groups than RP50 (**Figure 5.1d**); this stabilized RP50 flakes in water and limited the hydrophobic and π - π interactions between flakes.

A difference between PNIPAM and RP50 lays in the reversibility of the temperature-driven assembly: when cooled down to 25 °C, the RP50 aggregates cannot spontaneously disassemble, which was also previously observed for PNIPAM modified GO and rGO flakes [254],[255],[259],[261],[469]. However, it was possible to re-disperse the RP50 aggregates by cooling to room temperature and gently shaking the vial for 30 seconds; the re-dispersed flakes aggregated again upon heating to 70 °C (**Figure 5.4a**). The dispersion-aggregation transition was repeatable, as shown in **Figure 5.4b** by changes in UV-vis transmittance at 750 nm; the suspension-aggregation transition as temperature increasing was similar to that measured during the initial assembly process (inset in **Figure 5.4b**).

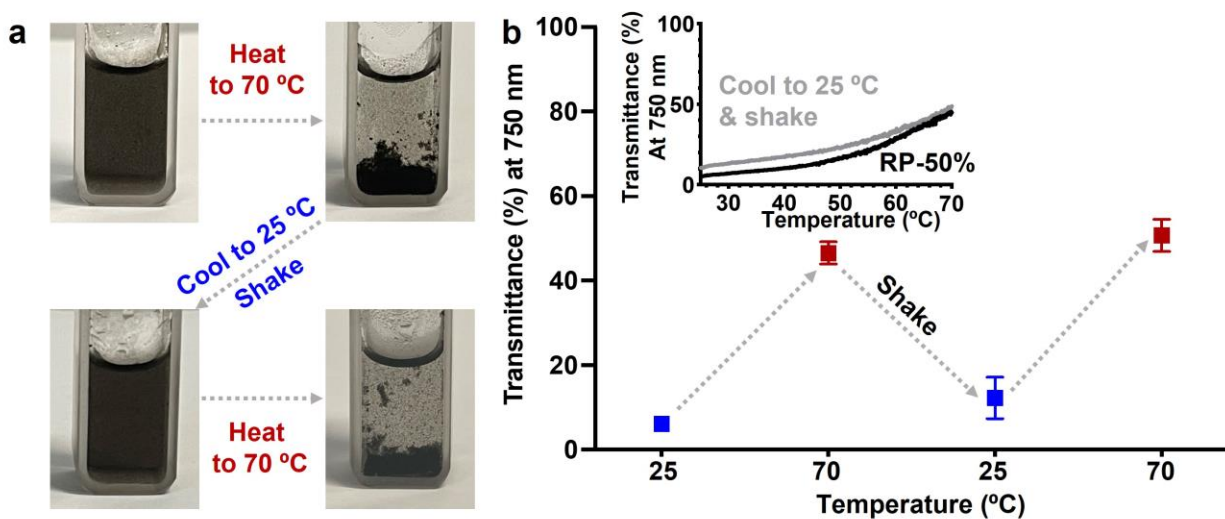


Figure 5.4. Reversibility of temperature-induced self-assembly. (a) Digital photographs showing suspensions or aggregations of RP50 (0.05 g/L) upon heating to 70 °C, cooling to 25 °C and shaking, as well as heating again to 70 °C. (b) UV-vis transmittance values measured at 750 nm for RP50 (0.05 g/L) at 25 °C, 70 °C, cooled down to 25 °C and redispersed, and re-heated to 70 °C. Inset: representative UV-vis transmittance values measured at 750 nm while heating (0.5 °C/min) RP50 (black), and re-dispersed RP50 (light grey).

5.3.3 Controlled structure of 2D and 3D materials via temperature induced self-assembly

In temperature responsive polymers, the increased hydrophobicity caused by temperature increase can lead to the formation of three-dimensional networks also known as hydrogels, through hydrophobic interactions. The gelation was observed with concentrated (10 g/L) suspensions of RP50: a gel was formed upon keeping at 70 °C, as the flakes assemble through hydrophobic and π - π interactions (**Figure 5.5a**). None of the other concentrated suspensions of RP samples nor GP50 were able to form a gel upon heating (**Figure 5.5a**), consistent with the behavior of low concentration dispersions (**Figure 5.2a**).

Figure 5.5b and **c** show scanning electron microscopy (SEM) images of an RP50 suspension (10 g/L) and of the corresponding hydrogel formed upon heating to 70 °C, after freezing at -20 °C for 24 hours and lyophilizing. The freeze-dried suspension showed a 3D network with large pores

(**Figure 5.5b**), while the freeze-dried hydrogel presented smaller and more compact pores (**Figure 5.5c**). This can be explained considering that during the freezing process, ice growth inside the RP50 hydrogels was hindered by the aggregated flakes, resulting in smaller pores after lyophilization; whereas if the RP50 suspension was frozen before gelation, flakes loosely contacting each other allowed ice crystals to grow. This difference was not observed for the GP50 samples (**Figure 5.5d and e**).

A similar phenomenon was observed if the RP50 flakes were assembled into membranes by air drying the suspensions (1 g/L) drop-casted on a polystyrene substrate either at 25 °C or after heating at 70 °C. After air drying at 25 °C, the films were peeled off the polystyrene substrate. Both films showed a layered structure, but those formed with the suspensions at 25 °C (**Figure 5.5f**) showed a less dense structure than the films formed with the suspensions heated at 70 °C (**Figure 5.5g**). The temperature-induced self-assembly enhanced the stacking of the rGO layers in films by improving the connection between flakes [470]. Previous studies found that the compact packing and higher alignment of flakes in rGO films enhanced the electrical conductivity [471]–[473]. We observed this phenomenon also for the RP50 films: the films formed with RP50 suspensions that were heated to induce self-assembly had higher electrical conductivity compared to films formed with unheated RP suspensions (**Figure 5.5h**). To verify that this result was not because of a difference in conductivity due to partial reduction while assembling the films at 70 °C, we heated to 70 °C the films prepared with the room temperature RP50 suspensions, and found no significant differences with the conductivity measured on the unheated films (**Figure 5.5h**). X-ray diffraction (XRD) spectra of films revealed broad diffraction peaks suggesting a wide range of interplanar spacing as the result of introduction of PDA and the reduction of GO (**Figure 5.S8**).

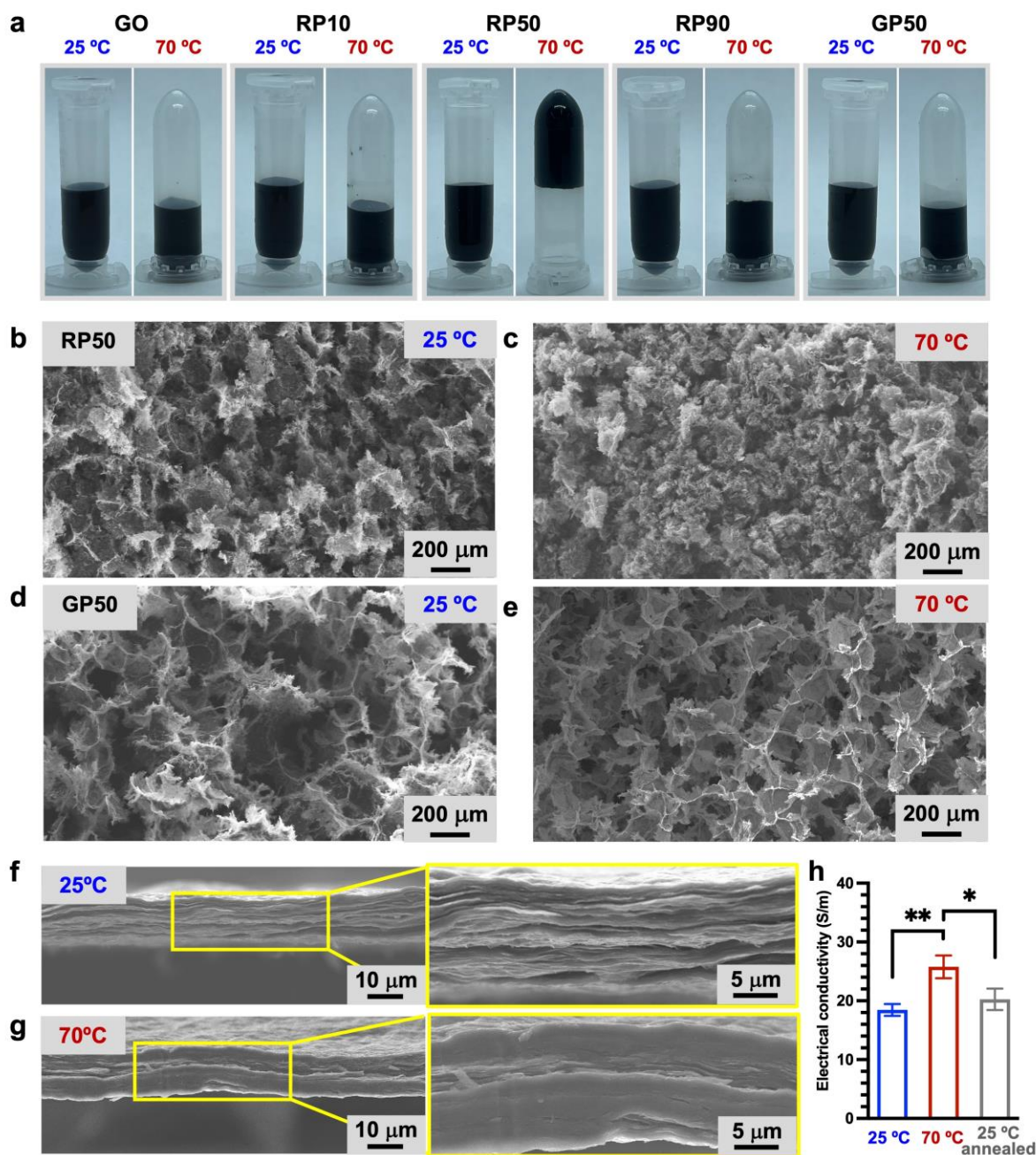


Figure 5.5. (a) Digital photographs showing GO, RP10, RP50, RP90, and GP50 (10 g/L) before and after heating at 70 °C for 30 minutes. SEM images of freeze-dried RP50 suspension (10 g/L) (b) and of an RP50 hydrogel formed after heating at 70 °C (c), and of GP50 suspensions (10 g/L) before (d) and after (e) heating at 70 °C. (f-g) SEM images of cross-sections of films prepared by drop-casting RP50 suspensions (1 g/L) at 25 °C (f) or heated at 70 °C (g). (h) Electrical conductivity of films prepared from RP50 suspensions (1 g/L) at 25 °C and 70 °C, and the films prepared from suspensions at 25 °C but annealed at 70 °C. $n = 3$ independent experiments, measured through a four-point van der Pauw method. The data are represented as the mean \pm standard deviation. The asterisks indicate statistically significant differences calculated by the Student's t -test (* $P < 0.05$, ** $P < 0.01$).

5.4 Conclusions

We developed temperature responsive rGO/PDA flakes by mimicking the amphiphilic structure of PNIPAM, where the flakes have hydrophobic rGO regions and hydrophilic PDA clusters bound on the rGO surface. The temperature-induced assembly of rGO/PDA is a continuous process that starts at approximately 30 °C and leads to flake sedimentation at 70 °C in low concentration suspensions, or hydrogel formation in high concentration suspensions. rGO/PDA flake aggregates do not disassemble spontaneously upon cooling, but can be dispersed again by mild shaking, and then re-assembled upon heating. Compact, small pores were observed in the freeze-dried hydrogels compared to the freeze-dried suspensions. Films with aligned rGO/PDA flakes could be prepared by air-drying the suspensions; the flakes were more compact packed in the films prepared with heated suspensions at 70 °C, which led to higher electrical conductivity in the resulting films.

This study introduces PDA surface modification of rGO as a one-step supramolecular strategy to induce temperature responsiveness in rGO flakes without the addition of any intrinsically temperature-responsive component. Since PDA can bind onto virtually any material, a similar strategy may potentially be adapted and extended to other hydrophobic nanomaterials (*e.g.*, carbon nanotubes, boron nitride flakes) to form PDA clusters that would impart amphiphilicity to the resulting composites. This in turn would enable temperature-induced self-assembly, allowing to control the properties of both suspensions and resulting solid materials.

5.5 Methods

5.5.1 Materials

Graphene oxide paste (25 wt%) was purchased from Abalonyx which was synthesized by a modified Hummers' method (product number 1.2A). Dopamine hydrochloride, tris(hydroxymethyl)aminomethane (tris salt, >99.8%), dialysis tubing cellulose membrane

(molecular weight cut-off 14,000 Da) were purchased from Sigma-Aldrich. Hydrochloric acid (HCl, 36.5-38%, ACS grade) was purchased from Fisher Scientific.

5.5.2 Preparation of polydopamine modified GO and rGO suspensions

GO paste were dispersed into GO suspension in deionized (DI) water at 2 g/L through stirring for 20 mins, following 20 mins of sonification. The Tris buffer (pH=8.5) was prepared following previous study [309]. 1.514 g of Tris salt was dissolved in 50 mL of DI water, and 0.32 mL of HCl was added into the solution. After stirring for 10 mins, 250 mL of DI water was added to obtain Tris-buffer with pH at 8.5. The synthesis of GO/PDA and rGO/PDA started with making 100 mL DA in Tris-buffer solution and adding 100 mL GO suspension (2 g/L) to the DA solution under stirring at room temperature for 30 mins. The DA concentration was calculated according to the weight ratio between DA and GO. To prepare GO/PDA, the mixed solution was stirred at room temperature for 24 hours. To prepare rGO/PDA, the mixing solution was heated under reflux at 80 °C in an oil bath with stirring for 24 h. The obtained dispersions were purified by dialysis against DI water with dialysis tubing cellulose membranes at room temperature for 72 hours. The DI water was changed every 24 hours.

5.5.3 Fabrication of RP50 porous monoliths and films

To produce porous monoliths, the hydrogels were obtained by keeping the RP50 (10 g/L, concentrated by centrifugation) in Eppendorf tubes at 70 °C for 30 mins in a water bath (Hedday Lab Water Bath Heater, accuracy 0.1 °C). Then, the unheated RP50 (10 g/L) suspensions and the hydrogels were frozen at -20 °C for 24 hours. After the freezing process, the samples were immediately freeze-dried at 0.22 mbar with collector temperature at -84 °C using Labconco FreeZone Freeze Dryer for 48 hours to eliminate the water and obtain porous monoliths.

To produce films, the unheated and heated (at 70 °C for 30 mins) RP50 (1 g/L) samples were carefully poured onto polystyrene dishes and dried in the air at 25 °C without disturbing. Films were peeled off for further experiments. For comparison, the films prepared by unheated RP50 were annealed at 70 °C for 30 mins.

5.5.4 Characterization

We analyzed surface elemental composition by X-ray photoelectron spectroscopy (XPS) on a Thermo Scientific K-Alpha photoelectron spectrometer (Thermo Fisher Scientific Inc., Waltham, Massachusetts, USA), equipped with an incident Ka X-ray source (1486.6eV, 0.843 nm) and an ultrahigh vacuum chamber (10^{-9} Torr). We used a flood gun of low energy electrons to prevent surface charging during the measurements. To detect elemental information and atomic content, we conducted survey scans in the step size of 1 eV and high-resolution scans for each detectable element in the step size of 0.1 eV. The analyzed spots were in 400 μm in diameter. We used Avantage Software to analysis the survey and high-resolution spectra and fitted C1s curves with five components: C–C (C=C), C-N, C–O, C=O, and π - π^* shake up at 284.8, 285.8, 286.6, 288.4 and 290.8 eV respectively [300],[309],[466],[467].

We obtained heated samples by keeping the suspensions at various temperature for 30 mins in the water bath and submitted to hydrodynamic diameter, zeta potential and contact angle analysis, and observed the flakes through optical microscopy, transmission electron microscopy (TEM), and atomic force microscopy (AFM).

We captured images of the dispersions or aggregations with an optical microscope (Olympus CKX41 connected with Canon EOS Rebel T3 single-lens reflex).

We measured the hydrodynamic diameter and zeta potential of RP and GP (0.05 g/L) with the Zetasizer Nano ZS (Malvern Instruments). We carried out dynamic light scattering (DLS) at a

scattering angle of 173° , and reported the intensity weighted mean size (Z-average) as the hydrodynamic diameter. The zeta potential that estimates the surface charge of flakes was obtained from electrophoretic mobility measurements and calculated from the Smoluchowski model with Henry's equation.

We performed TEM observations on a Thermo Scientific Talos F200X G2 S/TEM equipped with a Schottky field emission source, operating at an accelerating voltage of 200 kV. We prepared the samples by dropping materials onto a standard carbon-coated copper grid. We performed selected area electron diffraction (SAED) with the same instrument.

We performed AFM analysis on Cypher VRS scanning probe microscopy (SPM) equipped with an ARC2 controller (Asylum Research - Oxford Instruments, Santa Barbara, CA) in AC mode in air. The probes used were ACTA (Applied Nanostructures, Mountain View, CA) with nominal frequency of 300 kHz, spring constant of 37 N/m and tip radius 6 nm with scanning rate of 1 Hz. We prepared the samples by dropping materials on to silicon wafer and dried in air at room temperature.

For contact angle measurements, we drop-casted GP and RP samples (1 g/L) before and after heating (at 70° for 30 mins) on cleaned glass substrates and dried at room temperature. The wettability was measured against water through static contact angle using the OCA 150 Goniometer (DataPhysics Instrument). The dosing volume is 5.00 μL , and the dosing rate is 1.00 $\mu\text{L/s}$.

We performed ultraviolet-visible (UV-vis) measurements with Evolution 260 Bio UV-vis spectrophotometer, connected with a Peltier temperature controller and temperature probes (Thermo Scientific). We recorded the electronic absorption spectra of suspensions (0.05 g/L) at 25°C in the wavelength range of 200-900 nm with bandwidth of 1 nm. To monitor the self-assembly

process of flakes, we measured the transmittance of suspensions (0.05 g/L) with interval time of 0.1 min at wavelength of 750 nm as temperature increased from 25 °C to 70 °C (0.5 °C/min).

For scanning electron microscopy (SEM) observations on films and porous monoliths, we coated SEM samples with 4-nm-thick platinum with a Leica EM ACE 600 high vacuum coater (Leica Microsystems Inc., Wetzlar, Germany) and observed with a FEI Quanta 450 Field Emission Scanning Electron Microscope (FEI Company, Oregon, USA) under an accelerating voltage of 10 kV with spot size of 2 nm.

We measured the electrical conductivity of the RP50 films through a four-point setup and the Van der Pauw method. We cut the films into square shape, which we fixed on a glass slide by gluing each corner of the square with a drop of Ag paint. The measurements were carried out at room temperature. The film thickness was obtained through SEM cross-sections observations.

The X-ray diffraction (XRD) measurements were performed on the films through a Bruker D8 Advance X-ray diffractometer (Bruker-AXS Inc, Madison, Wisconsin, USA) (40 kV, 40 mA) with Cu Ka X-ray source ($\lambda=1.5418 \text{ \AA}$). A step size of 2-theta was set to 0.02° and the interlayer spacing was calculated according to Bragg's law as $d = \lambda / (2 \sin \theta)$.

5.6 Acknowledgement

The authors acknowledge the facilities, scientific and technical assistance of the McGill Institute for Advanced Materials, the McGill Chemistry Characterization Facility, The Quebec Centre for Advanced Material, the McGill Facility for Electron Microscopy Research, Professor Matthew J. Harrington and Mr. Mostafa Rammal. We gratefully acknowledge the support from the Canada Research Chair Foundation, the Natural Sciences and Engineering Research Council of Canada (NSERC), the Fonds de Recherche du Québec - Nature et Technologie (Doctoral research scholarship B2X).

5.7 Supporting Information

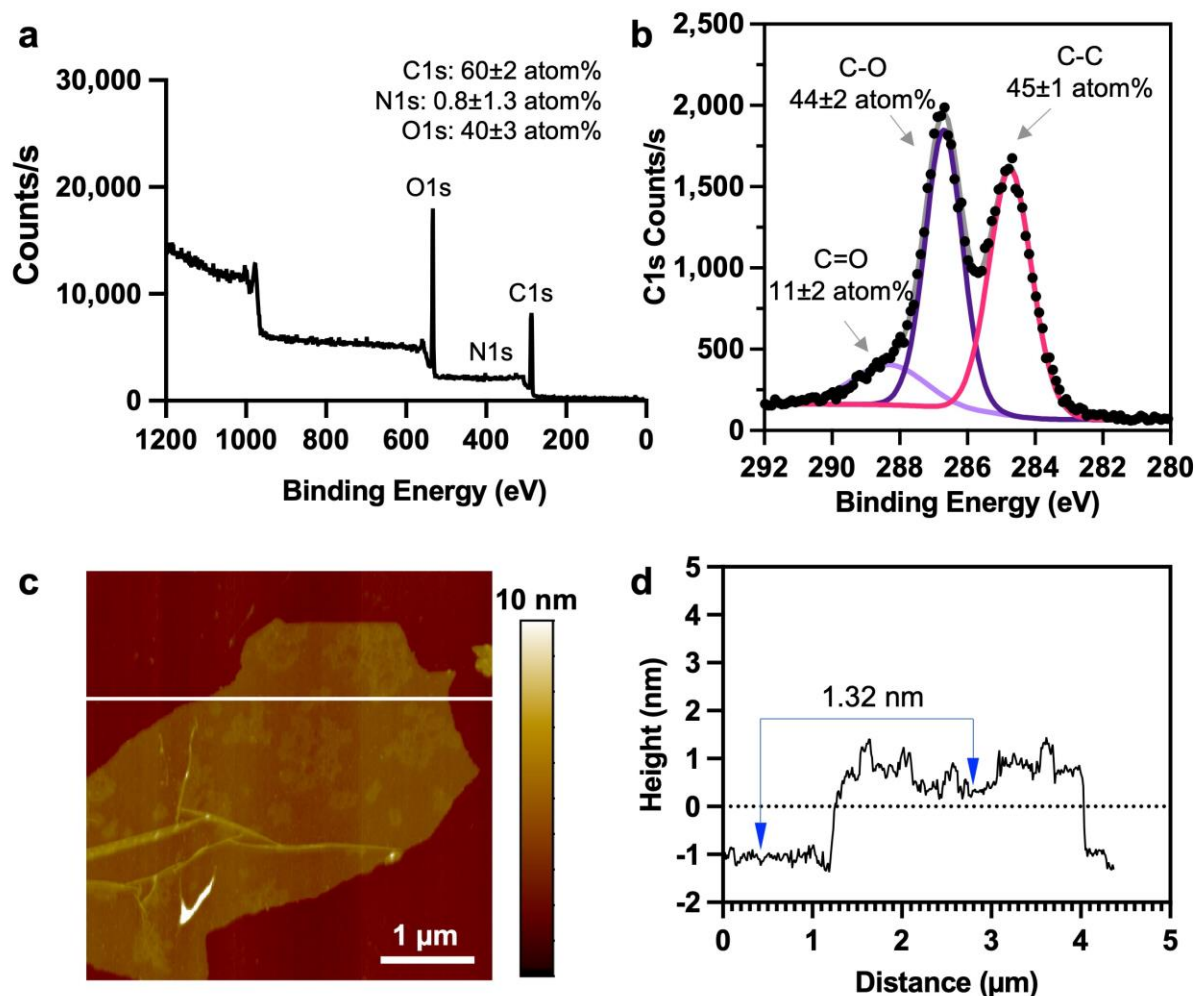


Figure 5.S1. Representative XPS (a) survey and (b) high resolution C1s spectra of pristine GO. The numbers shown in the figures display the atomic percentage of C1s, N1s, O1s from survey scans, and C-C, C-O, C=O atomic percentage from high resolution C1s scans. Nitrogen is an impurity deriving from sodium nitrate used in the Hummers' method for GO preparation. (c) AFM topography of a GO flake and (d) height profile corresponding to the cross section along the white line in panel (c).

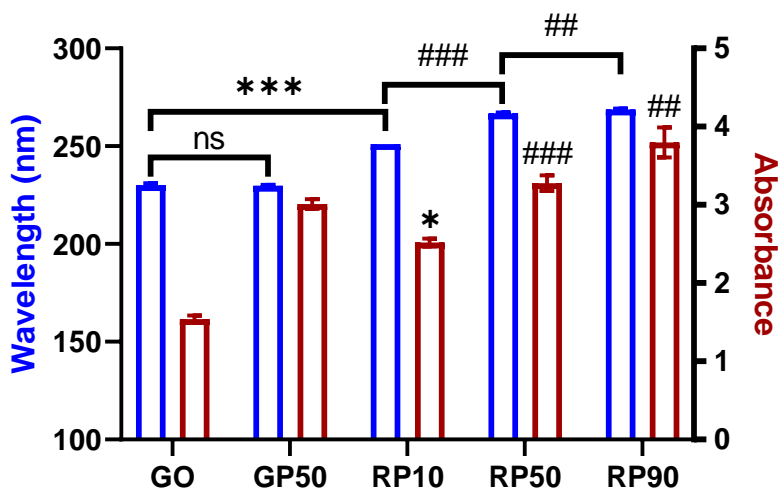


Figure 5.S2. Wavelength and corresponding maximum absorbance of the π - π^* transition peaks from UV-vis spectrophotometry data of GO, GP, and RP (concentration 0.05 mg/mL). ns: no significant difference between GO and GP50 ($P > 0.05$). *** and *: significant difference between GO and RP10 (*** $P < 0.001$, * $P < 0.05$). ## and ###: significant difference between RP10 and RP50, RP50 and RP90 (## $P = < 0.01$, ### $P = < 0.001$).

Table 5.S1. Surface composition derived from XPS survey data of RP and GP (n=3). C1s and O1s amounts were not compared because GO, rGO and PDA both contribute to these elements.

	RP10	RP50	RP90	GP50
C1s (atom%)	72.7±0.3	77.8±0.4	71.5±0.1	68.9±0.5
O1s (atom%)	24.4±0.4	17.5±0.1	23.0±0.2	27.4±0.1
N1s (atom%)	3.0±0.1	4.6±0.2***	5.5±0.2##	3.8±0.4

*** and ##: significant difference between RP10 and RP50 or between RP50 and RP90 (## $P = < 0.01$, *** $P = < 0.001$).

Table 5.S2. Atom% obtained from the deconvolution of high resolution XPS C1s spectra of RP and GP (n=3 experiment points). Statistical analysis for atom% of C-N, C-O and C=O is shown in **Figure 5.1**.

	GO	RP-10%	RP-50%	RP-90%	GP-50%
C-C (atom%)	45±1	48.1±0.3	53.1±0.4	49±1	45±3
C-N (atom%)	--	10.3±0.4	12.4±0.6	15.8±0.3	9±1
C-O (atom%)	44±2	29.0±0.5	19.3±0.8	18.0±0.4	37±3
C=O (atom%)	11±2	11.1±0.4	13±1	15.0±0.5	8.2±0.2

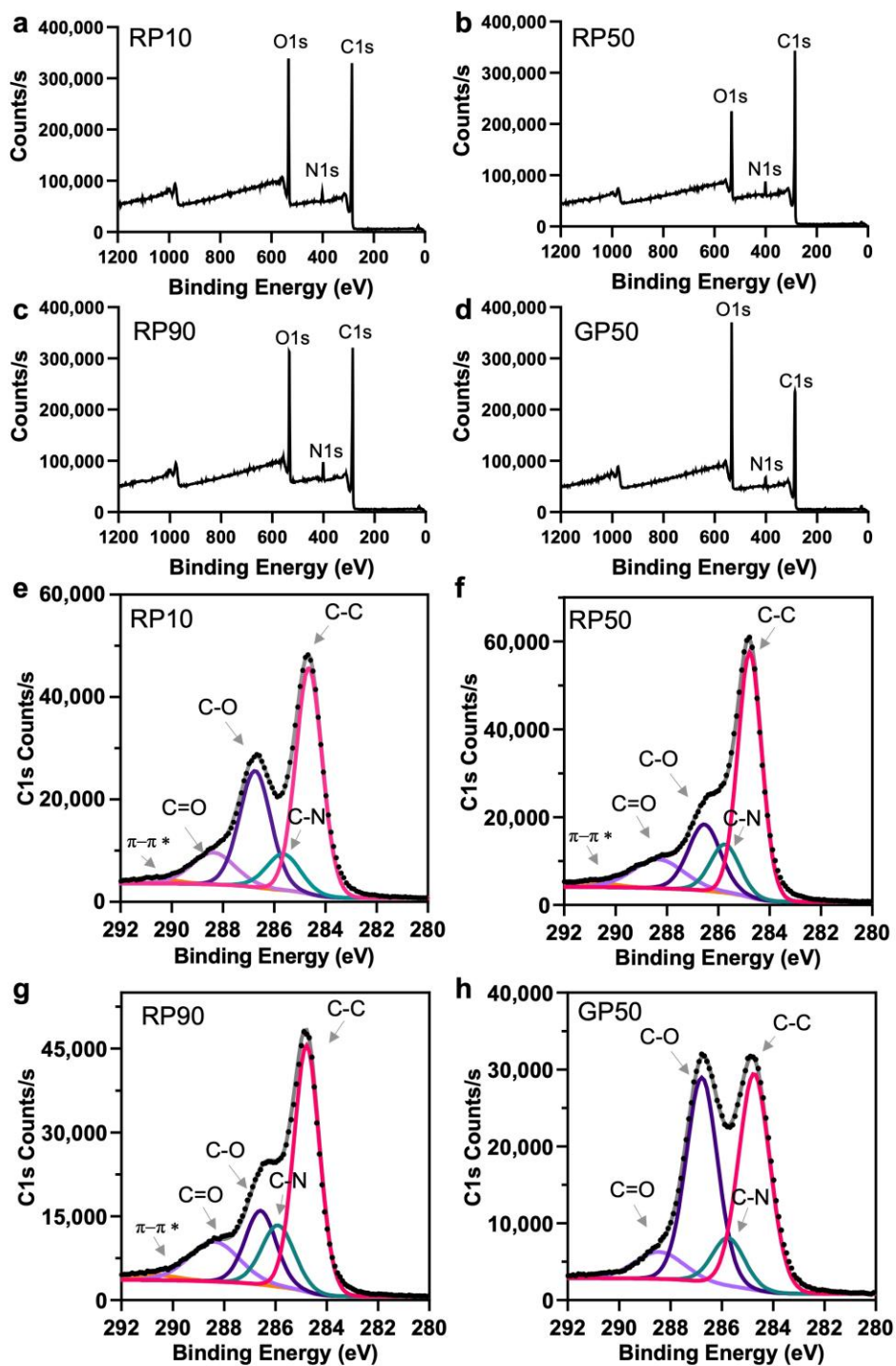


Figure 5.S3. Representative XPS survey (a-c) and high resolution C1s spectra (e-h) of rGO/PDA: (a, e) RP10, (b, f) RP50, (c, g) RP90, and GO/PDA: (d, h) GP50.

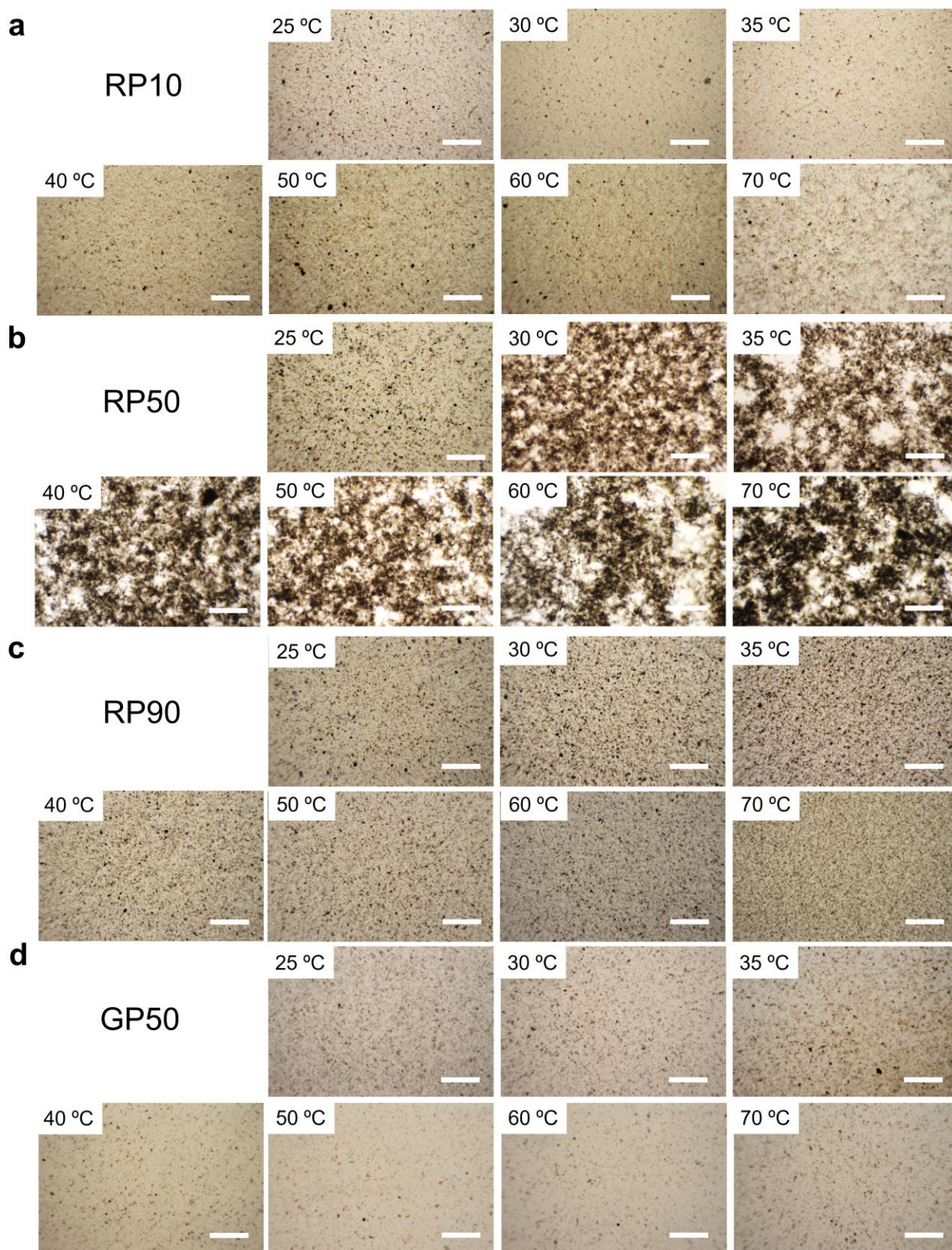


Figure 5.S4. Optical microscopy images of (a) RP10, (b) RP50, (c) RP90 and (d) GP50, at different temperatures. Scale bars = 500 μm in all panels.

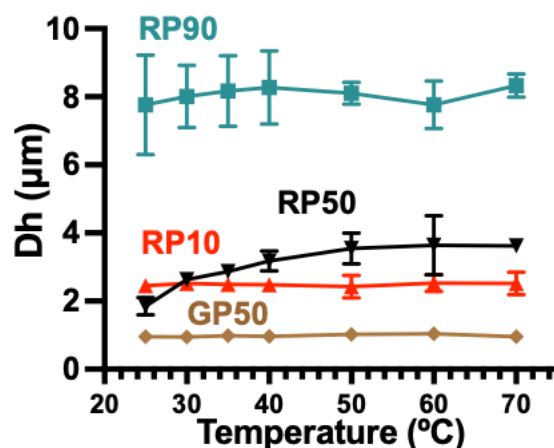


Figure 5.S5. Hydrodynamic diameter D_h of RP10, RP50, RP90 and GP50 after maintaining the indicated temperatures for 30 mins. There are $n = 3$ independent experiments. The data are represented as mean \pm standard deviation.

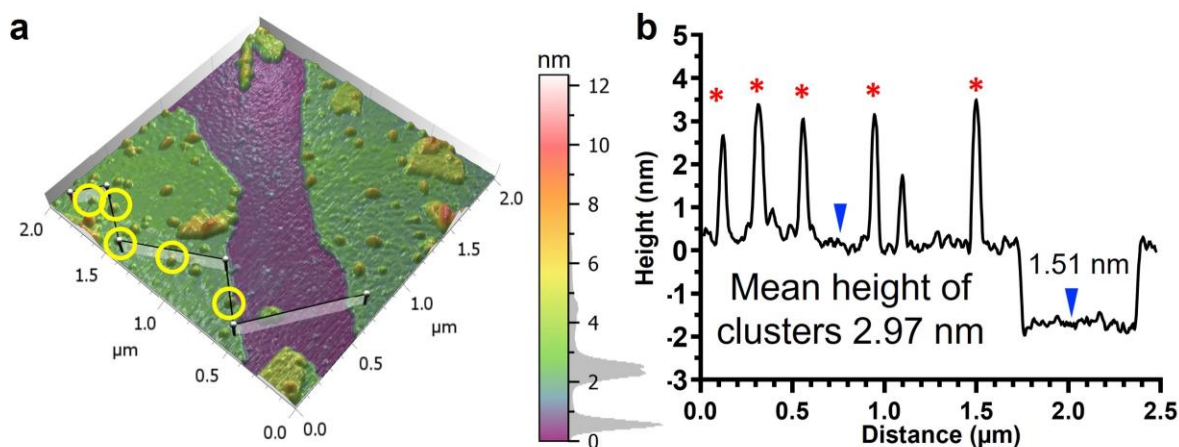


Figure 5.S6. (a) 3D AFM topography image of RP50 with corresponding histogram distribution of counts vs height. Representative PDA clusters are circled in yellow. (b) Height profile corresponding to the line in panel (a). The peaks indicated by red asterisks show the height of PDA clusters in panel (a). The height difference (1.51 nm) between blue arrows represents the height difference between RP50 flake (shown as green in panel a) and the substrate (shown as purple in panel a).

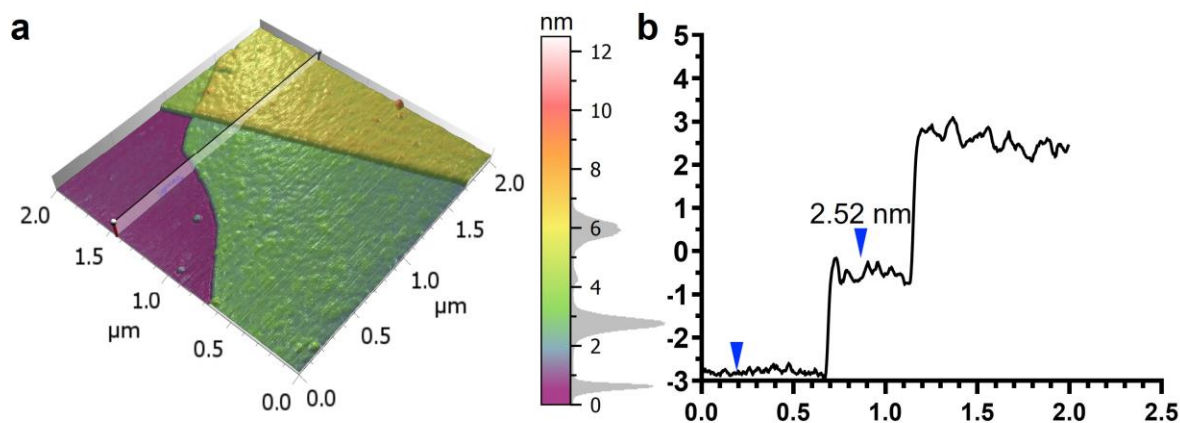


Figure 5.S7. (a) 3D AFM topography image of RP90 with corresponding histogram distribution of counts vs height. (b) Height profile corresponding to the line in panel (a).

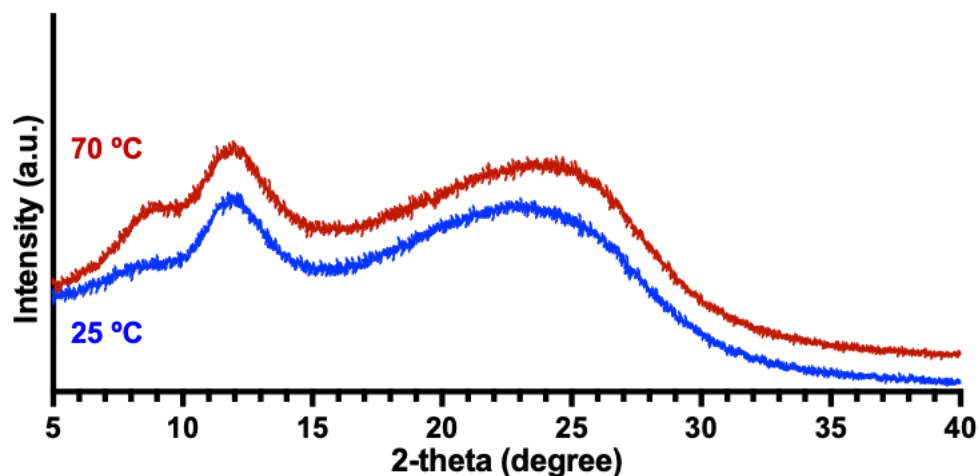


Figure 5.S8. XRD diffraction patterns of films prepared from RP50 at 25°C (bottom) and 70°C (top). The broad diffraction peaks at 2-theta \sim 8° indicate an expansion of the interlayer spacing due to the incorporation of PDA between layers [309],[472]. The broad peaks at 2-theta \sim 12° indicate an expansion due to the presence of oxygen-containing groups on the rGO attached between layers [474]. The peaks are assigned to the (0 0 2) graphitic diffraction order typical of rGO [100],[475].

6 Contributions to original knowledge

This work resulted in several contributions to original knowledge, as summarized below.

- i. We developed stable HIPEs in which the GO flakes are the only stabilizers, and the building blocks for GO-based scaffolds. Although previous studies have prepared GO stabilized HIPEs, stable emulsions with controllable droplet size required a considerable portion of co-emulsifiers or additives. Therefore, pure GO porous structure with tunable pore size could not be obtained. We have shown that when the amphiphilicity of GO is tuned by surface modification with a small amount of CTAB, the flakes can serve as both the stabilizers and the building materials to prepare porous materials only based on GO.
- ii. We developed a dual-templating strategy that combined HIPEs and ice templates and showed versatility in preparing GO, rGO, and GO composite scaffolds with interconnected hierarchical pore size distributions. We demonstrated that the size of the primary and secondary pores in the scaffolds can be controlled by adjusting the emulsion composition and freezing temperature. In addition to the new structural features, GO/polyacrylic acid, GO/elastin, and GO/hydroxyapatite scaffolds with interconnected pores in hierarchical size distributions were obtained for the first time. We demonstrated that the dual-templating method is a facile and versatile strategy that expands the structural complexity, the range of composite types and pore sizes that can be achieved in GO based porous monoliths.
- iii. We obtained water-stable GO scaffolds, investigated the proliferation, attachment, and infiltration of MSCs on GO hierarchical porous scaffolds, and laid the foundation for future research on GO scaffolds for BTE. We developed crosslinking and thermal treatments that allowed us to produce GO scaffolds ready for *in vitro* studies without

altering the morphology or the oxidized nature of GO. For the first time, 3D porous GO scaffolds were used for MSC cell culture, and results showed that cells can infiltrate through the scaffolds and grow into a 3D network as they proliferated and attached to the interconnected pores.

- iv. We introduced a GO and cobalt oxide composite Pickering emulsion system and demonstrated that this emulsion system can be used to design separate compartments of a 3D structure. We modified the surface of the Co_3O_4 particles to stabilize them in hexane to ensure the particles would be enclosed inside the rGO pores. We obtained closed pores of rGO by using GO emulsions with dispersed droplets as templates. We showed that the rGO/cobalt oxide electrodes preserving the architectural features can be easily obtained by hydrothermal treatment of GO/ Co_3O_4 Pickering emulsions. The particle surface modification strategy and emulsion system design can potentially be used to load other catalytic particles into rGO pores for different electrochemical reactions.
- v. We demonstrated that selective water electro-oxidation can be achieved by the architectural design of rGO/cobalt oxide electrodes. The closed rGO pore walls selectively hindered the transport of hydrated Cl^- because their size is larger than rGO interlayer distance, preventing competitive reactions. At the same time, the rGO nanochannels permitted the permeation of water and gas molecules, allowing the direct electrolysis of seawater without suffering from Cl^- competition. This architecture could be tailored and applied to prevent permeation of other species that can potentially poison catalysts for electrooxidation of water.
- vi. For the first time, we used synchrotron-based PCI to visualize the internal porous structure of graphene-family based materials. We developed methodologies to reveal the

porosity, interconnectivity of pores, as well as the structural configuration of different components inside graphene-based material.

- vii. We demonstrated that temperature response of rGO can be achieved by one-step PDA modification, through the formation of an amphiphilic structure mimicking the temperature responsive PNIPAM. We investigated amphiphilicity and colloidal properties of rGO/PDA flakes. We showed for the first time that the rGO flakes can be more than supportive and passive platforms in temperature-responsive systems. Instead, the interactions between flakes can be employed to induce self-assembly based on temperature changes, like in pH or ion responsive systems.
- viii. We proved that the rGO/PDA responsive self-assembly directly influenced the structures and properties of 2D nacre-like films and porous monoliths, which were made by drying the heated suspensions and hydrogels.
- ix. We introduced a supramolecular strategy and conveyed a concept that through surface modification, components and molecules can function cooperatively to impart properties that do not exist in either part. This concept can be used in nanomaterials beyond rGO: by using a one-step mussel-inspired surface modification, hydrophobic nanomaterials can be made amphiphilic and temperature responsive self-assembly can be achieved without temperature-responsive polymers.

7 General discussion and conclusions

7.1 General discussion

Previous works demonstrated that self-assembly can be used to obtain GO, rGO and composite materials, and numerous efforts have been done to develop different architectures in these materials [1],[3],[4]. Controllable self-assembly can be achieved at interfaces, or in response to environmental stimuli [4],[10]. In this thesis, we focused on GO Pickering emulsion templated assembly and temperature responsive self-assembly of rGO/PDA. We offered some insights on how to change the surface chemistry of GO and rGO to adjust their amphiphilicity, thus controlling the self-assembly of flakes.

Previous studies suggested that GO Pickering emulsion templating can efficiently create pores in 3D porous materials based on rGO [141],[151],[152], amorphous carbon [173], or polymers [153],[174], for applications such as sensing [152],[166],[174], absorption [165],[176], and drug delivery [139]. Efforts have been made to obtain stable emulsions by tuning the GO concentration [151], oil to water volume ratio [163], or adding additives to GO [139],[151],[166],[175], which affect the architecture of porous materials. However, the full potential of the emulsion templating strategy had not been exploited: pore size and interconnectivity were not precisely controlled, complex architectures with hierarchical pore size were not achieved, nor were structures with different components organized spatially in different locations. To fill these gaps, we developed a new strategy to achieve Pickering emulsions stabilized only by GO, and we used it to obtain GO and rGO based materials with architectures suitable for BTE and selective seawater oxidation applications in our third and fourth chapters, respectively.

In the third chapter, to obtain stable GO HIEs, we adjusted the amphiphilicity of GO by CTAB modification using 1 wt% of CTAB with respect to GO. We showed that lower content of CTAB brought minor change in GO amphiphilicity, therefore, resulting in phase separation between GO suspension and hexane. Higher content of CTAB caused the flocculation of emulsion droplets due to the increased hydrophobicity of GO flakes. The modification of GO with 1 wt% CTAB were sufficient to provide appropriate amphiphilicity to form stable oil-in-water HIEs. Therefore, we ensured that GO flakes are both the main stabilizers of the emulsion templates, and the building materials of the resulting porous structures only based on GO or rGO. The amphiphilicity of GO played a significant role, and as discussed, it is affected by the flake size, content of oxygen containing groups, and modification degree. Our study provides detailed information on these aspects, offering direct reference for future works in which emulsions stabilized only by GO or porous monoliths based on GO or rGO are desired.

Furthermore, in the third chapter, we were able to control the pore size of GO porous monoliths by tuning the GO concentration, oil-to-water volume ratio, and oil type in emulsion templates. The resulting pores had mean diameters of 100-300 μm , and the thickness of pore walls was increased as GO concentration increased or oil volume fraction decreased. These findings lay the foundation of our study in the fourth chapter.

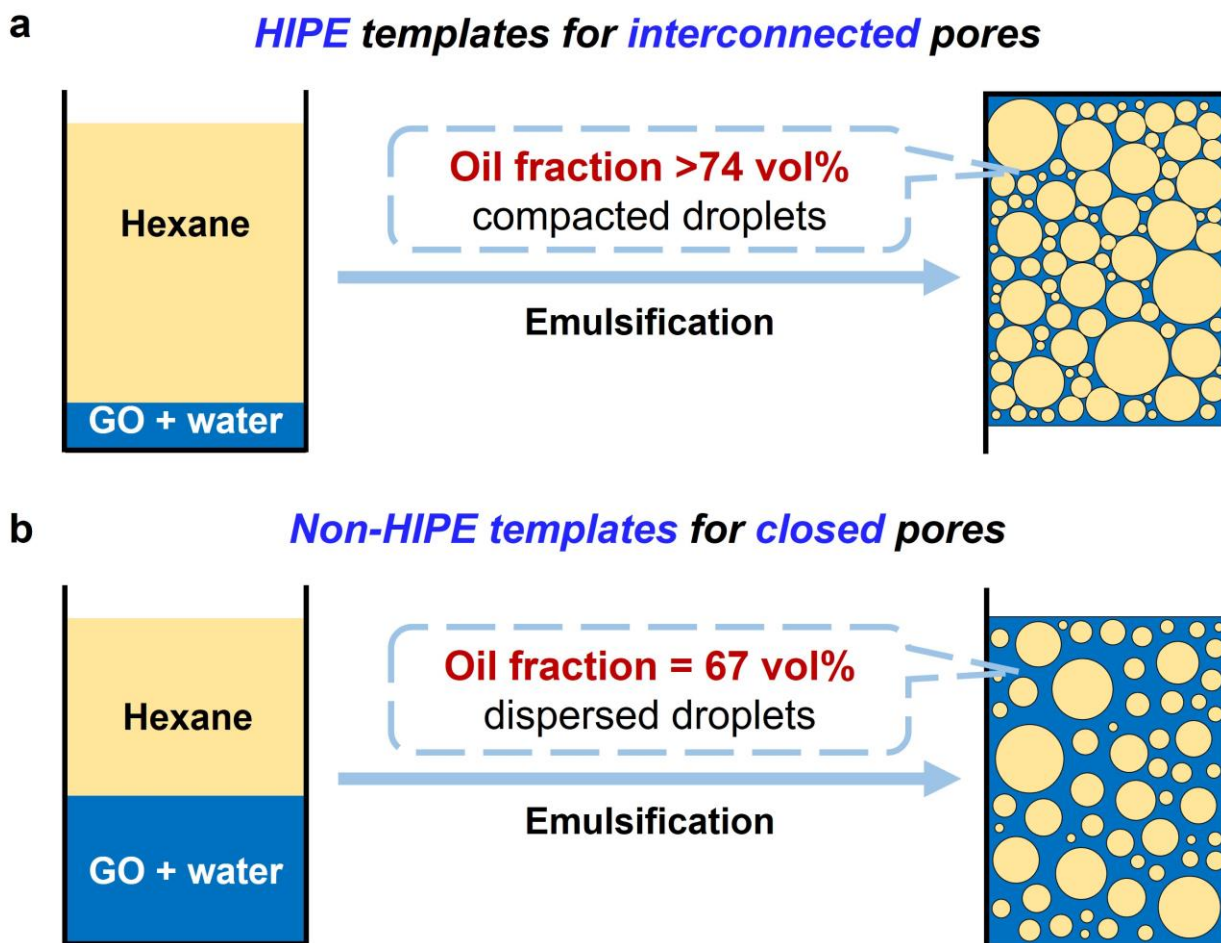


Figure 6.1. Illustrations of controlling the oil volume fraction to obtain (a) HIPE templates for porous monoliths with interconnected pores in Chapter 3, or (b) non-HIPE templates for porous monoliths with closed pores in Chapter 4.

In the third and fourth chapters, we tuned the oil to water volume ratio of emulsions in order to control the interconnectivity of porous monoliths. In the third chapter, we obtained HIPEs with compacted emulsion droplets due to the higher internal phase volume percentage (**Figure 6.1a**). The GO sheets formed thin barriers at the junctions between neighboring droplets, which were ruptured upon evaporation of hexane during freeze drying, leading to interconnected pores (**Figure 3.2a-f**). On the contrary, in the fourth chapter, we prepared emulsions with a lower internal phase volume fraction (**Figure 6.1b**), so that more GO flakes from a higher volume percentage of water

wrapped the oil droplets, allowing to create closed pores after hydrothermal reduction and solvent elimination (**Figure 4.3a** and **Figure 4.S7**).

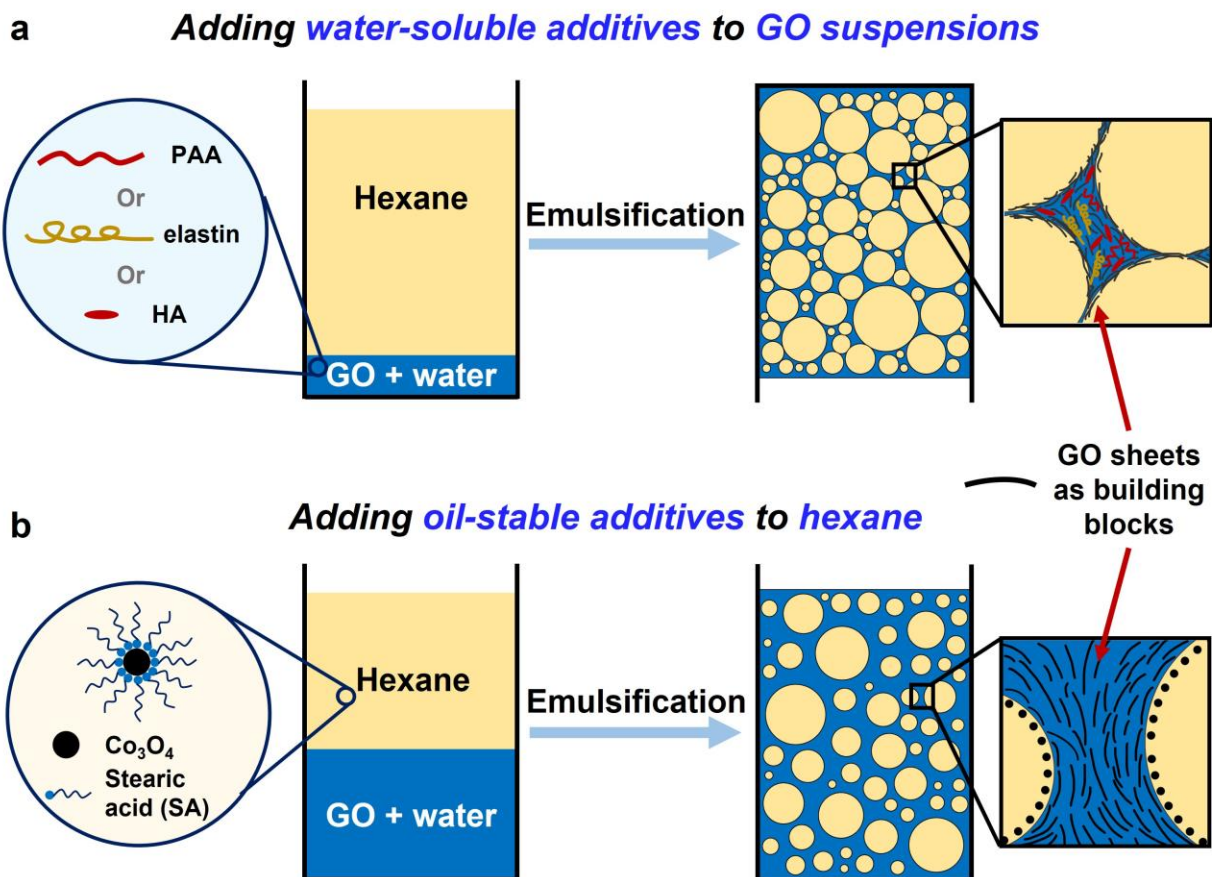


Figure 6.2. Illustrations of controlling the distribution of additives in porous monoliths. (a) Introducing water-soluble components to GO scaffolds by mixing additives with GO in the aqueous phase of emulsions (Chapter 3). (b) Introducing oil-stable components to rGO porous monoliths by dispersing additives in the hexane phase of emulsions (Chapter 4).

Different additives were added to different phases in the third and fourth chapters. In the third chapter, we mixed water-soluble additives to GO suspension (**Figure 6.2a**). These additives (PAA, elastin, or hydroxyapatite nanoparticles (HA NPs)) showed homogenous distribution in the matrix of GO scaffolds after freezing and drying (**Figure 3.4**). In Chapter 4, to protect the Co_3O_4 catalytic particles from contact with unfiltered water, we modified Co_3O_4 with hydrophobic moieties so that they could be stabilized in the oil phase (**Figure 6.2b**) and be enclosed inside the closed rGO pores (**Figure 4.2** and **Figure 4.3**).

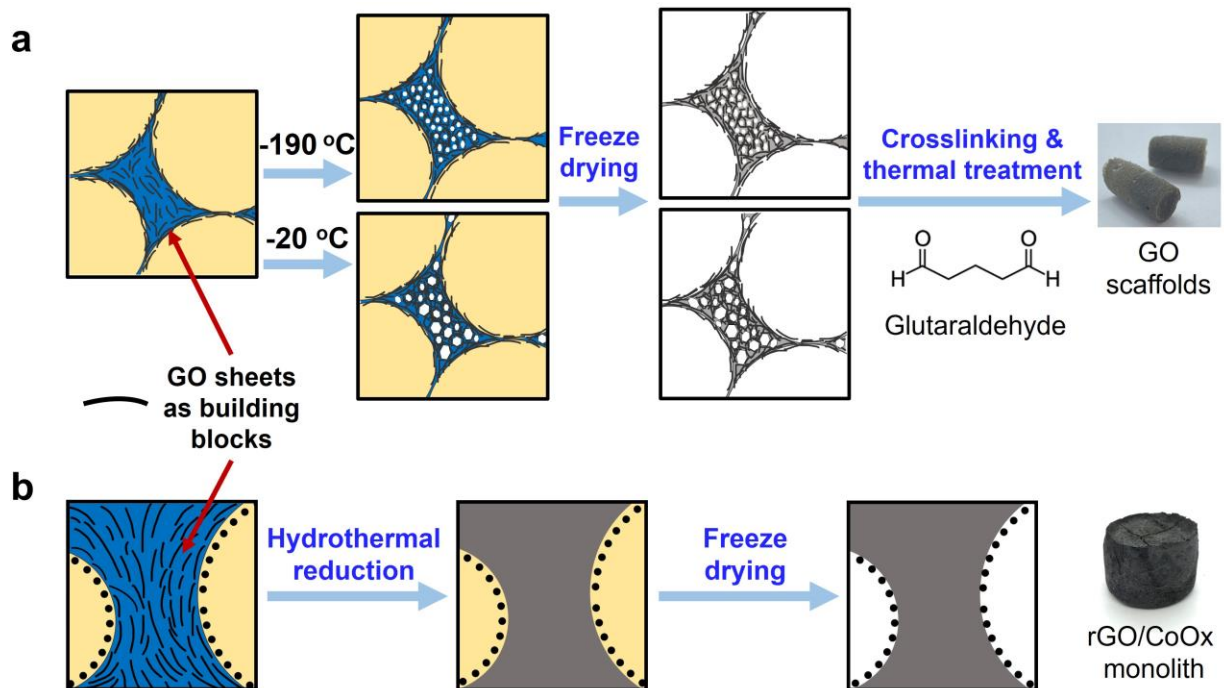


Figure 6.3. Illustrations of different post-treatments to obtain GO or rGO porous monoliths.

We conducted different post-treatments to create porous materials with different architectures. In Chapter 3, we froze the GO emulsions at different temperatures (**Figure 6.3a**). Without crosslinking, the free flakes loosely contacting each other allowed ice crystals to grow into different final sizes at different temperatures, and to become templates for the secondary pores. After freezing and drying steps, we conducted GA-vapor crosslinking and non-destructive thermal treatment, therefore, the architectures of GO scaffolds were preserved (**Figure 3.3c**). In Chapter 4, we obtained electrically conductive rGO electrodes through hydrothermal reduction of GO/Co₃O₄ emulsions and freeze-drying (**Figure 6.3b**). During hydrothermal reduction, GO flakes were immobilized as they formed networks. In the following freeze-drying step, the crosslinked rGO flakes, as well as the low freezing temperature ($-190\text{ }^{\circ}\text{C}$) impeded ice growth; therefore, closed pores enclosing catalytic particles were preserved (**Figure 4.3**).

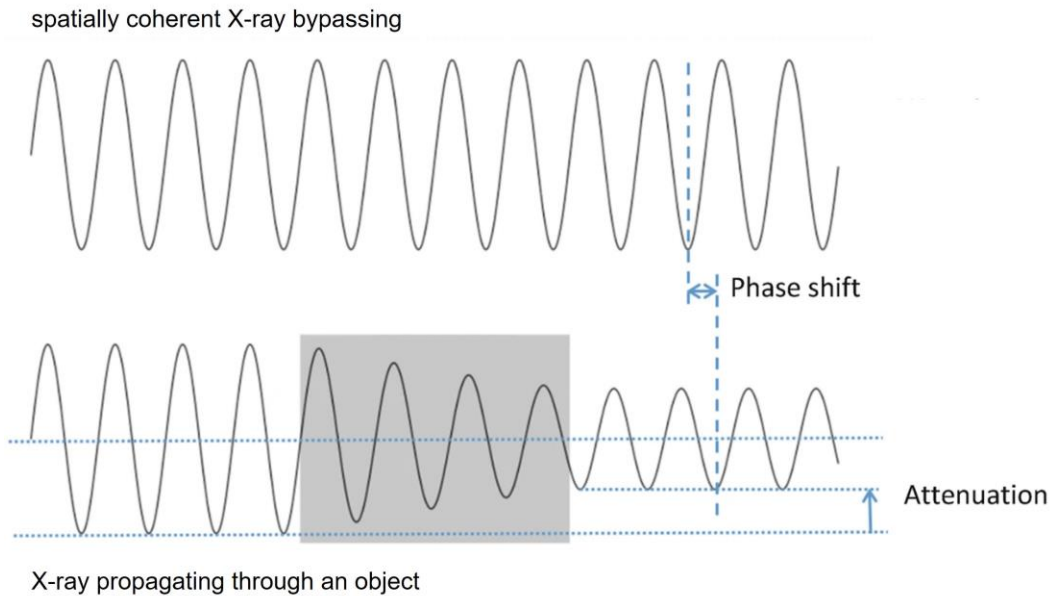


Figure 6.4. Illustration showing the change of X-ray intensity and phase when propagating through an object in X-ray PCI. Reproduced with permission from Ref.[476]. Copyright 2019, Springer Nature Switzerland AG.

In both Chapters 3 and 4, we investigated the architecture of the porous monoliths through synchrotron-based PCI. In previous studies on graphene porous monoliths, techniques such as AFM and SEM were commonly used to visualize local surface morphology. Unlike these techniques, X-ray tomography provides non-destructive 3D imaging of the material's internal architecture. Because conventional X-ray tomography infers sample structure by analyzing the distribution of transmitted X-rays from absorption, materials with elements of low atomic number (*e.g.*, carbon and oxygen in GO) yield low X-ray attenuation and insufficient absorption contrast for imaging [477],[478]. X-ray PCI measures refraction of X-ray in addition to attenuation: when spatially coherent X-ray propagates through a sample, attenuated light has phase shift compared to the incident light, and interference happens between the phase-shifted X-ray and the coherent reference X-ray (**Figure 6.4**) [478]–[481]. Using a synchrotron's high-brightness, spatially coherent beam, the X-ray PCI technique provides additional phase contrast information and enables imaging of light elements [477],[482]. For the first time, we adapted this technique to

graphene materials and developed methodologies to analyze their architectural properties. PCI analysis showed a highly interconnected porosity in the GO scaffolds synthesized in Chapter 3 and revealed the distribution and enclosure of cobalt oxide particles in the porous rGO synthesized in Chapter 4. These results were crucial to confirm that we had achieved the desired architecture for BTE and seawater oxidation applications.

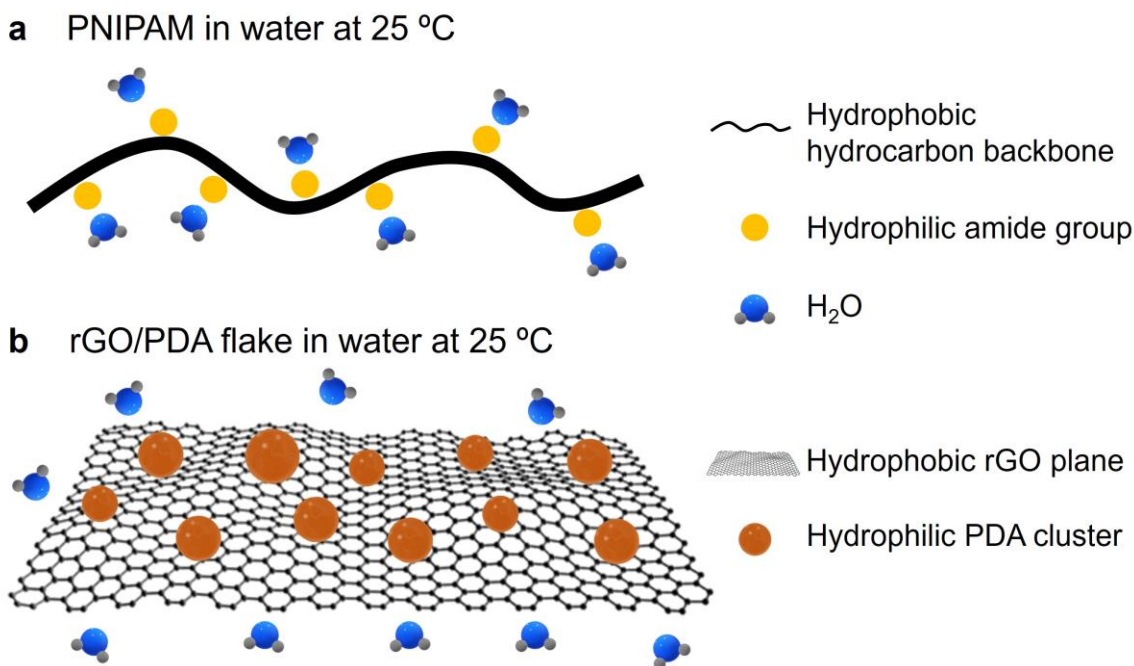


Figure 6.5. Simplified illustrations of amphiphilic structures of PNIPAM and rGO/PDA.

In Chapter 5, we showed that the amphiphilicity of rGO can be tuned to induce temperature responsiveness, so that the flakes can self-assemble into different architectures controlled by heat. Previous studies had shown that temperature responsive self-assembly of GO and rGO happened only when responsive polymers, such as PNIPAM [238],[254], were incorporated. In this study, we achieved responsive self-assembly by designing a supramolecular structure with rGO and PDA, two components that are not intrinsically responsive to temperature. Instead of using CTAB to increase the hydrophobicity of GO flakes like we did in the previous chapters, here we modified rGO hydrophilicity by optimizing the ratio between GO and DA and the reaction temperature. In

the resulting system, the PDA and rGO mimic the hydrophilic groups and hydrophobic backbone of PNIPAM, respectively (**Figure 6.5**): PDA provides stability of the flakes in water at low temperature, and the rGO plane provides the driving forces for self-assembly at higher temperature.

Based on the understanding and methods that we developed in this thesis, we propose several suggestions for future directions.

Chapter 3:

- i. Although CTAB only counted for up to 0.0025 wt% of GO HIPEs, and was removed in GO based scaffolds, we could potentially avoid the use of CTAB. It's possible to reduce GO to enhance the hydrophobicity and obtain HIPEs stabilized only by rGO flakes. In this case, the GO reduction degree should be carefully tuned to avoid aggregation of flakes in the aqueous phase. The freezing and drying steps could be studied to understand rGO assembly by ice templating in order to investigate the possibility of obtaining rGO scaffolds with hierarchical pore size distribution.
- ii. It's worth exploring the emulsion-ice dual-templating strategy to obtain hierarchically porous materials other than GO or rGO, due to the possibly wide applications across diverse fields, such as separation, adsorption, biomaterials and energy [483]. Potentially, by optimizing the concentration and oil-to-water volume ratio, amphiphilic macromolecules, such as cellulose could be used as both emulsion stabilizers and the building matrix. Surface modifications could be applied to adjust the amphiphilicity of nanomaterials beyond GO, such as boron nitride or carbon nanotubes, in order to stabilize Pickering emulsions and to produce hierarchically porous materials through dual templating.

- iii. The emulsion-ice dual-templating strategy was applied to the oil-in-water GO emulsion systems for the ice to crystallize in the external aqueous phase. It would be interesting to explore if it's possible to develop a similar system in water-in-oil emulsions, so that hierarchical pore size distributions can be easily achieved even with materials that can only stabilize w/o emulsions.
- iv. Future research can focus on *in vitro* osteogenic differentiation of MSCs, *in vivo* metabolic exchange, blood vessel ingrowth, and bone formation on GO and rGO-based 3D scaffolds with interconnected pores of hierarchically distributed size, to compare and evaluate their potential in non-load bearing BTE applications, such as the repair of calvarial defects.
- v. The compressive strength of GO scaffolds may be enhanced, so that they could be used as load-bearing scaffolds. Potential directions for future research could be adding reinforcing additives, optimizing porosity by tuning the emulsion and ice templates, and increasing the density of porous monoliths by using higher concentration of GO.

Chapter 4:

- vi. Although we were able to stabilize Co_3O_4 particles in hexane, the particles were aggregated. Future research may involve preventing the aggregation of the catalytic nanoparticles by modifying them with different surfactants or dispersing them in different solvents and investigating the effect on the electrocatalytic performance.
- vii. In this work, we only demonstrated the surface modification of Co_3O_4 particles and the suppression of Cl^- transport. Different catalytic particles can be loaded into the oil droplets of GO emulsions. Also, the closed rGO pores can be employed to prevent the permeation of species beyond Cl^- (such as sulfur-rich compounds, microbes, or corrosive

ions). Consequently, other electrocatalytic reactions requiring selectivity against interfering species or ions could be achieved.

Chapter 5:

- viii. Given the NIR sensitivity of rGO, the photothermal response of rGO/PDA would be an interesting topic for future study. The change in amphiphilicity of flakes, which could be triggered by NIR light, may be used for controlled release applications.
- ix. The PDA surface modification strategy could be extended to obtain amphiphilic structures in other hydrophobic nanomaterials and induce temperature responsive self-assembly without involving responsive polymers. To adjust amphiphilicity and obtain clusters on nanomaterials, conditions such as dopamine and nanomaterial concentration, reaction temperature, and pH, could be optimized. The resulting temperature-induced self-assembly could be applied to control the architectures and properties of other solid materials.

7.2 Conclusions

In summary, we achieved our aim to study the assembly of GO and rGO flakes into various architectures through the control of their amphiphilicity.

In Chapter 3, we tuned the amphiphilicity of GO with a cationic surfactant, CTAB. Through developing a dual-templating strategy, we controlled GO assembly at liquid-liquid and liquid-solid interfaces in HIPEs and ice. We obtained GO, rGO, and GO composite scaffolds with interconnected pores in hierarchical pore size distributions. We produced water-stable GO scaffolds through crosslinking and thermal treatment while preserving desired architecture for BTE. We applied for the first-time synchrotron-based PCI to visualize and analyze GO scaffolds. We tested the GO scaffolds for MSC *in vitro* cell culture and showed GO scaffolds can support cell proliferation, infiltration, and attachment due to their architectures. We proposed that the GO scaffolds are promising for non-load bearing BTE applications and the dual-templating strategy can be applied to obtain hierarchically porous materials beyond GO and rGO.

In Chapter 4, through GO emulsion templating, we developed 3D rGO electrodes with closed macropores that enclose catalytic cobalt oxide particles, and achieved selective electrocatalytic water oxidation. We modified Co_3O_4 particles and stabilized them in the oil phase of GO emulsions. We successfully designed GO/ Co_3O_4 Pickering emulsion templates and obtained rGO/CoOx electrodes preserving desired architecture through hydrothermal treatment and freeze-drying. Using synchrotron-based PCI, we visualized the porous structure and studied the particle distributions. We showed that the architectural features of rGO/CoOx electrodes ensured the high selectivity in the electrocatalytic water oxidation process. We proposed that the design of GO emulsion templates and the rGO-based electrode architecture may be successfully applied to

prevent the permeation of other species in water electrooxidation, or to load other catalytic particles into rGO pores for different electrochemical reactions.

In Chapter 5, we controlled the self-assembly of rGO flakes in response to temperature stimuli. We tuned the amphiphilicity of rGO by creating hydrophobic rGO domains and hydrophilic moieties *via* DA surface modification. We controlled the surface chemistry, including PDA formation and GO reduction degree by changing reaction conditions. We investigated the amphiphilicity and the colloidal properties of rGO/PDA flakes and studied the rGO/PDA self-assembly process in response to temperature change. Lastly, we controlled the architectures of rGO/PDA based materials through temperature responsive self-assembly process. Therefore, we provided a one-step strategy based on amphiphilicity design to induce temperature responsive self-assembly in nanomaterials without using responsive polymers.

In this thesis, we employed simple surface modification techniques to tune the amphiphilicity of GO and rGO, including CTAB adsorption and PDA modification. We demonstrated that GO Pickering emulsion templating is a versatile strategy that can be adapted to design different architectures, various compositions, and desirable properties in GO and rGO based porous materials. Furthermore, we introduced a one-step supramolecular strategy to create an amphiphilic structure in rGO/PDA, so that the temperature responsive self-assembly of the flake was enabled without introducing intrinsically temperature-responsive components. This thesis may contribute to the production and applications of graphene-based materials by providing insights on application-targeted architecture design and controllable preparation of functional materials *via* simple and versatile assembly strategies.

8 Copyright permissions

Chapter 3:

CCC RightsLink

Home Help Email Support Sign in Create Account

Dual-templating strategy for the fabrication of graphene oxide, reduced graphene oxide and composite scaffolds with hierarchical architectures

Author: Yiwen Chen, Xinyun Su, Dominic Esmail, Emily Buck, Simon D. Tran, Thomas Szkopek, Marta Cerruti
Publication: Carbon
Publisher: Elsevier
Date: 15 April 2022

© 2021 Elsevier Ltd. All rights reserved.

Journal Author Rights

Please note that, as the author of this Elsevier article, you retain the right to include it in a thesis or dissertation, provided it is not published commercially. Permission is not required, but please ensure that you reference the journal as the original source. For more information on this and on your other retained rights, please visit: <https://www.elsevier.com/about/our-business/policies/copyright#Author-rights>

BACK CLOSE WINDOW

© 2022 Copyright - All Rights Reserved | Copyright Clearance Center, Inc. | Privacy statement | Data Security and Privacy | For California Residents | Terms and Conditions
Comments? We would like to hear from you. E-mail us at customer-care@copyright.com

Chapter 4:

CCC RightsLink

Home Help Email Support Sign in Create Account

Selective Catalytic Electro-Oxidation of Water with Cobalt Oxide in Ion Impermeable Reduced Graphene Oxide Porous Electrodes

Author: Gabriele Capilli, Yiwen Chen, Thomas Szkopek, et al
Publication: ACS Nano
Publisher: American Chemical Society
Date: Aug 1, 2022

Copyright © 2022, American Chemical Society

PERMISSION/LICENSE IS GRANTED FOR YOUR ORDER AT NO CHARGE

This type of permission/license, instead of the standard Terms and Conditions, is sent to you because no fee is being charged for your order. Please note the following:

- Permission is granted for your request in both print and electronic formats, and translations.
- If figures and/or tables were requested, they may be adapted or used in part.
- Please print this page for your records and send a copy of it to your publisher/graduate school.
- Appropriate credit for the requested material should be given as follows: "Reprinted (adapted) with permission from {COMPLETE REFERENCE CITATION}. Copyright {YEAR} American Chemical Society." Insert appropriate information in place of the capitalized words.
- One-time permission is granted only for the use specified in your RightsLink request. No additional uses are granted (such as derivative works or other editions). For any uses, please submit a new request.

If credit is given to another source for the material you requested from RightsLink, permission must be obtained from that source.

BACK CLOSE WINDOW

© 2022 Copyright - All Rights Reserved | Copyright Clearance Center, Inc. | Privacy statement | Data Security and Privacy | For California Residents | Terms and Conditions
Comments? We would like to hear from you. E-mail us at customer-care@copyright.com

9 References

- [1] Cong, H.-P., Chen, J.-F. & Yu, S.-H. Graphene-based macroscopic assemblies and architectures: an emerging material system. *Chem. Soc. Rev.* **43**, 7295–7325 (2014).
- [2] Bolotin, K. I. *et al.* Ultrahigh electron mobility in suspended graphene. *Solid State Commun.* **146**, 351–355 (2008).
- [3] Sun, Z., Fang, S. & Hu, Y. H. 3D Graphene Materials: From Understanding to Design and Synthesis Control. *Chem. Rev.* **120**, 10336–10453 (2020).
- [4] Shao, J.-J., Lv, W. & Yang, Q.-H. Self-Assembly of Graphene Oxide at Interfaces. *Adv. Mater.* **26**, 5586–5612 (2014).
- [5] Dreyer, D. R., Todd, A. D. & Bielawski, C. W. Harnessing the chemistry of graphene oxide. *Chem. Soc. Rev.* **43**, 5288–5301 (2014).
- [6] R. Dreyer, D., Park, S., W. Bielawski, C. & S. Ruoff, R. The chemistry of graphene oxide. *Chem. Soc. Rev.* **39**, 228–240 (2010).
- [7] Pei, S. & Cheng, H.-M. The reduction of graphene oxide. *Carbon* **50**, 3210–3228 (2012).
- [8] Kim, J. *et al.* Graphene Oxide Sheets at Interfaces. *J. Am. Chem. Soc.* **132**, 8180–8186 (2010).
- [9] Zhang, J., Song, L., Zhang, Z., Chen, N. & Qu, L. Environmentally Responsive Graphene Systems. *Small* **10**, 2151–2164 (2014).
- [10] Yu, X. *et al.* Graphene-based smart materials. *Nat. Rev. Mater.* **2**, 1–13 (2017).
- [11] Crane, G. M., Ishaug, S. L. & Mikos, A. G. Bone tissue engineering. *Nat. Med.* **1**, 1322–1324 (1995).
- [12] Stevens, M. M. Biomaterials for bone tissue engineering. *Mater. Today* **11**, 18–25 (2008).
- [13] Lee, W. C. *et al.* Origin of Enhanced Stem Cell Growth and Differentiation on Graphene and Graphene Oxide. *ACS Nano* **5**, 7334–7341 (2011).
- [14] Nayak, T. R. *et al.* Graphene for Controlled and Accelerated Osteogenic Differentiation of Human Mesenchymal Stem Cells. *ACS Nano* **5**, 4670–4678 (2011).
- [15] Xie, X. *et al.* Graphene and hydroxyapatite self-assemble into homogeneous, free standing nanocomposite hydrogels for bone tissue engineering. *Nanoscale* **7**, 7992–8002 (2015).
- [16] Shi, X. *et al.* Regulating Cellular Behavior on Few-Layer Reduced Graphene Oxide Films with Well-Controlled Reduction States. *Adv. Funct. Mater.* **22**, 751–759 (2012).
- [17] Chen, G.-Y., Pang, D. W.-P., Hwang, S.-M., Tuan, H.-Y. & Hu, Y.-C. A graphene-based platform for induced pluripotent stem cells culture and differentiation. *Biomaterials* **33**, 418–427 (2012).
- [18] Zhou, C. *et al.* Collagen Functionalized With Graphene Oxide Enhanced Biomimetic Mineralization and in Situ Bone Defect Repair. *ACS Appl. Mater. Interfaces* **10**, 44080–44091 (2018).
- [19] Zhang, Y. *et al.* The effects of pore architecture in silk fibroin scaffolds on the growth and differentiation of mesenchymal stem cells expressing BMP7. *Acta Biomater.* **6**, 3021–3028 (2010).
- [20] Karageorgiou, V. & Kaplan, D. Porosity of 3D biomaterial scaffolds and osteogenesis. *Biomaterials* **26**, 5474–5491 (2005).
- [21] Hulbert, S. F. *et al.* Potential of ceramic materials as permanently implantable skeletal prostheses. *J. Biomed. Mater. Res.* **4**, 433–456 (1970).
- [22] Nie, W. *et al.* Three-dimensional porous scaffold by self-assembly of reduced graphene oxide and nano-hydroxyapatite composites for bone tissue engineering. *Carbon* **116**, 325–337 (2017).

- [23] W. Crowder, S. *et al.* Three-dimensional graphene foams promote osteogenic differentiation of human mesenchymal stem cells. *Nanoscale* **5**, 4171–4176 (2013).
- [24] Tong, W. *et al.* Electrolysis of low-grade and saline surface water. *Nat. Energy* **5**, 367–377 (2020).
- [25] Keane, T. P. & Nocera, D. G. Selective Production of Oxygen from Seawater by Oxidic Metallate Catalysts. *ACS Omega* **4**, 12860–12864 (2019).
- [26] Hsu, S.-H. *et al.* An Earth-Abundant Catalyst-Based Seawater Photoelectrolysis System with 17.9% Solar-to-Hydrogen Efficiency. *Adv. Mater.* **30**, 1707261 (2018).
- [27] Huang, L., Zhang, M., Li, C. & Shi, G. Graphene-Based Membranes for Molecular Separation. *J. Phys. Chem. Lett.* **6**, 2806–2815 (2015).
- [28] Abraham, J. *et al.* Tunable sieving of ions using graphene oxide membranes. *Nat. Nanotechnol.* **12**, 546–550 (2017).
- [29] R. Jadhav, A. *et al.* Stable complete seawater electrolysis by using interfacial chloride ion blocking layer on catalyst surface. *J. Mater. Chem. A* **8**, 24501–24514 (2020).
- [30] Feng, L. *et al.* Smart pH-Responsive Nanocarriers Based on Nano-Graphene Oxide for Combined Chemo- and Photothermal Therapy Overcoming Drug Resistance. *Adv. Healthc. Mater.* **3**, 1261–1271 (2014).
- [31] Bai, H., Li, C., Wang, X. & Shi, G. On the Gelation of Graphene Oxide. *J. Phys. Chem. C* **115**, 5545–5551 (2011).
- [32] Ono, Y. & Shikata, T. Hydration and Dynamic Behavior of Poly(N-isopropylacrylamide)s in Aqueous Solution: A Sharp Phase Transition at the Lower Critical Solution Temperature. *J. Am. Chem. Soc.* **128**, 10030–10031 (2006).
- [33] Cho, E. C., Lee, J. & Cho, K. Role of Bound Water and Hydrophobic Interaction in Phase Transition of Poly(N-isopropylacrylamide) Aqueous Solution. *Macromolecules* **36**, 9929–9934 (2003).
- [34] Maeda, Y., Higuchi, T. & Ikeda, I. Change in Hydration State during the Coil–Globule Transition of Aqueous Solutions of Poly(N-isopropylacrylamide) as Evidenced by FTIR Spectroscopy. *Langmuir* **16**, 7503–7509 (2000).
- [35] Singh, R., Deshmukh, S. A., Kamath, G., Sankaranarayanan, S. K. R. S. & Balasubramanian, G. Controlling the aqueous solubility of PNIPAM with hydrophobic molecular units. *Comput. Mater. Sci.* **126**, 191–203 (2017).
- [36] Futscher, M. H., Philipp, M., Müller-Buschbaum, P. & Schulte, A. The Role of Backbone Hydration of Poly(N-isopropyl acrylamide) Across the Volume Phase Transition Compared to its Monomer. *Sci. Rep.* **7**, 17012 (2017).
- [37] Silverstein, K. A. T., Haymet, A. D. J. & Dill, K. A. A Simple Model of Water and the Hydrophobic Effect. *J. Am. Chem. Soc.* **120**, 3166–3175 (1998).
- [38] Lee, H., Dellatore, S. M., Miller, W. M. & Messersmith, P. B. Mussel-Inspired Surface Chemistry for Multifunctional Coatings. *Science* **318**, 426–430 (2007).
- [39] Liu, Y., Ai, K. & Lu, L. Polydopamine and Its Derivative Materials: Synthesis and Promising Applications in Energy, Environmental, and Biomedical Fields. *Chem. Rev.* **114**, 5057–5115 (2014).
- [40] Sheng, W. *et al.* Brushing up from “anywhere” under sunlight: a universal surface-initiated polymerization from polydopamine-coated surfaces. *Chem. Sci.* **6**, 2068–2073 (2015).
- [41] Lee, H. A., Park, E. & Lee, H. Polydopamine and Its Derivative Surface Chemistry in Material Science: A Focused Review for Studies at KAIST. *Adv. Mater.* **32**, 1907505 (2020).

- [42] Cheng, C. *et al.* Biomimetic assembly of polydopamine-layer on graphene: Mechanisms, versatile 2D and 3D architectures and pollutant disposal. *Chem. Eng. J.* **228**, 468–481 (2013).
- [43] Jiang, J., Zhu, L., Zhu, L., Zhu, B. & Xu, Y. Surface Characteristics of a Self-Polymerized Dopamine Coating Deposited on Hydrophobic Polymer Films. *Langmuir* **27**, 14180–14187 (2011).
- [44] Yu, X., Fan, H., Liu, Y., Shi, Z. & Jin, Z. Characterization of Carbonized Polydopamine Nanoparticles Suggests Ordered Supramolecular Structure of Polydopamine. *Langmuir* **30**, 5497–5505 (2014).
- [45] Wang, Y. *et al.* Superior Performance of Artificial Nacre Based on Graphene Oxide Nanosheets. *ACS Appl. Mater. Interfaces* **9**, 4215–4222 (2017).
- [46] Chen, Y. *et al.* Dual-templating strategy for the fabrication of graphene oxide, reduced graphene oxide and composite scaffolds with hierarchical architectures. *Carbon* **189**, 186–198 (2022).
- [47] Capilli, G., Chen, Y., Szkopek, T. & Cerruti, M. Selective Catalytic Electro-Oxidation of Water with Cobalt Oxide in Ion Impermeable Reduced Graphene Oxide Porous Electrodes. *ACS Nano* **16**, 12488–12499 (2022).
- [48] Charlier, J.-C., Gonze, X. & Michenaud, J.-P. Graphite Interplanar Bonding: Electronic Delocalization and van der Waals Interaction. *Europhys. Lett. EPL* **28**, 403–408 (1994).
- [49] Birowska, M., Milowska, K. & Majewski, J. Van Der Waals Density Functionals for Graphene Layers and Graphite. *Acta Phys. Pol. Ser. A* **120**, 845–848 (2011).
- [50] Brodie, B. C. XIII. On the atomic weight of graphite. *Philos. Trans. R. Soc. Lond.* **149**, 249–259 (1859).
- [51] Staudenmaier, L. Verfahren zur Darstellung der Graphitsäure. *Berichte Dtsch. Chem. Ges.* **31**, 1481–1487 (1898).
- [52] Hofmann, U. & König, E. Untersuchungen über Graphitoxyd. *Z. Für Anorg. Allg. Chem.* **234**, 311–336 (1937).
- [53] Hummers, W. S. & Offeman, R. E. Preparation of Graphitic Oxide. *J. Am. Chem. Soc.* **80**, 1339–1339 (1958).
- [54] Brisebois, P. P. & Siaz, M. Harvesting graphene oxide – years 1859 to 2019: a review of its structure, synthesis, properties and exfoliation. *J. Mater. Chem. C* **8**, 1517–1547 (2020).
- [55] Talyzin, A. V. *et al.* Brodie vs Hummers graphite oxides for preparation of multi-layered materials. *Carbon* **115**, 430–440 (2017).
- [56] Chua, C. K., Sofer, Z. & Pumera, M. Graphite Oxides: Effects of Permanganate and Chlorate Oxidants on the Oxygen Composition. *Chem. – Eur. J.* **18**, 13453–13459 (2012).
- [57] Marcano, D. C. *et al.* Improved Synthesis of Graphene Oxide. *ACS Nano* **4**, 4806–4814 (2010).
- [58] Poh, H. L. *et al.* Graphenes prepared by Staudenmaier, Hofmann and Hummers methods with consequent thermal exfoliation exhibit very different electrochemical properties. *Nanoscale* **4**, 3515–3522 (2012).
- [59] Yu, H., Zhang, B., Bulin, C., Li, R. & Xing, R. High-efficient Synthesis of Graphene Oxide Based on Improved Hummers Method. *Sci. Rep.* **6**, 36143 (2016).
- [60] Eigler, S. Graphite sulphate – a precursor to graphene. *Chem. Commun.* **51**, 3162–3165 (2015).
- [61] Chen, J. *et al.* Water-enhanced oxidation of graphite to graphene oxide with controlled species of oxygenated groups. *Chem. Sci.* **7**, 1874–1881 (2016).
- [62] Zhao, J., Pei, S., Ren, W., Gao, L. & Cheng, H.-M. Efficient Preparation of Large-Area Graphene Oxide Sheets for Transparent Conductive Films. *ACS Nano* **4**, 5245–5252 (2010).

- [63] Chen, H., Du, W., Liu, J., Qu, L. & Li, C. Efficient room-temperature production of high-quality graphene by introducing removable oxygen functional groups to the precursor. *Chem. Sci.* **10**, 1244–1253 (2019).
- [64] Qin, J. *et al.* Room temperature production of graphene oxide with thermally labile oxygen functional groups for improved lithium ion battery fabrication and performance. *J. Mater. Chem. A* **7**, 9646–9655 (2019).
- [65] Dimiev, A. M. & Tour, J. M. Mechanism of Graphene Oxide Formation. *ACS Nano* **8**, 3060–3068 (2014).
- [66] Pan, S. & Aksay, I. A. Factors Controlling the Size of Graphene Oxide Sheets Produced via the Graphite Oxide Route. *ACS Nano* **5**, 4073–4083 (2011).
- [67] Shao, G. *et al.* Graphene oxide: the mechanisms of oxidation and exfoliation. *J. Mater. Sci.* **47**, 4400–4409 (2012).
- [68] Singh, R. K., Kumar, R. & Singh, D. P. Graphene oxide: strategies for synthesis, reduction and frontier applications. *RSC Adv.* **6**, 64993–65011 (2016).
- [69] Kovtyukhova, N. I. *et al.* Layer-by-Layer Assembly of Ultrathin Composite Films from Micron-Sized Graphite Oxide Sheets and Polycations. *Chem. Mater.* **11**, 771–778 (1999).
- [70] Ceriotti, G., Romanchuk, A. Y., Slesarev, A. S. & Kalmykov, S. N. Rapid method for the purification of graphene oxide. *RSC Adv.* **5**, 50365–50371 (2015).
- [71] Tam, B. & Yazaydin, O. Design of electric field controlled molecular gates mounted on metal–organic frameworks. *J. Mater. Chem. A* **5**, 8690–8696 (2017).
- [72] Tang, L. *et al.* Deep ultraviolet to near-infrared emission and photoresponse in layered N-doped graphene quantum dots. *ACS Nano* **8**, 6312–6320 (2014).
- [73] He, H., Riedl, T., Lerf, A. & Klinowski, J. Solid-State NMR Studies of the Structure of Graphite Oxide. *J. Phys. Chem.* **100**, 19954–19958 (1996).
- [74] Lian, B. *et al.* Extraordinary water adsorption characteristics of graphene oxide. *Chem. Sci.* **9**, 5106–5111 (2018).
- [75] Cai, C., Sang, N., Shen, Z. & Zhao, X. Facile and size-controllable preparation of graphene oxide nanosheets using high shear method and ultrasonic method. *J. Exp. Nanosci.* **12**, 247–262 (2017).
- [76] Qi, X. *et al.* Size-specified graphene oxide sheets: ultrasonication assisted preparation and characterization. *J. Mater. Sci.* **49**, 1785–1793 (2014).
- [77] Botas, C. *et al.* Optimization of the size and yield of graphene oxide sheets in the exfoliation step. *Carbon* **63**, 576–578 (2013).
- [78] Szabo, T., Maroni, P. & Szilagy, I. Size-dependent aggregation of graphene oxide. *Carbon* **160**, 145–155 (2020).
- [79] Dan, B. *et al.* Liquid crystals of aqueous, giant graphene oxide flakes. *Soft Matter* **7**, 11154–11159 (2011).
- [80] He, H., Klinowski, J., Forster, M. & Lerf, A. A new structural model for graphite oxide. *Chem. Phys. Lett.* **287**, 53–56 (1998).
- [81] Lerf, A., He, H., Forster, M. & Klinowski, J. Structure of Graphite Oxide Revisited. *J. Phys. Chem. B* **102**, 4477–4482 (1998).
- [82] Lerf, A., He, H., Riedl, T., Forster, M. & Klinowski, J. ¹³C and ¹H MAS NMR studies of graphite oxide and its chemically modified derivatives. *Solid State Ion.* **101–103**, 857–862 (1997).
- [83] Paci, J. T., Belytschko, T. & Schatz, G. C. Computational Studies of the Structure, Behavior upon Heating, and Mechanical Properties of Graphite Oxide. *J. Phys. Chem. C* **111**, 18099–18111 (2007).

- [84] Dave, S. H., Gong, C., Robertson, A. W., Warner, J. H. & Grossman, J. C. Chemistry and Structure of Graphene Oxide via Direct Imaging. *ACS Nano* **10**, 7515–7522 (2016).
- [85] Erickson, K. *et al.* Determination of the Local Chemical Structure of Graphene Oxide and Reduced Graphene Oxide. *Adv. Mater.* **22**, 4467–4472 (2010).
- [86] Cai, W. *et al.* Synthesis and solid-state NMR structural characterization of ¹³C-labeled graphite oxide. *Science* **321**, 1815–1817 (2008).
- [87] Gao, W., Alemany, L. B., Ci, L. & Ajayan, P. M. New insights into the structure and reduction of graphite oxide. *Nat. Chem.* **1**, 403–408 (2009).
- [88] Eigler, S., Dotzer, C., Hof, F., Bauer, W. & Hirsch, A. Sulfur Species in Graphene Oxide. *Chem. – Eur. J.* **19**, 9490–9496 (2013).
- [89] Pei, S., Wei, Q., Huang, K., Cheng, H.-M. & Ren, W. Green synthesis of graphene oxide by seconds timescale water electrolytic oxidation. *Nat. Commun.* **9**, 145 (2018).
- [90] Konkana, B. & Vasudevan, S. Understanding Aqueous Dispersibility of Graphene Oxide and Reduced Graphene Oxide through pKa Measurements. *J. Phys. Chem. Lett.* **3**, 867–872 (2012).
- [91] Dimiev, A. M., Alemany, L. B. & Tour, J. M. Graphene Oxide. Origin of Acidity, Its Instability in Water, and a New Dynamic Structural Model. *ACS Nano* **7**, 576–588 (2013).
- [92] Li, D., Müller, M. B., Gilje, S., Kaner, R. B. & Wallace, G. G. Processable aqueous dispersions of graphene nanosheets. *Nat. Nanotechnol.* **3**, 101–105 (2008).
- [93] Lowry, G. V. *et al.* Guidance to improve the scientific value of zeta-potential measurements in nanoEHS. *Environ. Sci. Nano* **3**, 953–965 (2016).
- [94] Gudarzi, M. M. Colloidal Stability of Graphene Oxide: Aggregation in Two Dimensions. *Langmuir* **32**, 5058–5068 (2016).
- [95] Chowdhury, I., Duch, M. C., Mansukhani, N. D., Hersam, M. C. & Bouchard, D. Colloidal Properties and Stability of Graphene Oxide Nanomaterials in the Aquatic Environment. *Environ. Sci. Technol.* **47**, 6288–6296 (2013).
- [96] Wu, L. *et al.* Aggregation Kinetics of Graphene Oxides in Aqueous Solutions: Experiments, Mechanisms, and Modeling. *Langmuir* **29**, 15174–15181 (2013).
- [97] Baskoro, F. *et al.* Graphene oxide-cation interaction: Inter-layer spacing and zeta potential changes in response to various salt solutions. *J. Membr. Sci.* **554**, 253–263 (2018).
- [98] Szabó, T. *et al.* Evolution of Surface Functional Groups in a Series of Progressively Oxidized Graphite Oxides. *Chem. Mater.* **18**, 2740–2749 (2006).
- [99] Wang, X., Bai, H. & Shi, G. Size Fractionation of Graphene Oxide Sheets by pH-Assisted Selective Sedimentation. *J. Am. Chem. Soc.* **133**, 6338–6342 (2011).
- [100] Park, S. *et al.* Hydrazine-reduction of graphite- and graphene oxide. *Carbon* **49**, 3019–3023 (2011).
- [101] Qi, Y., Xia, T., Li, Y., Duan, L. & Chen, W. Colloidal stability of reduced graphene oxide materials prepared using different reducing agents. *Environ. Sci. Nano* **3**, 1062–1071 (2016).
- [102] Zhang, J. *et al.* Reduction of graphene oxide via l - ascorbic acid. *Chem. Commun.* **46**, 1112–1114 (2010).
- [103] Azizighannad, S. & Mitra, S. Stepwise Reduction of Graphene Oxide (GO) and Its Effects on Chemical and Colloidal Properties. *Sci. Rep.* **8**, 10083 (2018).
- [104] Wang, Y., Shi, Z. & Yin, J. Facile Synthesis of Soluble Graphene via a Green Reduction of Graphene Oxide in Tea Solution and Its Biocomposites. *ACS Appl. Mater. Interfaces* **3**, 1127–1133 (2011).

- [105] Bose, S., Kuila, T., Kumar Mishra, A., Hoon Kim, N. & Hee Lee, J. Dual role of glycine as a chemical functionalizer and a reducing agent in the preparation of graphene: an environmentally friendly method. *J. Mater. Chem.* **22**, 9696–9703 (2012).
- [106] Paredes, J. I., Villar-Rodil, S., Martínez-Alonso, A. & Tascón, J. M. D. Graphene Oxide Dispersions in Organic Solvents. *Langmuir* **24**, 10560–10564 (2008).
- [107] Jalili, R. *et al.* Organic Solvent-Based Graphene Oxide Liquid Crystals: A Facile Route toward the Next Generation of Self-Assembled Layer-by-Layer Multifunctional 3D Architectures. *ACS Nano* **7**, 3981–3990 (2013).
- [108] Park, S. *et al.* Colloidal Suspensions of Highly Reduced Graphene Oxide in a Wide Variety of Organic Solvents. *Nano Lett.* **9**, 1593–1597 (2009).
- [109] Konios, D., Stylianakis, M. M., Stratakis, E. & Kymakis, E. Dispersion behaviour of graphene oxide and reduced graphene oxide. *J. Colloid Interface Sci.* **430**, 108–112 (2014).
- [110] Khan, U. *et al.* Solvent-Exfoliated Graphene at Extremely High Concentration. *Langmuir* **27**, 9077–9082 (2011).
- [111] Hernandez, Y. *et al.* High-yield production of graphene by liquid-phase exfoliation of graphite. *Nat. Nanotechnol.* **3**, 563–568 (2008).
- [112] Wang, S., Zhang, Y., Abidi, N. & Cabrales, L. Wettability and Surface Free Energy of Graphene Films. *Langmuir* **25**, 11078–11081 (2009).
- [113] Zhang, X. *et al.* Ultralight, Superelastic, and Fatigue-Resistant Graphene Aerogel Templated by Graphene Oxide Liquid Crystal Stabilized Air Bubbles. *ACS Appl. Mater. Interfaces* **11**, 1303–1310 (2019).
- [114] Liu, C. *et al.* CO₂/Water Emulsions Stabilized by Partially Reduced Graphene Oxide. *ACS Appl. Mater. Interfaces* **9**, 17613–17619 (2017).
- [115] He, Y. *et al.* Factors that Affect Pickering Emulsions Stabilized by Graphene Oxide. *ACS Appl. Mater. Interfaces* **5**, 4843–4855 (2013).
- [116] Walstra, P. Principles of emulsion formation. *Chem. Eng. Sci.* **48**, 333–349 (1993).
- [117] Cote, L. J. *et al.* Graphene oxide as surfactant sheets. *Pure Appl. Chem.* **83**, 95–110 (2010).
- [118] Berry, J. D., Neeson, M. J., Dagastine, R. R., Chan, D. Y. C. & Tabor, R. F. Measurement of surface and interfacial tension using pendant drop tensiometry. *J. Colloid Interface Sci.* **454**, 226–237 (2015).
- [119] Gamot, T. D. *et al.* Synthesis and Stability of Water-in-Oil Emulsion Using Partially Reduced Graphene Oxide as a Tailored Surfactant. *Langmuir* **33**, 10311–10321 (2017).
- [120] Yoon, K. Y. *et al.* Graphene oxide nanoplatelet dispersions in concentrated NaCl and stabilization of oil/water emulsions. *J. Colloid Interface Sci.* **403**, 1–6 (2013).
- [121] Chen, H. *et al.* Triple Phase Inversion of Emulsions Stabilized by Amphiphilic Graphene Oxide and Cationic Surfactants. *ACS Omega* **5**, 23524–23532 (2020).
- [122] Yi, W., Wu, H., Wang, H. & Du, Q. Interconnectivity of Macroporous Hydrogels Prepared via Graphene Oxide-Stabilized Pickering High Internal Phase Emulsions. *Langmuir* **32**, 982–990 (2016).
- [123] Aveyard, R., Binks, B. P. & Clint, J. H. Emulsions stabilised solely by colloidal particles. *Adv. Colloid Interface Sci.* **100–102**, 503–546 (2003).
- [124] Tambe, D. E. & Sharma, M. M. The effect of colloidal particles on fluid-fluid interfacial properties and emulsion stability. *Adv. Colloid Interface Sci.* **52**, 1–63 (1994).
- [125] Binks, B. P. & Lumsdon, S. O. Influence of Particle Wettability on the Type and Stability of Surfactant-Free Emulsions. *Langmuir* **16**, 8622–8631 (2000).

- [126] Binks, B. P. Particles as surfactants—similarities and differences. *Curr. Opin. Colloid Interface Sci.* **7**, 21–41 (2002).
- [127] Velikov, K. P. & Velev, O. D. Stabilization of Thin Films, Foams, Emulsions and Bifluid Gels with Surface-Active Solid Particles. in *Colloid Stability and Application in Pharmacy* 277–306 (John Wiley & Sons, Ltd, 2007).
- [128] Levine, S., Bowen, B. D. & Partridge, S. J. Stabilization of emulsions by fine particles I. Partitioning of particles between continuous phase and oil/water interface. *Colloids Surf.* **38**, 325–343 (1989).
- [129] Sun, P. *et al.* Selective Ion Penetration of Graphene Oxide Membranes. *ACS Nano* **7**, 428–437 (2013).
- [130] Moon, I. K., Lee, J., Ruoff, R. S. & Lee, H. Reduced graphene oxide by chemical graphitization. *Nat. Commun.* **1**, 73 (2010).
- [131] Xu, K. *et al.* Wetting Properties of Defective Graphene Oxide: A Molecular Simulation Study. *Molecules* **23**, 1439 (2018).
- [132] Hu, Y. *et al.* Functional nanoparticle-decorated graphene oxide sheets as stabilizers for Pickering high internal phase emulsions and graphene oxide based foam monoliths. *RSC Adv.* **5**, 103394–103402 (2015).
- [133] Creighton, M. A., Ohata, Y., Miyawaki, J., Bose, A. & Hurt, R. H. Two-Dimensional Materials as Emulsion Stabilizers: Interfacial Thermodynamics and Molecular Barrier Properties. *Langmuir* **30**, 3687–3696 (2014).
- [134] Guo, F. *et al.* Graphene-Based Environmental Barriers. *Environ. Sci. Technol.* **46**, 7717–7724 (2012).
- [135] Bunch, J. S. *et al.* Impermeable Atomic Membranes from Graphene Sheets. *Nano Lett.* **8**, 2458–2462 (2008).
- [136] Thickett, S. C. & Zetterlund, P. B. Graphene oxide (GO) nanosheets as oil-in-water emulsion stabilizers: Influence of oil phase polarity. *J. Colloid Interface Sci.* **442**, 67–74 (2015).
- [137] Sadgar, A. L., Deore, T. S., Hase, D. V. & Jayaram, R. V. Graphene Oxide Pickering Emulsion – A Novel Reaction Medium for the Synthesis of 2-Aminothiazole. *ChemistrySelect* **6**, 12446–12454 (2021).
- [138] McCoy, T. M., Pottage, M. J. & Tabor, R. F. Graphene Oxide-Stabilized Oil-in-Water Emulsions: pH-Controlled Dispersion and Flocculation. *J. Phys. Chem. C* **118**, 4529–4535 (2014).
- [139] Gu, X., Ning, Y., Yang, Y. & Wang, C. One-step synthesis of porous graphene-based hydrogels containing oil droplets for drug delivery. *RSC Adv.* **4**, 3211–3218 (2013).
- [140] Zheng, Z., Zheng, X., Wang, H. & Du, Q. Macroporous Graphene Oxide–Polymer Composite Prepared through Pickering High Internal Phase Emulsions. *ACS Appl. Mater. Interfaces* **5**, 7974–7982 (2013).
- [141] Barg, S. *et al.* Mesoscale assembly of chemically modified graphene into complex cellular networks. *Nat. Commun.* **5**, 4328 (2014).
- [142] Cameron, N. R. High internal phase emulsion templating as a route to well-defined porous polymers. *Polymer* **46**, 1439–1449 (2005).
- [143] Ikem, V. O., Menner, A., Horozov, T. S. & Bismarck, A. Highly Permeable Macroporous Polymers Synthesized from Pickering Medium and High Internal Phase Emulsion Templates. *Adv. Mater.* **22**, 3588–3592 (2010).
- [144] Kim, K. *et al.* Processable high internal phase Pickering emulsions using depletion attraction. *Nat. Commun.* **8**, 14305 (2017).

- [145] Kunieda, H., Solans, C., Shida, N. & Parra, J. L. The formation of gel-emulsions in a water/nonionic surfactant/oil system. *Colloids Surf.* **24**, 225–237 (1987).
- [146] Solans, C. *et al.* Studies on macro- and microstructures of highly concentrated water-in-oil emulsions (gel emulsions). *Langmuir* **9**, 1479–1482 (1993).
- [147] Lee, M. C., Tan, C., Ravanfar, R. & Abbaspourrad, A. Ultrastable Water-in-Oil High Internal Phase Emulsions Featuring Interfacial and Biphasic Network Stabilization. *ACS Appl. Mater. Interfaces* **11**, 26433–26441 (2019).
- [148] Ikem, V. O., Menner, A. & Bismarck, A. High Internal Phase Emulsions Stabilized Solely by Functionalized Silica Particles. *Angew. Chem.* **120**, 8401–8403 (2008).
- [149] T. Woodward, R. *et al.* Carbon foams from emulsion-templated reduced graphene oxide polymer composites: electrodes for supercapacitor devices. *J. Mater. Chem. A* **6**, 1840–1849 (2018).
- [150] Wong, L. L. C. *et al.* Macroporous polymer nanocomposites synthesised from high internal phase emulsion templates stabilised by reduced graphene oxide. *Polymer* **55**, 395–402 (2014).
- [151] Zhang, B. *et al.* Cellular graphene aerogel combines ultralow weight and high mechanical strength: A highly efficient reactor for catalytic hydrogenation. *Sci. Rep.* **6**, 25830 (2016).
- [152] Li, Y. *et al.* Highly Compressible Macroporous Graphene Monoliths via an Improved Hydrothermal Process. *Adv. Mater.* **26**, 4789–4793 (2014).
- [153] Liu, H. *et al.* Preparation of graphene-based aerogels by Pickering emulsion method and their performance. *Fuller. Nanotub. Carbon Nanostructures* **29**, 464–474 (2021).
- [154] Kuziel, A. W. *et al.* The True Amphipathic Nature of Graphene Flakes: A Versatile 2D Stabilizer. *Adv. Mater.* **32**, 2000608 (2020).
- [155] Woltornist, S. J. *et al.* Controlled 3D Assembly of Graphene Sheets to Build Conductive, Chemically Selective and Shape-Responsive Materials. *Adv. Mater.* **29**, 1604947 (2017).
- [156] Mi, X. *et al.* Modified reduced graphene oxide as stabilizer for Pickering w/o emulsions. *J. Mater. Sci.* **55**, 1946–1958 (2020).
- [157] Wang, J. *et al.* Facile fabrication of near-infrared light-responsive shape memory nanocomposite scaffolds with hierarchical porous structures. *J. Appl. Polym. Sci.* **138**, 50938 (2021).
- [158] Yang, S., Wu, H., Li, C., Xiong, Y. & Guo, S. Constructing Oriented Two-Dimensional Large-Sized Modified Graphene Oxide Barrier Walls in Brominated Butyl Rubber to Achieve Excellent Gas Barrier Properties. *ACS Appl. Mater. Interfaces* **12**, 3976–3983 (2020).
- [159] Huang, X., Sun, B., Su, D., Zhao, D. & Wang, G. Soft-template synthesis of 3D porous graphene foams with tunable architectures for lithium–O₂ batteries and oil adsorption applications. *J. Mater. Chem. A* **2**, 7973–7979 (2014).
- [160] He, Z. *et al.* Synergistic Regulation of the Microstructure for Multifunctional Graphene Aerogels by a Dual Template Method. *ACS Appl. Mater. Interfaces* **14**, 22544–22553 (2022).
- [161] Gai, T. *et al.* Synthesis of graphene gel loading TBP via a one-step method, and its application for uranyl extraction. *Sep. Purif. Technol.* **260**, 118224 (2021).
- [162] Chen, Y. *et al.* Hierarchical and reversible assembly of graphene oxide/polyvinyl alcohol hybrid stabilized Pickering emulsions and their templating for macroporous composite hydrogels. *Carbon* **111**, 38–47 (2017).
- [163] Wan, W. *et al.* Graphene oxide liquid crystal Pickering emulsions and their assemblies. *Carbon* **85**, 16–23 (2015).
- [164] Shang, Y. & Zhang, D. Preparation and characterization of three-dimensional graphene network encapsulating 1-hexadecanol composite. *Appl. Therm. Eng.* **111**, 353–357 (2017).

- [165] Pohan, N. A., Wahid, M. H., Zainal, Z. & Ibrahim, N. A. Pickering-emulsion-templated synthesis of 3D hollow graphene as an efficient oil absorbent. *RSC Adv.* **11**, 3963–3971 (2021).
- [166] Zhang, P. *et al.* Superelastic, Macroporous Polystyrene-Mediated Graphene Aerogels for Active Pressure Sensing. *Chem. – Asian J.* **11**, 1071–1075 (2016).
- [167] Chen, L.-C., Lei, S., Wang, M.-Z., Yang, J. & Ge, X.-W. Fabrication of macroporous polystyrene/graphene oxide composite monolith and its adsorption property for tetracycline. *Chin. Chem. Lett.* **27**, 511–517 (2016).
- [168] Wu, H., Lu, L., Zhang, Y., Sun, Z. & Qian, L. A facile method to prepare porous graphene with tunable structure as electrode materials for immobilization of glucose oxidase. *Colloids Surf. Physicochem. Eng. Asp.* **502**, 26–33 (2016).
- [169] Chen, X., Eggers, P. K., Slattery, A. D., Ogden, S. G. & Raston, C. L. Template-free assembly of three-dimensional networks of graphene hollow spheres at the water/toluene interface. *J. Colloid Interface Sci.* **430**, 174–177 (2014).
- [170] Nagarajan, S. *et al.* Porous Gelatin Membrane Obtained from Pickering Emulsions Stabilized by Graphene Oxide. *Langmuir* **34**, 1542–1549 (2018).
- [171] Bo, Y. *et al.* Preparation of elastic graphene aerogel and its adsorption of oil. *J. Porous Mater.* **28**, 39–56 (2021).
- [172] Zhang, R. *et al.* Pickering emulsion template method induced highly oriented functionalized graphene oxide in PDMS composites to achieve high gas barrier properties. *Polymer* **235**, 124273 (2021).
- [173] Liao, D. *et al.* Pickering emulsion strategy for high compressive carbon aerogel as lightweight electromagnetic interference shielding material and flexible pressure sensor. *Ceram. Int.* **47**, 23433–23443 (2021).
- [174] Zhang, P. *et al.* A versatile, superelastic polystyrene/graphene capsule-like framework. *J. Mater. Chem. A* **4**, 10118–10123 (2016).
- [175] Zhang, F. *et al.* Pickering emulsions stabilized by a metal–organic framework (MOF) and graphene oxide (GO) for producing MOF/GO composites. *Soft Matter* **13**, 7365–7370 (2017).
- [176] Jahandideh, H., Nguyen, Q. A. & Tufenkji, N. Polymer-Free Emulsion-Templated Graphene-Based Sponges for Contaminant Removal. *ACS Appl. Mater. Interfaces* **12**, 52095–52103 (2020).
- [177] Wang, X. *et al.* Self-assembling graphene oxide/modified amphipathic hydroxyethyl cellulose hybrid stabilized Pickering emulsion polymerization for functional hydrogel. *Colloids Surf. Physicochem. Eng. Asp.* **610**, 125742 (2021).
- [178] Wang, B., Dou, S., Gao, Y. & Li, W. Structure and electrically conductive properties of porous PAN-based nanocomposites prepared by Pickering emulsion template method. *J. Appl. Polym. Sci.* **137**, 49017 (2020).
- [179] Huang, Y. *et al.* Hypercrosslinked porous polymers hybridized with graphene oxide for water treatment: dye adsorption and degradation. *RSC Adv.* **8**, 13417–13422 (2018).
- [180] Zhang, W. *et al.* Novel porous carbon composites derived from a graphene-modified high-internal- phase emulsion for highly efficient separation and enrichment of triazine herbicides. *Anal. Chim. Acta* **1071**, 17–24 (2019).
- [181] Yang, L. *et al.* One-pot preparation of porous piezoresistive sensor with high strain sensitivity via emulsion-templated polymerization. *Compos. Part Appl. Sci. Manuf.* **101**, 195–198 (2017).

- [182] Xie, H., Ke, Q. & Xiong, X. Preparation of a Cu₂O/rGO porous composite through a double-sacrificial-template method for non-enzymatic glucose detection. *J. Mater. Sci.* **52**, 5652–5660 (2017).
- [183] Xu, Y., Sheng, K., Li, C. & Shi, G. Self-Assembled Graphene Hydrogel via a One-Step Hydrothermal Process. *ACS Nano* **4**, 4324–4330 (2010).
- [184] Hu, K., Xie, X., Szkopek, T. & Cerruti, M. Understanding Hydrothermally Reduced Graphene Oxide Hydrogels: From Reaction Products to Hydrogel Properties. *Chem. Mater.* **28**, 1756–1768 (2016).
- [185] Qiu, L., Liu, J. Z., Chang, S. L. Y., Wu, Y. & Li, D. Biomimetic superelastic graphene-based cellular monoliths. *Nat. Commun.* **3**, 1241 (2012).
- [186] Xie, X. *et al.* Large-range Control of the Microstructures and Properties of Three-dimensional Porous Graphene. *Sci. Rep.* **3**, 2117 (2013).
- [187] Zhu, X. *et al.* Precise control of versatile microstructure and properties of graphene aerogel via freezing manipulation. *Nanoscale* **12**, 4882–4894 (2020).
- [188] Liu, T. *et al.* Highly compressible anisotropic graphene aerogels fabricated by directional freezing for efficient absorption of organic liquids. *Carbon* **100**, 456–464 (2016).
- [189] Gao, Y.-Y. *et al.* Light-Responsive Actuators Based on Graphene. *Front. Chem.* **7**, (2019).
- [190] Rui-Hong, X. *et al.* Preparation and properties of graphene oxide-regenerated cellulose/polyvinyl alcohol hydrogel with pH-sensitive behavior. *Carbohydr. Polym.* **138**, 222–228 (2016).
- [191] Bai, H., Li, C., Wang, X. & Shi, G. A pH-sensitive graphene oxide composite hydrogel. *Chem. Commun.* **46**, 2376–2378 (2010).
- [192] Fang, M., Long, J., Zhao, W., Wang, L. & Chen, G. pH-Responsive Chitosan-Mediated Graphene Dispersions. *Langmuir* **26**, 16771–16774 (2010).
- [193] Kavitha, T., Abdi, S. I. H. & Park, S.-Y. pH-Sensitive nanocargo based on smart polymer functionalized graphene oxide for site-specific drug delivery. *Phys. Chem. Chem. Phys.* **15**, 5176–5185 (2013).
- [194] Paek, K., Yang, H., Lee, J., Park, J. & Kim, B. J. Efficient Colorimetric pH Sensor Based on Responsive Polymer–Quantum Dot Integrated Graphene Oxide. *ACS Nano* **8**, 2848–2856 (2014).
- [195] Savchuk, O. A., Carvajal, J. J., Massons, J., Aguiló, M. & Díaz, F. Determination of photothermal conversion efficiency of graphene and graphene oxide through an integrating sphere method. *Carbon* **103**, 134–141 (2016).
- [196] Robinson, J. T. *et al.* Ultrasmall Reduced Graphene Oxide with High Near-Infrared Absorbance for Photothermal Therapy. *J. Am. Chem. Soc.* **133**, 6825–6831 (2011).
- [197] Tian, B., Wang, C., Zhang, S., Feng, L. & Liu, Z. Photothermally Enhanced Photodynamic Therapy Delivered by Nano-Graphene Oxide. *ACS Nano* **5**, 7000–7009 (2011).
- [198] Acik, M. *et al.* Unusual infrared-absorption mechanism in thermally reduced graphene oxide. *Nat. Mater.* **9**, 840–845 (2010).
- [199] Tran, T. H. *et al.* Development of a Graphene Oxide Nanocarrier for Dual-Drug Chemophototherapy to Overcome Drug Resistance in Cancer. *ACS Appl. Mater. Interfaces* **7**, 28647–28655 (2015).
- [200] Chen, J. *et al.* One-step reduction and PEGylation of graphene oxide for photothermally controlled drug delivery. *Biomaterials* **35**, 4986–4995 (2014).
- [201] Zhang, W. *et al.* Synergistic effect of chemo-photothermal therapy using PEGylated graphene oxide. *Biomaterials* **32**, 8555–8561 (2011).

- [202] Liang, J. *et al.* Infrared-Triggered Actuators from Graphene-Based Nanocomposites. *J. Phys. Chem. C* **113**, 9921–9927 (2009).
- [203] Lu, Q., Jang, H. S., Han, W. J., Lee, J. H. & Choi, H. J. Stimuli-Responsive Graphene Oxide-Polymer Nanocomposites. *Macromol. Res.* **27**, 1061–1070 (2019).
- [204] Shi, K. *et al.* Near-Infrared Light-Responsive Poly(N-isopropylacrylamide)/Graphene Oxide Nanocomposite Hydrogels with Ultrahigh Tensibility. *ACS Appl. Mater. Interfaces* **7**, 27289–27298 (2015).
- [205] Han, B. *et al.* Plasmonic-Assisted Graphene Oxide Artificial Muscles. *Adv. Mater.* **31**, 1806386 (2019).
- [206] Su, Y. *et al.* Exceptional negative thermal expansion and viscoelastic properties of graphene oxide paper. *Carbon* **50**, 2804–2809 (2012).
- [207] Huh, S. H., Choi, S.-H., Ju, H.-M. & Kim, D.-H. Properties of interlayer thermal expansion of 6-layered reduced graphene oxide. *J. Korean Phys. Soc.* **64**, 615–618 (2014).
- [208] Han, B., Zhang, Y.-L., Chen, Q.-D. & Sun, H.-B. Carbon-Based Photothermal Actuators. *Adv. Funct. Mater.* **28**, 1802235 (2018).
- [209] Ji, M., Jiang, N., Chang, J. & Sun, J. Near-Infrared Light-Driven, Highly Efficient Bilayer Actuators Based on Polydopamine-Modified Reduced Graphene Oxide. *Adv. Funct. Mater.* **24**, 5412–5419 (2014).
- [210] Zhang, L., Pan, J., Liu, Y., Xu, Y. & Zhang, A. NIR–UV Responsive Actuator with Graphene Oxide/Microchannel-Induced Liquid Crystal Bilayer Structure for Biomimetic Devices. *ACS Appl. Mater. Interfaces* **12**, 6727–6735 (2020).
- [211] Ma, C. *et al.* Bioinspired Anisotropic Hydrogel Actuators with On–Off Switchable and Color-Tunable Fluorescence Behaviors. *Adv. Funct. Mater.* **28**, 1704568 (2018).
- [212] Wang, W. *et al.* Graphene Oxide/Nanofiber-Based Actuation Films with Moisture and Photothermal Stimulation Response for Remote Intelligent Control Applications. *ACS Appl. Mater. Interfaces* **13**, 48179–48188 (2021).
- [213] Wang, E., Desai, M. S. & Lee, S.-W. Light-Controlled Graphene-Elastin Composite Hydrogel Actuators. *Nano Lett.* **13**, 2826–2830 (2013).
- [214] Yang, Y., Liu, Y. & Shen, Y. Plasmonic-Assisted Graphene Oxide Films with Enhanced Photothermal Actuation for Soft Robots. *Adv. Funct. Mater.* **30**, 1910172 (2020).
- [215] Wang, W. *et al.* Photothermal and Moisture Actuator Made with Graphene Oxide and Sodium Alginate for Remotely Controllable and Programmable Intelligent Devices. *ACS Appl. Mater. Interfaces* **11**, 21926–21934 (2019).
- [216] Han, D.-D. *et al.* Biomimetic Graphene Actuators Enabled by Multiresponse Graphene Oxide Paper with Pretailored Reduction Gradient. *Adv. Mater. Technol.* **3**, 1800258 (2018).
- [217] Wang, W. *et al.* A complementary strategy for producing moisture and alkane dual-responsive actuators based on graphene oxide and PDMS bimorph. *Sens. Actuators B Chem.* **290**, 133–139 (2019).
- [218] Zhu, J. *et al.* Pseudonegative Thermal Expansion and the State of Water in Graphene Oxide Layered Assemblies. *ACS Nano* **6**, 8357–8365 (2012).
- [219] Heskins, M. & Guillet, J. E. Solution Properties of Poly(N-isopropylacrylamide). *J. Macromol. Sci. Part - Chem.* **2**, 1441–1455 (1968).
- [220] Schmaljohann, D. Thermo- and pH-responsive polymers in drug delivery. *Adv. Drug Deliv. Rev.* **58**, 1655–1670 (2006).

- [221] Wei, H., Zhang, X.-Z., Zhou, Y., Cheng, S.-X. & Zhuo, R.-X. Self-assembled thermoresponsive micelles of poly(N-isopropylacrylamide-*b*-methyl methacrylate). *Biomaterials* **27**, 2028–2034 (2006).
- [222] Long, H. *et al.* A dual drug delivery platform based on thermo-responsive polymeric micelle capped mesoporous silica nanoparticles for cancer therapy. *Microporous Mesoporous Mater.* **338**, (2022).
- [223] Liu, Z. *et al.* Temperature/pH-Responsive Carboxymethyl Cellulose/Poly (N-isopropyl acrylamide) Interpenetrating Polymer Network Aerogels for Drug Delivery Systems. *Polymers* **14**, (2022).
- [224] Schacher, F., Ulbricht, M. & Müller, A. H. E. Self-supporting, double stimuli-responsive porous membranes from polystyrene-block-poly(N,N-dimethylaminoethyl methacrylate) diblock copolymers. *Adv. Funct. Mater.* **19**, 1040–1045 (2009).
- [225] Menne, D., Pitsch, F., Wong, J. E., Pich, A. & Wessling, M. Temperature-modulated water filtration using microgel-functionalized hollow-fiber membranes. *Angew. Chem. - Int. Ed.* **53**, 5706–5710 (2014).
- [226] Liu, J. *et al.* Thermoresponsive Graphene Membranes with Reversible Gating Regularity for Smart Fluid Control. *Adv. Funct. Mater.* **29**, (2019).
- [227] Daumann, K., Frost, S. & Ulbricht, M. Tunable and switchable nanoparticle separation with thermo-responsive track-etched membranes prepared by controlled surface-initiated polymerization of poly(N-isopropylacrylamide). *RSC Adv.* **10**, 21028–21038 (2020).
- [228] Nie, L. *et al.* Temperature responsive hydrogel for cells encapsulation based on graphene oxide reinforced poly(N-isopropylacrylamide)/hydroxyethyl-chitosan. *Mater. Today Commun.* **31**, 103697 (2022).
- [229] Zhao, J. *et al.* Temperature-Responsive Aldehyde Hydrogels with Injectable, Self-Healing, and Tunable Mechanical Properties. *Biomacromolecules* **23**, 2552–2561 (2022).
- [230] Liang, W. *et al.* Thermoresponsive Hydrogels as Microniches for Growth and Controlled Release of Induced Pluripotent Stem Cells. *Adv. Funct. Mater.* **31**, (2021).
- [231] Seuring, J. & Agarwal, S. Polymers with Upper Critical Solution Temperature in Aqueous Solution. *Macromol. Rapid Commun.* **33**, 1898–1920 (2012).
- [232] Bordat, A., Boissenot, T., Nicolas, J. & Tsapis, N. Thermoresponsive polymer nanocarriers for biomedical applications. *Adv. Drug Deliv. Rev.* **138**, 167–192 (2019).
- [233] Pasparakis, G. & Tsitsilianis, C. LCST polymers: Thermoresponsive nanostructured assemblies towards bioapplications. *Polymer* **211**, 123146 (2020).
- [234] Fujishige, S., Kubota, K. & Ando, I. Phase transition of aqueous solutions of poly(N-isopropylacrylamide) and poly(N-isopropylmethacrylamide). *ACS Publications* <https://pubs.acs.org/doi/pdf/10.1021/j100345a085> (2002).
- [235] Fujishige, S., Kubota, K. & Ando, I. Phase transition of aqueous solutions of poly(N-isopropylacrylamide) and poly(N-isopropylmethacrylamide). *J. Phys. Chem.* **93**, 3311–3313 (1989).
- [236] Zhao, C., Ma, Z. & Zhu, X. X. Rational design of thermoresponsive polymers in aqueous solutions: A thermodynamics map. *Prog. Polym. Sci.* **90**, 269–291 (2019).
- [237] Ahmed, Z., Gooding, E. A., Pimenov, K. V., Wang, L. & Asher, S. A. UV Resonance Raman Determination of Molecular Mechanism of Poly(N-isopropylacrylamide) Volume Phase Transition. *J. Phys. Chem. B* **113**, 4248–4256 (2009).

- [238] Ma, X., Li, Y., Wang, W., Ji, Q. & Xia, Y. Temperature-sensitive poly(N-isopropylacrylamide)/graphene oxide nanocomposite hydrogels by in situ polymerization with improved swelling capability and mechanical behavior. *Eur. Polym. J.* **49**, 389–396 (2013).
- [239] Lei, Y., Zhang, G. & Li, H. Thermal-responsive nanocomposite hydrogel based on graphene oxide-polyvinyl alcohol/poly (N-isopropylacrylamide). *IOP Conf. Ser. Mater. Sci. Eng.* **274**, 012115 (2017).
- [240] Li, Z. *et al.* Preparation and characterization of pH- and temperature-responsive hydrogels with surface-functionalized graphene oxide as the crosslinker. *Soft Matter* **8**, 3139–3145 (2012).
- [241] Zhang, E. *et al.* Robust and thermo-response graphene–PNIPAm hybrid hydrogels reinforced by hectorite clay. *Carbon* **62**, 117–126 (2013).
- [242] Lo, C.-W., Zhu, D. & Jiang, H. An infrared-light responsive graphene - oxide incorporated poly(N -isopropylacrylamide) hydrogel nanocomposite. *Soft Matter* **7**, 5604–5609 (2011).
- [243] Zhu, S. *et al.* Grafting of graphene oxide with stimuli-responsive polymers by using ATRP for drug release. *J. Nanoparticle Res.* **14**, 1132 (2012).
- [244] Wang, H. *et al.* Thermo-sensitive graphene oxide–polymer nanoparticle hybrids: synthesis, characterization, biocompatibility and drug delivery. *J. Mater. Chem. B* **2**, 1362–1370 (2014).
- [245] Pan, Y., Bao, H., Sahoo, N. G., Wu, T. & Li, L. Water-Soluble Poly(N-isopropylacrylamide)–Graphene Sheets Synthesized via Click Chemistry for Drug Delivery. *Adv. Funct. Mater.* **21**, 2754–2763 (2011).
- [246] Song, Y., Lü, J., Liu, B. & Lü, C. Temperature responsive polymer brushes grafted from graphene oxide: an efficient fluorescent sensing platform for 2,4,6-trinitrophenol. *J. Mater. Chem. C* **4**, 7083–7092 (2016).
- [247] Lee, J. *et al.* Colorimetric Thermometer from Graphene Oxide Platform Integrated with Red, Green, and Blue Emitting, Responsive Block Copolymers. *Chem. Mater.* **28**, 3446–3453 (2016).
- [248] Qi, J. *et al.* A graphene -based smart catalytic system with superior catalytic performances and temperature responsive catalytic behaviors. *Nanoscale* **5**, 6275–6279 (2013).
- [249] Wang, D., Duan, H., Lü, J. & Lü, C. Fabrication of thermo-responsive polymer functionalized reduced graphene oxide@Fe₃O₄@Au magnetic nanocomposites for enhanced catalytic applications. *J. Mater. Chem. A* **5**, 5088–5097 (2017).
- [250] Zhu, J. *et al.* Graphene Oxide-Supported Catalyst with Thermoresponsive Smart Surface for Selective Hydrogenation of Cinnamaldehyde. *ACS Appl. Mater. Interfaces* **11**, 16443–16451 (2019).
- [251] Wang, P., Chen, S., Cao, Z. & Wang, G. NIR Light-, Temperature-, pH-, and Redox-Responsive Polymer-Modified Reduced Graphene Oxide/Mesoporous Silica Sandwich-Like Nanocomposites for Controlled Release. *ACS Appl. Mater. Interfaces* **9**, 29055–29062 (2017).
- [252] Yoon, H. J. *et al.* Tunable Thermal-Sensitive Polymer–Graphene Oxide Composite for Efficient Capture and Release of Viable Circulating Tumor Cells. *Adv. Mater.* **28**, 4891–4897 (2016).
- [253] Yao, N. *et al.* Norfloxacin and Bisphenol-A Removal Using Temperature-Switchable Graphene Oxide. *ACS Appl. Mater. Interfaces* **10**, 29083–29091 (2018).
- [254] Yang, Y. *et al.* Synthesis of PNIPAM polymer brushes on reduced graphene oxide based on click chemistry and RAFT polymerization. *J. Polym. Sci. Part Polym. Chem.* **50**, 329–337 (2012).

- [255] Zhang, H. *et al.* Temperature-Responsive Electrocatalysis Based on Poly(N-Isopropylacrylamide)-Modified Graphene Oxide (PNIPAm-GO). *Chem. – Eur. J.* **25**, 1535–1542 (2019).
- [256] Kavitha, T., Kang, I.-K. & Park, S.-Y. Poly(N-vinyl caprolactam) grown on nanographene oxide as an effective nanocargo for drug delivery. *Colloids Surf. B Biointerfaces* **115**, 37–45 (2014).
- [257] Sanna, R. *et al.* Synthesis and characterization of graphene-containing thermoresponsive nanocomposite hydrogels of poly(N-vinylcaprolactam) prepared by frontal polymerization. *J. Polym. Sci. Part Polym. Chem.* **50**, 4110–4118 (2012).
- [258] Jiang, X. *et al.* Thermo-Responsive Graphene Oxide/Poly(Ethyl Ethylene Phosphate) Nanocomposite via Ring Opening Polymerization. *Nanomaterials* **9**, 207 (2019).
- [259] Deng, Y. *et al.* Thermoresponsive graphene oxide-PNIPAM nanocomposites with controllable grafting polymer chains via moderate in situ SET-LRP. *J. Polym. Sci. Part Polym. Chem.* **50**, 4451–4458 (2012).
- [260] Wang, Y. *et al.* Thermo-responsive hydrogels with tunable transition temperature crosslinked by multifunctional graphene oxide nanosheets. *Compos. Sci. Technol.* **151**, 139–146 (2017).
- [261] Liu, J. *et al.* Thermosensitive graphene nanocomposites formed using pyrene-terminal polymers made by RAFT polymerization. *J. Polym. Sci. Part Polym. Chem.* **48**, 425–433 (2010).
- [262] Qi, J., Lv, W., Zhang, G., Zhang, F. & Fan, X. Poly(N-isopropylacrylamide) on two-dimensional graphene oxide surfaces. *Polym. Chem.* **3**, 621–624 (2012).
- [263] Emam, H. E. & Shaheen, T. I. Design of a dual pH and temperature responsive hydrogel based on esterified cellulose nanocrystals for potential drug release. *Carbohydr. Polym.* **278**, 118925 (2022).
- [264] Li, M. & Bae, J. Tunable swelling and deswelling of temperature- and light-responsive graphene oxide-poly(N-isopropylacrylamide) composite hydrogels. *Polym. Chem.* **11**, 2332–2338 (2020).
- [265] Uddin, Md. E., Layek, R. K., Kim, N. H., Hui, D. & Lee, J. H. Preparation and properties of reduced graphene oxide/polyacrylonitrile nanocomposites using polyvinyl phenol. *Compos. Part B Eng.* **80**, 238–245 (2015).
- [266] Kim, D., Lee, H. S. & Yoon, J. Highly bendable bilayer-type photo-actuators comprising of reduced graphene oxide dispersed in hydrogels. *Sci. Rep.* **6**, 20921 (2016).
- [267] Qiu, L. *et al.* Mechanically Robust, Electrically Conductive and Stimuli-Responsive Binary Network Hydrogels Enabled by Superelastic Graphene Aerogels. *Adv. Mater.* **26**, 3333–3337 (2014).
- [268] Li, W., Wang, J., Ren, J. & Qu, X. 3D Graphene Oxide–Polymer Hydrogel: Near-Infrared Light-Triggered Active Scaffold for Reversible Cell Capture and On-Demand Release. *Adv. Mater.* **25**, 6737–6743 (2013).
- [269] Zhu, C.-H., Lu, Y., Peng, J., Chen, J.-F. & Yu, S.-H. Photothermally Sensitive Poly(N-isopropylacrylamide)/Graphene Oxide Nanocomposite Hydrogels as Remote Light-Controlled Liquid Microvalves. *Adv. Funct. Mater.* **22**, 4017–4022 (2012).
- [270] Liu, W., Zhang, X., Zhou, L., Shang, L. & Su, Z. Reduced graphene oxide (rGO) hybridized hydrogel as a near-infrared (NIR)/pH dual-responsive platform for combined chemophotothermal therapy. *J. Colloid Interface Sci.* **536**, 160–170 (2019).
- [271] Chang, G. *et al.* Multifunctional Reduced Graphene Oxide Hydrogel as Drug Carrier for Localized and Synergic Photothermal/Photodynamics/Chemo Therapy. *J. Mater. Sci. Technol.* **8**, 753–762 (2016).

- [272] Zhang, P. *et al.* A Microstructured Graphene/Poly(N-isopropylacrylamide) Membrane for Intelligent Solar Water Evaporation. *Angew. Chem. Int. Ed.* **57**, 16343–16347 (2018).
- [273] Geng, H. *et al.* Plant leaves inspired sunlight-driven purifier for high-efficiency clean water production. *Nat. Commun.* **10**, 1512 (2019).
- [274] Bardajee, G. R., Hooshyar, Z., Farsi, M., Mobini, A. & Sang, G. Synthesis of a novel thermo/pH sensitive nanogel based on salep modified graphene oxide for drug release. *Mater. Sci. Eng. C* **72**, 558–565 (2017).
- [275] Kim, H., Lee, D., Kim, J., Kim, T. & Kim, W. J. Photothermally Triggered Cytosolic Drug Delivery via Endosome Disruption Using a Functionalized Reduced Graphene Oxide. *ACS Nano* **7**, 6735–6746 (2013).
- [276] Wang, C. *et al.* A chitosan-modified graphene nanogel for noninvasive controlled drug release. *Nanomedicine Nanotechnol. Biol. Med.* **9**, 903–911 (2013).
- [277] Jiang, Y. *et al.* Fabrication of novel PNIPAM@GO microspheres loaded with dual drugs featuring on-demand drug release capability. *J. Appl. Polym. Sci.* **139**, e52444 (2022).
- [278] Lu, N. *et al.* Tunable dual-stimuli response of a microgel composite consisting of reduced graphene oxide nanoparticles and poly(N-isopropylacrylamide) hydrogel microspheres. *J. Mater. Chem. B* **2**, 3791–3798 (2014).
- [279] Ding, Y. H., Floren, M. & Tan, W. Mussel-inspired polydopamine for bio-surface functionalization. *Biosurface Biotribology* **2**, 121–136 (2016).
- [280] Ho, C.-C. & Ding, S.-J. The pH-controlled nanoparticles size of polydopamine for anti-cancer drug delivery. *J. Mater. Sci. Mater. Med.* **24**, 2381–2390 (2013).
- [281] Hong, S. *et al.* Non-Covalent Self-Assembly and Covalent Polymerization Co-Contribute to Polydopamine Formation. *Adv. Funct. Mater.* **22**, 4711–4717 (2012).
- [282] Liu, R., Guo, Y., Odusote, G., Qu, F. & Priestley, R. D. Core-Shell Fe₃O₄ Polydopamine Nanoparticles Serve Multipurpose as Drug Carrier, Catalyst Support and Carbon Adsorbent. *ACS Appl. Mater. Interfaces* **5**, 9167–9171 (2013).
- [283] Liang, Y. *et al.* Adhesive Hemostatic Conducting Injectable Composite Hydrogels with Sustained Drug Release and Photothermal Antibacterial Activity to Promote Full-Thickness Skin Regeneration During Wound Healing. *Small* **15**, 1900046 (2019).
- [284] Ryu, J., Ku, S. H., Lee, H. & Park, C. B. Mussel-Inspired Polydopamine Coating as a Universal Route to Hydroxyapatite Crystallization. *Adv. Funct. Mater.* **20**, 2132–2139 (2010).
- [285] Liao, M. *et al.* Wearable, Healable, and Adhesive Epidermal Sensors Assembled from Mussel-Inspired Conductive Hybrid Hydrogel Framework. *Adv. Funct. Mater.* **27**, 1703852 (2017).
- [286] Gao, H., Sun, Y., Zhou, J., Xu, R. & Duan, H. Mussel-Inspired Synthesis of Polydopamine-Functionalized Graphene Hydrogel as Reusable Adsorbents for Water Purification. *ACS Appl. Mater. Interfaces* **5**, 425–432 (2013).
- [287] Ryou, M.-H., Lee, Y. M., Park, J.-K. & Choi, J. W. Mussel-Inspired Polydopamine-Treated Polyethylene Separators for High-Power Li-Ion Batteries. *Adv. Mater.* **23**, 3066–3070 (2011).
- [288] Qu, K., Zheng, Y., Dai, S. & Qiao, S. Z. Graphene oxide-polydopamine derived N, S-codoped carbon nanosheets as superior bifunctional electrocatalysts for oxygen reduction and evolution. *Nano Energy* **19**, 373–381 (2016).
- [289] Liebscher, J. *et al.* Structure of Polydopamine: A Never-Ending Story? *Langmuir* **29**, 10539–10548 (2013).
- [290] d’Ischia, M., Napolitano, A., Ball, V., Chen, C.-T. & Buehler, M. J. Polydopamine and eumelanin: from structure-property relationships to a unified tailoring strategy. *Acc. Chem. Res.* **47**, 3541–3550 (2014).

- [291] Li, Y., Liu, M., Xiang, C., Xie, Q. & Yao, S. Electrochemical quartz crystal microbalance study on growth and property of the polymer deposit at gold electrodes during oxidation of dopamine in aqueous solutions. *Thin Solid Films* **497**, 270–278 (2006).
- [292] Ding, Y. *et al.* Insights into the aggregation/deposition and structure of a polydopamine film. *Langmuir ACS J. Surf. Colloids* **30**, 12258–12269 (2014).
- [293] Della Vecchia, N. F. *et al.* Building-Block Diversity in Polydopamine Underpins a Multifunctional Eumelanin-Type Platform Tunable Through a Quinone Control Point. *Adv. Funct. Mater.* **23**, 1331–1340 (2013).
- [294] Alfieri, M. L. *et al.* Structural Basis of Polydopamine Film Formation: Probing 5,6-Dihydroxyindole-Based Eumelanin Type Units and the Porphyrin Issue. *ACS Appl. Mater. Interfaces* **10**, 7670–7680 (2018).
- [295] Della Vecchia, N. F. *et al.* Tris Buffer Modulates Polydopamine Growth, Aggregation, and Paramagnetic Properties. *Langmuir* **30**, 9811–9818 (2014).
- [296] Dreyer, D. R., Miller, D. J., Freeman, B. D., Paul, D. R. & Bielawski, C. W. Elucidating the Structure of Poly(dopamine). *Langmuir* **28**, 6428–6435 (2012).
- [297] Gebbie, M. A. *et al.* Tuning underwater adhesion with cation- π interactions. *Nat. Chem.* **9**, 473–479 (2017).
- [298] Hong, S., Wang, Y., Park, S. Y. & Lee, H. Progressive fuzzy cation- π assembly of biological catecholamines. *Sci. Adv.* **4**, eaat7457 (2018).
- [299] Fu, Y. *et al.* One-Pot Preparation of Polymer–Enzyme–Metallic Nanoparticle Composite Films for High-Performance Biosensing of Glucose and Galactose. *Adv. Funct. Mater.* **19**, 1784–1791 (2009).
- [300] Xu, L. Q., Yang, W. J., Neoh, K.-G., Kang, E.-T. & Fu, G. D. Dopamine-Induced Reduction and Functionalization of Graphene Oxide Nanosheets. *Macromolecules* **43**, 8336–8339 (2010).
- [301] Luo, J., Zhang, N., Liu, R. & Liu, X. In situ green synthesis of Au nanoparticles onto polydopamine-functionalized graphene for catalytic reduction of nitrophenol. *Rsc Adv.* **4**, 64816–64824 (2014).
- [302] Song, H., Wang, Z., Yang, J., Jia, X. & Zhang, Z. Facile synthesis of copper/polydopamine functionalized graphene oxide nanocomposites with enhanced tribological performance. *Chem. Eng. J.* **324**, 51–62 (2017).
- [303] Guo, L. *et al.* A mussel-inspired polydopamine coating as a versatile platform for the in situ synthesis of graphene-based nanocomposites. *Nanoscale* **4**, 5864–5867 (2012).
- [304] Majumdar, B., Bhattacharya, T. & Sarma, T. K. Gold Nanoparticle–Polydopamine–Reduced Graphene Oxide Ternary Nanocomposite as an Efficient Catalyst for Selective Oxidation of Benzylic C(sp³)–H Bonds Under Mild Conditions. *ChemCatChem* **8**, 1825–1835 (2016).
- [305] Luo, F. *et al.* Green reduction of graphene oxide by polydopamine to a construct flexible film: superior flame retardancy and high thermal conductivity. *J. Mater. Chem. A* **5**, 18542–18550 (2017).
- [306] Jing, X., Mi, H.-Y., Peng, X.-F. & Turng, L.-S. Biocompatible, self-healing, highly stretchable polyacrylic acid/reduced graphene oxide nanocomposite hydrogel sensors via mussel-inspired chemistry. *Carbon* **136**, 63–72 (2018).
- [307] Dong, Z., Zhang, F., Wang, D., Liu, X. & Jin, J. Polydopamine-mediated surface-functionalization of graphene oxide for heavy metal ions removal. *J. Solid State Chem.* **224**, 88–93 (2015).

- [308] Hu, W. *et al.* Polydopamine-Functionalization of Graphene Oxide to Enable Dual Signal Amplification for Sensitive Surface Plasmon Resonance Imaging Detection of Biomarker. *Anal. Chem.* **86**, 4488–4493 (2014).
- [309] Cui, W. *et al.* A Strong Integrated Strength and Toughness Artificial Nacre Based on Dopamine Cross-Linked Graphene Oxide. *ACS Nano* **8**, 9511–9517 (2014).
- [310] Zangmeister, R. A., Morris, T. A. & Tarlov, M. J. Characterization of Polydopamine Thin Films Deposited at Short Times by Autoxidation of Dopamine. *Langmuir* **29**, 8619–8628 (2013).
- [311] Ball, V., Frari, D. D., Toniazzo, V. & Ruch, D. Kinetics of polydopamine film deposition as a function of pH and dopamine concentration: Insights in the polydopamine deposition mechanism. *J. Colloid Interface Sci.* **386**, 366–372 (2012).
- [312] Bernsmann, F. *et al.* Melanin-Containing Films: Growth from Dopamine Solutions versus Layer-by-Layer Deposition. *ChemPhysChem* **11**, 3299–3305 (2010).
- [313] Wang, Y. *et al.* Superior Performance of Artificial Nacre Based on Graphene Oxide Nanosheets. *ACS Appl. Mater. Interfaces* **9**, 4215–4222 (2017).
- [314] Wang, Y. *et al.* Artificial Nacre from Supramolecular Assembly of Graphene Oxide. *ACS Nano* **12**, 6228–6235 (2018).
- [315] Li, M. *et al.* Preparation of and research on bioinspired graphene oxide/nanocellulose/polydopamine ternary artificial nacre. *Mater. Des.* **181**, 107961 (2019).
- [316] Wang, Y. *et al.* Artificial Nacre Epoxy Nanomaterials Based on Janus Graphene Oxide for Thermal Management Applications. *ACS Appl. Mater. Interfaces* **12**, 44273–44280 (2020).
- [317] Flouda, P., Shah, S. A., Lagoudas, D. C., Green, M. J. & Lutkenhaus, J. L. Highly Multifunctional Dopamine-Functionalized Reduced Graphene Oxide Supercapacitors. *Matter* **1**, 1532–1546 (2019).
- [318] Chen, C. *et al.* Self-Assembled Free-Standing Graphite Oxide Membrane. *Adv. Mater.* **21**, 3007–3011 (2009).
- [319] Shao, J.-J. *et al.* Hybridization of graphene oxide and carbon nanotubes at the liquid/air interface. *Chem. Commun.* **48**, 3706–3708 (2012).
- [320] Zhu, Y., Cai, W., Piner, R. D., Velamakanni, A. & Ruoff, R. S. Transparent self-assembled films of reduced graphene oxide platelets. *Appl. Phys. Lett.* **95**, 103104 (2009).
- [321] Eda, G., Fanchini, G. & Chhowalla, M. Large-area ultrathin films of reduced graphene oxide as a transparent and flexible electronic material. *Nat. Nanotechnol.* **3**, 270–274 (2008).
- [322] Putz, K. W. *et al.* Evolution of Order During Vacuum-Assisted Self-Assembly of Graphene Oxide Paper and Associated Polymer Nanocomposites. *ACS Nano* **5**, 6601–6609 (2011).
- [323] Cruz-Silva, R., Endo, M. & Terrones, M. Graphene oxide films, fibers, and membranes. *Nanotechnol. Rev.* **5**, 377–391 (2016).
- [324] Dikin, D. A. *et al.* Preparation and characterization of graphene oxide paper. *Nature* **448**, 457–460 (2007).
- [325] Deville, S., Saiz, E., Nalla, R. K. & Tomsia, A. P. Freezing as a Path to Build Complex Composites. *Science* **311**, 515–518 (2006).
- [326] Jackson, A. P., Vincent, J. F. V., Turner, R. M. & Alexander, R. M. The mechanical design of nacre. *Proc. R. Soc. Lond. B Biol. Sci.* **234**, 415–440 (1988).
- [327] Tang, P. *et al.* Mussel-Inspired Electroactive and Antioxidative Scaffolds with Incorporation of Polydopamine-Reduced Graphene Oxide for Enhancing Skin Wound Healing. *ACS Appl. Mater. Interfaces* **11**, 7703–7714 (2019).
- [328] Liao, Y., Wang, M. & Chen, D. Preparation of Polydopamine-Modified Graphene Oxide/Chitosan Aerogel for Uranium(VI) Adsorption. *Ind. Eng. Chem. Res.* **57**, 8472–8483 (2018).

- [329] Zhang, H. *et al.* Biomimetic epidermal sensors assembled from polydopamine-modified reduced graphene oxide/polyvinyl alcohol hydrogels for the real-time monitoring of human motions. *J. Mater. Chem. B* **8**, 10549–10558 (2020).
- [330] Zhang, P., He, M. & Zeng, Y. Ultrasensitive microfluidic analysis of circulating exosomes using a nanostructured graphene oxide/polydopamine coating. *Lab. Chip* **16**, 3033–3042 (2016).
- [331] Miao, J., Liu, H., Li, W. & Zhang, X. Mussel-Inspired Polydopamine-Functionalized Graphene as a Conductive Adhesion Promoter and Protective Layer for Silver Nanowire Transparent Electrodes. *Langmuir* **32**, 5365–5372 (2016).
- [332] Chabot, V. *et al.* A review of graphene and graphene oxide sponge: material synthesis and applications to energy and the environment. *Energy Environ. Sci.* **7**, 1564–1596 (2014).
- [333] Novoselov, K. S. *et al.* A roadmap for graphene. *Nature* **490**, 192–200 (2012).
- [334] Zhou, T. *et al.* Electrospun Poly(3-hydroxybutyrate-co-4-hydroxybutyrate)/Graphene Oxide Scaffold: Enhanced Properties and Promoted in Vivo Bone Repair in Rats. *ACS Appl. Mater. Interfaces* **9**, 42589–42600 (2017).
- [335] Saravanan, S. *et al.* Scaffolds containing chitosan, gelatin and graphene oxide for bone tissue regeneration in vitro and in vivo. *Int. J. Biol. Macromol.* **104**, 1975–1985 (2017).
- [336] Zhao, C. *et al.* Thermoresponsive Citrate-Based Graphene Oxide Scaffold Enhances Bone Regeneration from BMP9-Stimulated Adipose-Derived Mesenchymal Stem Cells. *ACS Biomater. Sci. Eng.* **4**, 2943–2955 (2018).
- [337] Hermenean, A. *et al.* Chitosan-Graphene Oxide 3D scaffolds as Promising Tools for Bone Regeneration in Critical-Size Mouse Calvarial Defects. *Sci. Rep.* **7**, 16641 (2017).
- [338] Kalita, S. J., Bose, S., Hosick, H. L. & Bandyopadhyay, A. Development of controlled porosity polymer-ceramic composite scaffolds via fused deposition modeling. *Mater. Sci. Eng. C* **23**, 611–620 (2003).
- [339] Akbarzadeh, R. *et al.* Hierarchical polymeric scaffolds support the growth of MC3T3-E1 cells. *J. Mater. Sci. Mater. Med.* **26**, 116 (2015).
- [340] Ito, Y. *et al.* High-Quality Three-Dimensional Nanoporous Graphene. *Angew. Chem.* **126**, 4922–4926 (2014).
- [341] Goenka, S., Sant, V. & Sant, S. Graphene-based nanomaterials for drug delivery and tissue engineering. *J. Controlled Release* **173**, 75–88 (2014).
- [342] Luan, V. H. *et al.* Synthesis of a highly conductive and large surface area graphene oxide hydrogel and its use in a supercapacitor. *J. Mater. Chem. A* **1**, 208–211 (2012).
- [343] Huang, X. *et al.* Functional Nanoporous Graphene Foams with Controlled Pore Sizes. *Adv. Mater.* **24**, 4419–4423 (2012).
- [344] Yang, M. *et al.* Biomimetic Architected Graphene Aerogel with Exceptional Strength and Resilience. *ACS Nano* **11**, 6817–6824 (2017).
- [345] Chen, C.-M. *et al.* Macroporous ‘bubble’ graphene film via template-directed ordered-assembly for high rate supercapacitors. *Chem. Commun.* **48**, 7149–7151 (2012).
- [346] Li, X. *et al.* Effects of graphene oxide aggregates on hydration degree, sorptivity, and tensile splitting strength of cement paste. *Compos. Part Appl. Sci. Manuf.* **100**, 1–8 (2017).
- [347] Zhang, Z., Tan, H., Zhao, Y., Wang, Q. & Wang, H. Facile synthesis of macroporous zwitterionic hydrogels templated from graphene oxide-stabilized aqueous foams. *J. Colloid Interface Sci.* **553**, 40–49 (2019).
- [348] Meng, W. *et al.* Structure and Interaction of Graphene Oxide–Cetyltrimethylammonium Bromide Complexation. *J. Phys. Chem. C* **119**, 21135–21140 (2015).

- [349] Yang, D. *et al.* Promoting Cell Migration in Tissue Engineering Scaffolds with Graded Channels. *Adv. Healthc. Mater.* **6**, 1700472 (2017).
- [350] Sui, G., Zhao, Y., Zhang, Q. & Fu, Q. Enhanced mechanical properties of olefin block copolymer by adding a quaternary ammonium salt functionalized graphene oxide. *RSC Adv.* **6**, 54785–54792 (2016).
- [351] Viana, R. B., da Silva, A. B. F. & Pimentel, A. S. Infrared Spectroscopy of Anionic, Cationic, and Zwitterionic Surfactants. *Adv. Phys. Chem.* **2012**, e903272 (2012).
- [352] Su, J., He, S., Zhao, Z., Liu, X. & Li, H. Efficient preparation of cetyltrimethylammonium bromide-graphene oxide composite and its adsorption of Congo red from aqueous solutions. *Colloids Surf. Physicochem. Eng. Asp.* **554**, 227–236 (2018).
- [353] Menner, A. & Bismarck, A. New Evidence for the Mechanism of the Pore Formation in Polymerising High Internal Phase Emulsions or Why polyHIPEs Have an Interconnected Pore Network Structure. *Macromol. Symp.* **242**, 19–24 (2006).
- [354] Kimmins, S. D. & Cameron, N. R. Functional Porous Polymers by Emulsion Templating: Recent Advances. *Adv. Funct. Mater.* **21**, 211–225 (2011).
- [355] Zhu, N., Chapman, D., Cooper, D., Schreyer, D. J. & Chen, X. X-Ray Diffraction Enhanced Imaging as a Novel Method to Visualize Low-Density Scaffolds in Soft Tissue Engineering. *Tissue Eng. Part C Methods* **17**, 1071–1080 (2011).
- [356] Yeh, C.-N., Raidongia, K., Shao, J., Yang, Q.-H. & Huang, J. On the origin of the stability of graphene oxide membranes in water. *Nat. Chem.* **7**, 166–170 (2015).
- [357] Gao, Y. *et al.* The Effect of Interlayer Adhesion on the Mechanical Behaviors of Macroscopic Graphene Oxide Papers. *ACS Nano* **5**, 2134–2141 (2011).
- [358] Lie *et al.* Thermal dehydration treatment and glutaraldehyde cross-linking to increase the biostability of collagen–chitosan porous scaffolds used as dermal equivalent. *J. Biomater. Sci. Polym. Ed.* **14**, 861–874 (2003).
- [359] Liu, Y., Ma, L. & Gao, C. Facile fabrication of the glutaraldehyde cross-linked collagen/chitosan porous scaffold for skin tissue engineering. *Mater. Sci. Eng. C* **32**, 2361–2366 (2012).
- [360] Hu, K., Szkopek, T. & Cerruti, M. Tuning the aggregation of graphene oxide dispersions to synthesize elastic, low density graphene aerogels. *J. Mater. Chem. A* **5**, 23123–23130 (2017).
- [361] Zhang, T. *et al.* Enhanced proliferation and osteogenic differentiation of human mesenchymal stem cells on biomineralized three-dimensional graphene foams. *Carbon* **105**, 233–243 (2016).
- [362] Grayson, W. L., Ma, T. & Bunnell, B. Human Mesenchymal Stem Cells Tissue Development in 3D PET Matrices. *Biotechnol. Prog.* **20**, 905–912 (2004).
- [363] Xie, H., Cao, T., Gomes, J. V., Castro Neto, A. H. & Rosa, V. Two and three-dimensional graphene substrates to magnify osteogenic differentiation of periodontal ligament stem cells. *Carbon* **93**, 266–275 (2015).
- [364] Qian, J., Xu, W., Yong, X., Jin, X. & Zhang, W. Fabrication and in vitro biocompatibility of biomorphic PLGA/nHA composite scaffolds for bone tissue engineering. *Mater. Sci. Eng. C* **36**, 95–101 (2014).
- [365] Gao, X. *et al.* Polydopamine-Templated Hydroxyapatite Reinforced Polycaprolactone Composite Nanofibers with Enhanced Cytocompatibility and Osteogenesis for Bone Tissue Engineering. *ACS Appl. Mater. Interfaces* **8**, 3499–3515 (2016).

- [366] Li, J. J. *et al.* Multiple Silk Coatings on Biphasic Calcium Phosphate Scaffolds: Effect on Physical and Mechanical Properties and In Vitro Osteogenic Response of Human Mesenchymal Stem Cells. *Biomacromolecules* **14**, 2179–2188 (2013).
- [367] Toquet, J. *et al.* Osteogenic potential in vitro of human bone marrow cells cultured on macroporous biphasic calcium phosphate ceramic. *J. Biomed. Mater. Res.* **44**, 98–108 (1999).
- [368] Wu, J. *et al.* Enhanced bone regeneration of the silk fibroin electrospun scaffolds through the modification of the graphene oxide functionalized by BMP-2 peptide. *Int. J. Nanomedicine* **14**, 733–751 (2019).
- [369] Depan, D., Girase, B., Shah, J. S. & Misra, R. D. K. Structure–process–property relationship of the polar graphene oxide-mediated cellular response and stimulated growth of osteoblasts on hybrid chitosan network structure nanocomposite scaffolds. *Acta Biomater.* **7**, 3432–3445 (2011).
- [370] Kolanthai, E. *et al.* Graphene Oxide—A Tool for the Preparation of Chemically Crosslinking Free Alginate–Chitosan–Collagen Scaffolds for Bone Tissue Engineering. *ACS Appl. Mater. Interfaces* **10**, 12441–12452 (2018).
- [371] Shao, W. *et al.* Enhanced bone formation in electrospun poly(l-lactic-co-glycolic acid)–tussah silk fibroin ultrafine nanofiber scaffolds incorporated with graphene oxide. *Mater. Sci. Eng. C* **62**, 823–834 (2016).
- [372] Salerno, A., Guarnieri, D., Iannone, M., Zeppetelli, S. & Netti, P. A. Effect of Micro- and Macroporosity of Bone Tissue Three-Dimensional-Poly(ϵ -Caprolactone) Scaffold on Human Mesenchymal Stem Cells Invasion, Proliferation, and Differentiation In Vitro. *Tissue Eng. Part A* **16**, 2661–2673 (2010).
- [373] Barba, A. *et al.* Osteoinduction by Foamed and 3D-Printed Calcium Phosphate Scaffolds: Effect of Nanostructure and Pore Architecture. *ACS Appl. Mater. Interfaces* **9**, 41722–41736 (2017).
- [374] Zhou, K. *et al.* Hierarchically Porous Hydroxyapatite Hybrid Scaffold Incorporated with Reduced Graphene Oxide for Rapid Bone Ingrowth and Repair. *ACS Nano* **13**, 9595–9606 (2019).
- [375] Liu, Y. *et al.* Facilitated vascularization and enhanced bone regeneration by manipulation hierarchical pore structure of scaffolds. *Mater. Sci. Eng. C* **110**, 110622 (2020).
- [376] Du, Y., Guo, J. L., Wang, J., Mikos, A. G. & Zhang, S. Hierarchically designed bone scaffolds: From internal cues to external stimuli. *Biomaterials* **218**, 119334 (2019).
- [377] Kar, T., Devivaraprasad, R., Kumar Singh, R., Bera, B. & Neergat, M. Reduction of graphene oxide – a comprehensive electrochemical investigation in alkaline and acidic electrolytes. *RSC Adv.* **4**, 57781–57790 (2014).
- [378] Cançado, L. G. *et al.* Quantifying Defects in Graphene via Raman Spectroscopy at Different Excitation Energies. *Nano Lett.* **11**, 3190–3196 (2011).
- [379] Kudin, K. N. *et al.* Raman Spectra of Graphite Oxide and Functionalized Graphene Sheets. *Nano Lett.* **8**, 36–41 (2008).
- [380] Tuinstra, F. & Koenig, J. L. Raman Spectrum of Graphite. *J. Chem. Phys.* **53**, 1126–1130 (1970).
- [381] Stankovich, S. *et al.* Synthesis of graphene-based nanosheets via chemical reduction of exfoliated graphite oxide. *Carbon* **45**, 1558–1565 (2007).
- [382] Araujo, P. T., Terrones, M. & Dresselhaus, M. S. Defects and impurities in graphene-like materials. *Mater. Today* **15**, 98–109 (2012).
- [383] Eigler, S., Dotzer, C. & Hirsch, A. Visualization of defect densities in reduced graphene oxide. *Carbon* **50**, 3666–3673 (2012).

- [384] Lucchese, M. M. *et al.* Quantifying ion-induced defects and Raman relaxation length in graphene. *Carbon* **48**, 1592–1597 (2010).
- [385] Ha, H., Shanmuganathan, K. & Ellison, C. J. Mechanically stable thermally crosslinked poly(acrylic acid)/reduced graphene oxide aerogels. *ACS Appl. Mater. Interfaces* **7**, 6220–6229 (2015).
- [386] Wang, E., Desai, M. S., Heo, K. & Lee, S.-W. Graphene-Based Materials Functionalized with Elastin-like Polypeptides. *Langmuir* **30**, 2223–2229 (2014).
- [387] Harley, B. A., Leung, J. H., Silva, E. C. C. M. & Gibson, L. J. Mechanical characterization of collagen–glycosaminoglycan scaffolds. *Acta Biomater.* **3**, 463–474 (2007).
- [388] Xiong, G., Luo, H., Zuo, G., Ren, K. & Wan, Y. Novel porous graphene oxide and hydroxyapatite nanosheets-reinforced sodium alginate hybrid nanocomposites for medical applications. *Mater. Charact.* **107**, 419–425 (2015).
- [389] Pekala, R. W., Alviso, C. T. & LeMay, J. D. Organic aerogels: microstructural dependence of mechanical properties in compression. *J. Non-Cryst. Solids* **125**, 67–75 (1990).
- [390] Ganesan, K., Dennstedt, A., Barowski, A. & Ratke, L. Design of aerogels, cryogels and xerogels of cellulose with hierarchical porous structures. *Mater. Des.* **92**, 345–355 (2016).
- [391] Ganesan, K., Barowski, A., Ratke, L. & Milow, B. Influence of hierarchical porous structures on the mechanical properties of cellulose aerogels. *J. Sol-Gel Sci. Technol.* **89**, 156–165 (2019).
- [392] Sui, Z.-Y., Cui, Y., Zhu, J.-H. & Han, B.-H. Preparation of Three-Dimensional Graphene Oxide–Polyethylenimine Porous Materials as Dye and Gas Adsorbents. *ACS Appl. Mater. Interfaces* **5**, 9172–9179 (2013).
- [393] Piao, Y. & Chen, B. One-pot synthesis and characterization of reduced graphene oxide–gelatin nanocomposite hydrogels. *RSC Adv.* **6**, 6171–6181 (2016).
- [394] Chen, Y., Chen, L., Bai, H. & Li, L. Graphene oxide–chitosan composite hydrogels as broad-spectrum adsorbents for water purification. *J. Mater. Chem. A* **1**, 1992–2001 (2013).
- [395] Menzel, R. *et al.* Joule Heating Characteristics of Emulsion-Templated Graphene Aerogels. *Adv. Funct. Mater.* **25**, 28–35 (2015).
- [396] Xia, X. *et al.* A New Type of Porous Graphite Foams and Their Integrated Composites with Oxide/Polymer Core/Shell Nanowires for Supercapacitors: Structural Design, Fabrication, and Full Supercapacitor Demonstrations. *Nano Lett.* **14**, 1651–1658 (2014).
- [397] Zhou, M. *et al.* Highly Conductive Porous Graphene/Ceramic Composites for Heat Transfer and Thermal Energy Storage. *Adv. Funct. Mater.* **23**, 2263–2269 (2013).
- [398] Zhang, Y. *et al.* Porous graphene oxide/carboxymethyl cellulose monoliths, with high metal ion adsorption. *Carbohydr. Polym.* **101**, 392–400 (2014).
- [399] Yousefi, N. *et al.* Hierarchically porous, ultra-strong reduced graphene oxide-cellulose nanocrystal sponges for exceptional adsorption of water contaminants. *Nanoscale* **10**, 7171–7184 (2018).
- [400] Deville, S. Freeze-Casting of Porous Biomaterials: Structure, Properties and Opportunities. *Materials* **3**, 1913–1927 (2010).
- [401] Huang, T. *et al.* Polydopamine coated graphene oxide aerogels and their ultrahigh adsorption ability. *Diam. Relat. Mater.* **86**, 117–127 (2018).
- [402] Tang, M. *et al.* Fabrication of graphene oxide aerogels loaded with catalytic AuPd nanoparticles. *Mater. Res. Bull.* **63**, 248–252 (2015).
- [403] Yang, J. *et al.* An ice-templated assembly strategy to construct graphene oxide/boron nitride hybrid porous scaffolds in phase change materials with enhanced thermal conductivity and

- shape stability for light–thermal–electric energy conversion. *J. Mater. Chem. A* **4**, 18841–18851 (2016).
- [404] Serrano, M. C. *et al.* 3D free-standing porous scaffolds made of graphene oxide as substrates for neural cell growth. *J. Mater. Chem. B* **2**, 5698–5706 (2014).
- [405] Mi, X. *et al.* Preparation of graphene oxide aerogel and its adsorption for Cu²⁺ ions. *Carbon* **50**, 4856–4864 (2012).
- [406] Deng, X. & Tüysüz, H. Cobalt-Oxide-Based Materials as Water Oxidation Catalyst: Recent Progress and Challenges. *ACS Catal.* **4**, 3701–3714 (2014).
- [407] Vos, J. G., Wezendonk, T. A., Jeremiase, A. W. & Koper, M. T. M. MnO_x/IrO_x as Selective Oxygen Evolution Electrocatalyst in Acidic Chloride Solution. *J. Am. Chem. Soc.* **140**, 10270–10281 (2018).
- [408] Salvatore, D. A., Dettelbach, K. E., Hudkins, J. R. & Berlinguette, C. P. Near-infrared-driven decomposition of metal precursors yields amorphous electrocatalytic films. *Sci. Adv.* **1**, e1400215 (2015).
- [409] Wu, L. *et al.* Heterogeneous Bimetallic Phosphide Ni₂P-Fe₂P as an Efficient Bifunctional Catalyst for Water/Seawater Splitting. *Adv. Funct. Mater.* **31**, 2006484 (2021).
- [410] Cui, B. *et al.* Heterogeneous lamellar-edged Fe-Ni(OH)₂/Ni₃S₂ nanoarray for efficient and stable seawater oxidation. *Nano Res.* **14**, 1149–1155 (2021).
- [411] Kuang, Y. *et al.* Solar-driven, highly sustained splitting of seawater into hydrogen and oxygen fuels. *Proc. Natl. Acad. Sci.* **116**, 6624–6629 (2019).
- [412] Yu, L. *et al.* Non-noble metal-nitride based electrocatalysts for high-performance alkaline seawater electrolysis. *Nat. Commun.* **10**, 5106 (2019).
- [413] Okada, T. *et al.* A Bilayer Structure Composed of Mg|Co-MnO₂ Deposited on a Co(OH)₂ Film to Realize Selective Oxygen Evolution from Chloride-Containing Water. *Langmuir* **36**, 5227–5235 (2020).
- [414] Gerken, J. B. *et al.* Electrochemical Water Oxidation with Cobalt-Based Electrocatalysts from pH 0–14: The Thermodynamic Basis for Catalyst Structure, Stability, and Activity. *J. Am. Chem. Soc.* **133**, 14431–14442 (2011).
- [415] Zhang, L., Chen, L., Wan, H., Chen, J. & Zhou, H. Synthesis and Tribological Properties of Stearic Acid-Modified Anatase (TiO₂) Nanoparticles. *Tribol. Lett.* **41**, 409–416 (2011).
- [416] I. Kharisov, B. *et al.* Solubilization, dispersion and stabilization of magnetic nanoparticles in water and non-aqueous solvents: recent trends. *RSC Adv.* **4**, 45354–45381 (2014).
- [417] Zeng, Y.-X., Zhong, X.-W., Liu, Z.-Q., Chen, S. & Li, N. Preparation and enhancement of thermal conductivity of heat transfer oil-based MoS₂ nanofluids. *J. Nanomater.* **2013**, 3:3 (2013).
- [418] Li, Y. *et al.* Well Shaped Mn₃O₄ Nano-octahedra with Anomalous Magnetic Behavior and Enhanced Photodecomposition Properties. *Small* **7**, 475–483 (2011).
- [419] A. Pudney, P. D., J. Mutch, K. & Zhu, S. Characterising the phase behaviour of stearic acid and its triethanolamine soap and acid–soap by infrared spectroscopy. *Phys. Chem. Chem. Phys.* **11**, 5010–5018 (2009).
- [420] Tang, C.-W., Wang, C.-B. & Chien, S.-H. Characterization of cobalt oxides studied by FT-IR, Raman, TPR and TG-MS. *Thermochim. Acta* **473**, 68–73 (2008).
- [421] Liu, Y. *et al.* Concave Co₃O₄ octahedral mesocrystal: polymer-mediated synthesis and sensing properties. *CrystEngComm* **14**, 6264–6270 (2012).
- [422] Diallo, A., Beye, A. C., Doyle, T. B., Park, E. & Maaza, M. Green synthesis of Co₃O₄ nanoparticles via *Aspalathus linearis*: Physical properties. *Green Chem. Lett. Rev.* **8**, 30–36 (2015).

- [423] Lorite, I., Romero, J. J. & Fernández, J. F. Effects of the agglomeration state on the Raman properties of Co₃O₄ nanoparticles. *J. Raman Spectrosc.* **43**, 1443–1448 (2012).
- [424] Hadjiev, V. G., Iliev, M. N. & Vergilov, I. V. The Raman spectra of Co₃O₄. *J. Phys. C Solid State Phys.* **21**, L199–L201 (1988).
- [425] Xu, C. Y., Zhang, P. X. & Yan, L. Blue shift of Raman peak from coated TiO₂ nanoparticles. *J. Raman Spectrosc.* **32**, 862–865 (2001).
- [426] Wasalathilake, K. C., Galpaya, D. G. D., Ayoko, G. A. & Yan, C. Understanding the structure-property relationships in hydrothermally reduced graphene oxide hydrogels. *Carbon* **137**, 282–290 (2018).
- [427] Hu, K., Xie, X., Cerruti, M. & Szkopek, T. Controlling the Shell Formation in Hydrothermally Reduced Graphene Hydrogel. *Langmuir* **31**, 5545–5549 (2015).
- [428] Powell, C. NIST X-ray Photoelectron Spectroscopy Database, Version 4.1, NIST Standard Reference Database 20. (2012).
- [429] Biesinger, M. C. *et al.* Resolving surface chemical states in XPS analysis of first row transition metals, oxides and hydroxides: Cr, Mn, Fe, Co and Ni. *Appl. Surf. Sci.* **257**, 2717–2730 (2011).
- [430] BENG JIT TAN, KLABUNDE, K. J. & SHERWOOD, P. M. A. XPS studies of solvated metal atom dispersed catalysts. Evidence for layered cobalt-manganese particles on alumina and silica. *XPS Stud. Solvated Met. At. Dispersed Catal. Evid. Layer. Cobalt-Manganese Part. Alumina Silica* **113**, 855–861 (1991).
- [431] Petitto, S. C., Marsh, E. M., Carson, G. A. & Langell, M. A. Cobalt oxide surface chemistry: The interaction of CoO(100), Co₃O₄(110) and Co₃O₄(111) with oxygen and water. *J. Mol. Catal. Chem.* **281**, 49–58 (2008).
- [432] Rao, S., Upadhyay, J., Polychronopoulou, K., Umer, R. & Das, R. Reduced Graphene Oxide: Effect of Reduction on Electrical Conductivity. *J. Compos. Sci.* **2**, 25 (2018).
- [433] Iskandar, F., Bityasmawan Abdillah, O., Stavila, E. & Hasdi Aimon, A. The influence of copper addition on the electrical conductivity and charge transfer resistance of reduced graphene oxide (rGO). *New J. Chem.* **42**, 16362–16371 (2018).
- [434] Wang, J. *et al.* Recent Progress in Cobalt-Based Heterogeneous Catalysts for Electrochemical Water Splitting. *Adv. Mater.* **28**, 215–230 (2016).
- [435] Singh, S. P., Samuel, S., Tiwari, S. K. & Singh, R. N. Preparation of thin Co₃O₄ films on Ni and their electrocatalytic surface properties towards oxygen evolution. *Int. J. Hydrog. Energy* **21**, 171–178 (1996).
- [436] Spinolo, G., Ardizzzone, S. & Trasatti, S. Surface characterization of Co₃O₄ electrodes prepared by the sol-gel method. *J. Electroanal. Chem.* **423**, 49–57 (1997).
- [437] Fradette, N. & Marsan, B. Surface Studies of Cu_xCo_{3-x}O₄ Electrodes for the Electrocatalysis of Oxygen Evolution. *J. Electrochem. Soc.* **145**, 2320 (1998).
- [438] Longhi, M. & Formaro, L. An old workhorse of oxide investigations: new features of Co₃O₄. *J. Electroanal. Chem.* **464**, 149–157 (1999).
- [439] Lyu, J. *et al.* Electrochemical performance of hydrothermally synthesized rGO based electrodes. *Mater. Today Energy* **13**, 277–284 (2019).
- [440] Yang, I., Kim, S.-G., Kwon, S. H., Kim, M.-S. & Jung, J. C. Relationships between pore size and charge transfer resistance of carbon aerogels for organic electric double-layer capacitor electrodes. *Electrochimica Acta* **223**, 21–30 (2017).
- [441] Zhang, X. *et al.* Morphological control of RGO/CdS hydrogels for energy storage. *CrystEngComm* **18**, 1090–1095 (2016).

- [442] Cooper, S. J., Bertei, A., Finegan, D. P. & Brandon, N. P. Simulated impedance of diffusion in porous media. *Electrochimica Acta* **251**, 681–689 (2017).
- [443] Yoo, H. D., Jang, J. H., Ryu, J. H., Park, Y. & Oh, S. M. Impedance analysis of porous carbon electrodes to predict rate capability of electric double-layer capacitors. *J. Power Sources* **267**, 411–420 (2014).
- [444] Moberg, L. & Karlberg, B. An improved N,N'-diethyl-p-phenylenediamine (DPD) method for the determination of free chlorine based on multiple wavelength detection. *Anal. Chim. Acta* **407**, 127–133 (2000).
- [445] Brundle, C. R. The application of electron spectroscopy to surface studies. *J. Vac. Sci. Technol.* **11**, 212–224 (1974).
- [446] Sordello, F., Ghibauda, M. & Minero, C. Photoelectrochemical Performance of the Ag(III)-Based Oxygen-Evolving Catalyst. *ACS Appl. Mater. Interfaces* **9**, 23800–23809 (2017).
- [447] Wu, Z.-S. *et al.* Synthesis of Graphene Sheets with High Electrical Conductivity and Good Thermal Stability by Hydrogen Arc Discharge Exfoliation. *ACS Nano* **3**, 411–417 (2009).
- [448] Booth, T. J. *et al.* Macroscopic Graphene Membranes and Their Extraordinary Stiffness. *Nano Lett.* **8**, 2442–2446 (2008).
- [449] Balandin, A. A. *et al.* Superior Thermal Conductivity of Single-Layer Graphene. *Nano Lett.* **8**, 902–907 (2008).
- [450] Li, M., Yang, X., Ren, J., Qu, K. & Qu, X. Using Graphene Oxide High Near-Infrared Absorbance for Photothermal Treatment of Alzheimer's Disease. *Adv. Mater.* **24**, 1722–1728 (2012).
- [451] Yang, F., Liu, Y., Gao, L. & Sun, J. pH-Sensitive Highly Dispersed Reduced Graphene Oxide Solution Using Lysozyme via an in Situ Reduction Method. *J. Phys. Chem. C* **114**, 22085–22091 (2010).
- [452] Chowdhury, I., Mansukhani, N. D., Guiney, L. M., Hersam, M. C. & Bouchard, D. Aggregation and Stability of Reduced Graphene Oxide: Complex Roles of Divalent Cations, pH, and Natural Organic Matter. *Environ. Sci. Technol.* **49**, 10886–10893 (2015).
- [453] Robinson, J. T. *et al.* Ultrasmall Reduced Graphene Oxide with High Near-Infrared Absorbance for Photothermal Therapy. *J. Am. Chem. Soc.* **133**, 6825–6831 (2011).
- [454] Bai, H., Li, C., Wang, X. & Shi, G. A pH-sensitive graphene oxide composite hydrogel. *Chem. Commun.* **46**, 2376–2378 (2010).
- [455] Liu, J., Cui, L. & Losic, D. Graphene and graphene oxide as new nanocarriers for drug delivery applications. *Acta Biomater.* **9**, 9243–9257 (2013).
- [456] Hu, H., Yu, J., Li, Y., Zhao, J. & Dong, H. Engineering of a novel pluronic F127/graphene nanohybrid for pH responsive drug delivery. *J. Biomed. Mater. Res. A* **100A**, 141–148 (2012).
- [457] Oh, Y. *et al.* Understanding the pH-responsive behavior of graphene oxide membrane in removing ions and organic micropollutants. *J. Membr. Sci.* **541**, 235–243 (2017).
- [458] Chen, J.-L. & Yan, X.-P. Ionic strength and pH reversible response of visible and near-infrared fluorescence of graphene oxide nanosheets for monitoring the extracellular pH. *Chem. Commun.* **47**, 3135–3137 (2011).
- [459] Thermo-sensitive graphene oxide-polymer nanoparticle hybrids: synthesis, characterization, biocompatibility and drug delivery - Journal of Materials Chemistry B (RSC Publishing) DOI:10.1039/C3TB21538E. <https://pubs-rsc-org.proxy3.library.mcgill.ca/en/content/articlehtml/2014/tb/c3tb21538e>.
- [460] Pelton, R. H. & Chibante, P. Preparation of aqueous latices with N-isopropylacrylamide. *Colloids Surf.* **20**, 247–256 (1986).

- [461] Liu, J. *et al.* Bioinspired graphene membrane with temperature tunable channels for water gating and molecular separation. *Nat. Commun.* **8**, 2011 (2017).
- [462] Pei, S., Wei, Q., Huang, K., Cheng, H.-M. & Ren, W. Green synthesis of graphene oxide by seconds timescale water electrolytic oxidation. *Nat. Commun.* **9**, 145 (2018).
- [463] Fu, L., Lai, G., Jia, B. & Yu, A. Preparation and Electrocatalytic Properties of Polydopamine Functionalized Reduced Graphene Oxide-Silver Nanocomposites. *Electrocatalysis* **6**, 72–76 (2015).
- [464] Luo, D., Zhang, G., Liu, J. & Sun, X. Evaluation Criteria for Reduced Graphene Oxide. *J. Phys. Chem. C* **115**, 11327–11335 (2011).
- [465] Zhou, Y., Bao, Q., Tang, L. A. L., Zhong, Y. & Loh, K. P. Hydrothermal Dehydration for the “Green” Reduction of Exfoliated Graphene Oxide to Graphene and Demonstration of Tunable Optical Limiting Properties. *Chem. Mater.* **21**, 2950–2956 (2009).
- [466] Xu, Y., Sheng, K., Li, C. & Shi, G. Self-Assembled Graphene Hydrogel via a One-Step Hydrothermal Process. *ACS Nano* **4**, 4324–4330 (2010).
- [467] Mattevi, C. *et al.* Evolution of Electrical, Chemical, and Structural Properties of Transparent and Conducting Chemically Derived Graphene Thin Films. *Adv. Funct. Mater.* **19**, 2577–2583 (2009).
- [468] Lowry, G. V. *et al.* Guidance to improve the scientific value of zeta-potential measurements in nanoEHS. *Environ. Sci. Nano* **3**, 953–965 (2016).
- [469] Lv, W. *et al.* Functionalization of carbon and gold nanomaterials using PNIPAAm grafted dextran: a general route towards robust and smart nanomaterials. *J. Mater. Chem.* **22**, 11290–11296 (2012).
- [470] Thebo, K. H. *et al.* Highly stable graphene-oxide-based membranes with superior permeability. *Nat. Commun.* **9**, 1486 (2018).
- [471] Zhong, J. *et al.* Efficient and scalable synthesis of highly aligned and compact two-dimensional nanosheet films with record performances. *Nat. Commun.* **9**, 3484 (2018).
- [472] Zou, R. *et al.* Carbonized polydopamine nanoparticle reinforced graphene films with superior thermal conductivity. *Carbon* **149**, 173–180 (2019).
- [473] Ludwig, T. *et al.* Boosting nitrogen-doping and controlling interlayer spacing in pre-reduced graphene oxides. *Nano Energy* **78**, 105286 (2020).
- [474] Krishnamoorthy, K., Veerapandian, M., Yun, K. & Kim, S.-J. The chemical and structural analysis of graphene oxide with different degrees of oxidation. *Carbon* **53**, 38–49 (2013).
- [475] Stobinski, L. *et al.* Graphene oxide and reduced graphene oxide studied by the XRD, TEM and electron spectroscopy methods. *J. Electron Spectrosc. Relat. Phenom.* **195**, 145–154 (2014).
- [476] Mayo, S. & Endrizzi, M. X-Ray Phase Contrast Methods. in *Handbook of Advanced Nondestructive Evaluation* (eds. Ida, N. & Meyendorf, N.) 1053–1093 (Springer International Publishing, 2019).
- [477] Raven, C. *et al.* Phase-contrast microtomography with coherent high-energy synchrotron x rays. *Appl. Phys. Lett.* **69**, 1826–1828 (1996).
- [478] Momose, A., Takeda, T., Itai, Y. & Hirano, K. Phase-contrast X-ray computed tomography for observing biological soft tissues. *Nat. Med.* **2**, 473–475 (1996).
- [479] Auweter, S. D. *et al.* X-ray phase-contrast imaging of the breast—advances towards clinical implementation. *Br. J. Radiol.* **87**, 20130606 (2014).
- [480] Momose, A. & Fukuda, J. Phase-contrast radiographs of nonstained rat cerebellar specimen. *Med. Phys.* **22**, 375–379 (1995).

- [481] Baruchel, J., Lodini, A., Romanzetti, S., Rustichelli, F. & Scrivani, A. Phase-contrast imaging of thin biomaterials. *Biomaterials* **22**, 1515–1520 (2001).
- [482] Arfelli, F. *et al.* Mammography with Synchrotron Radiation: Phase-Detection Techniques. *Radiology* **215**, 286–293 (2000).
- [483] Yang, X.-Y. *et al.* Hierarchically porous materials: synthesis strategies and structure design. *Chem. Soc. Rev.* **46**, 481–558 (2017).